

UNIVERSITY OF SOUTHAMPTON

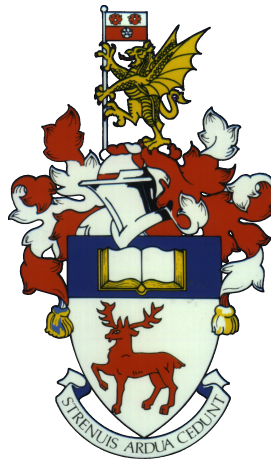
FACULTY OF ENGINEERING AND THE ENVIRONMENT

Airbus Noise Technology Centre

High-Order Numerical Investigations into Landing Gear Wheel Noise

by

Meng Wang



Thesis for the degree of Doctor of Philosophy

March 2017

UNIVERSITY OF SOUTHAMPTON

ABSTRACT

FACULTY OF ENGINEERING AND THE ENVIRONMENT

Airbus Noise Technology Centre

Doctor of Philosophy

High-Order Numerical Investigations into Landing Gear Wheel Noise

by **Meng Wang**

Wheels are significant landing gear noise sources. In this project, high-order numerical simulations were conducted to investigate the landing gear wheel noise generation mechanisms and noise reduction treatments. The high-order solver solves the Navier-Stokes equations on multi-block structured grids. In this work, a modified solver was developed based on cell-centred formulation, which can provide more accurate solutions than cell-vertex space. This solver applies a finite-difference scheme at interior control points and at block interfaces with smooth grid metrics. At discontinuous block interfaces, a finite-volume method is employed as an interface condition. Two sets of interpolation schemes were developed to apply the finite volume method. This cell-centred high-order solver is accurate and robust for aeroacoustic simulations of complex geometries.

The numerical solver was applied to investigate the major noise sources of a 33% scaled isolated landing gear wheel by simulating three different wheel configurations using a hybrid CFD/FW-H approach. The configurations simulated include a baseline wheel with a hub cavity and two rim cavities. Two additional simulations were performed; one with the hub cavity covered and the other with both the hub cavity and rim cavities covered. The tyre is the main low frequency noise source and shows a lift dipole and side force dipole pattern depending on the frequency. The hub cavity is identified as the dominant middle frequency noise source and radiates in a frequency range centred around the first and second depth modes of the cylindrical hub cavity. The rim cavities are the main high-frequency noise sources. The largest noise reduction is achieved by covering both hub and rim cavities in the hub side direction.

Simulations of two wheels in tandem were also performed to study the wheel interaction noise at different angles of attack. The interaction noise is greatest at zero angle of attack, radiating towards the two sideline directions with a spectral peak at $St_W = 0.19$, based on the width of the wheel. The dominant interaction noise source is the upstream shoulder of the downstream wheel. The wheel interaction noise is reduced at positive angles of attack, as less of the downstream wheel is immersed in the wake of the upstream wheel. A gap fairing was simulated, and it can significantly reduce the interaction noise by eliminating large-scale turbulent structures in the gap region. The downstream wheel hub and rim cavities do not have large contributions to the far-field acoustics.

Contents

1	Introduction	1
1.1	Research background and objectives	1
1.2	Original contributions	3
1.3	Thesis outline	4
2	Literature Review	5
2.1	Fundamental of aerodynamic sound	5
2.2	Bluff body flows and acoustics	6
2.2.1	Single circular cylinder	7
2.2.2	Tandem circular cylinders	11
2.2.3	Section summary	12
2.3	Landing gear wheel flows and acoustics	12
2.3.1	Wheels in landing gear configurations	12
2.3.2	Isolated wheels	15
2.3.3	Section summary	17
2.4	Cylindrical cavity flow and noise	17
2.4.1	Cavity resonance	17
2.4.2	Mean and unsteady flow features	18
2.4.3	Section summary	20
2.5	Computational aeroacoustics	21
2.5.1	Acoustic modelling	21
2.5.2	Numerical issues	25
2.5.3	Section summary	28
2.6	Chapter summary	28
3	Numerical Methodology	29
3.1	Introduction	29
3.2	Governing equations	29
3.3	Spatial discretisation	31
3.3.1	Interior scheme	32
3.3.2	Boundary schemes	33
3.4	Filtering scheme	33
3.5	Temporal scheme	35
3.6	Boundary conditions	38
3.6.1	Far-field pressure boundary condition	38
3.6.2	Outflow boundary condition	39
3.7	Turbulence model	40

3.7.1	S-A model	40
3.7.2	DDES method	42
3.8	Parallel implementation	42
3.9	Grid parameters	42
3.10	Acoustic radiation model	44
3.11	Dynamic mode decomposition	45
3.12	Chapter summary	46
4	Numerical Development of a Cell-Centred Solver	49
4.1	Introduction	49
4.2	Motivation for a cell-centred method	51
4.2.1	Vortex convection problem	53
4.2.2	2D single cylinder flow	55
4.2.3	Section summary	58
4.3	Numerical techniques in FV interface condition	58
4.3.1	Cell-centred interpolation schemes	58
4.3.2	Implementation of FV interface condition	65
4.3.3	Section summary	66
4.4	Eigenvalue analysis	66
4.5	Grid convergence study	69
4.6	Validations of cell-centred method	70
4.6.1	Single cylinder flow	71
4.6.2	Tandem cylinders flow	74
4.6.3	Section summary	85
4.7	Chapter summary	88
5	An Isolated Landing Gear Wheel	91
5.1	Introduction	91
5.2	Grid detail and computational setup	92
5.3	Aerodynamic results	95
5.3.1	Forces	96
5.3.2	Instantaneous flow field	97
5.3.3	Time-averaged flow quantities	98
5.3.4	Unsteady flow data	106
5.3.5	Section summary	108
5.4	Acoustic results	109
5.4.1	Validation of far-field acoustics	111
5.4.2	Far-field acoustics of the baseline geometry	114
5.4.3	Effects of covering hub and rim cavities	122
5.4.4	Section summary	123
5.5	Chapter summary	124
6	Landing Gear Wheels in Tandem	127
6.1	Introduction	127
6.2	Computational setup	128
6.3	Aerodynamic results at zero angle of attack	130
6.3.1	Instantaneous flow field	130










6.3.2	Forces	131
6.3.3	Steady and unsteady statistics	132
6.3.4	Section summary	138
6.4	Acoustic results at zero angle of attack	139
6.4.1	Acoustics of the baseline geometry	139
6.4.2	Effects of covering hub and rim cavities on the downstream wheel	149
6.4.3	Effects of a gap fairing	149
6.4.4	Section summary	150
6.5	Effects of angle of attack	151
6.5.1	Aerodynamic results	151
6.5.2	Acoustic results	156
6.5.3	Section summary	156
6.6	Chapter summary	157
7	Conclusions and Recommendations	161
7.1	Conclusions	161
7.1.1	Cell-centred numerical method development	161
7.1.2	Isolated landing gear wheel simulations	162
7.1.3	Tandem landing gear wheels simulations	164
7.2	Recommendations for future work	165
7.2.1	Development of numerical techniques	165
7.2.2	Physics of landing gear wheel flows and acoustics	166
A	Temporal Scheme Error Analysis	167
A.1	Inviscid vortex convection	167
A.2	Circular cylinder flow	168
B	Validation of S-A Turbulence Model	171
C	Cell-Centred Interpolation Schemes	173
C.1	FVI boundary closure schemes	173
C.2	HRI boundary closure schemes using halo point	175
D	Roe's Riemann Solver	177
E	Acoustic Corrections for Long-Span Bodies	179
F	Resonant Frequencies of Acoustic Cavities	181
F.1	Cylindrical cavities	181
F.2	Cylindrical cavities with annular volume	182
G	Cylindrical Cavity Simulations	185
G.1	Introduction	185
G.2	Computational setup	185
G.3	Validations and verifications	187
G.4	Effects of depth-to-diameter ratios on aerodynamic results	194
G.5	Effects of depth-to-diameter ratios on acoustic results	199
G.6	Summary	200

H Vortex Structures for Tandem Wheels	203
References	205

List of Figures

2.1	Front view of experimental setup for a short circular cylinder by Zdravkovich <i>et al.</i> [13], where flow is in the positive x direction. The origin of the axes is at the centre of the cylinder. The spanwise length and the diameter of the cylinder are W and D , respectively.	8
2.2	Flow structures around free ends of a short circular cylinder by Zdravkovich <i>et al.</i> [13]. The axes origin is at the centre of the circular cylinder, and the streamwise, transverse and spanwise flow directions are along the x axis, y axis and z axis, respectively.	9
2.3	Pressure coefficient C_p distributions on an upper half cylinder surface at $W/D = 1$ by Zdravkovich <i>et al.</i> [13], where $\theta = 0^\circ$ is the stagnation point and z represents the spanwise direction.	9
2.4	Sketch of flow features past a coin-like circular cylinder by Zdravkovich <i>et al.</i> [14]. IS: primary separation; 2S: secondary separation; SI: separation islet; RA: re-attachment; ---: separation bubble; - - - -: streamwise vortex filaments.	10
2.5	Velocity magnitude and direction between upstream and downstream wheels, from Lazos [27].	13
2.6	Surface flow topology, together with mean surface pressure coefficients, with flow separations and attachments highlighted, from Lazos [33]. . . .	14
2.7	Schematic of a cylindrical cavity geometry.	18
2.8	Surface oil flow on side and bottom walls of a cylindrical cavity at $\varpi = 0.47$ [51], where $\theta = 0^\circ, 180^\circ$ indicate the upstream and downstream directions, respectively. The vortex centre is located at $\theta \approx 65^\circ$ on the upstream sidewall and exits the cavity at $\theta \approx 220^\circ$ on the downstream sidewall.	19
2.9	Vortex tube visualisation at $\varpi = 0.47$, reproduced from Ref. [52].	19
2.10	Acoustic models in different flow regions.	21
2.11	The spectral resolution characteristics of a standard explicit fourth-order scheme (—), a standard explicit sixth-order scheme (—), an optimised fourth-order DRP scheme (—) [69], a low dispersive and low dissipative explicit fourth-order scheme (—) [83], an optimised prefactored fourth-order scheme (—) [84] and an optimised pentadiagonal compact fourth-order scheme (—) [85]. The exact numerical solution is given by —. . .	27
3.1	The spectral resolution of the compact central spatial scheme in Equation 3.12.	32
3.2	The spectral resolution errors for the fully biased boundary spatial schemes (Equation 3.13).	34

3.3	The spectral resolution errors for the boundary spatial schemes using halo point information (in Equation 3.14).	34
3.4	The transfer function profiles for the compact filter in Equation 3.15.	35
4.1	Two types of interface conditions with cell vertices (grid points) and cell centres indicated by circles and triangles, respectively. Block one, block two and block interface are coloured in blue, red and black, respectively, and halo (ghost) points are given by dashed line.	52
4.2	A one-dimensional cluster of cell vertices (\bullet) and cell centres (\blacktriangle).	53
4.3	Pressure contours at different time levels, obtained by the cell-centred one-to-one interface condition.	54
4.4	Error levels at one-to-one interface against time for a vortex convection problem.	55
4.5	Instantaneous field of Mach number around a cylinder using cell-vertex one-to-one and cell-centred one-to-one methods, where the one-to-one interfaces are highlighted by --- .	56
4.6	Grid quality metric values at block interfaces (---) for the single cylinder case.	57
4.7	Grid point cluster of cell centres (\blacktriangle) and cell vertices (\bullet) for an one-dimensional problem.	60
4.8	Transfer function profiles for FVI and HRI schemes.	65
4.9	A multi-block grid point cluster for eigenvalue analysis, \blacktriangle cell centres, \bullet cell vertices.	68
4.10	Eigenvalue distributions for single-block and two-block cases where $N = 64$.	69
4.11	Pressure contours at different time levels for a grid convergence study of the FV interface treatment.	69
4.12	Convergence rate for a grid convergence study of the FV interface treatment.	70
4.13	Instantaneous iso-contour of $Q = 1.0 \times U_\infty^2/D^2$ colored by local Mach number, where the grey scale shows instantaneous density in a range of $0.94 < \rho/\rho_\infty < 1.02$. The one-to-one interfaces and FV interfaces are highlighted by --- and --- , respectively.	72
4.14	Mean pressure and skin friction coefficients for the cylinder flow case.	74
4.15	Grid quality metric values at block interfaces (---) for the tandem cylinders case.	76
4.16	Instantaneous iso-contour of $Q = 1.0 \times U_\infty^2/D^2$ colored by local Mach number, where the grey scale shows instantaneous density in a range of $0.97 < \rho/\rho_\infty < 1.01$. The one-to-one interfaces and FV interfaces are highlighted by --- and --- , respectively.	77
4.17	Instantaneous spanwise vorticity on $x - y$ plane for the tandem cylinders case with one-to-one interfaces (---) and FV interfaces (---).	78
4.18	Two steady states observed in simulations using the one-to-one interface condition, where interfaces are given by --- .	79
4.19	Mean surface pressure coefficients for the tandem cylinders case.	81
4.20	Root-mean-square surface pressure coefficients for the tandem cylinders case.	82
4.21	Surface pressure spectra at FV interfaces for the tandem cylinders case.	82
4.22	Resolved 2D TKE in the gap region for the tandem cylinders case, with one-to-one interfaces and FV interfaces highlighted by --- and --- , respectively.	84

4.23	Resolved 2D TKE around the downstream cylinder for the tandem cylinders case, with one-to-one interfaces and FV interfaces highlighted by  and  , respectively.	85
4.24	Resolved 2D TKE along two lines of $y/D = 0$ and $x/D = 3$ in the gap region, with the location of FV interfaces indicated by 	86
4.25	Resolved 2D TKE along two lines of $y/D = 0$ and $x/D = 4.45$ around the downstream cylinder, with the location of FV interfaces indicated by 	86
4.26	Far-field acoustic pressure spectra at three microphone positions for the tandem cylinder case using different interface conditions.	87
4.27	Pressure perturbations ($-1.5 \times 10^{-4} < p'/\rho_\infty c_\infty^2 < 1.5 \times 10^{-4}$) for the tandem cylinders case obtained by FV interface () condition.	87
5.1	The geometry of the CADWIE wheel in the simulations. The origin of the axes is at the wheel centre.	92
5.2	The cross section of three geometry configurations on the $x/D = 0$ plane. (a) Baseline geometry; (b) No Hub Cavity (NHC) geometry; (c) No Hub Cavity and Rim Cavities (NHCRC) geometry.	93
5.3	The computational domain and boundary conditions in the simulations.	93
5.4	Mesh topology and grid distribution around the CADWIE wheel on the $x/D = 0$ plane.	94
5.5	Aerodynamic experimental setup of the CADWIE wheel in closed section wind tunnel tests [41].	96
5.6	PSD of force coefficients for different geometry configurations.	97
5.7	Left: instantaneous Q -criterion, where $Q = 10 \times U_\infty^2/D^2$ and is coloured by the local Mach number. Right: instantaneous local Mach number and flow features on the $y/D = 0$ plane highlighted on the left.	99
5.8	Mean surface pressure coefficient on the central plan of the baseline configuration ($z/D = 0$).	100
5.9	Surface topology patterns at locations of flow separation and attachment in the CADWIE wheel case. Left: attachment patterns; right: separation patterns [33].	101
5.10	Surface shear stress lines on the side face with typical flow features highlighted. A: unstable regular node; B, F: saddle of separation; D, H, I, J: saddle of attachment;  : positive open bipartite line;  : negative open bipartite line.	102
5.11	Ground side of shear stress lines from the baseline configuration. A: unstable regular node; F: stable spiral node (focus); E: saddle of separation;  : positive open bipartite line.	103
5.12	Rearward face of shear stress lines from the baseline configuration. A: stable regular node; B, E: saddle of separation; C, D: unstable regular node; F: stable spiral node (focus);  : positive open bipartite line.	103
5.13	Comparisons of streamwise, transverse velocities and streamlines in the wake region on $z/D = 0$ plane (baseline configuration).	105
5.14	Vorticity magnitude on different downstream x planes in the wake region.	106
5.15	Wall pressure spectra at four monitors on the hub.	107

5.16	Instantaneous dynamic modes of surface pressures on CADWIE wheel at different frequencies, with low pressure (LP) regions, high pressure (HP) regions and separation lines (SL) highlighted. Only the real part of the dynamic modes is plotted.	108
5.17	Acoustic experimental setup of the CADWIE wheel in the NTF anechoic wind tunnel [41].	110
5.18	Demonstrations of observer angles, where the hub side observer, sidewall side observer and ground side observer refer to the positions of $(\psi = 90^\circ, \phi = 180^\circ)$, $(\psi = 90^\circ, \phi = 0^\circ)$ and $(\psi = 90^\circ, \phi = 270^\circ)$, respectively.	110
5.19	Comparisons of acoustic pressure spectra at different far-field observers. The experimental data are plotted in the most reliable frequency range, i.e. $f > 300$ Hz; --- first depth mode (646 Hz), --- second depth mode (1292 Hz). The observer angle is defined in Figure 5.18.	112
5.20	Far-field acoustic spectra at the hub side $(\psi = 90^\circ, \phi = 180^\circ)$ and sidewall side $(\psi = 90^\circ, \phi = 0^\circ)$, in the simulation. --- first depth mode (646 Hz), --- second depth mode (1292 Hz).	112
5.21	Far-field experimental acoustic spectra at the hub side $(\psi = 90^\circ, \phi = 180^\circ)$ in Strouhal number scale and frequency scale. The spectra are collapsed using the M^6 power law. --- first depth mode (646 Hz), --- second depth mode (1292 Hz).	113
5.22	Far-field acoustic directivity comparisons. The SPL is integrated between 300 Hz and 6000 Hz.	113
5.23	The value of coherence function γ^2 between the wall pressure fluctuations and the far-field acoustic pressures at the hub side $(\psi = 90^\circ, \phi = 180^\circ)$	114
5.24	PSD and CPSD of far-field acoustic pressures from different parts of the wheel, against both frequency and two Strouhal numbers. ---: first depth mode (646 Hz); ---: second depth mode (1292 Hz). hc , s and t are hub cavity, sidewall and tyre respectively. p is the farfield acoustic pressure.	116
5.25	Directivity of OASPL [dB] against polar and azimuthal angles.	118
5.26	Directivity of narrow band SPL [dB] against polar and azimuthal angles at different frequencies.	118
5.27	The noise source strength $\mathcal{N}(\mathbf{y}, f)$ for the far-field observer at the hub side $(\psi = 90^\circ, \phi = 180^\circ)$	120
5.28	The noise source strength $\mathcal{N}(\mathbf{y}, f)$ for the far-field observer at the sidewall side $(\psi = 0^\circ, \phi = 180^\circ)$	121
5.29	The noise source strength $\mathcal{N}(\mathbf{y}, f)$ for the far-field observer at the ground side $(\psi = 270^\circ, \phi = 180^\circ)$	121
5.30	Far-field acoustic pressure spectra obtained from simulations of the baseline configuration, No Hub Cavity (NHC) configuration and No Hub Cavity and Rim Cavities (NHCRC) configuration. --- first depth mode (646 Hz), --- second depth mode (1292 Hz).	123
5.31	Comparisons of the far-field acoustic directivity obtained from different configurations.	123
6.1	The numerical setup of the tandem wheels.	128
6.2	The grid distributions around the tandem wheels.	129
6.3	Instantaneous iso-contour of $Q = 10 \times U_\infty^2/D^2$ colored by the Mach number.	130

6.4	PSD of the force coefficients in the baseline and control cases.	131
6.5	Mean pressure coefficient C_p on the central plane ($z/D = 0$) of the upstream and downstream wheels.	133
6.6	Pressure coefficient R.M.S. C_p^{rms} on the central plane ($z/D = 0$) of the upstream and downstream wheels.	133
6.7	The vorticity and streamlines of mean flow in the gap region, in comparison with the isolated single wheel case.	134
6.8	The vortex structure visualised by λ_2 criterion.	135
6.9	The instantaneous streamwise velocity in the range of $-0.15 < u/c < 0.3$, and the streamlines, on the $y/D = 0$ plane. P1 and P2 are two surface pressure monitors at the leading edge of the downstream wheel shoulder.	136
6.10	The coherence between surface pressures monitored at two points (P1 and P2) at the leading edge of the downstream wheel in Figure 6.9.	136
6.11	The eigenvalues and modified energy of the dynamic modes for the tandem wheels case, where the blue and the red symbols represent the baseline case and control case, respectively. The number of snapshots is $N = 512$	137
6.12	The instantaneous dynamic mode of the surface pressure on the downstream wheel at $St_W = 0.19$ for the baseline case, where the scale range is $-0.008 < p/\rho_\infty c_\infty^2 < 0.008$ and only the real part of the dynamic mode is plotted.	137
6.13	Far-field acoustics from the Upstream Wheel (UW), Downstream Wheel (DW) and both wheels (Total), in comparison with the isolated Single Wheel (SW) case. --- first depth mode (646 Hz), --- second depth mode (1292 Hz).	140
6.14	CPSD of the far-field acoustics at three different observer positions, using the upstream wheel and downstream wheel acoustic data. --- first depth mode (646 Hz), --- second depth mode (1292 Hz).	140
6.15	Directivity of the OASPL [dB] on different planes.	141
6.16	Directivity of OASPL [dB] against polar angle ψ and azimuthal angle ϕ	142
6.17	Directivity of narrow band SPL [dB] against polar and azimuthal angles at different typical frequencies.	143
6.18	Coherence γ^2 between far-field acoustics from the upstream wheel and the downstream wheel on the $x/D = 0$ plane varying with ϕ . \circ $St_W = 0.19$, $+$ $St_W = 0.38$, — sidewall side ($\phi = 0^\circ, 360^\circ$), — wing side ($\phi = 90^\circ$), — hub side ($\phi = 180^\circ$), — ground side ($\phi = 270^\circ$).	144
6.19	Coherence γ^2 at $f = 80$ Hz ($St_W = 0.19$) between wall pressure fluctuations and far-field acoustic pressures at the hub side.	144
6.20	The noise source strength $\mathcal{N}(\mathbf{y}, f)$ on the upstream (left) and downstream (right) wheels for the far-field observer at $\phi = 180^\circ$ (hub side).	146
6.21	The noise source strength $\mathcal{N}(\mathbf{y}, f)$ on the upstream (left) and downstream (right) wheels for the far-field observer at $\phi = 0^\circ$ (sidewall side).	147
6.22	The noise source strength $\mathcal{N}(\mathbf{y}, f)$ on the upstream (left) and downstream (right) wheels for the far-field observer at $\phi = 270^\circ$ (ground side).	148
6.23	Effects of covering the hub cavity and rim cavities on the sound generated by the downstream wheel. --- first depth mode (646 Hz), --- second depth mode (1292 Hz).	149
6.24	Effects of the gap fairing on the far-field acoustics at three observer positions. --- first depth mode (646 Hz), --- second depth mode (1292 Hz).	150

6.25	Directivity of OASPL [dB] for the baseline case and control case, on the $x/D = 0$ plane.	150
6.26	Mean pressure coefficient C_p on the central plane ($z/D = 0$) of the upstream and downstream wheels obtained at different angles of attack.	152
6.27	The z -vorticity and streamlines of mean flow in the gap region ($z/D = 0$) at different angles of attack.	153
6.28	The pressure perturbation R.M.S. $-0.07 < p^{rms}/\rho_\infty c_\infty^2 < 0.07$ in the gap region ($z/D = 0$) at different angles of attack.	154
6.29	The effective mass flow rate through the gap region.	154
6.30	Far-field acoustics at different angles of attack. --- first depth mode (646 Hz), --- second depth mode (1292 Hz).	156
6.31	Directivity of OASPL [dB] at different angles of attack.	157
A.1	Pressure errors against different grid resolutions using the Implicit Time Stepping (ITS) method and the explicit Low-Dispersion and low-Dissipation Runge-Kutta (LDDRK) method.	168
A.2	Mean pressure coefficient using two time-stepping methods with different CFL numbers.	169
A.3	PSD of the lift coefficient C_L using the two time-stepping methods with different CFL numbers.	169
A.4	Instantaneous local CFL number with the global $CFL_{max} = 25$	170
B.1	The computational setup for the 2D flat plate case [127].	171
B.2	Comparisons of non-dimensional velocity profiles and eddy viscosity profiles at $x = 0.97$ for the 2D flat plate case.	172
C.1	Transfer function profiles for HRI boundary schemes using halo points.	176
E.1	Schematic of a long-span body divided by N subsections [119].	179
F.1	Schematic of a cylindrical cavity geometry.	181
F.2	Schematic of a cylindrical cavity geometry with annular volume at the centre.	183
G.1	Computational domain and boundary conditions for cylindrical cavity simulations.	186
G.2	Mesh topology and grid distributions at cylindrical cavity opening on the $y/D = 0$ plane.	187
G.3	Definitions of observer angles θ and ϕ	187
G.4	Pressure coefficients on the sidewall.	188
G.5	Pressure coefficients on the bottom wall.	188
G.6	Comparisons of mean and R.M.S. streamwise velocity profiles. \circ Experiments [54], — simulation (resolved), — simulation (resolved+modelled), --- monitor positions.	189
G.7	Comparisons of wall pressure spectra at $r/D = 0.35$ on the bottom wall. — Experiments [133], — LES simulation [133], — LBM simulation [134], — DDES simulation.	191
G.8	Comparisons of wall pressure spectra at $y/D = -0.186$ on the sidewall. — Experiments [133], — LES simulation [133], — DDES simulation.	192

G.9	Wall pressure spectra on the sidewall at $y/D = -0.1$ and bottom wall at $r/D = 0.375$. $\circ f_{100}$, $\square f_{110}$, $+ f_{120}$, $\triangle f_{130}$.	193
G.10	Comparisons of far-field acoustic spectra at $\theta = 90^\circ$. — Experiments [133], — LES simulation with direct noise computation [133], — LBM simulation with FW-H solution [134], — DDES simulation with FW-H solution.	194
G.11	Pressure coefficients on cavity walls at different depth-to-diameter ratios.	195
G.12	Visualisation of the vortex structure inside the cavity by plotting iso-contour of pressure coefficient ($C_p = -0.1$).	196
G.13	Wall pressure spectra at $\theta = 0^\circ$, $r/D = 0.35$ on the bottom wall. — $\varpi = 0.3$, — $\varpi = 0.6$, — $\varpi = 1.0$, — $\varpi = 1.5$.	197
G.14	Wall pressure spectra on the cavity bottom wall at $r/D = 0.375$. $\circ f_{100}$, $\square f_{110}$, $+ f_{120}$, $\triangle f_{130}$.	197
G.15	Coherence γ^2 between $p'(\theta)$ and $p'(\theta + 180^\circ)$ on the bottom wall at $r/D = 0.375$. $\circ f_{100}$, $\square f_{110}$, $+ f_{120}$, $\triangle f_{130}$.	198
G.16	Pressure spectra measured at overhead positions with varying distances to the cavity. — $y/D = 0$, — $y/D = 0.5$, — $y/D = 1.0$, — $y/D = 1.5$, — $y/D = 2.0$, — $y/D = 2.5$, --- f_{100} .	199
G.17	Instantaneous pressure fluctuations $p'/\rho_\infty c_\infty^2$ in a range of $[-5, 5] \times 10^{-5}$ at different depth-to-diameter ratios.	200
G.18	Far-field acoustic pressure spectra at $\phi = 90^\circ$ (overhead position) from different depth-to-diameter ratios. — FW-H results, --- f_{100} .	201
G.19	Far-field acoustic directivity of OASPL [dB] at different depth-to-diameter ratios.	202
H.1	Vortex structure in the gap region visualised by λ_2 criterion at different angles of attack.	203

List of Tables

2.1	Table of landing gear wheel studies. LG - Landing Gear, TKE - Turbulence Kinetic Energy.	16
2.2	Features of different interface conditions in CAA.	28
4.1	Parameters that are used to optimise the characteristic resolution of HRI schemes.	63
4.2	Coefficients in HRI scheme for interior grid points in Equation 4.18. . . .	64
4.3	Coefficients in HRI schemes with fully biased boundary treatment in Equation 4.26.	64
4.4	Steady and unsteady statistics for the single cylinder case.	74
4.5	The computational cost in the single cylinder simulations. The computational speed is defined as the total CPU time per grid point per time step, and the relative expense is obtained by comparing with the cell-centred one-to-one interface condition. The total number of processors is 128. . . .	75
4.6	The computational cost in the single cylinder simulations. The computational speed is defined as the total CPU time per grid point per time step, and the relative expense is obtained by comparing with the cell-centred one-to-one interface condition. The total number of processors is 144. . . .	75
4.7	Steady and unsteady statistics for the tandem cylinders case.	80
5.1	Summary of two grid resolutions for the CADWIE wheel case.	93
5.2	Different computational cases in the isolated landing gear wheel simulations. .	95
5.3	Force coefficients from different geometries for the isolated landing gear wheel simulations.	96
6.1	Summary of seven cases in the simulations, where UW and DW represent the upstream wheel and downstream wheel, respectively.	129
6.2	Summary of force coefficients from the isolated Single Wheel (SW) case, the Upstream Wheel (UW) and Downstream Wheel (DW) of the tandem wheels baseline case, and the control case with a gap fairing applied. . . .	131
6.3	Summary of the OASPL [dB] at different far-field observers obtained from Single Wheel (SW) case, and Upstream Wheel (UW), Downstream Wheel (DW) and both wheels (Total) in the tandem wheels case.	141
6.4	The force coefficients obtained at different angles of attack in the tandem wheels simulations.	152
A.1	Mean drag coefficient \bar{C}_D using two time-stepping schemes with different CFL numbers.	169

C.1	Parameters that are used to optimise the characteristic resolution of HRI boundary schemes using halo point information.	175
C.2	Coefficients in HRI schemes using halo point information in Equation C.5.	176
F.1	Cylindrical cavity resonant frequencies [kHz] with different depth-to-diameter ratios.	182
F.2	Resonant frequencies [kHz] for a cylindrical cavity with annular volume at the centre.	184

DECLARATION OF AUTHORSHIP

I, **Meng Wang** , declare that the thesis entitled “*High-Order Numerical Investigations into Landing Gear Wheel Noise*”, and the work presented in the thesis are both my own, and have been generated by me as the result of my own original research. I confirm that:

- This work was done wholly or mainly while in candidature for a research degree at this University;
- Where any part of this thesis has previously been submitted for a degree or any other qualification at this University or any other institution, this has been clearly stated;
- Where I have consulted the published work of others, this is always clearly attributed;
- Where I have quoted the work of others, the source is always given. With the exception of such quotations, this thesis is entirely my own work;
- I have acknowledged all main sources of help;
- Where the thesis is based on work done by myself jointly with others, I have made clear what was done by others and what I have contributed myself;
- Parts of this work have been published as shown in Section [1.2](#).

Signed:

Date:

Acknowledgements

I would like to thank my supervisors Doctor David Angland, and Professor Xin Zhang. Thank Doctor David Angland for his invaluable support, guidance, and patience throughout the course of my Ph.D, which were important for the completion of this work. Thank Professor Xin Zhang for trusting this undergraduate student, who has no previous research experience, to start this Ph.D project directly. Thanks must also go to Doctor Ryu Fattah for his support on code development during the first two years.

I would like to acknowledge the Engineering and Physical Sciences Research Council (EPSRC), and Airbus, who provided and supported this project through the Airbus Noise Technology Centre (ANTC). I would like to acknowledge the IRIDIS High Performance Computing Facility and the associated support services at the University of Southampton, fundamental in the completion of this work.

I would like to thank my colleagues and friends at the University of Southampton for their invaluable support and all the nice times. Thanks go to Fuyang, Guangda, Fernando, James, Shuming, Yu, Stefano, Mathias, Tim, Michael, Utsav.

Finally, I would like to thank my parents and family for everything else.

Nomenclature

Alphanumeric

a, b, c	Coefficients	
c	Speed of sound	m/s
c_p	Specific heat at constant pressure	J/(kg·K)
c_v	Specific heat at constant volume	J/(kg·K)
C_f	Coefficient of skin friction	
C_L, C_D, C_S	Lift, drag and sideforce coefficients	
C_p	Coefficient of pressure	
D	Diameter	m
E	Total energy density	J/kg
e	Specific internal energy density	J/kg
ΔF	Grid quality metric	
f	Frequency	1/s
f_{ijk}	Resonant frequency	1/s
f_i	Function variable at index i	
f'_i	Derivative at index i	
H	Height	m
$H()$	Heaviside function	
J	Jacobian	1/m ³
k	Wavenumber	1/m
L	Length quantity	m

L_i	Dipole source	$\text{kg}/(\text{m}\cdot\text{s}^2)$
M	Mach number	
\mathcal{N}	Noise source strength variable	m/s
p	Pressure	N/m^2
Pr	Prandtl number	
Pr_t	Turbulent prandtl number	
Re	Reynolds number	
S	Surface	
S_{ij}	Symmetric strain rate tensor	$1/\text{s}$
St	Strouhal number	
T	Temperature	K
t	Time	s
T_{ij}	Lighthill stress tensor	$\text{kg}/(\text{m}\cdot\text{s}^2)$
u, v, w	Velocity components in the x, y and z directions	m/s
u^+	Velocity non-dimensionalised by the boundary layer inner scales	
u_τ	Skin friction velocity	m/s
W	Width	m
x, y, z	Cartesian coordinate system	m
y^+	Wall distance non-dimensionalised by the boundary layer inner scales	

Greek

$\alpha, \beta, \gamma_{ij}$	Coefficients	
γ	Ratio of specific heat coefficients	
λ	Spectral radius of the convective flux Jacobian	
γ^2	Coherence function	
Δ	Subgrid length scale	m
δ_{ij}	Dirac delta function	

κ	Modified wavenumber	
κ_c	Cut-off wavenumber	
θ, ψ, ϕ	Observer angles	degrees
θ_{sep}	Separation angle	degrees
μ	Dynamic viscosity	kg/(m · s)
ν	Kinematic viscosity	m ² /s
$\tilde{\nu}$	Modified eddy viscosity	m ² /s
ξ, η, ζ	Computational coordinate system	
ϖ	Depth-to-diameter ratio	
ρ	Density	kg/m ³
σ	Damping functions	
τ	Pseudo time	s
τ_{ij}	Viscous stress tensor	1/s
Φ_i	Dynamic mode	
Ψ	Deviation angle	degrees
$\omega_x, \omega_y, \omega_z$	Vorticity in the x, y and z directions	1/s

Subscripts

$()_0$	Reference quantity
$()_\infty$	Freestream quantity
$()_t$	Turbulent quantity

Superscripts

$()'$	Perturbation quantity
$()^e$	East face quantity
$()^H$	Quantity for high resolution interpolation schemes
$()^w$	West face quantity

$()^{rms}$	Root-mean-square quantity
$\langle \rangle$	Ensemble averaged quantity of variable

Abbreviations

2D	Two Dimensional	
3D	Three Dimensional	
ACARE	Advisory Council for Aeronautical Research in Europe	
ANTC	Airbus Noise Technology Centre	
AoA	Angle of Attack	degree
APE	Acoustic Perturbation Equations	
CAA	Computational Aeroacoustics	
CADWIE	Control of Approach Drag Without Impact on the Environment	
CFD	Computational Fluid Dynamics	
CFL	Courant-Friedrichs-Lewy condition, also referred to as the Courant number	
CIC	Characteristic Interface Condition	
DDES	Delayed Detached Eddy Simulation	
DES	Detached Eddy Simulation	
DMD	Dynamic Mode Decomposition	
DNS	Direct Numerical Simulation	
DRP	Dispersion Relationship Preserving	
DW	Downstream Wheel	
EPSRC	Engineering and Physical Sciences Research Council	
FD	Finite Difference	
FV	Finite Volume	
FVI	Finite Volume Interpolation	
FW-H	Ffowcs Williams and Hawkings	
HPC	High Performance Computing	

HRI	High Resolution Interpolation	
IDDES	Improved Delayed Detached Eddy Simulation	
LDE	Linearised Divergence Equations	
LEE	Linearised Euler Equations	
LES	Large Eddy Simulation	
LG	Landing Gear	
LNE	Linearised Navier-Stokes Equations	
N-S	Navier-Stokes	
NHC	No Hub Cavity	
NHCRC	No Hub Cavity and Rim Cavities	
NTF	Noise Test Facility	
OASPL	OverAll Sound Pressure Level, $p_{\text{ref}} = 20 \mu\text{Pa}$	dB
PPW	Points Per Wavelength	
PSD	Power Spectral Density, $p_{\text{ref}} = 20 \mu\text{Pa}$	dB/Hz
RANS	Reynolds Averaged Navier-Stokes	
RLG	Rudimentary Landing Gear	
RMS	Root Mean Square	
S-A	Spalart-Allmaras	
SPL	Sound Pressure Level, $p_{\text{ref}} = 20 \mu\text{Pa}$	dB
SW	Single Wheel	
TKE	Turbulence Kinetic Energy	
URANS	Unsteady Reynolds Averaged Navier-Stokes	
UW	Upstream Wheel	
ZCBC	Zonal Characteristic Boundary Condition	
ZDES	Zonal Detached Eddy Simulation	

Chapter 1

Introduction

1.1 Research background and objectives

Airframe noise can lead to significant noise pollution by commercial aircraft during landing or take-off. Airframe noise can affect both residents near airports and passengers within aircraft. A commercial aircraft is not allowed to land at most airports without acquiring a noise certification by International Civil Aviation Organization (ICAO). Many aerospace companies and research organizations are trying to deliver innovative noise reduction technologies for tomorrow's aircraft. The Advisory Council for Aeronautical Research in Europe (ACARE) set a target to reduce noise emissions from aircraft by 10 dB by 2020 [1], and to eliminate all noise nuisances outside airport boundaries. Recently, the Flightpath 2050 was set to reduce the perceived noise by 65% by 2050 [2].

Landing gear noise is recognised as one of the major components of airframe noise for commercial aircraft. Therefore, enhancing the knowledge of landing gear noise enables better noise reduction methods to be devised, which is vital for achieving the noise reduction targets for 2020 [1] and 2050 [2]. Most of the early previous landing gear noise studies are based on an experimental approach and the noise predictions are obtained by empirical and semi-empirical methods. Recently, due to the growth of computational capability, many works have been done on numerical simulations of landing gear noise, providing more detailed near-field flow information and far-field acoustic results compared to the previous experimental measurements. These numerical investigations focus on the complete landing gears that contain a large number of basic components with different geometrical scales. Due to the geometrical complexity, the flow field around a complete landing gear is highly turbulent with strong flow interactions between different components, which increases the difficulty of numerical investigations into landing gear noise generation mechanisms. An alternative approach is to study the noise produced by basic landing gear components separately. Wheels are one of the major landing gear components, which can be considered as the most significant noise sources for simplified

two-wheel nose landing gears [3] and important noise contributors for four-wheel and six-wheel main landing gears [4]. However, the majority of the previous experimental and numerical works were performed using complete landing gear configurations, and there is a need to comprehensively study the isolated wheel flows and acoustics due to their significant contributions to the total landing gear noise. This research focuses on noise generation by isolated high-fidelity landing gear wheel models. Thus, the current project can fill in the gap, providing knowledge on the physics of wheel acoustics and aid in noise reduction treatments. The key objectives of this project are summarised as:

1. Development of high-order numerical simulation tools

High-order numerical schemes are required in Computational Aeroacoustics (CAA) due to small components of acoustic fluctuations on a background mean flow. However, high-order simulations are more sensitive to grid quality and less numerically stable, and thereby they are difficult to be applied to complex geometries. This research firstly aims to improve the accuracy and robustness of an in-house high-order CAA solver. This is achieved by:

- (a) Applying a cell-centred formulation to improve numerical accuracy on multi-block structured grids.
- (b) Developing a finite-volume interface condition to reduce grid-induced errors along block interfaces.
- (c) Developing two interpolation schemes to implement the finite-volume method at block interfaces.

2. Isolated landing gear wheel noise

Wheels are a significant noise source for landing gears. A high-fidelity wheel model containing a hub cavity and two rim cavities (see Figure 5.1) is studied, which aims to investigate:

- (a) The aerodynamic and acoustic characteristics of an isolated landing gear wheel.
- (b) The noise sources and noise generation mechanisms of an isolated wheel.
- (c) The effectiveness of noise reduction by covering the hub and rim cavities on an isolated wheel.

3. Interaction noise from two wheels in tandem

Significant aerodynamic and acoustic interactions can occur between the upstream and downstream wheels for four-wheel and six-wheel landing gear configurations. In this thesis, the following perspectives are studied:

- (a) The characteristics of near-field aerodynamic interactions between two wheels in tandem and the features of flow interaction noise.
- (b) The effectiveness of noise reduction by covering the hub and rim cavities on the downstream wheel.

- (c) The effectiveness of noise reduction by using a gap fairing.
- (d) The effects of angle of attack on near-field aerodynamic interactions and far-field acoustic results.

1.2 Original contributions

Some parts of the work in this thesis have been published in conference and journal papers, and some are also intended for publications. They are summarised as follows:

1. Development of a cell-centred high-order CAA solver

Structured grids for complex geometries can contain discontinuous grid metrics at multi-block interfaces. In this project it is demonstrated that the grid-induced errors from such interfaces can be reduced by applying finite difference schemes in the cell-centred space. Further reduction of these grid-induced errors can be achieved by applying an additional finite volume method, which serves as an interface condition. A novel hybrid high-order cell-centred finite difference and finite volume method is developed. The stability and order of accuracy of this hybrid method are demonstrated and the method is validated by simulations of flow around a single cylinder, tandem cylinders, and a complex isolated wheels. Accurate results and robustness are obtained for high-order simulations.

Meng Wang, Ryu Fattah, David Angland, and Xin Zhang, “High-Order Hybrid Cell-Centred Method for Computational Aeroacoustics,” in *21st AIAA/CEAS Aeroacoustics Conference*, AIAA 2015-3279, 2015.

Meng Wang, Ryu Fattah, David Angland, and Xin Zhang, “High-Order Hybrid Cell-Centred Method for Computational Aeroacoustics,” *Journal of Computational Physics*, (under preparation), 2017.

2. Isolated landing gear wheel noise simulations

The major noise sources of a 33% scaled isolated landing gear wheel are investigated by simulating three different wheel configurations using high-order numerical simulations. The baseline configuration is a wheel with a hub cavity and two rim cavities. Two additional simulations are performed; one with the hub cavity covered (NHC) and the other with both the hub cavity and rim cavities covered (NHCRC). These simulations isolate the effects of the hub cavity and rim cavities on the overall wheel noise. The tyre is the main low frequency noise source and shows a lift dipole and side force dipole pattern depending on the frequency. The hub cavity is identified as the dominant middle frequency noise source and radiates in a frequency range centred around the first and second depth modes of the cylindrical hub cavity. The rim cavities are the main high-frequency noise sources. With the hub cavity and rim

cavities covered, the largest reduction in OverAll Sound Pressure Level (OASPL) is achieved in the hub side direction. In the other directivities, there is also a reduction in the radiated sound.

Meng Wang, David Angland, Xin Zhang, and Ryu Fattah, “High-Order Numerical Simulations of An Isolated Landing Gear Wheel with A Hub Cavity,” in *22nd AIAA/CEAS Aeroacoustics Conference*, AIAA 2016-2902, 2016.

Meng Wang, David Angland, and Xin Zhang, “The Noise Generated by a Landing Gear Wheel with Hub and Rim Cavities,” *Journal of Sound and Vibration*, vol. 392, pp. 127-141, 2017, DOI: [10.1016/j.jsv.2016.12.045](https://doi.org/10.1016/j.jsv.2016.12.045).

3. Simulations of interaction noise from two wheels in tandem

The major noise sources of two wheels in tandem are investigated at four angles of attack. The interaction noise is found to be mainly in the side direction with a spectral peak at a Strouhal number of $St_W = 0.19$, based on the wheel width W . The hub and rim cavities on the downstream wheel are not significant contributors to the far-field acoustics. Significant reductions in the low-frequency interaction noise are achieved in all the directions by applying a gap fairing. At non-zero angles of attack, the interaction noise in the side direction is reduced.

Meng Wang, David Angland, and Aline Scotto, “Interaction Noise from Tandem Landing Gear Wheels with Hub and Rim Cavities,” in *23rd AIAA/CEAS Aeroacoustics Conference*, (extended abstract accepted), 2017.

1.3 Thesis outline

An extensive review of the previous work related to the landing gear wheel noise and computational aeroacoustics is provided in Chapter 2. Chapter 3 details the numerical techniques involved in the simulations, including governing equations, spatial and temporal schemes, numerical filtering, boundary conditions, acoustic radiation models, etc. The numerical development of a hybrid high-order cell-centred method and validation tests are illustrated in Chapter 4. Chapter 5 shows the simulations of an isolated landing gear wheel. Chapter 6 investigates the aerodynamic and acoustic interactions by two wheel in tandem. The conclusions and findings in this research are provided in Chapter 7 with recommendations for future work.

Chapter 2

Literature Review

2.1 Fundamental of aerodynamic sound

Aeroacoustics is a subject to study the sound generated as a by-product of turbulence and its interaction with solid bodies. The theory of sound generation from unbounded flows was initially proposed by Lighthill [5]. In this theory, the Navier-Stokes equations are rearranged to form an exact, inhomogeneous wave equation containing noise sources within a turbulent region. The fluid is assumed to be at rest at infinity with mean pressure p_0 , density ρ_0 and speed of sound c_0 , respectively. The Lighthill's equation is written as [5],

$$\left(\frac{\partial^2}{\partial t^2} - c_0^2 \nabla^2 \right) (\rho - \rho_0) = \frac{\partial^2 T_{ij}}{\partial x_i \partial x_j}, \quad (2.1)$$

where T_{ij} is called the Lighthill stress tensor and defined by,

$$T_{ij} = \rho u_i u_j + ((p - p_0) - c_0^2 (\rho - \rho_0)) \delta_{ij} - \tau_{ij}, \quad (2.2)$$

and τ_{ij} is the viscous stress tensor. The first term $\rho u_i u_j$ in Equation 2.2 is the Reynolds stress produced by the turbulent motion, and it is very large in the source region containing turbulence. The second term shows the excess of momentum transfer due to wave amplitude nonlinearity and mean density variations in the source flow. The viscous stress tensor τ_{ij} is a dissipative quantity to attenuate the sound, the effect of which could be ignored for most acoustic radiation problems. The Lighthill's theory implies that the acoustic radiation equation in a stationary, ideal medium with quadrupole sources whose strength per unit volume is the Lighthill stress tensor T_{ij} could be applied to predict the aerodynamic sound generated by unbounded turbulence.

One of the restrictions of Lighthill's theory is that it fails to account for the presence of solid bodies in the flow. In most cases, turbulence can be generated in the boundary layer due to the flow interactions with solid bodies. It is likely that significant sound can be also produced by the unsteady surface forces, which was studied by Curle [6]

by introducing a control surface S that may either enclose a solid body or just contain fluid. The generalised solution to Lighthill's equation for the sound generated by the turbulence in the vicinity of an arbitrary, fixed surface $f(x) = 0$ ($f(x) > 0$ for x out of control surface S and $f(x) < 0$ for x within S) is derived as [6],

$$\left(\frac{\partial^2}{\partial t^2} - c_0^2 \nabla^2 \right) ((\rho - \rho_0) H(f)) = \frac{\partial}{\partial t} (Q \delta(f)) - \frac{\partial}{\partial x_i} (L_i \delta(f)) + \frac{\partial^2 (T_{ij} H(f))}{\partial x_i \partial x_j}, \quad (2.3)$$

where $H(f)$ is the Heaviside unit function. Compared to Lighthill's theory, Curle's equation contains two additional noise sources. The first one is a monopole source $Q = \rho u_n$ due to the unsteady mass flow through the control surface S (volume pulsations), where u_n is the fluid velocity in the surface-normal direction. $L_i = \rho u_i u_n + P_{ij} n_j$, with $P_{ij} = (p - p_0) \delta_{ij} - \tau_{ij}$, is the second additional noise source, and has a dipole behaviour. If S is merely an artificial control surface and just encloses fluids, the surface dipole sources are responsible for the influence of this fluid region on the sound radiated outside S . If S is the boundary of a solid body, the unsteady surface forces represent the surface dipole source which is a result of interactions between the turbulence and the solid bodies.

Curle's equation is valid throughout all space with the presence of stationary solid bodies, and it was extended by Ffowcs Williams and Hawkings (FW-H) [7] to account for arbitrary convective motions of solid bodies with a velocity of v by modifying the source terms in Curle's theory, which are given by [7],

$$\begin{aligned} Q &= \rho_0 v_n + \rho (u_n - v_n), \\ L_i &= \rho u_i (u_n - v_n) + P_{ij} n_j, \end{aligned} \quad (2.4)$$

where v_n is the body moving velocity v projected in the surface-normal direction. In the FW-H equation, the direct acoustic powers radiated by monopoles, dipoles and quadrupoles are scaled with the 4th, 6th and 8th power of the Mach number (M) [8]. The presence of solid bodies increases the acoustic radiation efficiency by a factor of $1/M^4$ for monopoles and a factor of $1/M^2$ for dipoles, compared to the unbounded turbulent motions (which are quadrupole noise sources). For flows over a stationary solid body at low M , the dominant noise source is the dipole of surface unsteady forces. The FW-H equation is a more generalised solution to sound radiation problems. It is a rearrangement of the Navier-Stokes equations and is used to calculate the far-field acoustics from the near-field sources obtained in the numerical simulations.

2.2 Bluff body flows and acoustics

A landing gear wheel can be simplified as a bluff body. To understand the mechanisms of landing gear flows and acoustics, the aerodynamic and acoustic features of bluff body

flows are firstly reviewed in this section.

2.2.1 Single circular cylinder

Long spanwise length circular cylinder

The physics of circular cylinders in cross flow was firstly investigated by Vincenc Strouhal [9] and Theodore von Kármán [10], who found vortex shedding of circular cylinder flows. A complete review on circular cylinder flows was provided by Zdravkovich [11]. It has been found that the Reynolds number Re , based on the flow speed and cylinder diameter, determines the flow characteristics around circular cylinders. Firstly, at a very low Reynolds number of $Re < 4$, the flow is fully attached to the cylinder. At $4 < Re < 40$, the flow starts to separate at the back of the cylinder, leading to a stationary pair of vortices in the wake. At $40 < Re < 150$, the separated flow behind the cylinder turns unstable and two vortices are shed alternatively, forming a laminar Kármán vortex street. The flow at $Re > 150$ can be divided into three distinct flow regimes, which are summarised as:

1. Subcritical flow regime

The upper limit of the Reynolds number in this flow regime is roughly at $Re = 3 \times 10^5$, where a laminar separation occurs at a polar angle of $\theta \approx 80^\circ$. This earlier separation angle induces a wider wake, a low frequency vortex shedding at $St \approx 0.2$, and a higher pressure drag coefficient C_D . The vortex street behind the cylinder is turbulent.

2. Postcritical flow regime

This refers to the flow condition at $Re > 1.9 \times 10^6$. In this flow regime, the boundary layer is fully turbulent, and the separation is delayed due to the fact that the turbulent boundary layer is less susceptible (more resistant) to separation with greater momentum, leading to a narrower wake and a higher vortex shedding frequency at $0.25 < St < 0.3$. An upstream movement of the separation point and an increase in the drag coefficient C_D are observed with Re increasing in this flow regime.

3. Critical flow regime

Between the previous two flow regimes is a critical flow regime, where a boundary layer transition from laminar to turbulence occurs before flow separation. The separation point is delayed from $\theta \approx 80^\circ$ to $\theta \approx 120^\circ$ at $Re = 3 \times 10^5$, causing a sudden increase in the vortex shedding frequency St and a decrease in the drag coefficient C_D . In this flow regime, the flow features are sensitive to the boundary layer transition, which can be affected by the freestream turbulence and surface roughness.

The aerodynamic sound generated by flows around circular cylinders is related to the unsteady surface forces [12]. The fluctuating lift dominates drag, and thereby the far-field acoustics are characterised mainly by a lift dipole directivity at the vortex shedding

frequency. As Re increases, the flow field becomes more turbulent and the spanwise correlation length of the shedding is lower, leading to a more broadband acoustic spectrum.

Short spanwise length circular cylinder

The flow field around a short spanwise length circular cylinder has unique features due to the end effects. Zdravkovich *et al.* [13] performed experiments to systematically investigate the features of flow past free-end circular cylinders of spanwise length-to-diameter ratio W/D varying between 1 and 10. The experimental setup is shown in Figure 2.1, with W and D representing the spanwise length and diameter, respectively.

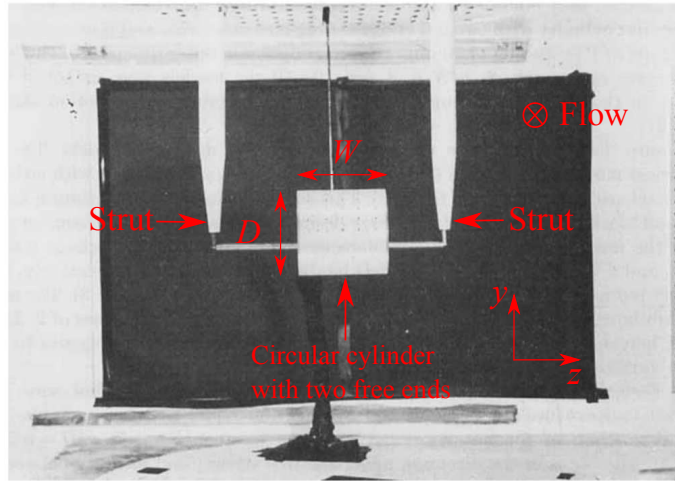


Figure 2.1: Front view of experimental setup for a short circular cylinder by Zdravkovich *et al.* [13], where flow is in the positive x direction. The origin of the axes is at the centre of the cylinder. The spanwise length and the diameter of the cylinder are W and D , respectively.

Figure 2.2 shows the flow field topology around two free ends, which is from the experimental measurements by Zdravkovich *et al.* [13]. The flow features are firstly characterised by an inflow of fluid into a near wake space behind a cylinder at its two free ends in the (x, z) plane of symmetry. This inflow can increase the base pressure, and thus decrease the drag coefficient. This inflow can also widen the separated shear layer in the (x, y) plane and enlarge the vortex formulation region, resulting in a decrease of vortex shedding frequency, compared to an infinite spanwise length circular cylinder. The end effects also induce separated shear layers from the sharp-edged ends, and the development of two counter-rotating vortices, the strength of which is enhanced by the inflow in the (x, z) plane as they are convected downstream. The end effects become more important and the flow field tends to be more three-dimensional as the spanwise length-to-diameter ratio W/D decreases. As a result, the vortex shedding is more irregular with a wider shedding frequency peak, indicating a more broadband sound field.

An asymmetric flow pattern was found when $W/D < 3$. This asymmetry has been shown to be bistable and can be biased to either side of the short cylinder [13]. The surface oil flow and the surface pressure distributions (Figure 2.3) were measured by

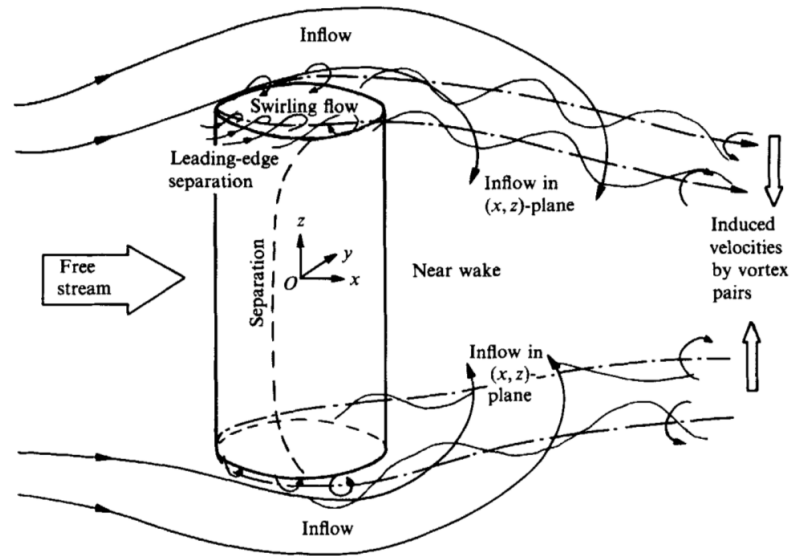


Figure 2.2: Flow structures around free ends of a short circular cylinder by Zdravkovich *et al.* [13]. The axes origin is at the centre of the circular cylinder, and the streamwise, transverse and spanwise flow directions are along the x axis, y axis and z axis, respectively.

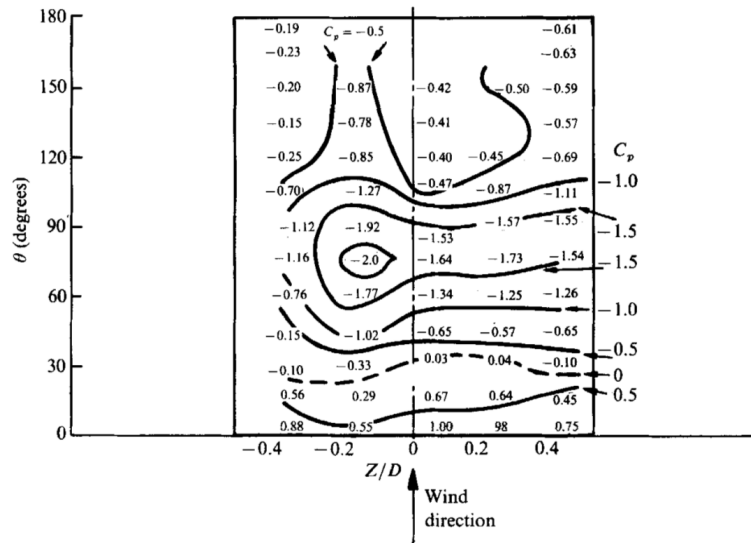


Figure 2.3: Pressure coefficient C_p distributions on an upper half cylinder surface at $W/D = 1$ by Zdravkovich *et al.* [13], where $\theta = 0^\circ$ is the stagnation point and z represents the spanwise direction.

Zdravkovich *et al.* [13] in their experiments, and the surface flow patterns were shown to be asymmetric relative to both the x and y axes of symmetry of the cylinder. This asymmetry was also observed in the experiments of round free-end shapes [13].

Zdravkovich *et al.* [14] performed further experiment in another work to investigate flow features around circular cylinders at very low spanwise length-to-diameter ratios of $0.025 < W/D < 0.89$, which covers the typical ratio of $W/D = 0.3$ for a landing gear wheel geometry. The very short aspect ratio circular cylinders were referred to as coin-like geometries in their experiments. The flow topology is shown in Figure 2.4.

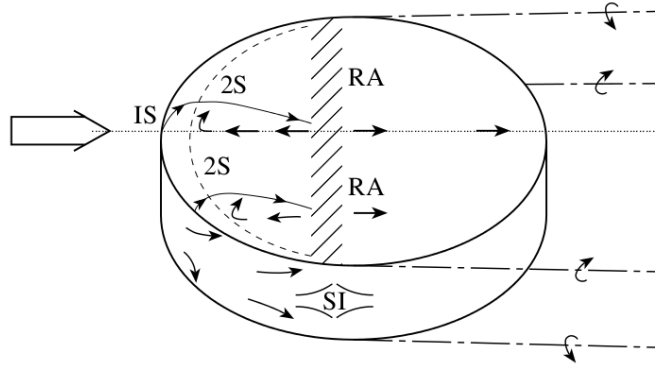


Figure 2.4: Sketch of flow features past a coin-like circular cylinder by Zdravkovich *et al.* [14]. IS: primary separation; 2S: secondary separation; SI: separation islet; RA: re-attachment; ---: separation bubble; -.-.-: streamwise vortex filaments.

The flow firstly separates from the sharp edges along the circumference, and this is the primary separation. The separated flow re-attaches on the flat side, and the re-attachment line is almost straight, perpendicular to the flow direction. Between the primary separation line and the re-attachment line is a separation bubble, and the flow is moving towards the upstream due to an adverse pressure gradient and induces a secondary separation (2S) before reaching the leading edge. An increase in the separation bubble length was found by Zdravkovich *et al.* [14] as W/D increases. This separation bubble can be eliminated by rounding the edges, which produced a significant reduction in the drag coefficient [14]. A crescent-shape region is shown between the primary and secondary separations. On the cylindrical segment, the flow separates at two sides, forming two separation islets, which are different from separation lines observed by long spanwise circular cylinders. The separation islets are induced by the disruption of separation lines by the flow at the edges. There are four vortices formed after the trailing edge, and any two neighbouring vortices are counter rotating.

The end effects observed in the experiments by Zdravkovich *et al.* [13, 14] have also been confirmed by many numerical simulations, which can be found in Refs. [15–18].

2.2.2 Tandem circular cylinders

Two circular cylinders in tandem have many applications on a landing gear geometry, such as tandem wheels geometry, and the drag-stay and main strut geometry. Significant aerodynamic and acoustic interactions can occur between two cylinders in tandem. The flow features surrounding a tandem circular cylinders configuration can be grouped into three regimes [19, 20], depending on their separation distance L/D :

1. Slender-body regime

The separation distance in this regime is at $1 < L/D < 1.2$ to 1.8 , depending on the Reynolds number [19]. The separated shear layers from the upstream cylinder roll up after the downstream cylinder and do not reattach to the downstream cylinder, due to the small separation distance. The vortex shedding behind the downstream cylinder is formed by the detached shear layer from the upstream cylinder. Compared to a single cylinder case, the shedding frequency is higher and the wake is narrower [21] for a tandem cylinders configuration. The downstream cylinder behaves like a short splitter plate [21], and the drag coefficient is negative [20], indicating a thrust force acting on the downstream cylinder body.

2. Re-attachment regime

This regime occurs at 1.2 to $1.8 < L/D < 3.0$ to 3.8 , depending on the Reynolds number [22]. The separated shear layers of the upstream cylinder re-attach on the rear surface (smaller L/D) and front surface (larger L/D) of the downstream cylinder [21]. The gap region is characterised by a relatively steady re-attachment field, and vortex shedding is only present behind the downstream cylinder. This downstream cylinder vortex shedding is affected by the presence of the upstream cylinder, and the vortex formation depends on the upstream separated shear layer [23]. As the separation distance increases, the shedding frequency decreases and becomes slower than a single cylinder case [20].

3. Co-shedding regime

This regime refers to a separation distance of $L/D > 3.0$ to 3.8 , depending on the Reynolds number [19, 24]. The separated shear layers of the upstream cylinder roll up before reaching the downstream cylinder, and vortex shedding occurs for both cylinders at the same frequency. The shedding frequency gradually increases towards the single cylinder case with L/D increasing [20]. The unstable flow features in the gap generate highly fluctuating pressure and lift coefficients for the downstream cylinder. Independent vortex formation and shedding from the two cylinders can be expected at $L/D > 6$ to 8 [25].

An aeroacoustic benchmark case of tandem circular cylinders, with a separation distance of $L = 3.7D$ at $Re = 1.66 \times 10^5$, was proposed to represent tandem landing gear

wheels [26]. In this benchmark experiment, a co-shedding state was found with both cylinders shedding vortices [26]. The downstream cylinder was demonstrated to be the dominant noise source, which was characterised with tonal noise at the shedding frequency. Numerous simulations have been performed on this benchmark case, and they were summarised by Lockard [26], who demonstrated that the turbulence model, numerical schemes and grids were significant to correctly simulate the aerodynamic and acoustic behaviours of this tandem cylinders. This benchmark case is also used to validate the numerical methodology in this thesis in Chapter 4.

2.2.3 Section summary

Landing gear wheels are essentially bluff bodies. In this section, the flow and acoustic features of single and tandem circular cylinders were reviewed. The Reynolds number and separation distance determine the flow regimes of single cylinder and tandem cylinders, respectively. For a cylinder with a short spanwise length, the end effects lead to an asymmetric mean flow with respect to the plane of symmetry, and four vortices induced by flow separations from two free ends. For coin-like circular cylinders, complex flow topologies were demonstrated at the two sides. The end effects become more prominent as the spanwise length-to-diameter ratio decreases.

2.3 Landing gear wheel flows and acoustics

Both nose and main landing gears include a large number of components, such as wheels, axles, shafts with lateral support struts, drag braces, actuators and doors. These components result in a broadband noise spectrum in nature but with spectral peaks in low and middle range frequencies [27]. Wheels are one of the most major components, which can be considered as significant low and middle frequency noise sources [3, 4, 28–32]. In this section, the previous work on wheel flows and acoustics in both landing gear configurations and isolated configurations will be reviewed.

2.3.1 Wheels in landing gear configurations

Heller and Dobrzynski [28] conducted pioneering landing gear experiments. They used simplified scaled models of both two-wheel and four-wheel landing gears and found that the major components, such as shaft, actuators, drag braces, and wheels combined to produce a haystack-shaped acoustic spectrum. They identified that one of the dominant noise sources for a four-wheel landing gear was the wheel interaction, which was caused by flow separations from the upstream wheel and wake impingements on the downstream wheel.

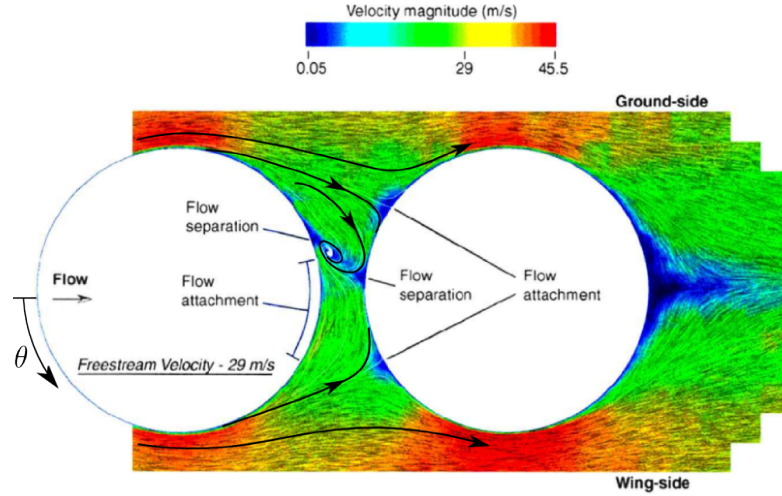


Figure 2.5: Velocity magnitude and direction between upstream and downstream wheels, from Lazos [27].

Lazos [27] performed an experiment to study the mean flow characteristics in the wheel gap region of a generic four-wheel landing gear configuration at $Re = 6 \times 10^5$ (based on the wheel diameter), and the mean velocity field is shown in Figure 2.5, where a vortex is shown at the ground side. The separated flow from the upstream wheel re-attaches on the front face of the downstream wheel at $\theta = 30^\circ$ and $\theta = -35^\circ$ at the wing side and ground side, respectively, presenting a 5° asymmetry. This asymmetry is due to a velocity deflect at the wing side of the upstream wheel at 90° , compared to the ground side of the upstream wheel at $\theta = -90^\circ$. This asymmetry allows the flow from the wing side to penetrate further into the gap region, forcing the separated flow from the upstream wheel at the ground side to roll up into a vortex. The vortex is oscillating in the gap region, and its position was hypothesised by Lazos [27] to depend on the unstable vorticity layer developed by the flow separation at the ground side of the upstream wheel. Additionally, two flow states were identified in the experiment. One state was associated with a late flow separation from the upstream wheel, and the second presented a massive flow separation. These two states can change between each other, indicating a flow sensitivity, which might be related to the critical Reynolds number in this experiment.

Lazos [33] further investigated the surface flow topology by an analysis of shear stress lines in surface oil flow. The flow separations and attachments were highlighted, which can be considered as potential noise sources. The basic surface flow patterns are demonstrated in Figure 5.9 in Section 5.3.3. The most complex surface flow patterns are on the rear face of the upstream wheel in Figure 2.6(a) and the front face of the downstream wheel in Figure 2.6(b), due to the flow interactions in the gap region. The complexity in the surface flow topology highlights the difficulty in performing accurate numerical predictions of landing gear wheel flows and acoustics.

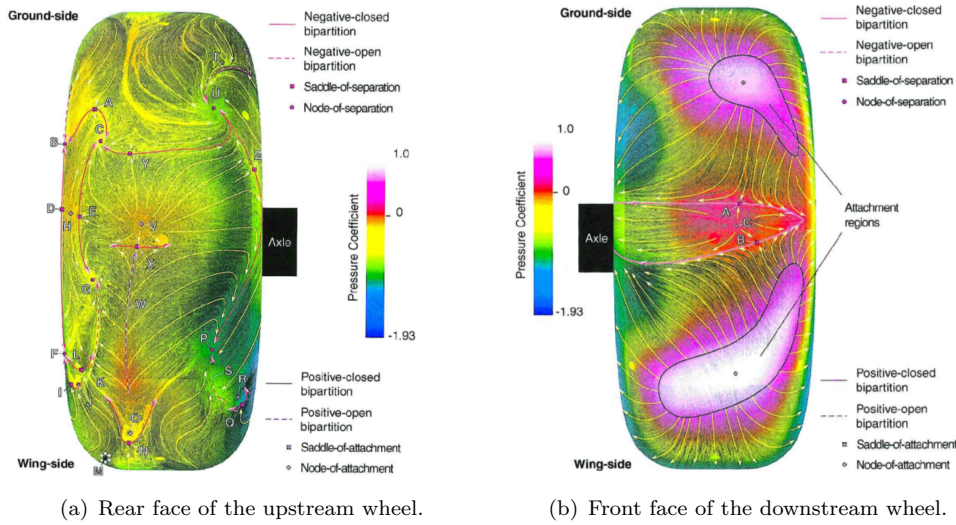


Figure 2.6: Surface flow topology, together with mean surface pressure coefficients, with flow separations and attachments highlighted, from Lazos [33].

Several other experimental and numerical tests have been performed to study the flow features and far-field acoustics of landing gear wheels. Neuhart *et al.* [34] performed aerodynamic experiments of a Gulfstream G550 nose landing gear. They reported that the hub area on the wheels might be one of the stronger noise sources due to the high levels of turbulence kinetic energy and pressure perturbations found around the hub area. Yokokawa *et al.* [31] measured the far-field acoustics generated from a two-wheel main landing gear. They found that the dominant noise sources were the tyre and the sidebrace, compared to the cylinder, the axle, the torque link and the landing gear door. In a four-wheel Rudimentary Landing Gear (RLG) test, complex flow interactions were found between the upstream and downstream wheels [35, 36], which might be a significant noise source. Quayle *et al.* [37] performed phased microphone array measurements to study a simplified four-wheel landing gear. They observed that the far-field acoustics increased in a broadband frequency range as the upstream wheel edge radius increased, and decreased between 2-6 kHz as the downstream wheel edge radius increased [37]. They also observed a reduction of 8 dB with a gap fairing applied to reduce flow interactions [37], and such a reduction was also noticed by Khorrami and Lockard [38] in their simulations. Liu *et al.* [3] performed high-order simulations of a generic two-wheel nose landing gear and found that the wheel noise dominated the strut noise and the axle noise. They observed that more wheel noise radiated towards the sideline direction. The same geometry was investigated numerically by Casalino *et al.* [39], who observed two acoustic tones. The first tone is related to a plane wave corresponding to the floor-to-floor cavity distance, while the second tone is from an azimuthal mode of the wheel cavities [39]. Jaeger *et al.* [40] experimentally studied the noise generated by a high-fidelity six-wheel landing gear, and found 3 dB reduction in the far-field acoustic Sound Pressure Level (SPL) can be achieved by covering the wheel hub cavity with a

flat plate.

All these works highlight the importance of wheels to the overall landing gear noise. However, due to the complex flow interactions between different components in a complete landing gear configuration, the mechanisms of wheel flows and acoustics cannot be revealed by these works, and there is a need to study the landing gear wheel geometry separately from a landing gear configuration.

2.3.2 Isolated wheels

Compared to a complete landing gear geometry, the isolated wheel configuration has been relatively less studied. The previous efforts were demonstrated by Zhang *et al.* [41] and Spagnolo *et al.* [42, 43].

Zhang *et al.* [41] performed aerodynamic and aeroacoustic experiments of an isolated high-fidelity landing gear wheel including a tyre, a sidewall, a hub, a hub cavity and rim cavities. They found that the wheel noise was characterised by broadband middle frequency noise centred around 630 Hz and 1250 Hz, which were fixed by the geometry dimensions and did not scale with flow velocities. This middle frequency noise will be shown in Chapter 5 to be due to the hub cavity resonance of depth modes. Zhang *et al.* [41] also observed that the mean flow field in the wake was not symmetrical with respect to the horizontal plane inspite of a symmetrical geometry. This asymmetry will be detailed in Chapter 5. The experimental measurements by Zhang *et al.* [41] were limited to a few far-field acoustic observer positions where the acoustics were less affected by the strut and background noise. Thus, the experimental measurements by Zhang *et al.* [41] are only used to validate the numerical simulations in this project, and the simulations will be analysed in more detail in Chapter 5 to comprehensively study the noise generation mechanisms.

The second work on the isolated wheel configuration was given by Spagnolo *et al.* [42, 43], who experimentally and numerically studied the aerodynamic forces (lift and drag) of tandem wheels at different angles of attack (0° , 10° and 20°) and separation distances ($L/D = 1.1$, 1.3 and 1.5), at Reynolds numbers in the critical regime. The wheel model was simplified as a short circular cylinder. In their experiments, both fix transition treatment and free transition treatment of the boundary layer were tested, and the flow field was significantly different, indicating that the flow around a tandem wheels configuration is highly sensitive to the Reynolds number. Their numerical study highlighted the importance of an appropriate treatment of the boundary layer in the turbulence model, in order to correctly predict the aerodynamic forces at Reynolds numbers in the critical regime. No acoustic measurements were provided in their tandem wheels experiment.

Year	Authors	Geometry	Measurement	Comments
1976	Heller and Dobrzynski [28]	Simplified scaled 2 & 4-wheel LG	Experiment	Pioneers, haystack-shaped acoustic spectrum, significant wheel interaction noise.
2002	Lazos [27]	Simplified 31%-scaled 4-wheel LG	Experiment	Mean flow features measured in the gap region with an unstable vortex; two different flow states.
2002	Lazos [33]	Simplified 31%-scaled 4-wheel LG	Experiment	Surface flow topology with separations and attachments considered as potential noise sources.
2002	Jaeger <i>et al.</i> [40]	High-fidelity 26%-scaled 6-wheel LG	Experiment	3 dB reduction in SPL in the sideline direction by covering the wheel hub cavity.
2007	Quayle <i>et al.</i> [37]	Simplified 8.3%-scaled 4-wheel LG	Experiment	Wheel edge radius effects on the noise generation; wheel interaction noise reduction by gap fairing.
2009	Heuhart <i>et al.</i> [34]	High-fidelity 25%-scaled 2-wheel LG	Experiment	High levels of TKE and p^{rms} on wheel hub area, which might be stronger noise sources.
2010	Yokokawa <i>et al.</i> [31]	Simplified 40%-scaled 2-wheel LG	Experiment	Tyre and sidebrace are the dominant noise sources.
2011	Spalart and Mejia [35]	Rudimentary scaled 4-wheel LG	Experiment & simulation	Strong flow interactions in the gap region, which might be significant noise sources.
2013	Liu <i>et al.</i> [3]	Simplified 40%-scaled 2-wheel LG	Numerical simulation	Wheels are the dominant noise sources, with a side force sound radiating pattern.
2013	Zhang <i>et al.</i> [41]	High-fidelity 33%-scaled isolated wheel	Experiment	Asymmetric mean flow features in the wake; middle frequency noise does not scale with velocity.
2014	Casalino <i>et al.</i> [39]	Simplified 40%-scaled 2-wheel LG	Numerical simulation	Two acoustic tones are generated by the resonance of two facing rim cavities.
2015	Spagnolo <i>et al.</i> [42]	Simplified 12.5%-scaled tandem wheels	Experiment	Flow is sensitive to boundary layer treatment due to critical Re . No acoustic measurements.
2015	Spagnolo <i>et al.</i> [43]	Simplified 12.5%-scaled tandem wheels	Numerical simulation	Correct modelling of boundary layer turbulence transition is important due to critical Re .

Table 2.1: Table of landing gear wheel studies. LG - Landing Gear, TKE - Turbulence Kinetic Energy.

2.3.3 Section summary

In this section, the flow and acoustic features of wheels in both landing gear and isolated configurations were reviewed, and the summary is provided in Table 2.1.

Wheels are one of the major components on landing gears. Most of the previous work concentrate on the landing gear geometry. The mechanisms of wheel noise generation cannot be revealed due to complex flow interactions. Isolated wheels are relatively less studied. The isolated wheel noise investigations by Zhang *et al.* [41] can only provide a limited experimental database due to the background and strut noise. The isolated tandem wheels studied by Spagnolo *et al.* [42, 43] were performed with simplified models, which are short circular cylinders, and no acoustic measurements were conducted. Wheels are significant sources of landing gear noise. Therefore, there is a need to systematically study the aerodynamic and acoustic characteristics of isolated and tandem wheels with high-fidelity geometries.

2.4 Cylindrical cavity flow and noise

Cylindrical cavity geometries can exist on landing gear wheels, such as hub cavities [41] and inner facing rim cavities [39]. It has been shown that the wheel cavities can generate tonal and broadband acoustics due to the cavity resonance [39, 41]. In this section, the flow and acoustic features of cylindrical cavities will be reviewed, which can provide more insight into the landing gear wheel noise generation mechanisms.

2.4.1 Cavity resonance

Intensive discrete and broadband noise can be generated by cavity flows, due to interactions between shear layers at the opening and coherent structures inside the cavities. For rectangular cavities, the dominant mechanism of the self-sustained flow is the acoustic feedback which is described by the Rossiter formula [44]. However, for cylindrical cavities shown in Figure 2.7, tones are generated due to the cavity resonance [45, 46], and these tones are fixed by the geometry and independent of flow speed. The resonant frequencies for a cylindrical cavity can be written as [47],

$$f_{ijk} = \frac{c_\infty}{2\pi} \sqrt{\frac{4\lambda_{jk}^2}{D^2} + \frac{i^2\pi^2}{4H^2}}, \quad (2.5)$$

where i , j and k denote the depth modes, azimuthal modes and radial modes, D is the diameter of the cavity and H represents the depth, λ_{ij} is the root of the first-kind Bessel function,

$$J'_j(\lambda_{jk}) = 0. \quad (2.6)$$

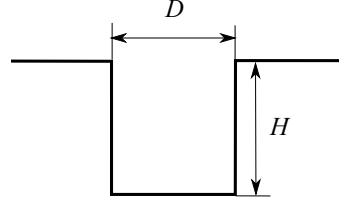


Figure 2.7: Schematic of a cylindrical cavity geometry.

Pollack [48] and Parhasarathy *et al.* [45] showed experimentally that the quarter-wave resonator formula, $f = nc_\infty / (4H)$, $n = 1, 3, 5, \dots$, dominated the oscillations. Recently, Marsden *et al.* [46] conducted acoustic experiments on cylindrical cavities and also found that the most dominant tone was associated with the cavity depth modes. They developed a tonal noise prediction model based on the method of Elder [49]. In their model, the motion of shear layers is coupled with the depth modes and the cavity flow is divided into two processes. The first one is termed by the forward transfer function, which describes the effect of the depth modes on the shear layer at the cavity opening. The second process is called the backward transfer function, representing the efficiency of conversion of shear layer motions into acoustic energy. The product of the two transfer functions will be 1.0 when the energy is balanced at the self-sustained state, when cavity tones will be generated.

For cavity flows, the ratio of the energy stored in the cavity and the energy exchanged at the opening was given by Heller *et al.* [50] as,

$$Q = \frac{\mathcal{A}^2 \times V}{\mathcal{A}^2 \times S}, \quad (2.7)$$

where \mathcal{A} is the oscillation amplitude, V and S are the cavity volume and opening area. The Q factor in Equation 2.7 can be simplified as $Q = H$. For shallow cavities, Q is small and the depth modes are hardly excited [50]. Thus, it is expected that the shallow cylindrical cavity noise presents a more broadband spectrum.

2.4.2 Mean and unsteady flow features

Gaudet and Winter [51] performed experiments to investigate the flow features inside cylindrical cavities and they showed a large vortex tube with a rotation axis normal to the streamwise direction inside the cavity. This vortex was fully rooted at the sidewall for most depth-to-diameter ratios ($\varpi = H/D$) between 0.04 and 1.34, except $\varpi = 0.47$. They observed that at $\varpi = 0.47$ one side of the vortex axis was rooted at the sidewall and the other side extended outside the cavity, exiting at approximately $\theta = 220^\circ$ at the downstream edge, as shown in Figures 2.8 and 2.9. They also measured the pressure induced drag coefficient (C_D^P) and found a maximum value at $\varpi = 0.47$ among different depth-to-diameter ratios. They explained that the drag increment at $\varpi = 0.47$ was due

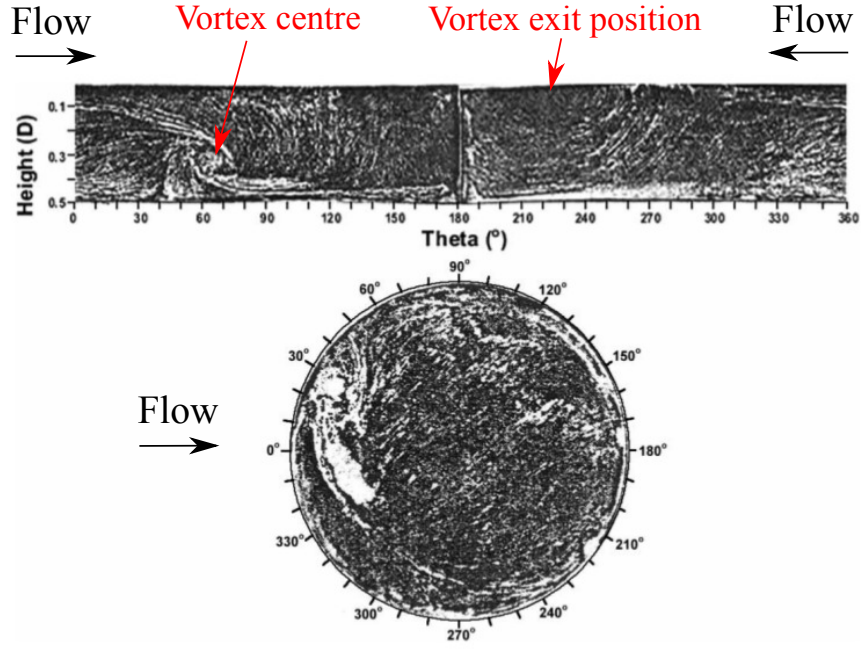


Figure 2.8: Surface oil flow on side and bottom walls of a cylindrical cavity at $\varpi = 0.47$ [51], where $\theta = 0^\circ, 180^\circ$ indicate the upstream and downstream directions, respectively. The vortex centre is located at $\theta \approx 65^\circ$ on the upstream sidewall and exits the cavity at $\theta \approx 220^\circ$ on the downstream sidewall.

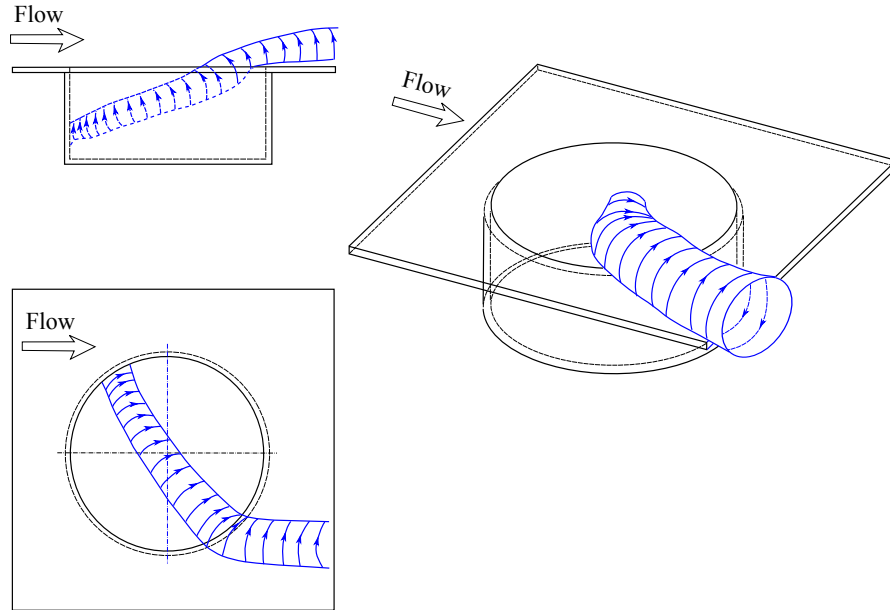


Figure 2.9: Vortex tube visualisation at $\varpi = 0.47$, reproduced from Ref. [52].

to the interaction between the vortex tube and the outside fluid, as a result of which more fluid was swept into the cavity with impingement on the downstream sidewall.

Hiwada *et al.* [53] systematically studied the characteristics of cylindrical cavity flows in the experiments. They tested a variety of depth-to-diameter ratios from 0.1 to 1.0. They found two unstable flow patterns based on the mean pressure coefficient profiles

on the bottom wall and sidewall. The first unstable behaviour is flapping flow and the flow can switch from one state to another by itself randomly in time. This flapping flow happened at a range of depth-to-diameter ratios from $\varpi = 0.2$ to $\varpi = 0.4$. The second unstable pattern is switching flow, where there are generally two stable states, and the flow will be locked into one of them. This switching flow pattern can occur at $0.4 < \varpi < 0.6$. A slant recirculating vortex was observed in the switching region and mean pressure coefficients on the sidewall and bottom wall were asymmetrical with regard to the freestream direction. These findings have been confirmed by numerical simulations by Marsden *et al.* [54]. Hiwada *et al.* [53] also observed that an additional C_D^P would occur in the unstable region and a maximum value was found at $\varpi = 0.5$, close to $\varpi = 0.47$ reported by Gaudet and Winter [51]. The mean flow is expected to be stable and symmetric when $\varpi \leq 0.2$ and $0.8 \leq \varpi \leq 1.0$.

Dybenko and Savory [52] experimentally investigated the cavity surface pressure, velocity, and turbulence at the wake for $\varpi = 0.20, 0.47$ and 0.70 . The wake velocity measurements suggested the existence of an asymmetric trailing vortex at $\varpi = 0.47$. The mean and turbulence distributions in their experiments showed that the cavity at $\varpi = 0.47$ disrupted the wake flow far more than $\varpi = 0.20$ and 0.47 , and an increased drag coefficient was seen for this configuration. Mincu *et al.* [55] conducted numerical simulations at $\varpi = 0.5$ and found highly broadband noise emission towards the upstream direction.

The depth-to-diameter ratio ϖ also plays an important role on the wall pressure spectral characteristics and far-field acoustics. For deep cylindrical cavities ($\varpi \geq 1.0$), significant tones were found [45, 46, 49] due to the interactions between acoustic resonances and shear layers. However, for shallow cavities ($\varpi \leq 0.5$), it was found by Marsden *et al.* [56] that the smaller depth scale was no longer sufficient to generate strong tones and the wall pressure spectra were more broadband. They also found that tonal components were still visible for certain depths, but the tonal frequencies were away from the depth modes, which might be related to the Rossiter-like feedback in the shear layer instead of the cavity resonance [56].

2.4.3 Section summary

Cylindrical cavities exist on landing gear wheels. Cylindrical cavity sound is produced by acoustic resonance of depth modes. The effect of depth modes on the cavity noise generation tends to be weaker at low depth-to-diameter ratios (ϖ), and thereby the acoustic spectra become more broadband. The mean flow field is asymmetric at $0.2 < \varpi < 0.8$. The pressure induced drag is maximum at $\varpi \approx 0.47$, due to the presence of a vortex extending to the outside of cavity, which can sweep fluid into the cavity and induce higher pressure distributions on the downstream cavity sidewall.

2.5 Computational aeroacoustics

Computational Aeroacoustics (CAA) is a numerical approach to calculate the sound generated by fluid dynamics. There are two important aspects in CAA, and they are the acoustic modelling and the numerical techniques. The former provides governing equations for aeroacoustics, which are reviewed in Section 2.5.1. The numerical issues to solve these acoustic governing equations are described in Section 2.5.2.

2.5.1 Acoustic modelling

Aerodynamic sound can be computed directly by solving the compressible Navier-Stokes equations in a computational domain that includes noise sources. Aeroacoustic problems are time dependent and the generated sound can propagate over a wide distance to the far field without being dissipated. Thus, a large computational domain with sufficient grid resolutions is required to directly compute the aeroacoustics, which is computationally expensive. An alternative approach is to split the aeroacoustic domain into a source region, a sound propagation region and a sound radiation region, as shown in Figure 2.10. Different acoustic models and numerical treatments can be applied in these three regions to obtain the acoustic results at a reduced computational cost without losing accuracy.

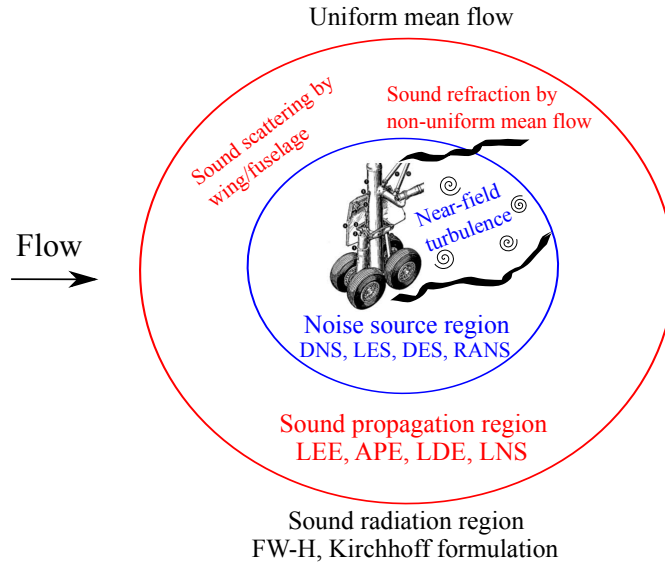


Figure 2.10: Acoustic models in different flow regions.

Noise source modelling

In the near-field source region, the acoustic solution is strongly coupled with the aerodynamic field. Aerodynamics and acoustics cannot be separated and they have significantly non-linear effects on each other. The compressible unsteady Navier-Stokes (N-S) equations are applied in this region to predict the aerodynamics and acoustics together. The

source region includes the highly turbulent flow field surrounding the solid body. The near-field turbulence contains a broad range of spatial and temporal scales, which leads to the broadband nature of the acoustics [57]. Therefore, in the aeroacoustic simulations, it is a requirement to capture the turbulent fluctuations over a wide range. The spatial scales of the turbulence start from the smallest dissipative scales (Kolmogorov scales), up to the integral scale, associated with the motions containing most of the kinetic energy. Relative to the largest scales, the Kolmogorov temporal scales decrease as $Re^{-1/2}$, and the Kolmogorov spatial scales decrease as $Re^{-3/4}$ [58]. Direct Numerical Simulation (DNS) is most desirable, since they can resolve the entire range of spatial and temporal scales of the turbulence. The number of grid points (N) required by a DNS is $N \geq Re^{9/4}$ [58]. At moderate and high Re in the industrial applications, the demand on computational resources by a DNS will exceed the capacity of the computers currently available. Therefore, turbulence models should be applied to increase the computational efficiency.

1. Reynolds Averaged Navier-Stokes (RANS) model

RANS equations are time-averaged equations of motion for fluid flow. The quantities within the N-S equations are decomposed into their mean and fluctuating components. This decomposition results in an extra Reynolds stress term $(-\rho \overline{u'_i u'_j})$, which can be solved by RANS turbulence models (turbulent-viscosity models or Reynolds-stress models). The advantages of RANS models are that they can provide good predictions of mean flow features at relatively coarse grid resolutions, compared with LES and DNS, and they are less dependent on spatial schemes, because of the large levels of dissipations produced by these models. However, since the RANS simulations aim to model the effects of turbulent fluctuations on the mean flow field, the flow unsteadiness cannot be accurately captured. This can lead to the failure of direct aeroacoustic simulations where the sound is generated by unsteady turbulent motions.

2. Large Eddy Simulation (LES) model

The Kolmogorov's theory of self similarity shows that the large eddies of flow are dependent on the geometry while the smaller scales are more universal [58]. LES solves the large scales of fluid motions by removing the small-scale information from the numerical solution via low-pass filtering of the N-S equations. Thus, the entire range of turbulent scales is divided into a resolved region and an unresolved region. The boundary between them depends on the local grid resolution. The effects of unresolved small scales on the large energetic scales are modelled by sub-grid scale models.

Because the large-scale unsteadiness are resolved, LES simulations are more accurate and reliable than RANS simulations for flows dominated by large-scale unsteady motions, such as the bluff body flows where unsteady separations and vortex shedding will occur [58]. However, for a LES of wall-bounded flows, sufficient mesh resolution

is required to capture the most energetic motions. These motions in the boundary layer scale with the viscous lengthscale δ_v , and decrease approximately as $Re^{-0.88}$ relative to δ (outer boundary layer scale) [58]. Therefore, LES is limited to low and moderate Re . For simulations of practical geometries at high Re encountered in the industrial problems, LES is highly computationally expensive, and therefore LES is not adopted in this thesis.

3. Hybrid RANS/LES model

Hybrid RANS/LES method is a combination of RANS models in the near-wall region and LES models in the flow separation field. The RANS models aim to model instead of resolve the turbulent fluctuations in the near-wall field. Thus, although the turbulent length scale near the solid boundaries is very small at high Re , the turbulent scales can be modelled by applying RANS models with a relatively coarse mesh resolution. The grid resolution is not as demanding as pure LES, thereby considerably decreasing the computational cost for wall-bounded flows. In the separation region where the flow is highly unsteady and turbulent, the hybrid RANS/LES model switches to the LES mode to explicitly compute the energetic motions (large scales). Thus, the majority of flow unsteadiness can be captured by a hybrid RANS/LES approach.

The switch from RANS to LES can be achieved by modifying the length scale in the RANS turbulence models. Typical examples of the hybrid RANS/LES method are Detached Eddy Simulation (DES) [59], Delayed DES (DDES) [60], Improved DDES (IDDES) [61] and Zonal DES (ZDES) [62]. These hybrid methods have been successfully applied to landing gear noise simulations [3, 4, 30, 63–68].

Sound propagation modelling

The sound propagation region represents the field surrounding the near-field source region. In this propagation region, the turbulent motions have been significantly dissipated, and the acoustic field is weakly coupled with the aerodynamic solution. Thus, it can be assumed that the aerodynamic flow field affects the acoustic wave propagations without feedback from the acoustic field [57]. Furthermore, the sound generated in the source region is considered to propagate on a stationary background mean flow field from the aerodynamic solution. Since acoustic perturbation quantities are much smaller compared to the background mean flow data, this sound propagation problem can be investigated by solving the Linearised Euler Equations (LEE) [69], Acoustic Perturbation Equations (APE) [70], Linearised Divergence Equations (LDE) [71] or Linearised Navier-Stokes Equations (LNS) [72].

For simulations of an installed landing gear, this sound propagation region can include a fuselage and a wing, due to which the background mean flow is generally non-uniform. Acoustic refractions, diffractions and scatterings can occur in the propagation field.

However, for the current project, the solid objects (landing gear wheels) are positioned in a free space. Therefore, the sound propagation issue is not addressed in this thesis.

Sound radiation modelling

In this region, sound radiates to the far field on a uniform background flow field. The acoustic motions are independent to the aerodynamic solutions. Solutions to sound radiation problems are provided by integral methods, such as Ffowcs Williams-Hawkings (FW-H) formulation [7] and Kirchhoff formulation [73]. The FW-H formulation is based on the conservation laws, and is analytically superior than the Kirchhoff method, which is derived from wave equations. The FW-H integration surface can be placed in either linear region (sound propagation or far-field region) or non-linear region (near-field source region), affording a greater degree of flexibility than the Kirchhoff approach in linear region [74].

Since the sound radiation distance is different between a far-field observer position and different source locations on the integration surface, the time-domain FW-H formulation can be solved by a retarded-time method [75] or an advanced-time approach [76]. The retarded-time strategy evaluates the signal received by a far-field observer at a given observer time t_{observer} through a summation of all the disturbances reaching this observer (the source time t_{source} is retarded to take the radiation distance into account), thus requiring to store all the flow data on the integration surface in near-field flow simulations. The advanced-time approach allows small data storage by explicitly computing the disturbances received by an observer at a given source time t_{source} (the observer time t_{observer} is advanced to take the radiation distance into account), and far-field acoustics are finally obtained through a summation over the interpolations of disturbances from source time t_{source} to observer time t_{observer} . The advanced-time method requires the source and observer positions to be known in the near-field flow simulations, and once the simulations are finished, the source information on the integration surface cannot be recovered. Thus, it is more advantageous to use the retarded-time approach, since it provides more flow data for post processing. One of the most commonly used retarded-time methods is the Formulation 1A of Farassat [75], where the quadrupole source is neglected and the surface sources are divided into loading noise (generated by unsteady surface forces) and thickness noise (produced by unsteady mass through the integration surface). More details on the Formulation 1A of Farassat is provided in Section 3.10.

Theoretically, the FW-H integration surface can be located either on the solid geometry surface of objects, or in the fluid region (permeable surface) where flow can go through. However, Spalart *et al.* [66, 77] performed numerical simulations on a rudimentary landing gear and found strong unphysical growth of acoustic predictions at middle frequencies using the permeable FW-H surface, leading to an overprediction of OASPL by 5 dB. This overestimation by the permeable FW-H surface data has also been observed by many other researchers [4, 67, 68, 78–80]. When vortical and entropy waves pass through the permeable surface, they can produce both surface and volume sources in

the FW-H formulation that cancel each other out [81]. However, the volume sources are neglected in the simulations to reduce storage requirement. The absence of volume sources is responsible for the overprediction of far-field acoustics. This problem can be avoided by solid surface without vortical and entropy disturbances passing through, and thus the solid surface can predict landing gear noise more accurately [4, 66–68, 77–80]. Furthermore, the solid FW-H surface can generally provide a higher resolvable frequency range, considering that the mesh away from solid bodies is stretched. Therefore, the solid FW-H integration surface is applied in this thesis.

2.5.2 Numerical issues

Most of aeroacoustic problems are broadband in nature and there is a significant requirement to solve high frequency waves with minimum number of Points Per Wavelength (PPW). Acoustic perturbations are small fluctuations on the background flow, and solutions are sensitive to numerical errors. In order to capture acoustics more accurately, numerical dissipation and dispersion must be minimised. As a result, high-order finite-difference schemes using large stencils are widely used in CAA. Liu *et al.* [3] applied a fourth-order prefactored scheme and a second-order explicit scheme to simulate landing gear noise. They demonstrated that a high-order scheme can more accurately predict acoustic spectral levels and resolve a wider frequency range, compared to a low-order scheme. In this section, both the spatial schemes and the numerical block interface treatments are reviewed.

High-order schemes

Lele [82] extended the finite-difference method to compact schemes that implicitly computed spatial derivatives with smaller stencils at the same order of accuracy. The compact schemes were derived by Fourier analysis to improve the representation of a range of wavenumbers rather than accurate resolution of a single wave [82]. The procedure to optimise the spatial resolution over a wide wavenumber range was generalised by Tam and Webb [69]. They proposed a Dispersion-Relationship-Preserving (DRP) finite-difference scheme by first considering an approximation of first derivative f'_l at the l -th node on an uniform grid,

$$f'_l \simeq \frac{1}{\Delta x} \sum_{j=-N}^M a_j f_{l+j}, \quad (2.8)$$

where Δx is the grid spacing and a_j are the coefficients that can be constructed by matching the Taylor series up to the highest order of accuracy. However, for acoustic problems, a high-order scheme does not guarantee a good quality numerical wave solution [69]. Improved numerical accuracy can be achieved by improving the spectral resolution of a spatial scheme even at a cost of losing order of accuracy. Therefore, the coefficients a_j in DRP schemes are determined in the wavenumber domain. Applying the Fourier

transform to both sides of Equation 2.8 yields,

$$ik\tilde{f} \simeq \left(\frac{1}{\Delta x} \sum_{j=-N}^M a_j e^{ijk\Delta x} \right) \tilde{f}, \quad (2.9)$$

where $i = \sqrt{-1}$ and k is the exact wavenumber. The effective wavenumber (k^*) represented by the spatial scheme is,

$$k^* = \frac{-i}{\Delta x} \sum_{j=-N}^M a_j e^{ijk\Delta x}. \quad (2.10)$$

In order to provide a good approximation over a range of wavenumbers of interest, the schemes are optimised to minimise the dispersion and dissipation errors that are quantified in the following form,

$$\text{Error} = \int_{-\frac{\pi}{2}}^{\frac{\pi}{2}} |k\Delta x - k^*\Delta x|^2 d(k\Delta x). \quad (2.11)$$

The coefficients a_j are finally obtained after this optimisation. The optimised fourth-order DRP scheme showed improved spectral resolution characteristics than the standard sixth-order scheme constructed by the truncated Taylor series method [69]. More importantly, the size of stencil used by the two schemes is the same, suggesting that improved accuracy in acoustic simulations can be obtained with the same stencil by optimising scheme coefficients.

Since the DRP scheme by Tam and Webb, many efforts have been made to improve the spectral resolution characteristics of finite-difference schemes through Fourier analysis, such as the low dispersive and low dissipative explicit scheme by Bogey and Bailly [83], the optimised prefactored scheme by Ashcroft and Zhang [84] and the optimised pentadiagonal compact scheme by Kim [85]. Among these optimised schemes, the last one provides the highest spectral resolution (as shown in Figure 2.11), and therefore it is used in the current project. More details on the optimised pentadiagonal compact scheme by Kim are provided in Section 3.3.

Grid metrics discontinuities and interface conditions

High-order finite-difference schemes in CAA are applied on multi-block structured grids using a large stencil. Thus, aeroacoustic simulations are more sensitive to grid quality. It is a challenge to generate high-quality curvilinear grids around complex geometries, and abrupt changing in grid spacings and grid line directions is inevitable, particularly along multi-block interfaces. The finite-difference method is solved on the computational domain $(\xi, \eta$ and $\zeta)$, which is transformed from the physical domain $(x, y$ and $z)$ using the grid metrics $\partial(\xi, \eta, \zeta) / \partial(x, y, z)$. The limited grid smoothness along block interfaces can lead to discontinuities in the grid metrics. Fattah *et al.* [86] demonstrated a strong

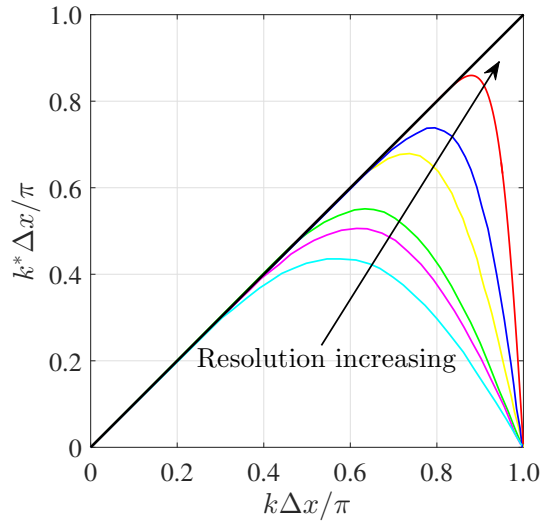


Figure 2.11: The spectral resolution characteristics of a standard explicit fourth-order scheme (—), a standard explicit sixth-order scheme (—), an optimised fourth-order DRP scheme (—) [69], a low dispersive and low dissipative explicit fourth-order scheme (—) [83], an optimised prefactored fourth-order scheme (—) [84] and an optimised pentadiagonal compact fourth-order scheme (—) [85]. The exact numerical solution is given by —.

correlation between grid transformation errors and accuracy of solution field. The conventional one-to-one interface condition, which applies central spatial scheme using the information from adjacent block directly, is incapable of handling the grid metric discontinuities [87–90]. Therefore, reducing grid metric errors by a proper interface condition is needed for aeroacoustic simulations.

Kim and Lee [87] proposed a characteristic interface condition on the generalised coordinates. In their method, the N-S equations are firstly transformed to the characteristic domain, and the characteristics waves are then upwinded at block interfaces to update the inviscid flux derivatives. Gao [88] developed a flux reconstruction method, which firstly modifies the fluxes at the interface in the computational space then applies biased schemes to get the flux derivatives. Du and Morris [89] studied the similarity of the FD and FV method and proposed an equivalent FV treatment at the block interface. This equivalent FV method requires to be implemented in the computational space using the grid metrics and Jacobian to represent the cell faces and cell volume. These interface treatments have been successfully applied [87–89], and they are required to be applied in the cell-vertex space with one overset grid point along block interfaces. These methods are summarised in Table 2.2.

In comparison to the cell-vertex method, the cell-centred formulation proposed by Wang *et al.* [90] is less sensitive to the grid metric discontinuities, because the control points are located away from the origin of the discontinuities. This allows more interfaces to be evaluated using a conventional one-to-one interface condition with high-order central

schemes, which is less dissipative than biased schemes involved in the above interface conditions, and can provide more accurate solutions. However, an additional interface treatment is still required to handle large grid metric discontinuities even in the cell-centred formulation. Wang *et al.* [90] proposed a finite-volume interface condition in the cell-centred space. The communication between two connected blocks is achieved by correcting fluxes through the common interfaces (cell faces) shared by two adjacent blocks. This method was shown to be accurate for aeroacoustic simulations of complex geometries. More details on this cell-centred interface condition are provided in Chapter 4.

Year	Authors	Interface condition	Formulation	Schemes
N/A	N/A	One-to-one	Cell-vertex	Low/High-order central schemes
2003	Kim and Lee [87]	Characteristic condition	Cell-vertex	High-order biased schemes
2013	Gao [88]	Flux reconstruction	Cell-vertex	High-order biased schemes
2015	Du and Morris [89]	Equivalent finite volume	Cell-vertex	Low-order central schemes
2015	Wang <i>et al.</i> [90]	One-to-one	Cell-centred	High-order central schemes
2015	Wang <i>et al.</i> [90]	Complete finite volume	Cell-centred	High-order biased schemes

Table 2.2: Features of different interface conditions in CAA.

2.5.3 Section summary

Aeroacoustic problems can be categorised into three groups, i.e. sound generation, sound propagation and sound radiation. The different acoustic models and strategies to solve them were reviewed in this section. High-order schemes and numerical challenges in CAA were also reviewed.

2.6 Chapter summary

Wheels are significant landing gear noise sources, and they can be considered as bluff bodies. Firstly, this Chapter reviewed the circular cylinder flow and acoustic characteristics, together with the end effects by short cylinders. Previous works on wheels in isolated and landing gear configurations were then provided, highlighting the significance and motivation of this project. The acoustic modelling strategies and numerical methods in CAA were finally reviewed. Accurate and stable numerical treatments are key to perform aeroacoustic numerical simulations of landing gear wheels.

Chapter 3

Numerical Methodology

3.1 Introduction

The landing gear wheel noise simulations are performed using a hybrid CFD/FW-H numerical methodology. In this hybrid approach, the near-field noise sources are firstly calculated using an in-house high-order CAA solver, SotonCAA, with a Delayed Detached Eddy Simulation (DDES) turbulence model. Then, the Ffowcs Williams and Hawkings (FW-H) equation is solved to predict the far-field acoustics based on the near-field solution obtained from the high-order simulations. In this Chapter, the governing equations and numerical methods in this hybrid numerical methodology are outlined and the guidelines to use them in the high-order simulations are also provided.

3.2 Governing equations

SotonCAA solves the compressible Navier-Stokes (N-S) equations, and the variables are non-dimensionalised by,

$$\begin{aligned} x_i &= x_i^*/L_\infty^*, & u_i &= u_i^*/c_\infty^*, & t &= t^*c_\infty^*/L_\infty^*, \\ p &= p^*/(\rho_\infty^*(c_\infty^*)^2), & \rho &= \rho^*/\rho_\infty^*, & \mu &= \mu^*/\mu_\infty^*, \end{aligned} \quad (3.1)$$

where the asterisk represents the dimensional variables and the subscript ∞ stands for the freestream quantities. The generalised form of the N-S equations can be expressed as,

$$\frac{\partial \mathbf{Q}}{\partial t} + \frac{\partial (\mathbf{E} - \mathbf{E}_v)}{\partial x} + \frac{\partial (\mathbf{F} - \mathbf{F}_v)}{\partial y} + \frac{\partial (\mathbf{G} - \mathbf{G}_v)}{\partial z} = 0, \quad (3.2)$$

where x , y and z are the physical coordinates, t is time, and $\mathbf{Q} = [\rho, \rho u, \rho v, \rho w, \rho E]^T$ are the conserved variables. The flux vectors are given by,

$$\mathbf{E} = \begin{bmatrix} \rho u \\ \rho u u + p \\ \rho u v \\ \rho u w \\ (\rho E + p) u \end{bmatrix}, \mathbf{E}_v = \begin{bmatrix} 0 \\ \tau_{xx} \\ \tau_{xy} \\ \tau_{xz} \\ b_x + u\tau_{xx} + v\tau_{xy} + w\tau_{xz} \end{bmatrix}, \quad (3.3a)$$

$$\mathbf{F} = \begin{bmatrix} \rho v \\ \rho v u \\ \rho v v + p \\ \rho v w \\ (\rho E + p) v \end{bmatrix}, \mathbf{F}_v = \begin{bmatrix} 0 \\ \tau_{yx} \\ \tau_{yy} \\ \tau_{yz} \\ b_y + u\tau_{yx} + v\tau_{yy} + w\tau_{yz} \end{bmatrix}, \quad (3.3b)$$

$$\mathbf{G} = \begin{bmatrix} \rho w \\ \rho w u \\ \rho w v \\ \rho w w + p \\ (\rho E + p) w \end{bmatrix}, \mathbf{G}_v = \begin{bmatrix} 0 \\ \tau_{zx} \\ \tau_{zy} \\ \tau_{zz} \\ b_z + u\tau_{zx} + v\tau_{zy} + w\tau_{zz} \end{bmatrix}, \quad (3.3c)$$

where ρ and p are density and pressure, u , v , w are velocity components in the x , y and z directions, respectively. E is the total energy density defined by,

$$E = e + \frac{1}{2} (u^2 + v^2 + w^2), \quad (3.4)$$

and e is the specific internal energy density. The pressure can be obtained from the density, total energy density and velocities from the following relationship,

$$p = (\gamma - 1) \left(\rho E - \frac{1}{2} \rho (u^2 + v^2 + w^2) \right), \quad (3.5)$$

where $\gamma = c_p/c_v$ is the ratio of specific heat coefficients and is 1.4 in the current simulations. The shear stresses τ_{ij} and heat fluxes are given by,

$$\tau_{ij} = \frac{M}{Re} \left(-\frac{2}{3} \mu \frac{\partial u_i}{\partial x_i} \delta_{ij} + 2\mu S_{ij} \right), \quad (3.6a)$$

$$S_{ij} = \frac{1}{2} \left(\frac{\partial u_i}{\partial x_j} + \frac{\partial u_j}{\partial x_i} \right), \quad (3.6b)$$

$$b_i = \frac{M}{Re(\gamma - 1) Pr} \frac{\partial T}{\partial x_i}. \quad (3.6c)$$

where M and Re are the Mach number and Reynolds number, and T is the temperature. SotonCAA solves the N-S equations by using high-order finite difference methods along gridlines, which requires transforming Equation 3.2 from physical coordinates (x , y and z) to computational coordinates (ξ , η and ζ). The generalised governing equations on

the curvilinear coordinates can be expressed as,

$$\frac{\partial \hat{Q}}{\partial t} + \frac{\partial (\hat{\mathbf{E}} - \hat{\mathbf{E}}_v)}{\partial \xi} + \frac{\partial (\hat{\mathbf{F}} - \hat{\mathbf{F}}_v)}{\partial \eta} + \frac{\partial (\hat{\mathbf{G}} - \hat{\mathbf{G}}_v)}{\partial \zeta} = 0, \quad (3.7)$$

where,

$$\hat{Q} = Q/J, \quad (3.8a)$$

$$\hat{\mathbf{E}} = (\xi_x \mathbf{E} + \xi_y \mathbf{F} + \xi_z \mathbf{G})/J, \quad (3.8b)$$

$$\hat{\mathbf{F}} = (\eta_x \mathbf{E} + \eta_y \mathbf{F} + \eta_z \mathbf{G})/J, \quad (3.8c)$$

$$\hat{\mathbf{G}} = (\zeta_x \mathbf{E} + \zeta_y \mathbf{F} + \zeta_z \mathbf{G})/J, \quad (3.8d)$$

$$\hat{\mathbf{E}}_v = (\xi_x \mathbf{E}_v + \xi_y \mathbf{F}_v + \xi_z \mathbf{G}_v)/J, \quad (3.8e)$$

$$\hat{\mathbf{F}}_v = (\eta_x \mathbf{E}_v + \eta_y \mathbf{F}_v + \eta_z \mathbf{G}_v)/J, \quad (3.8f)$$

$$\hat{\mathbf{G}}_v = (\zeta_x \mathbf{E}_v + \zeta_y \mathbf{F}_v + \zeta_z \mathbf{G}_v)/J, \quad (3.8g)$$

and J is the Jacobian obtained by,

$$J^{-1} = \begin{vmatrix} x_\xi & x_\eta & x_\zeta \\ y_\xi & y_\eta & y_\zeta \\ z_\xi & z_\eta & z_\zeta \end{vmatrix}, \quad (3.9)$$

and the grid metrics are calculated in a geometric conservation form by [91],

$$\begin{cases} \xi_x/J = (y_\eta z)_\zeta - (y_\zeta z)_\eta, & \xi_y/J = (z_\eta x)_\zeta - (z_\zeta x)_\eta, & \xi_z/J = (x_\eta y)_\zeta - (x_\zeta y)_\eta, \\ \eta_x/J = (y_\zeta z)_\xi - (y_\xi z)_\zeta, & \eta_y/J = (z_\zeta x)_\xi - (z_\xi x)_\zeta, & \eta_z/J = (x_\zeta y)_\xi - (x_\xi y)_\zeta, \\ \zeta_x/J = (y_\xi z)_\eta - (y_\eta z)_\xi, & \zeta_y/J = (z_\xi x)_\eta - (z_\eta x)_\xi, & \zeta_z/J = (x_\xi y)_\eta - (x_\eta y)_\xi. \end{cases} \quad (3.10)$$

It should also be noted that the spatial discretisation schemes employed in Equation 3.10 should be the same as the high-order schemes, given in Section 3.3, applied to compute the flux derivatives.

In order to increase numerical stability, the derivatives of inviscid fluxes, which are in conservative form in Equation 3.7, are split into conservative and non-conservative parts by a skew-symmetric splitting method [92],

$$\frac{\partial (ab)}{\partial x} = \frac{1}{2} \frac{\partial (ab)}{\partial x} + \frac{1}{2} a \frac{\partial b}{\partial x} + \frac{1}{2} b \frac{\partial a}{\partial x}. \quad (3.11)$$

3.3 Spatial discretisation

The numerical solution is obtained by solving the governing equations in discretisation space. The spatial schemes implemented in SotonCAA are fourth-order compact schemes of Kim [85] and Kim and Sandberg [93], including two sets of boundary closure schemes.

Those schemes have been optimised to achieve a higher resolvable wavenumber. In this section, the interior and boundary spatial schemes are outlined.

3.3.1 Interior scheme

The interior scheme used in current simulations is a penta-diagonal compact finite difference scheme, which can be expressed as [85],

$$\beta f'_{i-2} + \alpha f'_{i-1} + f'_i + \alpha f'_{i+1} + \beta f'_{i+2} = \frac{1}{\Delta x} \sum_{m=1}^3 a_m (f_{i+m} - f_{i-m}), \quad (3.12)$$

where f_i and f'_i represent an objective function $f(x)$ and its spatial derivative, respectively. All grid points are equally spaced by a constant distance Δx . The coefficients are firstly restricted to match the Taylor series expansion up to fourth-order accuracy and then optimised using a Fourier transform to minimise the dispersion errors. The coefficients in Equation 3.12 are provided by Kim [85] and the spectral resolution is plotted in Figure 3.1, where k and k^* are the exact and modified wavenumber respectively. For a central scheme, the modified wavenumber is real-valued, and the difference between k and k^* in Figure 3.1 is the dispersion error by the central spatial scheme in Equation 3.12. Figure 3.1 shows that the penta-diagonal compact scheme stays close to the exact differentiation over a large range of wavenumbers.

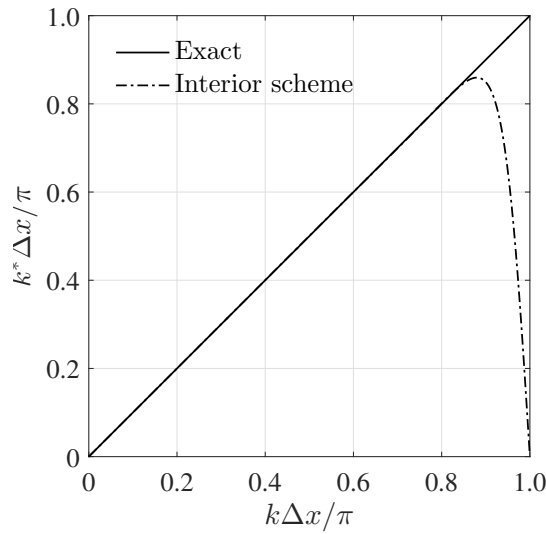


Figure 3.1: The spectral resolution of the compact central spatial scheme in Equation 3.12.

3.3.2 Boundary schemes

Equation 3.12 is valid at interior grid points $3 \leq i \leq N - 3$, where $i = 0$ and $i = N$ are boundaries. At physical boundaries of a computational domain (inflow, outflow, wall etc.), one set of closure schemes is derived from extrapolations of both f and f' outside the domain, which eventually lead to a set of biased compact schemes near and at the boundaries ($i = 0, 1, 2$), and they are written as [85],

$$\begin{aligned}
 i = 0 : \quad f'_0 + \gamma_{01}f'_1 + \gamma_{02}f'_2 &= \frac{1}{\Delta x} \sum_{m=1}^6 b_{0m} (f_m - f_0), \\
 i = 1 : \quad \gamma_{10}f'_0 + f'_1 + \gamma_{12}f'_2 + \gamma_{13}f'_3 &= \frac{1}{\Delta x} \sum_{m=0, \neq 1}^6 b_{1m} (f_m - f_1), \\
 i = 2 : \quad \gamma_{20}f'_0 + \gamma_{21}f'_1 + f'_2 + \gamma_{23}f'_3 + \gamma_{24}f'_4 &= \frac{1}{\Delta x} \sum_{m=0, \neq 2}^6 b_{2m} (f_m - f_2).
 \end{aligned} \tag{3.13}$$

At block interfaces, another set of boundary closure schemes is derived to use the information from the adjacent block during parallel computing [93]. These boundary schemes involve three halo (ghost) cells (f_{-3}, f_{-2}, f_{-1}) from the adjacent block and are given by [93],

$$\begin{aligned}
 i = 0 : \quad f'_0 + \gamma_{01}^h f'_1 + \gamma_{02}^h f'_2 &= \frac{1}{\Delta x} \sum_{m=-3, \neq 0}^4 b_{0m}^h (f_m - f_0), \\
 i = 1 : \quad \gamma_{10}^h f'_0 + f'_1 + \gamma_{12}^h f'_2 + \gamma_{13}^h f'_3 &= \frac{1}{\Delta x} \sum_{m=-3, \neq 1}^4 b_{1m}^h (f_m - f_1).
 \end{aligned} \tag{3.14}$$

The coefficients in the boundary closure schemes of Equations 3.13 and 3.14 are given by Kim [85] and Kim and Sandberg [93], respectively. Figures 3.2 and 3.3 demonstrate the dispersion error (real part) and the dissipation error (imaginary part) of the boundary schemes. In SotonCAA, those schemes are solved by a LU decomposition method [94].

3.4 Filtering scheme

The high resolution of the compact schemes does not guarantee numerical stabilities and their non-dissipative nature often yields spurious solutions when applied to non-linear problems or complex configurations. In order to ensure the numerical stability, a sixth-order compact filter with various cut-off wavenumbers [95] is applied in the simulation. The general form of this compact filter based on differential quantities is expressed as

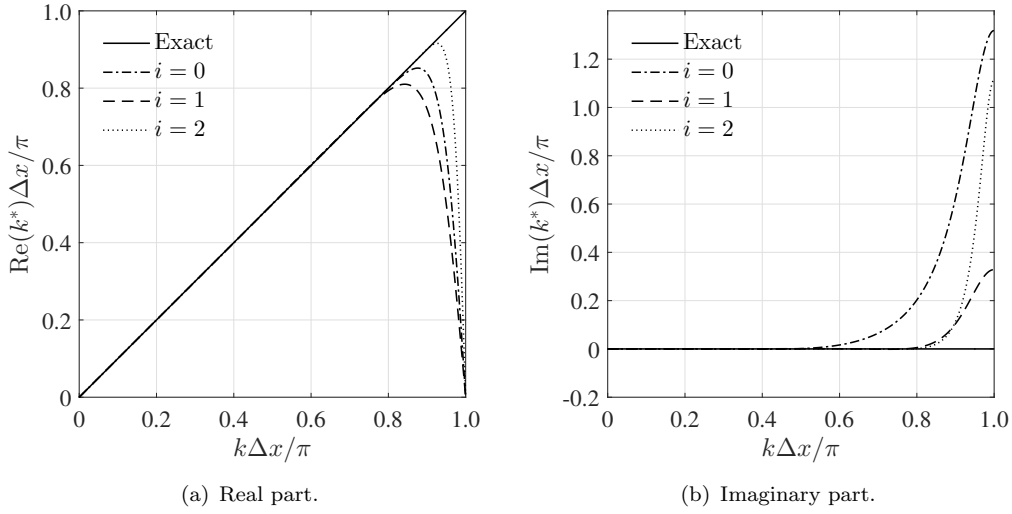


Figure 3.2: The spectral resolution errors for the fully biased boundary spatial schemes (Equation 3.13).

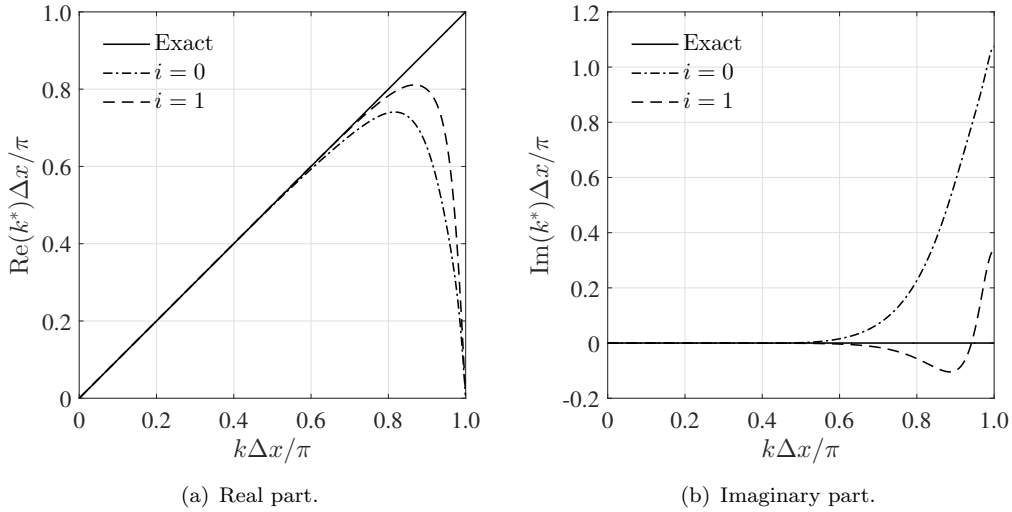


Figure 3.3: The spectral resolution errors for the boundary spatial schemes using halo point information (in Equation 3.14).

[95],

$$\beta_F \hat{\Delta} f_{i-2} + \alpha_F \hat{\Delta} f_{i-1} + \hat{\Delta} f_i + \alpha_F \hat{\Delta} f_{i+1} + \beta_F \hat{\Delta} f_{i+2} = \sum_{m=1}^3 a_{Fm} (f_{i-m} - 2f_i + f_{i+m}), \quad (3.15)$$

where $\hat{\Delta} f_i = \hat{f}_i - f_i$ is the difference between the filtered variable \hat{f}_i and the original variable f_i . All the coefficients in Equation 3.15 can be expressed as functions of an effective cut-off wavenumber $\kappa_c \equiv k\Delta x$ [95]. The boundary closure schemes are provided in Ref. [95]. The spectral characteristics of the compact six-order filter with different cut-off wavenumbers are shown in Figure 3.4, where an abrupt change in the filtering

profile is demonstrated around the effective cut-off wavenumber κ_c , and therefore the high-wavenumber modes can be filtered without affecting the low-wavenumber waves. The effective cut-off wavenumber used in the single and tandem cylinders simulations is $\kappa_c = 0.8\pi$ at interior grid points and $\kappa_c = 0.78\pi$ at boundaries. In the landing gear wheel simulations, κ_c is reduced to 0.75π and 0.73π at the interior points and boundaries, respectively, in order to increase numerical stability.

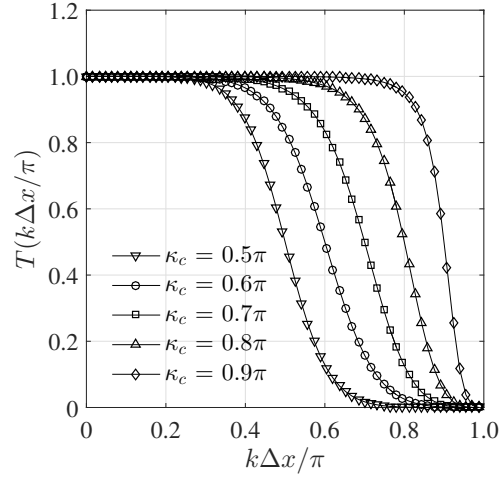


Figure 3.4: The transfer function profiles for the compact filter in Equation 3.15.

3.5 Temporal scheme

Both explicit and implicit time-stepping methods have been implemented in SotonCAA. The explicit scheme is a Low-Dispersion and low-Dissipation Runge-Kutta (LDDRK) method by Hu *et al.* [96], which is fourth-order accurate for linear problems and requires the Courant–Friedrichs–Lewy (CFL) number to be smaller than 1.0 for numerical stability. For practical simulations with boundary layers, the grid size needs to be fine enough in the wall-normal direction to resolve boundary layer profiles. The small CFL number required by the explicit time-stepping method limits the physical timestep Δt in simulations. In order to reduce the computational cost, the current simulation results are obtained with an implicit time marching method, which can achieve a larger CFL number without numerical instabilities.

The basic idea of the implicit time stepping method is to introduce a pseudo time τ and use subiterations to march the solution by computing fluxes implicitly in τ until reaching a steady state at each time step [97]. The governing equation (Equation 3.7) with respect to the pseudo time τ is given as,

$$\frac{\partial \hat{Q}}{\partial \tau} + \frac{\partial \hat{Q}}{\partial t} + \hat{R} + \hat{R}_v = 0, \quad (3.16)$$

where $\hat{\mathbf{R}}$ and $\hat{\mathbf{R}}_v$ are the residuals due to inviscid and viscous fluxes, respectively. When the steady state is reached, $\partial\hat{\mathbf{Q}}/\partial\tau$ will disappear and Equation 3.7 can be recovered. A second-order and first-order backward differential schemes can be employed to get the derivatives of $\hat{\mathbf{Q}}$ with respect to the physical time t and pseudo time τ . The discretised formulation of Equation 3.16 is then,

$$\left[\left(\frac{1}{\Delta\tau} + \frac{3}{2\Delta t} \right) \mathbf{I} + \frac{\partial\hat{\mathbf{R}}^m}{\partial\hat{\mathbf{Q}}} + \frac{\partial\hat{\mathbf{R}}_v^m}{\partial\hat{\mathbf{Q}}} \right] \Delta\hat{\mathbf{Q}}^m = \hat{\mathbf{R}}^{*m}, \quad (3.17)$$

with,

$$\hat{\mathbf{R}}^{*m} = \hat{\mathbf{R}}^m + \hat{\mathbf{R}}_v^m + \frac{1}{2} \left(3\hat{\mathbf{Q}}^m - 4\hat{\mathbf{Q}}^n + \hat{\mathbf{Q}}^{n-1} \right), \quad (3.18)$$

where m and n denote the pseudo and physical time step, \mathbf{I} is the identity matrix, $\Delta\hat{\mathbf{Q}}$ is the increasement of conserved variables. The inviscid residuals can be obtained numerically by,

$$\begin{aligned} \hat{\mathbf{R}}_{i,j,k} = & \hat{\mathbf{E}}_{i+1/2,j,k} - \hat{\mathbf{E}}_{i-1/2,j,k} + \\ & \hat{\mathbf{F}}_{i,j+1/2,k} - \hat{\mathbf{F}}_{i,j-1/2,k} + \hat{\mathbf{G}}_{i,j,k+1/2} - \hat{\mathbf{G}}_{i,j,k-1/2}. \end{aligned} \quad (3.19)$$

The flux along ξ at $(i + 1/2, j, k)$ can be estimated by using a first-order scheme,

$$\hat{\mathbf{E}}_{i+1/2,j,k} = \frac{1}{2} \left(\hat{\mathbf{E}}_{i,j,k} + \hat{\mathbf{E}}_{i+1,j,k} \right) - \frac{1}{2} |\lambda_i| \left(\hat{\mathbf{Q}}_{i+1,j,k} - \hat{\mathbf{Q}}_{i,j,k} \right), \quad (3.20)$$

and $|\lambda_i|$ is the spectral radius of the convective flux Jacobian along ξ direction and it can be obtained by,

$$|\lambda_i| = \alpha (|uS_x + vS_y + wS_z| + c|S|), \quad (3.21)$$

where c is the local speed of sound and α is a relaxing factor, which is set to be 1.05 in the simulations. The cell surface information can be computed using the grid metrics and Jacobian by,

$$\begin{aligned} S_x &= \frac{1}{J} \sqrt{\left(\frac{\partial\xi}{\partial x} \right)^2}, S_y = \frac{1}{J} \sqrt{\left(\frac{\partial\xi}{\partial y} \right)^2}, S_z = \frac{1}{J} \sqrt{\left(\frac{\partial\xi}{\partial z} \right)^2}, \\ S &= \frac{1}{J} \sqrt{\left(\frac{\partial\xi}{\partial x} \right)^2 + \left(\frac{\partial\xi}{\partial y} \right)^2 + \left(\frac{\partial\xi}{\partial z} \right)^2}. \end{aligned} \quad (3.22)$$

Using the Taylor expansion theory, the flux $\hat{\mathbf{E}}_{i+1/2,j,k}^{m+1}$ can be approximated by,

$$\begin{aligned} \hat{\mathbf{E}}_{i+1/2,j,k}^{m+1} &\approx \hat{\mathbf{E}}_{i+1/2,j,k}^m + \frac{\partial\hat{\mathbf{E}}_{i+1/2,j,k}^m}{\partial\hat{\mathbf{Q}}_{i,j,k}^m} \Delta\hat{\mathbf{Q}}_{i,j,k}^m + \frac{\partial\hat{\mathbf{E}}_{i+1/2,j,k}^m}{\partial\hat{\mathbf{Q}}_{i+1,j,k}^m} \Delta\hat{\mathbf{Q}}_{i+1,j,k}^m \\ &= \hat{\mathbf{E}}_{i+1/2,j,k}^m + \left(\hat{\mathbf{A}}_{i,j,k}^+ \Delta\hat{\mathbf{Q}}_{i,j,k}^m + \hat{\mathbf{A}}_{i+1,j,k}^- \Delta\hat{\mathbf{Q}}_{i+1,j,k}^m \right), \end{aligned} \quad (3.23)$$

where,

$$\hat{\mathbf{A}}^\pm = \frac{1}{2} \left(\frac{\partial \hat{\mathbf{F}}}{\partial \hat{\mathbf{Q}}} \pm |\lambda_i| \mathbf{I} \right). \quad (3.24)$$

Now, the inviscid fluxes have been treated implicitly in Equation 3.23. Inside the boundary layer, the local Reynolds number based on the local cell size is very small and it will be advantageous to treat the viscous fluxes implicitly to avoid numerical instabilities. With an approximation of viscous effects by their spectral radii [97], the total spectral radius of flux Jacobian $|\lambda_i^t|$ can be obtained by,

$$|\lambda_i^t| = |\lambda_i| + \gamma \left(\frac{\mu}{\text{Pr}} + \frac{\mu_t}{\text{Pr}_t} \right) \frac{S^2 J}{\rho}, \quad (3.25)$$

where μ and μ_t are the dynamic viscosity and turbulent eddy viscosity, and Pr and $(\text{Pr})_t$ are the Prandtl number and turbulent Prandtl number. The matrices \mathbf{A}^\pm are given by,

$$\mathbf{A}^\pm = \frac{1}{2} \left(\frac{\partial \hat{\mathbf{F}}}{\partial \hat{\mathbf{Q}}} \pm |\lambda_i^t| \mathbf{I} \right). \quad (3.26)$$

Similarly, the fluxes along η and ζ directions can also be computed implicitly. Finally, Equation 3.17 can be approximated by,

$$(\mathbf{D} + \mathbf{L}) \mathbf{D}^{-1} (\mathbf{D} + \mathbf{U}) \Delta \hat{\mathbf{Q}}^m = \hat{\mathbf{R}}^{*m}, \quad (3.27)$$

with,

$$\begin{aligned} \mathbf{D} &= \left(\frac{1}{\Delta \tau} + \frac{3}{2\Delta t} + |\lambda_i^t| + |\lambda_j^t| + |\lambda_k^t| \right) \mathbf{I}, \\ \mathbf{U} &= - \begin{bmatrix} \mathbf{A}_{i-1,j,k}^+ & \mathbf{B}_{i,j-1,k}^+ & \mathbf{C}_{i,j,k-1}^+ \end{bmatrix}, \\ \mathbf{L} &= \begin{bmatrix} \mathbf{A}_{i+1,j,k}^- & \mathbf{B}_{i,j+1,k}^- & \mathbf{C}_{i,j,k+1}^- \end{bmatrix}, \end{aligned} \quad (3.28)$$

which can be solved with a lower and upper sweeping process as,

$$\begin{aligned} \Delta \hat{\mathbf{Q}}^* &= \mathbf{D}^{-1} \left(\hat{\mathbf{R}}^* - \mathbf{L} \Delta \hat{\mathbf{Q}}^* \right), \\ \Delta \hat{\mathbf{Q}} &= \Delta \hat{\mathbf{Q}}^* - \mathbf{D}^{-1} \mathbf{U} \Delta \hat{\mathbf{Q}}. \end{aligned} \quad (3.29)$$

In order to reduce the computational cost, the matrix computations, along ξ direction for example, in Equation 3.29 can be avoided by the following approximation,

$$\begin{aligned} \mathbf{A}^\pm \Delta \hat{\mathbf{Q}} &= \frac{1}{2} \left(\frac{\partial \hat{\mathbf{F}}}{\partial \hat{\mathbf{Q}}} \Delta \hat{\mathbf{Q}} \pm |\lambda_i^t| \Delta \hat{\mathbf{Q}} \right) \\ &\approx \frac{1}{2} \left(\hat{\mathbf{F}}(\hat{\mathbf{Q}} + \Delta \hat{\mathbf{Q}}) - \hat{\mathbf{F}}(\hat{\mathbf{Q}}) \pm |\lambda_i^t| \Delta \hat{\mathbf{Q}} \right). \end{aligned} \quad (3.30)$$

The matrix-free implicit time stepping method is solved with subiterations in the pseudo time τ . In the current simulations, the number of subiterations is set to be four to

decrease the residuals of at least one order. The validation and verification of this implicit time-stepping method are shown in Appendix A.

3.6 Boundary conditions

The numerical solution to the governing equations is affected by boundary conditions. An isothermal no-slip wall condition is imposed at the wall. In the aeroacoustic studies, non-reflecting boundary conditions are required at the computational domain edges. In this section, a far-field pressure condition and an outflow boundary condition are outlined.

3.6.1 Far-field pressure boundary condition

In the far field, vortical waves are very weak and viscous effects can be neglected. Therefore, two locally Riemann invariants can be introduced based on a one-dimensional assumption,

$$R^{\pm} = \bar{u} \pm \frac{2c}{\gamma - 1}, \quad (3.31)$$

where \bar{u} is the local velocity normal to the far-field edge. R^+ can be computed locally from inside the computational domain, while R^- can be determined from the freestream quantities outside the domain. The normal velocity and speed of sound at boundaries can then be obtained by,

$$\begin{aligned} \bar{u} &= \frac{1}{2} (R^+ + R^-), \\ c &= \frac{\gamma - 1}{4} (R^+ - R^-). \end{aligned} \quad (3.32)$$

The entropy $s = p/\rho^\gamma$ is evaluated from the freestream quantities for inflow condition and from inside the domain for outflow condition. Finally, the density and pressure at the computational edge can be determined by,

$$\begin{aligned} \rho &= \left(\frac{c^2}{\gamma s} \right)^{\frac{1}{\gamma-1}}, \\ p &= \frac{\rho c^2}{\gamma}. \end{aligned} \quad (3.33)$$

This far-field pressure boundary condition is used as an incoming flow condition in all the current simulations.

3.6.2 Outflow boundary condition

At the outflow edge with wake turbulence going through, strong vortical motions exist, which can lead to reflected waves if inappropriate boundary conditions are imposed. To avoid the computational domain contaminated by reflected waves, a Zonal Characteristic Boundary Condition (ZCBC) [98] is applied in the simulations. The basic idea of ZCBC is to transform the N-S equations in the characteristic domain, where there are four outgoing waves leaving the computational domain and one acoustic wave travelling into the domain for subsonic flow. The incoming waves can be calculated based on the local information and freestream quantities. The characteristic form of the governing equations in the ξ direction can be expressed as [99, 100],

$$\frac{\partial \mathbf{R}}{\partial t} + \mathbf{L} = \mathbf{S}_C, \quad (3.34)$$

where \mathbf{R} is the characteristic vector, \mathbf{L} is the convective term and \mathbf{S}_C is the source term. They can be written as [99, 100],

$$\begin{aligned} \delta \mathbf{R} &= \mathbf{P}^{-1} \delta \mathbf{Q}, \\ \mathbf{L} &\equiv \lambda \frac{\partial \mathbf{R}}{\partial \xi} = \mathbf{P}^{-1} \left(\xi_x \frac{\partial \mathbf{E}}{\partial \xi} + \xi_y \frac{\partial \mathbf{F}}{\partial \xi} + \xi_z \frac{\partial \mathbf{G}}{\partial \xi} \right), \\ \mathbf{S}_C &= J \mathbf{P}^{-1} \left[\frac{\partial \hat{\mathbf{E}}_v}{\partial \xi} + \frac{\partial \hat{\mathbf{F}}_v}{\partial \eta} + \frac{\partial \hat{\mathbf{G}}_v}{\partial \zeta} - \right. \\ &\quad \left. \mathbf{E} \frac{\partial}{\partial \xi} \left(\frac{\xi_x}{J} \right) - \mathbf{F} \frac{\partial}{\partial \xi} \left(\frac{\xi_y}{J} \right) - \mathbf{G} \frac{\partial}{\partial \xi} \left(\frac{\xi_z}{J} \right) - \frac{\partial \hat{\mathbf{F}}}{\partial \eta} - \frac{\partial \hat{\mathbf{G}}}{\partial \zeta} \right]. \end{aligned} \quad (3.35)$$

The transform matrix \mathbf{P} and its inverse \mathbf{P}^{-1} can be found in Refs. [99, 100]. The characteristic differential variables and their corresponding convective speeds can be obtained by [99, 100],

$$\partial \mathbf{R} = \begin{bmatrix} \partial \rho - \frac{\partial p}{c^2} \\ \partial \tilde{W} \\ \partial \tilde{V} \\ \frac{\partial p}{\rho c} + \partial \tilde{U} \\ \frac{\partial p}{\rho c} - \partial \tilde{U} \end{bmatrix}, \quad \lambda(\text{diag}) = \begin{bmatrix} U \\ U \\ U \\ U + c \sqrt{\xi_x^2 + \xi_y^2 + \xi_z^2} \\ U - c \sqrt{\xi_x^2 + \xi_y^2 + \xi_z^2} \end{bmatrix}, \quad (3.36)$$

where the tilde denotes a variable normalised by the metric vector amplitude $\sqrt{\xi_x^2 + \xi_y^2 + \xi_z^2}$. The contravariant velocity is given by,

$$U = \xi_x u + \xi_y v + \xi_z w. \quad (3.37)$$

Under the subsonic flow condition, at the outflow boundary, one characteristic wave L_5 is travelling into the computational domain since $\lambda_5 < 0$. This incoming wave in the

outflow boundary zone is determined by,

$$L_5^* = L_5 - \sigma(x) \left(L_5 - L_5^{\text{target}} \right), \quad (3.38)$$

where the superscript * represents modified variables. The target value can be obtained by [99, 100],

$$\begin{aligned} L_5^{\text{target}} &= k[(p - p_\infty)/\rho c], \\ k &= 0.25 (1 - M^2) (c/l), \end{aligned} \quad (3.39)$$

where l is the distance from the outflow edge to the noise source and M is the local Mach number. The damping function $\sigma(x)$ is given by [98],

$$\sigma(x) = \frac{1}{2} \left[1 + \cos \left(\frac{x - x_s}{x_{\text{out}} - x_s} \pi \right) \right], \quad (3.40)$$

where x_s and x_{out} stand for the starting and end positions of the boundary zone where the ZCBC is applied. This ZCBC has been shown can significantly suppress pressure waves generated by vortical waves going through outflow boundaries [98].

3.7 Turbulence model

The one equation Spalart-Allmaras (S-A) model, using a Delayed Detached Eddy Simulation (DDES) strategy, is employed to take the effects of unresolved scales into account. In this section, the one equation S-A model is first provided and the DDES method is then outlined.

3.7.1 S-A model

The one equation S-A turbulence model, omitting the trip term, is given by the following expression [101],

$$\frac{\partial \hat{\nu}}{\partial t} + u_j \frac{\partial \hat{\nu}}{\partial x_j} = c_{b1} \hat{\nu} \hat{S} + \frac{1}{\sigma} \left[\frac{\partial}{\partial x_j} \left((\nu + \hat{\nu}) \frac{\partial \hat{\nu}}{\partial x_j} \right) + c_{b2} \frac{\partial \hat{\nu}}{\partial x_i} \frac{\partial \hat{\nu}}{\partial x_i} \right] - c_{w1} f_w \left(\frac{\hat{\nu}}{d_w} \right)^2. \quad (3.41)$$

The turbulent eddy viscosity is computed from the the pseudo eddy viscosity $\hat{\nu}$ by,

$$\mu_t = \rho \hat{\nu} f_{v1}, \quad (3.42)$$

where,

$$\begin{aligned}\chi &= \frac{\hat{\nu}}{\nu}, \\ f_{v1} &= \frac{\chi^3}{\chi^3 + c_{v1}^3}.\end{aligned}\tag{3.43}$$

The production term is obtained from,

$$\begin{aligned}\hat{S} &= \Omega + \frac{\hat{\nu}}{\kappa^2 d_w^2} f_{v2}, \\ \Omega &= \sqrt{2S_{ij}S_{ij}},\end{aligned}\tag{3.44}$$

where d_w is the distance to the nearest wall point, and,

$$\begin{aligned}f_{v2} &= 1 - \frac{\chi}{1 + \chi f_{v1}}, \quad f_w = g \left[\frac{1 + c_{w3}^6}{g^6 + c_{w3}^6} \right]^{1/6}, \\ g &= r + c_{w2} (r^6 - r), \quad r = \min \left[\frac{\hat{\nu}}{\hat{S} \kappa^2 d^2}, 10 \right], \\ S_{ij} &= \frac{1}{2} \left(\frac{\partial u_i}{\partial x_j} - \frac{\partial u_j}{\partial x_i} \right).\end{aligned}\tag{3.45}$$

The constants used in the S-A model are,

$$\begin{aligned}c_{b1} &= 0.1355, \quad \sigma = 2/3, \quad c_{b2} = 0.622, \quad \kappa = 0.41, \\ c_{w2} &= 0.3, \quad c_{w3} = 2, \quad c_{v1} = 7.1, \quad c_{w1} = \frac{c_{b1}}{\kappa^2} + \frac{1 + c_{b2}}{\sigma}.\end{aligned}\tag{3.46}$$

The production term in Equation 3.44 can be negative when $1.0 \leq \chi \leq 18.4$, which will cause robustness problem. In order to avoid numerical instabilities, the production term is computed in a modified way [102],

$$\begin{aligned}\hat{S} &= \Omega + \bar{S}, \quad \text{if } \bar{S} \geq -c_2 \Omega, \\ \hat{S} &= \Omega + \frac{\Omega (c_2^2 \Omega + c_3 \bar{S})}{(c_3 - 2c_2) \Omega - \bar{S}}, \quad \text{if } \bar{S} < -c_2 \Omega,\end{aligned}\tag{3.47}$$

with,

$$\bar{S} = \frac{\hat{\nu}}{\kappa^2 d^2} f_{v2},\tag{3.48}$$

and $c_2 = 0.7$, $c_3 = 0.9$.

The convection and diffusion terms in the S-A turbulence model are computed using a first-order upwind scheme and a second-order central scheme [101]. The time advancing method for the turbulence model is an implicit approximate factorisation method [101], where the convection, diffusion and destruction terms are treated implicitly, while the production term is computed explicitly to ensure the diagonal dominated property. The inflow turbulent boundary condition is $\hat{\nu}/\nu_\infty = 5$ in the simulations. Validation of this S-A turbulence model is provided in Appendix B.

3.7.2 DDES method

The Reynolds Averaged Navier-Stokes (RANS) aims to model the turbulent flow behaviour in the near-wall region, and it is too dissipative for separated flows. Large Eddy Simulation (LES) is an efficient way to simulate unsteady flow motions but is not affordable at high Reynolds numbers for wall-bounded flows. On the other hand, hybrid RANS/LES methods can be applied which utilize RANS in the near-wall region and switch to LES method in the flow separations. The SA-based DDES model [60] is one of the hybrid RANS/LES methods, and the different turbulence treatments are accomplished by changing the length scale by,

$$d_{\text{DDES}} = d_w - f_d \max(0, d_w - C_{\text{DES}} \Delta), \quad (3.49)$$

where C_{DES} is a constant (0.65), Δ is the cubic root of the local cell volume, and,

$$f_d = 1 - \tanh \left(\left(8 \frac{\nu + \nu_t}{\sqrt{\frac{\partial u_i}{\partial x_j} \frac{\partial u_i}{\partial x_j} \kappa^2 d_w^2}} \right)^3 \right), \quad (3.50)$$

where f_d is 1 in the LES region and close to 0 inside the boundary layer, thereby ensuring that a RANS solution can be obtained in the boundary layer region.

3.8 Parallel implementation

Parallelisation is important to speed up the high-order code for practical simulations. The computational domain is firstly divided into multi blocks, which are then distributed into different processors with the consideration of CPU balance. Three halo points are required by the spatial schemes in Equation 3.14 at block interfaces, the information from adjacent blocks is communicated by Message Passing Interface (MPI) asynchronously to reduce CPU waiting time. The pseudocode of the parallel version of SotonCAA is provided below. The simulations are performed on IRIDIS 4, which is the fourth generation of High Performance Computing (HPC) cluster at the University of Southampton.

3.9 Grid parameters

The grids used in the current work are generated by the commercial software *Gridgen*. In boundary layers, the nondimensional wall distance y^+ is give by,

$$y^+ = \frac{u_\tau y}{\nu}, \quad (3.51)$$

Algorithm 1 The pseudocode of SotonCAA.

```

1: procedure SOTONCAA
2:   read input parameters and grid information
3:   flow initialisation
4:   calculate the grid metrics and Jacobian
5:   for each block do
6:     send the local conserved variables to the adjacent blocks (MPI_Isnd)
7:   for each time step do
8:     for each block do
9:       get the conserved variables from the adjacent blocks (MPI_Irecv)
10:      wait the conserved variables to be fully stored in the local processor
        (MPI_Wait)
11:      compute the residuals using high-order schemes
12:      for each block do
13:        advance the solution using implicit time stepping method
14:        send the local conserved variables to the adjacent blocks (MPI_Isnd)
15:      for each block do
16:        get the conserved variables from the adjacent blocks (MPI_Irecv)
17:        wait the conserved variables to be fully stored in the local processor
        (MPI_Wait)
18:      filter spurious waves using the compact filter
19:      set boundary conditions
20:      send the conserved variables to the adjacent blocks (MPI_Isnd)
21:    output solutions

```

where $u_\tau = \sqrt{\tau/\rho}$ is the friction velocity at the wall, and $\tau = \mu \frac{\partial u}{\partial y}$ is the wall shear stress (which is calculated in the viscous sublayer), y is the distance to the wall and ν is the local kinematic viscosity of fluid. Typical DDES simulations require the viscous sublayer to be resolved by ensuring $y^+ < 10$ in the simulations. The fine grid resolution close to wall is gradually relaxed in the wall-normal direction towards outside the boundary layer.

Another important parameter for aeroacoustic simulations is the Points Per Wavelength (PPW), which describes the ability to capture acoustic waves and is mainly determined by the spatial schemes and filtering profiles. Due to the high resolution of the spatial schemes in Section 3.3, the PPW at the frequency of interests can be reduced to 8 in the acoustic propagation region [85]. However, in the near wall domain, a larger value of PPW is required, considering that the extra numerical filtering and eddy viscosity will dissipate the acoustic waves.

3.10 Acoustic radiation model

The far-field acoustics are obtained by solving the FW-H equation, and the differential form is written as [7],

$$\left(\frac{1}{c_0^2} \frac{\partial^2}{\partial t^2} - \nabla^2 \right) (c_0^2 \rho' H(f)) = \frac{\partial^2}{\partial x_i \partial x_j} (T_{ij} H(f)) - \frac{\partial}{\partial x_i} (L_i \delta(f)) + \frac{\partial}{\partial t} (Q \delta(f)), \quad (3.52)$$

where the source terms are given by,

$$\begin{aligned} T_{ij} &= \rho u_i u_j + [(p - p_0) - c_0^2 (\rho - \rho_0)] \delta_{ij} - \tau_{ij}, \\ L_i &\equiv L_{ij} \hat{n}_j = [\rho u_i (u_j - v_j) + (p - p_0) \delta_{ij} - \tau_{ij}] \hat{n}_j, \\ Q &\equiv Q_j \hat{n}_j = [\rho (u_j - v_j) + \rho_0 v_j] \hat{n}_j, \end{aligned} \quad (3.53)$$

and f determines the shape of the FW-H integration surface \mathbf{S} , $H()$ and $\delta()$ are the Heaviside and Dirac delta functions, u_i and v_i are the velocity components of the fluid and integration surface, τ_{ij} is the viscous stress tensor, and $\hat{\mathbf{n}} = (\hat{n}_1, \hat{n}_2, \hat{n}_3)$ gives the unit outward normal vector to surface \mathbf{S} . The superscript $'$ and subscript $_0$ represent the perturbation and mean quantities, respectively.

The solution to Equation 3.52 can be obtained with the convolution of the free-space Green's function, and the final integration form is provided below,

$$\begin{aligned} 4\pi p'(\mathbf{x}, t) &= \frac{\partial^2}{\partial x_i \partial x_j} \int_V \left[\frac{T_{ij}}{r|1 - M_r|} \right]_{Ret} d\mathbf{y}^3 + \frac{\partial}{\partial t} \int_{\mathbf{S}} \left[\frac{\rho' (u_n - v_n) + \rho_0 u_n}{r|1 - M_r|} \right]_{Ret} d\mathbf{S} - \\ &\quad \frac{\partial}{\partial x_i} \int_{\mathbf{S}} \left[\frac{(p - p_0) \delta_{ij} \hat{n}_j - \rho u_i (u_n - v_n)}{r|1 - M_r|} \right]_{Ret} d\mathbf{S}, \end{aligned} \quad (3.54)$$

where $M_r = M_i \hat{r}_i$ and \hat{r}_i is the i th component of the unit vector pointing from the source point \mathbf{y} to the observer location \mathbf{x} , u_n and v_n are the velocities of u_i and v_i projecting to the surface-normal direction, V is the control volume defined by the FW-H integration surface \mathbf{S} , the subscript *Ret* represents the values at the retarded time τ , which can be calculated by $\tau = t - |\mathbf{x} - \mathbf{y}|/c_0$.

The third integral in Equation 3.54 can be converted into time derivative. After the conversion and ignoring the quadrupole sources, the formulation 1A of Farassat [75] can be expressed as a sum of loading noise p'_L and thickness noise p'_T ,

$$p'(\mathbf{x}, t) = p'_L(\mathbf{x}, t) + p'_T(\mathbf{x}, t), \quad (3.55)$$

with,

$$\begin{aligned} p'_L(\mathbf{x}, t) = & \frac{1}{4\pi} \int_{\mathbf{S}} \left[\frac{\rho_0(\dot{U}_n + U_{\dot{n}})}{r(1 - M_r)^2} \right]_{Ret} d\mathbf{S} + \\ & \frac{1}{4\pi} \int_{\mathbf{S}} \left[\frac{\rho_0 U_n (r\dot{M}_r + c_0 M_r - c_0 M^2)}{r^2(1 - M_r)^3} \right]_{Ret} d\mathbf{S}, \end{aligned} \quad (3.56)$$

$$\begin{aligned} p'_T(\mathbf{x}, t) = & \frac{1}{4\pi c_0} \int_{\mathbf{S}} \left[\frac{\dot{L}_r}{r(1 - M_r)^2} \right]_{Ret} d\mathbf{S} + \frac{1}{4\pi} \int_{\mathbf{S}} \left[\frac{L_r - L_M}{r^2(1 - M_r)^2} \right] d\mathbf{S} + \\ & \frac{1}{4\pi c_0} \int_{\mathbf{S}} \left[\frac{L_r (r\dot{M}_r + c_0 M_r - c_0 M^2)}{r^2(1 - M_r)^3} \right]_{Ret} d\mathbf{S}, \end{aligned} \quad (3.57)$$

where the dot represents differentiation with respect to the retarded time τ .

The source terms in Equations 3.56 and 3.57 are firstly interpolated from the near-field high-order simulations with a second-order inverse distance method. The retarded values are then evaluated using a fourth-order polynomial interpolation scheme and the time derivatives are finally obtained from a fourth-order central scheme. The FW-H code is parallelized using MPI to reduce computational cost for multi-observer conditions.

3.11 Dynamic mode decomposition

Dynamic Mode Decomposition (DMD) was firstly introduced by Schmid [103] to analyse flow field data by computing eigenvalues and eigenvectors [104]. It can extract frequencies, growth rate and spatial structures of each dynamic mode, and therefore it is a powerful tool to provide insights into the physics of the current aerodynamic and aeroacoustic simulations. The flow data are represented by a snapshot sequence,

$$\mathbf{V}_1^N = \{\mathbf{v}_1, \mathbf{v}_2, \dots, \mathbf{v}_N\}, \quad (3.58)$$

where \mathbf{v}_i is the i -th snapshot of the flow field (can be pressure, velocity or density), and the subscript and superscript of \mathbf{V}_1^N denote the index of the snapshot in the first and last columns, respectively. These snapshots are assumed to be related by a linear operator,

$$\mathbf{v}_{i+1} = \mathbf{A}\mathbf{v}_i. \quad (3.59)$$

The last snapshot \mathbf{v}_N is a linear combination of the previous ones, given by,

$$\mathbf{v}_N = a_1 \mathbf{v}_1 + \dots + a_{N-1} \mathbf{v}_{N-1} + \mathbf{r}, \quad (3.60)$$

and \mathbf{r} is the residual. Therefore,

$$\mathbf{V}_2^N = \mathbf{A}\mathbf{V}_1^{N-1} = \mathbf{V}_1^{N-1}\mathbf{S} + \mathbf{r}\mathbf{e}_{N-1}^T, \quad (3.61)$$

where \mathbf{S} is the companion matrix,

$$\mathbf{S} = \begin{bmatrix} 0 & 0 & \dots & 0 & a_1 \\ 1 & 0 & \dots & 0 & a_2 \\ 0 & 1 & \dots & 0 & a_3 \\ \vdots & \vdots & \ddots & \vdots & \vdots \\ 0 & 0 & \dots & 1 & a_{N-1} \end{bmatrix}. \quad (3.62)$$

The dynamic modes can thus be obtained by solving the eigenvalue and eigenvectors of \mathbf{S} . However, this numerical procedure can yield an ill-conditioned matrix and cannot extract more than the first or first two dominant dynamic modes [103]. A more robust algorithm is to firstly perform a singular value decomposition of \mathbf{V}_1^{N-1} ,

$$\mathbf{V}_1^{N-1} = \mathbf{U}\mathbf{\Sigma}\mathbf{W}^T. \quad (3.63)$$

Substituting Equation 3.63 into Equation 3.61 can provide,

$$\mathbf{U}^T \mathbf{A} \mathbf{U} = \mathbf{U}^T \mathbf{V}_2^N \mathbf{W} \mathbf{\Sigma}^{-1} \equiv \tilde{\mathbf{S}}. \quad (3.64)$$

The matrix $\tilde{\mathbf{S}}$ is related to \mathbf{A} via a similarity transformation. After computing the eigenvalues λ_i of $\tilde{\mathbf{S}}$, the DMD mode can thus be obtained by [104],

$$\Phi = \mathbf{V}_1^{N-1} \mathbf{T}^{-1}, \quad (3.65)$$

where \mathbf{T} is the Vandermonde matrix defined as $\mathbf{T} = \left(\lambda_i^{j-1} \right)_{i,j}$. The frequency f_i and growth rate σ_i of each DMD mode are given by,

$$\begin{aligned} f_i &= \frac{\arg(\lambda_i)}{2\pi\Delta t}, \\ \sigma_i &= \frac{\log(|\lambda_i|)}{\Delta t}, \end{aligned} \quad (3.66)$$

where the unstable and damping dynamic modes are indicated by $\sigma_i > 0$ and $\sigma_i < 0$, respectively. The modified energy of each dynamic mode taking account of the growth ratio is [104],

$$E_i = |\lambda_i^N| \|\Phi_i\|, \quad (3.67)$$

where N is the number of snapshots. The ranking of E_i can help to select the most significant dynamic modes in the flow data.

3.12 Chapter summary

In this chapter, details of the numerical methodology applied in the current work are provided, including governing equations, spatial schemes, temporal schemes, filtering

schemes, boundary conditions, FW-H equation and dynamic mode decomposition. The validations and verifications of the implicit time-stepping method and the S-A turbulence model are given in Appendices [A](#) and [B](#), respectively.

Chapter 4

Numerical Development of a Cell-Centred Solver

4.1 Introduction

Computational Aeroacoustic (CAA) methods have been applied to a wide range of studies. The acoustic fluctuations on a background mean flow require the use of high-order, low-dispersion and low-dissipation spatial schemes such as the compact schemes by Lele [82], the Dispersion Relation Preserving (DRP) scheme by Tam and Webb [69] and the optimised compact schemes by Kim [85] and Kim and Sandberg [93]. These high-order Finite Difference (FD) schemes have been applied successfully to simulations of noise and turbulence [3, 93, 105–107]. However, their applications are limited to geometries with simple surface profiles, such as cylinders [87], jets [93, 107], multi-element airfoils [106] or cavities [108]. A large stencil is required to implement these high-order FD schemes. The limited smoothness at block interfaces in curvilinear meshes can generate numerical errors when the high-order schemes are applied to complex geometries. An additional treatment is therefore required at these interfaces to reduce grid-induced errors.

Kim and Lee [87] proposed a FD Characteristic Interface Condition (CIC) on the generalised coordinates to directly correct the flux derivatives normal to the block interface by biased schemes. Gao [88] developed a FD flux reconstruction method, which firstly modifies the fluxes at the interface in the computational space then applies biased schemes to get the flux derivatives. Du and Morris [89] studied the similarity of the FD and Finite Volume (FV) method and proposed an equivalent FV treatment at the block interface. This equivalent FV method requires to be implemented in the computational space using the grid metrics and Jacobian to represent the cell faces and cell volume. The grid metrics and Jacobian can be discontinuous and generate grid-induced errors on limited smooth grids. In this paper, the FV method is applied at block interfaces in the physical space to avoid the use of grid metrics, and the FD method is employed at block

interior points. The above interface treatments have been successfully applied [87–89]. The CIC and flux reconstruction methods apply biased spatial schemes containing more dissipation errors in comparison to high-order central schemes in the conventional one-to-one interface condition. Additionally, Du and Morris showed that CIC can generate unphysical solutions when the flow direction is parallel to the interface [89]. In such a condition, only two acoustic waves through interfaces can be modified by CIC, and these two acoustic waves are much weaker than the vortical and entropy waves, which are parallel to interfaces and will remain unchanged in CIC [89]. Numerical inaccuracy in capturing these two weak acoustic waves at block interfaces by biased schemes will lead to a failure of CIC. However, in this situation where flow is parallel to block interfaces, the conventional one-to-one interface condition employs central spatial schemes, and central spatial schemes contain less dissipation errors than biased spatial schemes. Thus, the conventional one-to-one interface condition can more accurately communicate information between two adjacent blocks with smooth grid metrics along interfaces. More computational cost is also required to implement the above additional interface treatments. Thus, applying these interface conditions only at block boundaries with large grid metric discontinuities where the conventional one-to-one interface method cannot be employed, instead of all the block boundaries, can provide more accurate solutions at reduced computational cost.

Numerical solvers can be based on either cell-vertex form or cell-centred form. In comparison to the cell-vertex method, the cell-centred formulation has control points located at cell centres, half grid size away from the origin of the grid metric discontinuities (block interface grid points). Therefore, the cell-centred formulation is less sensitive to the grid metric discontinuities. This allows more interfaces to be evaluated by the conventional one-to-one interface condition with high-order central schemes, which, as mentioned previously, are more favourable than biased schemes in CAA. However, an additional interface treatment is still required to handle large grid metric discontinuities even in the cell-centred formulation. The above interface conditions [87–89], mentioned previously, need to be implemented at overset control points along block connections. Therefore, applying them in the cell-centred space on a multi-block structured grid requires to transform related variables between cell centres and block interfaces, and the transformation procedure will generate numerical errors in simulations.

Alternatively, the implementation of FV method in the cell-centred space does not require any overset control points (cell centres) at block interface. The communication between two connected blocks can be achieved by correcting fluxes through the common interfaces (cell faces) using a Riemann solver. Additionally, numerical errors in the grid metrics at discontinuous interfaces can lead to violation of geometric conservation law [91] and therefore generate grid-induced errors. However, the geometric conservation law can be fulfilled by the FV method, because the FV method is applied directly in the physical space and does not require grid transformation by grid metrics that can contain

grid-induced errors at discontinuous block interfaces. In this work, the FV method is employed as an interface condition in high-order FD simulations using cell-centred formulation. This work combines the FD and FV techniques, which consists of four key points as follows:

- The conserved variables are evaluated at the cell centres instead of the cell vertices (grid points).
- Block interior control points are evaluated using FD methods.
- Block interfaces that contain smooth grid metrics are treated by one-to-one interface condition with FD method using central schemes.
- Block interfaces with discontinuous grid metrics are treated by FV method with biased schemes.

The control points are located only at cell centres. The cell-centred formulation has been chosen as it was found to reduce grid-induced errors along block interfaces around complex geometries compared with the cell-vertex form. Further details related to this finding are discussed later in Sections 4.2 and 4.6. Overall, this chapter aims to answer the following questions:

1. Which of the cell-vertex and the cell-centred formulations is more advantageous for high-order computational aeroacoustic simulations?
2. How to develop a stable and accurate cell-centred interface condition that is able to handle large grid metric discontinuities where the conventional one-to-one interface condition cannot be applied?

This chapter is structured in the following manner. The motivation for the cell-centred method is firstly demonstrated in Section 4.2. In Section 4.3, the development of a hybrid cell-centred FD and FV method is outlined. The stability and the grid convergence rate of the FV interface treatment are studied in Sections 4.4 and 4.5. In Section 4.6, the proposed hybrid method is validated by simulating flows around a single cylinder and tandem cylinders. Comparisons with experimental measurements and numerical predictions are also provided.

4.2 Motivation for a cell-centred method

For multi-block structured grids, the most standard block interface condition is a conventional one-to-one interface method (as shown in Figure 4.1(a)), where information

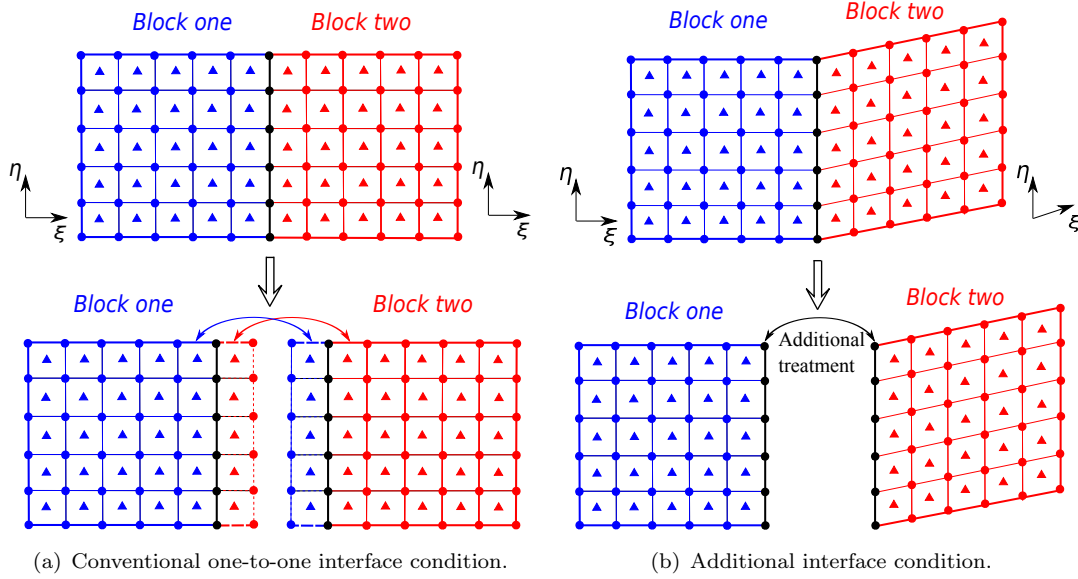


Figure 4.1: Two types of interface conditions with cell vertices (grid points) and cell centres indicated by circles and triangles, respectively. Block one, block two and block interface are coloured in blue, red and black, respectively, and halo (ghost) points are given by dashed line.

from adjacent blocks is firstly passed to halo (ghost) points of local blocks, and interface points are then treated as interior points with the same central spatial schemes. This conventional interface treatment is computationally efficient and easy to implement, but requires that grid distributions are continuous and smooth across interfaces, which cannot be satisfied by a mesh around a complex geometry. In such a case with grid metric discontinuities in Figure 4.1(b), additional interface conditions should be applied with biased schemes at interfaces, and several specific treatments have been discussed in Section 4.1. Central spatial schemes are non-dissipative in nature, and are more advantageous than the dissipative biased spatial schemes in aeroacoustic simulations. Thus, it is significant to reduce the grid metric discontinuities at the block interfaces, which can enable more interfaces to be treated by the conventional one-to-one interface condition using central spatial schemes.

Numerical solvers can be based on either cell-vertex space or cell-centred space, and these two spaces are demonstrated in Figure 4.1. In the cell-vertex formulation, cell vertices (grid points) are control points where dynamic variables (ρ , u , v , w , p) are stored. This formulation is used by most high-order FD CAA solvers. Alternatively, control points can be at cell centres, presenting a cell-centred space. The cell-centred formulation was originally proposed to implement the FV method, and has been rarely applied in high-order FD CAA solvers. In this section, it will be shown that the cell-centred space can offer advantages over the cell-vertex space, when handling discontinuous grids that generate grid-induced numerical errors in simulations.

Figure 4.2 shows a one-dimensional cluster of cell vertices and cell centres with a discontinuous angle of 30° at the I^{th} cell vertex, where I and i are the indices of cell vertices (block triangles) and cell centres (black circles). The 30° discontinuous angle measured by cell vertices is reduced to 15° in the cell-centred formulation, due to the fact that the cell centres are away from the origin of discontinuity, which is the I^{th} cell vertex in Figure 4.2. This example shows that grid metric discontinuities can be reduced by shifting control points from cell vertices to cell centres, and therefore numerical accuracy in simulations can be improved. The comparisons of cell-centred and cell-vertex formulations in high-order simulations are further assessed by analyses of a vortex convection problem in Section 4.2.1 and a single cylinder flow case in Section 4.2.2.

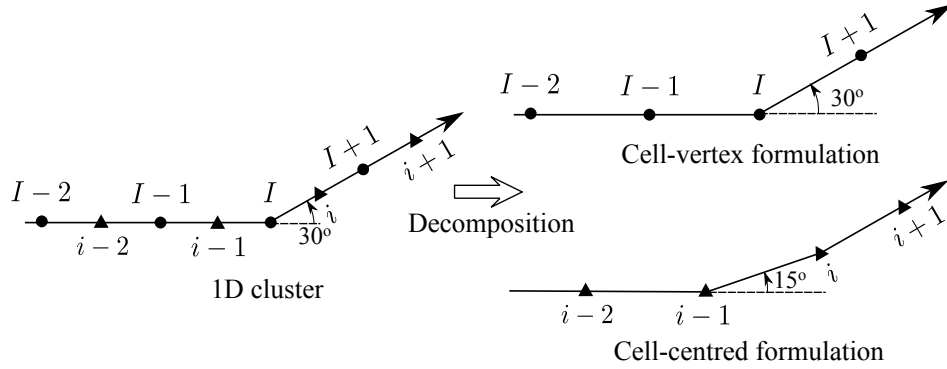


Figure 4.2: A one-dimensional cluster of cell vertices (●) and cell centres (▲).

4.2.1 Vortex convection problem

The accuracy of cell-vertex and cell-centred formulations in the conventional one-to-one interface condition can be evaluated by solving the Euler equations to simulate propagation of an inviscid vortex in a subsonic base flow at $M_\infty = 0.2$, which is prescribed by,

$$\rho(x, y, t) = \rho_\infty [1 - (\gamma - 1) \phi^2(\hat{x}, y) / 2]^{1/(\gamma-1)}, \quad (4.1a)$$

$$u(x, y, t) = u_\infty + a_\infty (y/R) \phi(\hat{x}, y), \quad (4.1b)$$

$$v(x, y, t) = -a_\infty (\hat{x}/R) \phi(\hat{x}, y), \quad (4.1c)$$

$$p(x, y, t) = p_\infty (\rho/\rho_\infty)^\gamma, \quad (4.1d)$$

with,

$$\hat{x} = x - u_\infty t, \quad (4.2a)$$

$$\phi(x, y) = \frac{\epsilon}{2\pi} \sqrt{\exp[1 - (x^2 + y^2)/R^2]}, \quad (4.2b)$$

where the computational domain was $L \leq x \leq L$, $L \leq y \leq L$ and L was 50 m in this case. $R = 0.008L$ was given to specify the size of vortex and ϵ was 0.1 to determine the vortex strength.

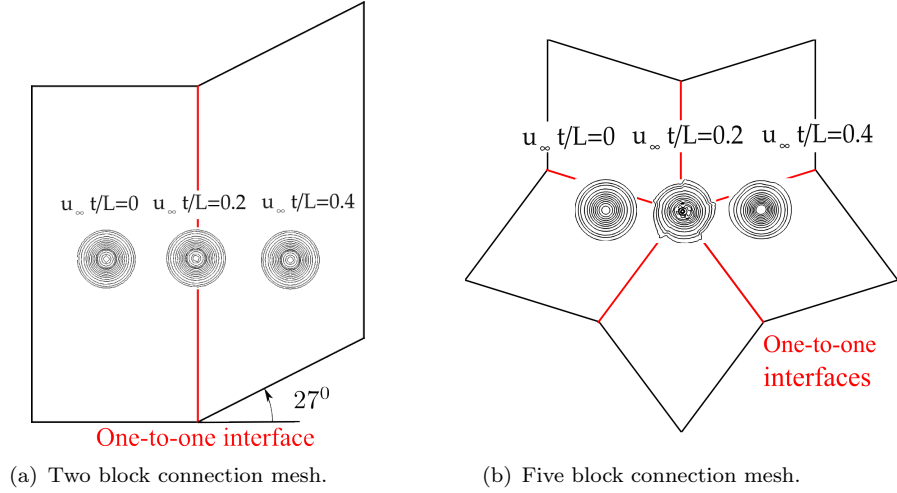


Figure 4.3: Pressure contours at different time levels, obtained by the cell-centred one-to-one interface condition.

Two mesh topologies have been tested. The first one is a two-block connected mesh with a gridline discontinuity angle of 27° at the interface, and the block topology is shown in Figure 4.3(a). The grids are uniform in each block. This interface gridline discontinuity can occur in surface grids and flow of interest region for complex geometries. The simulation accuracy for this case is obtained by calculating errors in pressure along the one-to-one interface at different time steps, given by,

$$\text{Error} = \sqrt{\sum_{i=1}^N (p_i - p_a(x, y))^2 / (N p_\infty^2)}, \quad \text{at block interface}, \quad (4.3)$$

where p_a is the analytical pressure given by Equation 4.1d, and N is the number of points at the one-to-one interface.

The second grid used in the current study is a five-block connected mesh in Figure 4.3(b). This topology can occur at the connection of O-type mesh and H-type mesh for multi-block structured grids around complex geometries. In this case, all the interfaces are treated with the one-to-one condition. The grid metric discontinuity is largest at the five-block connection point. Errors in pressure are measured at this five-block connection point by,

$$\text{Error} = |p - p_a(x, y)| / p_\infty, \quad \text{at the five-block connection point}. \quad (4.4)$$

A grid resolution of $\Delta x/L = 4 \times 10^{-3}$ is applied in both cases, which is adequate to maintain the vortex structure in simulations. The temporal integration is performed using the 4-6 stage low-dispersion and low-dissipation Runge-Kutta optimised scheme of Hu *et al.* [96] with a constant Courant number of 0.1. This small Courant number aims to minimise the errors from the temporal discretisation.

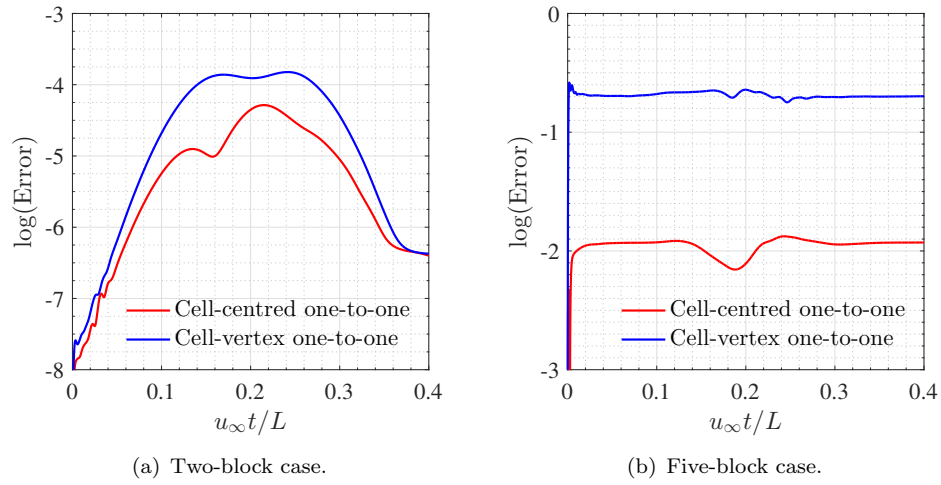


Figure 4.4: Error levels at one-to-one interface against time for a vortex convection problem.

The numerical errors at different time steps are demonstrated in Figure 4.4. For the two block connection case in Figure 4.4(a), pressure errors reach largest when the vortex core is passing through the interface, whereas lower error levels are achieved by the cell-centred method, compared to the cell-vertex approach. Pressure errors become larger in the five-block connection case, as shown in Figure 4.4(b), due to worse grid quality. The cell-vertex method shows more errors in the prediction of vortex pressures at the five-block connection point. Compared to the two-block case in Figure 4.3(a), the vortex core is slightly distorted when reaching the five-block connection point at $u_\infty t/L = 0.2$ in Figure 4.3(b). It will be shown in Section 4.5 that higher accuracy at this connection point can be obtained by applying a finite-volume interface condition. These two cases show that, compared to the cell-vertex space, the cell-centred formulation is less sensitive to the grid metric discontinuities at block interfaces, and thereby reduces grid-induced errors and provides more accurate solutions.

4.2.2 2D single cylinder flow

A comparison was conducted where two simulations of a two-dimensional cylinder flow with the same mesh and flow conditions ($M = 0.2$ and $Re = 3 \times 10^6$ based on the diameter D) were performed using cell-vertex and cell-centred methods. In this example, all block connections were treated with the conventional one-to-one boundary condition, aiming to further evaluate which of the two formulations (cell-vertex and cell-centred) is advantageous to reduced grid-related errors in high-order viscous flow simulations.

The instantaneous flow fields obtained using cell-centred and cell-vertex formulations are shown in Figure 4.5. In Figure 4.5(a) numerical errors in the velocity field along block interfaces are present. These errors are largest towards the downstream corners

where five blocks are connected. The source of these errors is the discontinuity in grid metrics. In Figure 4.5(b) where solution is obtained with the cell-centred method using the same mesh and under the same flow conditions, the flow field is less contaminated.

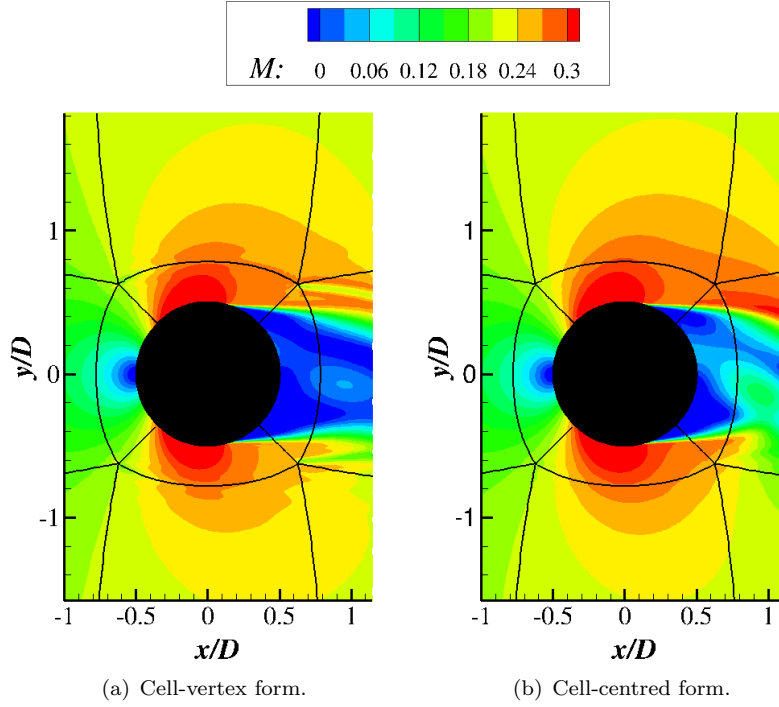


Figure 4.5: Instantaneous field of Mach number around a cylinder using cell-vertex one-to-one and cell-centred one-to-one methods, where the one-to-one interfaces are highlighted by —.

The grid-induced errors caused by grid metric discontinuities are lower in the cell-centred space, which has control points located at a half cell size away from the origin of discontinuities. This movement of control points can reduce errors in the Jacobian and grid metrics during the transformation from physical space to computational space. This effect can be also demonstrated by evaluating grid qualities at block interfaces by measuring grid metric discontinuities using filtering schemes (proposed by Fattah *et al.* [86]). For example, at a block interface with constant ξ , the grid quality metric (ΔF) is computed by [86],

$$(\Delta F)^2 = \frac{\left(\hat{\Delta} \frac{\partial x}{\partial \xi}\right)^2 + \left(\hat{\Delta} \frac{\partial y}{\partial \xi}\right)^2 + \left(\hat{\Delta} \frac{\partial z}{\partial \xi}\right)^2}{\left(\frac{\partial x}{\partial \xi}\right)^2 + \left(\frac{\partial y}{\partial \xi}\right)^2 + \left(\frac{\partial z}{\partial \xi}\right)^2}, \quad (4.5)$$

where $\hat{\Delta}$ is the difference between filtered and unfiltered values. The application of filtering schemes in Equation 4.5 can help to highlight high-wavenumber modes of grid features that are generated by discontinuities in grid line directions or grid spacings. These modes cannot be resolved by spatial schemes due to insufficient spatial resolutions, thereby inducing grid-related errors in numerical simulations. Fattah *et al.* [86] found that there is a strong correlation between the grid quality metric ΔF and the solution

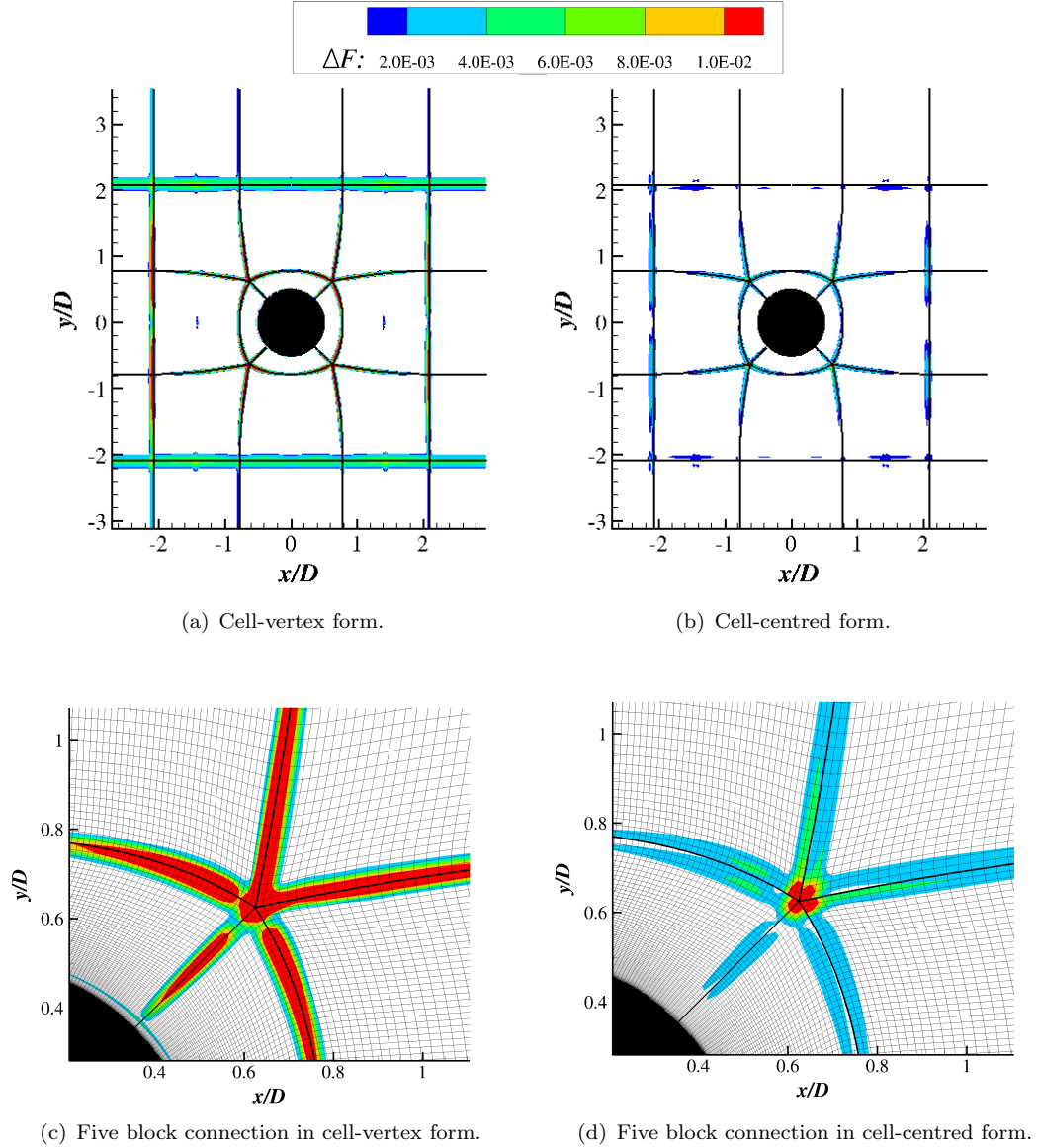


Figure 4.6: Grid quality metric values at block interfaces (—) for the single cylinder case.

accuracy for high-order simulations. Thus, the grid quality metric in Equation 4.5 can provide an indication to potential grid-induced errors in numerical simulations.

Figure 4.6 shows the grid quality metric evaluated in both cell-vertex and cell-centred spaces for the single cylinder mesh. The most problematic region is the five-block connection point as shown in Figures 4.6(c) and 4.6(d). The interface grid errors calculated in the cell-vertex formulation in Figures 4.6(a) and 4.6(c) are decreased by the cell-centred treatment in Figures 4.6(b) and 4.6(d). The cell-centred formulation is therefore advantageous as it improves numerical accuracy through reducing grid metric discontinuities by shifting control points to cell centres.

4.2.3 Section summary

High-order FD method applied on multi-block structured grids is widely used in CAA. There are two space formulations based on the location of control points. The first is cell-vertex space where fluid variables are stored at cell vertices (grid points). The second approach is to shift control points to cell centres, providing a cell-centred formulation.

Compared to the cell-vertex treatment, the cell-centred method can reduce grid metric discontinuities, considering that the control points (cell centres) are half cell size away from the origin of grid discontinuities (cell vertices at block interfaces), and thereby improved accuracy can be achieved in numerical simulations. This advantage is confirmed by simulations of a vortex convection case and a single cylinder flow case, with conventional one-to-one interface condition applied in cell-vertex space and cell-centred space, respectively. A grid quality metric proposed by Fattah *et al.* [86] is used to evaluate grid qualities at block interfaces in the single cylinder case, and it is demonstrated that potential grid-related errors in high-order simulations are decreased by changing from cell-vertex space to cell-centred space.

Despite the advantage of cell-centred method in reducing grid metric discontinuities, numerical inaccuracies are still considerable in regions containing large grid metric discontinuities. For a simulation of a vortex convecting on a five-block connected mesh, the vortex structure has been shown to be distorted at the five-block connection point. Therefore, there is a need to develop an additional interface treatment that can be applied on the cell-centred space.

FV method has been widely applied to many CFD solvers applied in cell-centred space. Thus it can be applied at block interfaces serving as an interface condition, and couples with the FD solutions inside the blocks, presenting a hybrid method. This hybrid method is based on the cell-centred formulation.

4.3 Numerical techniques in FV interface condition

In this section, details of the numerical techniques involved in the hybrid cell-centred FD and FV methods are provided. The conserved variables at cell faces are interpolated from the cell centres. The FV method is employed as an interface treatment using interpolation schemes developed in Section 4.3.1. In Section 4.3.2, the implementation procedure of the hybrid cell-centred method is outlined.

4.3.1 Cell-centred interpolation schemes

In the FV treatment along block interfaces containing grid metric discontinuities, interpolation schemes are required to obtain fluxes at cell faces from conserved variables

at cell centres. Two sets of interpolation schemes will be presented. The first one is the Finite Volume Interpolation (FVI) schemes, which are derived from optimised FD spatial schemes in Section 3.3 using the FV concept. The second scheme is developed to increase the spectral resolution and named as High Resolution Interpolation (HRI) schemes.

FVI schemes

Before the introduction of FVI schemes, the FD spatial scheme by Kim [85] in Section 3.3 is revisited:

$$\beta f'_{i-2} + \alpha f'_{i-1} + f'_i + \alpha f'_{i+1} + \beta f'_{i+2} = \frac{1}{\Delta x} \sum_{m=1}^3 a_m (f_{i+m} - f_{i-m}). \quad (4.6)$$

This scheme is used at interior grid points.

FVI interpolation schemes are derived following the method of Popescu *et al.* [109]. In their work, the DRP [69] and optimised prefactored schemes [84] were modified to provide a FV solution. For brevity, the derivation of the interpolation schemes will be demonstrated only for the interior scheme, given by Equation 4.6. The boundary closure schemes are provided in Appendix C.1. Firstly, we consider a one-dimensional linear wave equation defined by,

$$\frac{\partial f}{\partial t} + c_\infty \frac{\partial f}{\partial x} = 0, \quad (4.7)$$

where c_∞ is the speed of sound. The discretisation of this wave equation is based on a grid point cluster shown in Figure 4.7 where a control volume can be defined along the i^{th} cell. The left and right cell faces of the control volume are defined as the West and East faces respectively. The FV method on the control volume in Figure 4.7 can be expressed in the discretised form as,

$$\frac{\partial \bar{f}_i}{\partial t} \Delta x + c_\infty (f_i^e - f_i^w) = 0, \quad (4.8)$$

where \bar{f} is the volume averaged quantity and f^e , f^w are the variables at the East and West faces. By comparing the FV representation given by Equation 4.8 to the differential representation in Equation 4.7, the following expression can be obtained,

$$\bar{f}'_i = \frac{1}{\Delta x} (f_i^e - f_i^w). \quad (4.9)$$

In order to obtain cell-centred interpolation schemes, the derivatives f'_i at the left hand side in Equation 4.6 are replaced by the volume averaged variables \bar{f}'_i . By substituting the right hand side terms of Equation 4.9 into the left hand side terms of Equation 4.6,

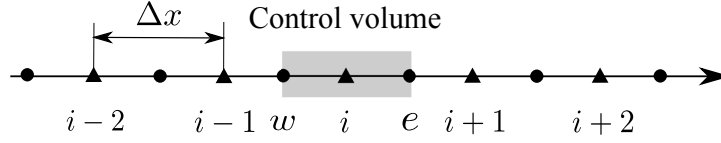


Figure 4.7: Grid point cluster of cell centres (▲) and cell vertices (●) for an one-dimensional problem.

the FV version of Equation 4.6 can be obtained as,

$$\begin{aligned} \beta (f_{i-2}^e - f_{i-2}^w) + \alpha (f_{i-1}^e - f_{i-1}^w) + (f_i^e - f_i^w) + \\ \alpha (f_{i+1}^e - f_{i+1}^w) + \beta (f_{i+2}^e - f_{i+2}^w) = \sum_{m=1}^3 a_m (f_{i+m} - f_{i-m}). \end{aligned} \quad (4.10)$$

Equation 4.10 can be split into two schemes based on the relation that $f_i^e = f_{i+1}^w$. These schemes are outlined below, which are written in terms of the East and West faces.

$$\beta f_{i-2}^e + \alpha f_{i-1}^e + f_i^e + \alpha f_{i+1}^e + \beta f_{i+2}^e = \sum_{m=-3}^3 a_m^e f_{i+m}, \quad (4.11a)$$

$$\beta f_{i-2}^w + \alpha f_{i-1}^w + f_i^w + \alpha f_{i+1}^w + \beta f_{i+2}^w = \sum_{m=-3}^3 a_m^w f_{i+m}. \quad (4.11b)$$

The coefficients on the left hand side remain the same as the original optimised FD scheme in Equation 4.6, and their values are [85],

$$\begin{aligned} \alpha &= 0.5862704032801503, \\ \beta &= 0.09549533555017055. \end{aligned} \quad (4.12)$$

The new coefficients a_m^e and a_m^w can be obtained by matching Equations 4.11a and 4.11b with Equation 4.10. This leads to the following relations,

$$\begin{aligned} a_{-3}^e &= a_3^w = 0, \\ a_{-2}^e &= a_3^e = a_{-3}^w = a_2^w = a_3 = 0.007140953479797, \\ a_{-1}^e &= a_2^e = a_{-2}^w = a_1^w = a_2 + a_3 = 0.265742055829304, \\ a_0^e &= a_1^e = a_{-1}^w = a_0^w = a_1 + a_2 + a_3 = 0.908882729521220. \end{aligned} \quad (4.13)$$

The order of accuracy of the East and West face interpolation schemes in Equation 4.11a and 4.11b can be confirmed by applying the Taylor-series expansion theory, which can yield,

$$f_i^e = f_{i+\frac{1}{2}} - 0.04167 f_{i+\frac{1}{2}}^{(2)} \Delta x^2 - 0.01527 f_{i+\frac{1}{2}}^{(4)} \Delta x^4 + O(\Delta x^6), \quad (4.14a)$$

$$f_i^w = f_{i-\frac{1}{2}} - 0.04167 f_{i-\frac{1}{2}}^{(2)} \Delta x^2 - 0.01527 f_{i-\frac{1}{2}}^{(4)} \Delta x^4 + O(\Delta x^6), \quad (4.14b)$$

indicating that the interpolation schemes for the East and West faces are second-order accurate. However, the fourth-order accuracy of the FD scheme in Equation 4.6 can still be recovered if the East and West face interpolation schemes are combined together. This can be demonstrated by substituting Equations 4.14a and 4.14b into Equation 4.9,

$$\begin{aligned}\bar{f}'_i &= \frac{1}{\Delta x} (f_i^e - f_i^w) \\ &= \frac{1}{\Delta x} \left(f_{i+\frac{1}{2}} - f_{i-\frac{1}{2}} \right) - \\ &\quad 0.04167 \left(f_{i+\frac{1}{2}}^{(2)} - f_{i-\frac{1}{2}}^{(2)} \right) \Delta x - \\ &\quad 0.01527 \left(f_{i+\frac{1}{2}}^{(4)} - f_{i-\frac{1}{2}}^{(4)} \right) \Delta x^3 + O(\Delta x^5).\end{aligned}\tag{4.15}$$

The variables at $i + \frac{1}{2}$ and $i - \frac{1}{2}$ in Equation 4.15 can be further expanded at i , and this will eventually lead to,

$$\bar{f}'_i = f'_i - 0.01649 f_i^{(4)} \Delta x^4 + O(\Delta x^6),\tag{4.16}$$

which is fourth-order accurate. Equation 4.16 is also the exact Taylor truncation form of the original optimised penta-diagonal FD scheme in Equation 4.6. Although the interpolation schemes are second-order accurate, the truncation errors up to the fourth order in the East and West face interpolations can be cancelled if they are combined by Equation 4.9, and finally the FD spatial scheme in Equation 4.6 can be recovered. This suggests that the dispersion relations of the FD scheme (Equation 4.6) and the FV schemes (Equations 4.11a and 4.11b) are equivalent for a linear case where Equation 4.9 is applied after FV interpolations.

However, for a non-linear case (inviscid Burgers' equation) given by,

$$\frac{\partial f}{\partial t} + \frac{\partial f^2}{\partial x} = 0,\tag{4.17}$$

the interpolation schemes in Equation 4.11a and Equation 4.11b are firstly applied to obtain the conserved variables f_i^e and f_i^w at the East face and the West face, which are then used to reconstruct the fluxes $f_i^{2,e}$ and $f_i^{2,w}$. This reconstruction procedure will change the original relationship in truncation errors between the East and West interpolation schemes, as a result of which the fourth-order accuracy of the FD spatial derivative scheme cannot be recovered with the application of $(f_i^{2,e} - f_i^{2,w})/\Delta x$ after flux reconstructions, for a non-linear case. However, for a realistic problem, the interpolation schemes are only applied at block interfaces requiring the FV treatment, and the fourth-order optimised FD schemes are employed at the majority of computational domain. Previous research has shown that global high-order accuracy can be maintained even with low-order boundary closure schemes [84]. It will also be demonstrated in Section 4.5 that the order of accuracy of a vortex convection problem is still close to fourth

order at FV interfaces. Popescu *et al.* [109] tested a non-linear wave case described by Equation 4.17 using a FD DRP scheme (fourth-order accurate) and its equivalent FV interpolation schemes (second-order accurate). The initial condition and final solution in their test are discontinuous to evaluate the performances of FD and FV schemes on handling high gradients and discontinuities. They showed that the FV interpolation schemes have significantly higher accuracy over the original FD schemes in regions with high gradients and discontinuities, since the conservation law can be better satisfied by the FV method in these regions. The high gradients in their test can refer to velocities in the boundary layer, and the discontinuities can occur in the grid metrics at block interfaces with large gridline and grid spacing changes. The test of the non-linear case (Equation 4.17) by Popescu *et al.* [109] suggests that the FV treatment is more desirable than the FD scheme to increase numerical accuracy in the boundary layer region and at block interfaces with grid metric discontinuities.

HRI schemes

In order to achieve high-order accuracy for non-linear problems, a set of High Resolution Interpolation (HRI) schemes have been developed, which aim to increase spectral resolution by decreasing dissipation errors in high wavenumber range measured by an interpolation transfer function. Consistent with FVI schemes, HRI schemes are also based on a penta-diagonal compact system [82],

$$\beta^H f_{i-\frac{5}{2}} + \alpha^H f_{i-\frac{3}{2}} + f_{i-\frac{1}{2}} + \alpha^H f_{i+\frac{1}{2}} + \beta^H f_{i+\frac{3}{2}} = \sum_{m=1}^3 a_m^H (f_{i-1+m} - f_{i-m}). \quad (4.18)$$

A fourth-order accuracy can be achieved with the condition of,

$$\begin{aligned} 1 + 2(\alpha^H + \beta^H) &= 2(a_1^H + a_2^H + a_3^H), \\ \alpha^H + 4\beta^H &= \frac{1}{4}(a_1^H + 9a_2^H + 25a_3^H). \end{aligned} \quad (4.19)$$

The boundary closure schemes can be obtained by a fourth-order polynomial extrapolation of both $f_{i-\frac{1}{2}}$ and f_i at $i = -1, -2$ and -3 , where the grid points start from $i = 0$. The fourth-order polynomial extrapolation can guarantee a fourth-order accuracy for interpolation schemes at boundaries. The extrapolations can be written as,

$$\begin{aligned} g_{i-\frac{1}{2}} &= f_{-\frac{1}{2}} + \sum_{m=1}^4 c_m i^m, \quad i = -1, -2, \\ g_i &= f_0 + \sum_{m=1}^4 d_m i^m, \quad i = -1, -2, -3, \end{aligned} \quad (4.20)$$

where $g_{i-\frac{1}{2}}$ and g_i are the extrapolated cell-faced and cell-centred variables beyond the boundary, and c_m, d_m are the extrapolation coefficients. These coefficients can be determined firstly by matching $g_{i-\frac{1}{2}}$ and g_i with interior values. This will provide the

following conditions,

$$\begin{aligned} g_{i-\frac{1}{2}} &= f_{i-\frac{1}{2}}, \quad i = 1, 2, \\ g_i &= f_i, \quad i = 1, 2, 3, 4. \end{aligned} \quad (4.21)$$

In order to maintain a penta-diagonal system, the conditions of $g_{\frac{5}{2}} = f_{\frac{5}{2}}$ and $g_{\frac{7}{2}} = f_{\frac{7}{2}}$ are not considered. Another two conditions are set to make the extrapolated variables satisfy Equation 4.18 at boundaries of $i = 0$ and $i = 1$,

$$\begin{aligned} \beta^H g_{-\frac{5}{2}} + \alpha^H g_{-\frac{3}{2}} + f_{-\frac{1}{2}} + \\ \alpha f_{\frac{1}{2}} + \beta f_{\frac{3}{2}} = a_1^H (f_0 + g_{-1}) + a_2^H (f_1 + g_{-2}) + a_3^H (f_2 + g_{-3}), \end{aligned} \quad (4.22a)$$

$$\begin{aligned} \beta^H g_{-\frac{3}{2}} + \alpha^H f_{-\frac{1}{2}} + f_{\frac{1}{2}} + \\ \alpha^H f_{\frac{3}{2}} + \beta^H f_{\frac{5}{2}} = a_1^H (f_1 + f_0) + a_2^H (f_2 + g_{-1}) + a_3^H (f_3 + g_{-2}). \end{aligned} \quad (4.22b)$$

Now, the coefficients of c_m and d_m can be expressed as a function of interior variables. Transfer function of Equation 4.18 is given by Equation 4.23. The improved resolutions of the interpolation schemes are determined by minimising $\int |T(k) - 1|^2 dk$ to resolve a wider wavenumber range with optimised transfer function profiles.

$$T(k) = \frac{2a\cos\left(\frac{k}{2}\right) + 2b\cos\left(\frac{3k}{2}\right) + 2c\cos\left(\frac{5k}{2}\right)}{1 + 2a\cos(k) + 2b\cos(2k)}. \quad (4.23)$$

The following two requirements are proposed by Lele [82] to optimise the shape of the transfer function, and they are also used in the current work,

$$T(k_1) = 1, \quad \frac{\partial T(k_1)}{\partial k} = 0. \quad (4.24)$$

Another limitation is imposed to control the profile in high-wavenumber range, which can be expressed as,

$$T(k_2) = 0.95. \quad (4.25)$$

In the current study, the values of k_1 and k_2 for both interior and boundary schemes are obtained by trial and errors to provide stable and higher resolvable wavenumbers. The values of parameters used in this study are listed in Table. 4.1.

	$i = 0$	$i = 1$	$i = 2$	Interior
k_1	0.408π	0.479π	0.5π	0.5π
k_2	0.7π	0.729π	0.771π	0.8π

Table 4.1: Parameters that are used to optimise the characteristic resolution of HRI schemes.

The coefficients in Equation 4.18 for interior grids (interior scheme) can be finally obtained through the constraints in Equations 4.19, 4.24 and 4.25 and they are illustrated in Table 4.2.

Coefficients	Value
α^H	0.497107133346296
β^H	0.046568659361936
a_1^H	0.842462272120975
a_2^H	0.196204575226641
a_3^H	0.005008945360617

Table 4.2: Coefficients in HRI scheme for interior grid points in Equation 4.18.

Through solving Equations 4.19, 4.20, 4.21, 4.22, 4.24 and 4.25, the boundary closure schemes which are optimised by using the parameters in Table 4.2 can be derived as,

$$\begin{aligned}
i = 0 : \quad & f_{-\frac{1}{2}} + \gamma_{01}^H f_{\frac{1}{2}} + \gamma_{02}^H f_{\frac{3}{2}} = \sum_{m=0}^4 b_{0m}^H f_m, \\
i = 1 : \quad & \gamma_{10}^H f_{-\frac{1}{2}} + f_{\frac{1}{2}} + \gamma_{12}^H f_{\frac{3}{2}} + \gamma_{13}^H f_{\frac{5}{2}} = \sum_{m=0}^4 b_{1m}^H f_m, \\
i = 2 : \quad & \gamma_{20}^H f_{-\frac{1}{2}} + \gamma_{21}^H f_{\frac{1}{2}} + f_{\frac{3}{2}} + \gamma_{23}^H f_{\frac{5}{2}} + \gamma_{24}^H f_{\frac{7}{2}} = \sum_{m=0}^4 b_{2m}^H f_m,
\end{aligned} \tag{4.26}$$

with the coefficients provided in Table 4.3. Another set of boundary closure schemes using halo point information has also been derived and is provided in Appendix C.2.

Coefficients	$i = 0$	$i = 1$	$i = 2$
γ_{i0}^H	N/A	0.123259484686095	0.021095289927329
γ_{i1}^H	4.432150748399510	N/A	0.817915883652646
γ_{i2}^H	-1.937388412775828	0.170980625725473	N/A
γ_{i3}^H	N/A	-0.086367864306800	0.439507048062401
γ_{i4}^H	N/A	N/A	0.021095289927329
b_{i0}^H	3.742465025073278	0.566312404002169	0.142073222312129
b_{i1}^H	0.682535782838336	0.789970189302203	0.817915883652646
b_{i2}^H	-0.869341248661536	-0.133915825896421	0.819959990402501
b_{i3}^H	-0.109728364026333	-0.014761083181540	0.141051168937201
b_{i4}^H	0.048831140399945	0.000266561878355	0.000204410674986

Table 4.3: Coefficients in HRI schemes with fully biased boundary treatment in Equation 4.26.

The transfer function profiles of the FVI and HRI schemes are plotted in Figure 4.8. In Figure 4.8(a), the real part of the FVI interior scheme goes above 1.0 in the mid-wavenumber range. As mentioned previously, the FVI interpolation schemes are second-order accurate. The anti-diffusion profile in the mid-wavenumber range is due to the third-order and fourth-order truncation errors. In Figure 4.8(a), the HRI interior scheme provides higher resolutions up to $k\Delta x/\pi = 0.8$. The HRI boundary schemes ($i = 0, 1, 2$) are more dissipative than the HRI interior scheme for cell-face interpolations in the mid- and high-wavenumber ranges. Due to the biased treatment, the imaginary part of the transfer function of the boundary closure schemes is not zero, and the interpolation dispersion errors are shown in Figure 4.8(b). It should also be emphasised that the transfer function profile of the FVI scheme in Figure 4.8 is obtained from the East

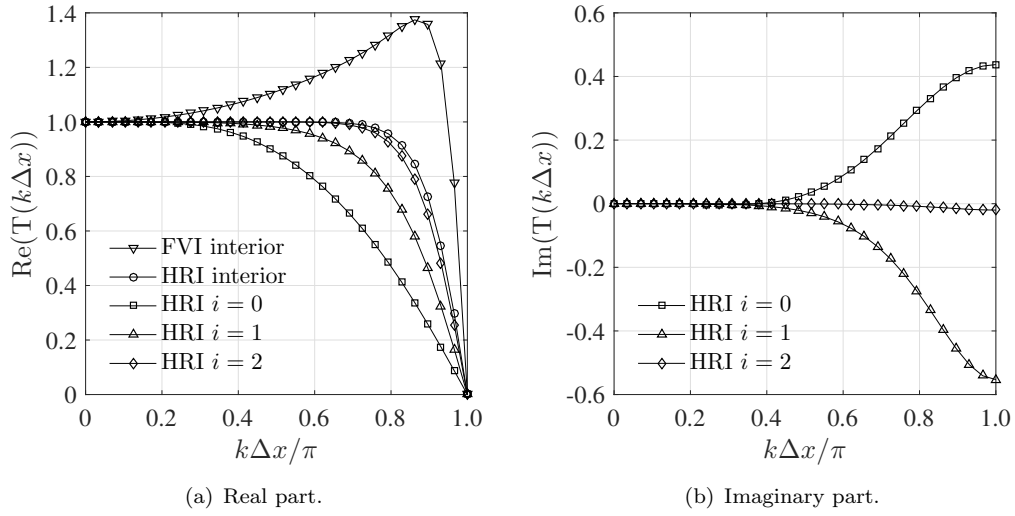


Figure 4.8: Transfer function profiles for FVI and HRI schemes.

face interpolation or the West face interpolation. These two interpolation schemes are required to be applied together in the implementation of the FV treatment. Although any of the two FVI interpolation schemes cannot individually show a good spectral resolution in Figure 4.8(a), they can still provide the optimised dispersion relationship in Figure 3.12 of the original FD spatial derivative scheme (Equation 4.6) for a linear case, considering that after these two interpolation schemes are combined together by Equation 4.9, the third-order and fourth-order truncation errors can cancel each other. The performance of the FVI and HRI schemes will be further compared by an eigenvalue analysis (Section 4.4), a grid convergence study (Section 4.5) and simulations of test cases (Section 4.6).

4.3.2 Implementation of FV interface condition

In the current work, the FV method is applied at block interfaces with large grid metric discontinuities to communicate flow information between connected blocks. The application procedure is detailed below:

1. Interpolate conserved variables (ρ , ρu , ρv , ρw , ρe) from cell centres (control points) onto cell faces using FVI or HRI schemes ¹.
2. Reconstruct inviscid fluxes at block interfaces from the interpolated conserved variables.

¹It should be noted that FVI and HRI schemes are only used at block interfaces with FV treatment. At interior grid points, the original optimised penta-diagonal FD scheme in Equation 4.6 is employed.

3. Correct the inviscid fluxes using a Riemann solver of Roe [110]².
4. Compute viscous fluxes using an explicit low-order central scheme³.
5. Apply the FV method at block interfaces to obtain residuals and march the solution in time.

4.3.3 Section summary

In this section, a hybrid cell-centred FD and FV solver has been developed. The FD approach is more accurate for smooth grid metrics. However, grid metric discontinuities are inevitable for multi-block structured grids around complex geometries, and they can generate grid-induced errors in the simulations. The implementation of FV method is based on the geometric information of local cells (such as cell volumes, cell face vectors and areas, etc.) and does not require the use of grid metrics. Thus, the FV method is advantageous over the FD method to reduce errors induced by poor grid quality at block interfaces. Thus, the proposed hybrid method utilizes FD method at block interior points and applies FV method along block interfaces with grid metric discontinuities.

The FV treatment is accomplished by interpolation schemes, which are used to obtain the fluxes through cell faces. In this section, two sets of interpolation schemes have been developed. The first one is derived from optimised FD schemes and called FVI schemes, which contain two separate schemes for the East face and West face interpolations. The FVI schemes are second-order accurate. However, the third-order and fourth-order truncation errors can be cancelled when combining the East face and West face schemes together. The second scheme (HRI scheme) is developed to improve spectral resolution measured by the transfer function, and ensure a fourth-order accuracy, for cell-face interpolations. The boundary closure treatments for the HRI schemes are derived from fourth-order extrapolations.

4.4 Eigenvalue analysis

To assess the numerical stability of the proposed FV interface treatment, the eigenvalue analysis was performed by considering the one-dimensional scalar wave propagation problem, given by Equation 4.7. A domain defined by $x \in [0, L]$ is decomposed into N

²This procedure is similar to the Characteristic Interface Condition (CIC), and both upwind characteristic waves in the characteristic domain. However, CIC modifies flux derivatives and Roe's Riemann solver changes the fluxes directly. The Roe's Riemann solution is provided in Appendix D.

³Both standard explicit second-order and fourth-order central schemes have been tested, showing similar results at high Re .

evenly spaced intervals of width $\Delta x = L/N$. The interpolation schemes for the East-face and West-face fluxes can be written in matrix form,

$$\mathbf{P}^e \mathbf{f}^e = \mathbf{Q}^e \mathbf{f}, \quad (4.27a)$$

$$\mathbf{P}^w \mathbf{f}^w = \mathbf{Q}^w \mathbf{f}, \quad (4.27b)$$

where \mathbf{f} is an N -dimensional vector which represents the object function at the cell-centred points and \mathbf{f}^e and \mathbf{f}^w are the vectors standing for the fluxes through the East and West faces. The variables \mathbf{P}^e , \mathbf{P}^w , \mathbf{Q}^e and \mathbf{Q}^w are $N \times N$ matrices containing the scheme coefficients. By using Equation 4.9, the following expression can be obtained,

$$\bar{\mathbf{f}}' = \frac{1}{\Delta x} \mathbf{M} \mathbf{f} = \frac{1}{\Delta x} (\mathbf{M}^e - \mathbf{M}^w) \mathbf{f}, \quad (4.28)$$

where $\mathbf{M}^e = [\mathbf{P}^e]^{-1} \mathbf{Q}^e$ and $\mathbf{M}^w = [\mathbf{P}^w]^{-1} \mathbf{Q}^w$.

Similarly, the filtered variables can be calculated by solving Equation 3.15 corresponding to the compact filter,

$$\mathbf{R} \hat{\Delta} \mathbf{f} = \mathbf{S} \mathbf{f}, \quad (4.29)$$

where $\hat{\Delta} \mathbf{f}$ is an N -dimensional vector representing the filtered variables and \mathbf{R} , \mathbf{S} are $N \times N$ matrices. After filtering, the numerical derivatives can be expressed as,

$$\mathbf{f}' = \frac{1}{\Delta x} \mathbf{M} (\mathbf{I} + \mathbf{R}^{-1} \mathbf{S}) \mathbf{f}. \quad (4.30)$$

Substituting Equation 4.30 into Equation 4.7 then leads to a matrix-vector form,

$$\frac{\partial \mathbf{f}}{\partial t} = -\frac{c_\infty}{\Delta x} \mathbf{M} (\mathbf{I} + \mathbf{R}^{-1} \mathbf{S}) \mathbf{f}. \quad (4.31)$$

Equation 4.31 is a system of ordinary differential equations with constant coefficients. Therefore, the eigenvalue problem can be obtained after imposing the normal modes $\mathbf{f} = \mathbf{f}_0 e^{w t}$ into Equation 4.31,

$$-\mathbf{M} (\mathbf{I} + \mathbf{R}^{-1} \mathbf{S}) \mathbf{f}_0 = \omega \mathbf{f}_0, \quad (4.32)$$

where $\omega = w \Delta x / c_\infty$ is the dimensionless eigenvalue and \mathbf{f}_0 is the corresponding eigenvector. The real part of the eigenvalues should be not greater than zero to ensure numerical stability, i.e. $|e^{\omega t}| \leq 1$.

Figure 4.9 is an illustration of a two-block system, where the cell-centred FV method is applied at the interface between the control points i and $i + 1$. A boundary condition $f(x = 0, t) = 0$ is set without loss of generality [111] in the first block. The boundary condition in the second block is $f_{i+1}^w = f_i^e$ aiming to upwind the fluxes through the West face of the $(i + 1)^{\text{th}}$ cell, since the wave in Equation 4.7 is travelling from the left to the

right block. Then, the FV method is applied to obtain the derivatives by Equation 4.28, after which the eigenvalues in the system of Equation 4.32 can be evaluated numerically.

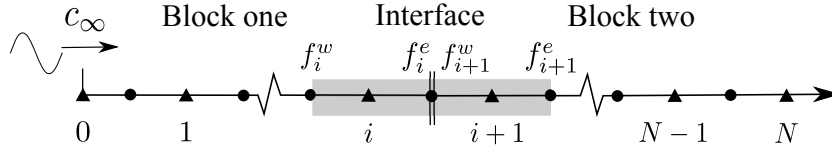


Figure 4.9: A multi-block grid point cluster for eigenvalue analysis, ▲ cell centres, ● cell vertices.

The eigenvalue distributions obtained from the FVI schemes and the HRI schemes for a single block case and a two-block case are illustrated in Figure 4.10 where $N = 64$ and the cut-off wavenumber for the compact filter is $\kappa_c = 0.8\pi$, which is the value used in the forthcoming single and tandem cylinders simulations in the validation Section 4.6. Other values of N and κ_c have also been tested in this eigenvalue analysis, and they demonstrated the same distribution patterns. The imaginary part of the eigenvalues indicates the wavenumber of modes existing in the one-dimensional system evaluated by the numerical schemes. For the single block case in Figure 4.10(a), the highest wavenumber that can be resolved by the FVI schemes before filtering is approximately 0.8π , which is higher than 0.6π by the FVI schemes with filtering and 0.6π by the HRI schemes without any filtering. However, the high wavenumber range ($0.6\pi < \text{Im}(\omega) < 0.8\pi$) of the FVI schemes is dominated by unstable modes due to the positive real part, and these unstable modes are successfully damped by numerical filtering. The HRI schemes can provide a stable solution without filtering.

For the two-block system in Figure 4.10(b), some eigenvalues ($0.6\pi < \text{Im}(\omega) < 0.8\pi$) from the FVI schemes without filtering are located across the right half plane, suggesting unstable modes. However, this wavenumber range is not resolved by the HRI schemes and hence only stable modes are present for the HRI schemes under the two-block condition. After filtering, the unstable modes in the FVI schemes are damped to become stable.

In conclusion, in the linear eigenvalue analysis, the FVI schemes can resolve a higher wavenumber range than the HRI schemes, but the modes in the higher wavenumber range are not stable. The HRI schemes are slightly more dissipative and more stable compared to the FVI schemes, due to the fact that the high-wavenumber modes are unresolved. However, the instabilities from the FVI schemes can be avoided by the application of filtering, after which the FVI schemes show a comparable resolvable wavenumber range with the HRI schemes. Overall, stable solutions to the FV interface condition can be obtained from both the FVI and HRI schemes. Further comparisons of the FVI and HRI schemes applied to nonlinear problems will be discussed in Section 4.6.

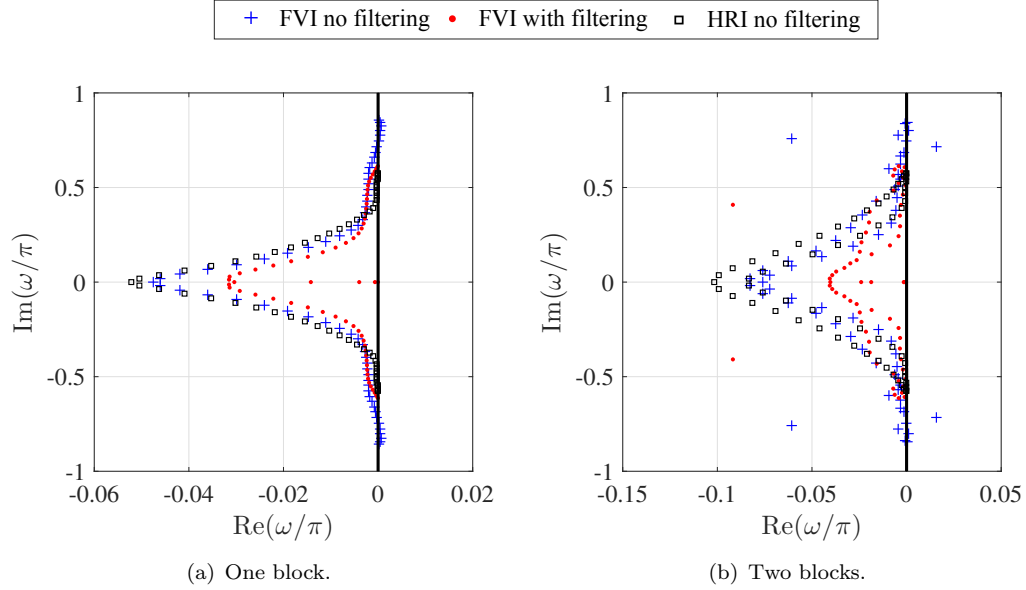


Figure 4.10: Eigenvalue distributions for single-block and two-block cases where $N = 64$.

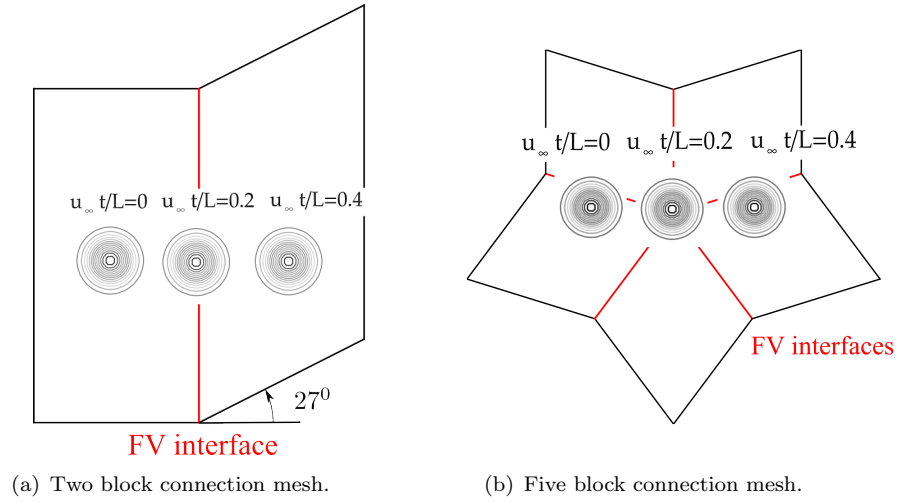


Figure 4.11: Pressure contours at different time levels for a grid convergence study of the FV interface treatment.

4.5 Grid convergence study

The order of accuracy of the FV interface treatment can be evaluated by solving the vortex convection problem detailed in Section 4.2 on a two-block connected mesh and a five-block connected mesh. The numerical errors in pressure are calculated by Equations 4.3 and 4.4, respectively, at a non-dimensional time of $u_\infty t/L = 0.2$ at different grid resolutions. The pressure contours are shown in Figure 4.11.

Figure 4.12(a) plots the error convergence rate in the two-block case. It shows that the decay rate of errors for both schemes follows a fourth-order slope. The HRI schemes

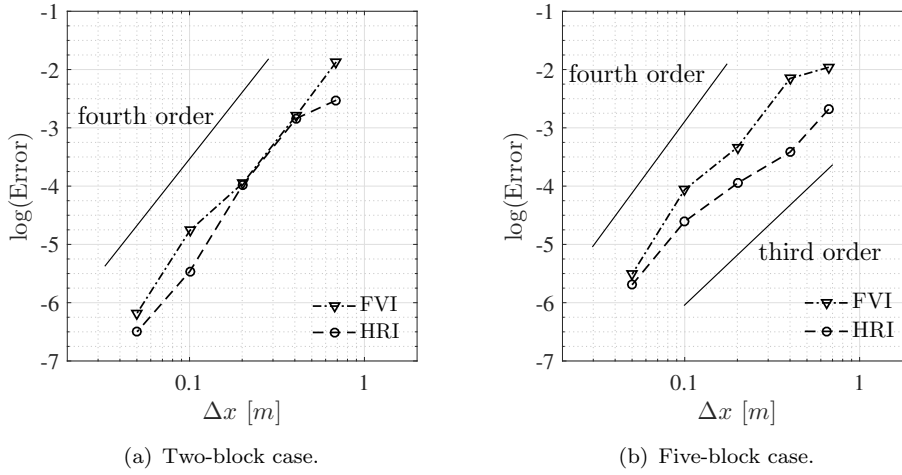


Figure 4.12: Convergence rate for a grid convergence study of the FV interface treatment.

performs with slightly higher accuracy compared to the FVI schemes in this case. For the five block case in Figure 4.11(b), the vortex core is maintained when passing through the five-block connection point, more accurate than the one-to-one interface condition in Figure 4.3(b). In the five-block case shown in Figure 4.12(b), the HRI schemes is more accurate over the FVI schemes at low grid resolutions. However, errors from HRI schemes at the five-block connection point converge slower (close to the third-order slope) compared to the FVI schemes (close to the fourth-order slope), and as a result the pressure errors from both schemes are comparable at the highest grid resolution of $\Delta x = 0.05$ m.

In conclusion, for the two-block connection mesh, the performance of FVI and HRI schemes is comparable at the FV interface. At the five-block connection point, HRI schemes show a higher accuracy at lower grid resolutions.

4.6 Validations of cell-centred method

To verify and validate the accuracy of the cell-centred one-to-one and FV interface treatments, two three-dimensional simulations were conducted. The first one is a single cylinder case. The second validation case is an aeroacoustic benchmark case of the flow around tandem cylinders. The simulations of both cases contain block interfaces that are treated using one-to-one and FV interface methods.

4.6.1 Single cylinder flow

The grid is based on the previous two-dimensional case in Section 4.2.2 and the computational domain extends by $18D$ in the upstream direction, $31D$ in the downstream direction and $20D$ in the transverse direction, from the cylinder centre, where D is the diameter of cylinder. The first grid point is at a distance of $2.5 \times 10^{-5}D$ away from the wall, and the maximum y^+ in the simulation was shown to be approximately 4.0 in the suction region of the cylinder surface. A grid stretching ratio of 1.2 in the wall normal direction is used to relax the grid distribution in the boundary layer. The cylinder is discretised by 400 grid points in the circumferential direction. The spanwise flow is resolved using a grid resolution of $\Delta z/D = 0.05$ with 60 points and is modelled with a periodic boundary condition. The total grid points for this case are 9×10^6 . The current grid resolution has been previously demonstrated to be sufficient for aerodynamic and aeroacoustic simulations of a single circular flow [80]. The flow condition were $M = 0.2$ and $Re = 3 \times 10^6$, based on the cylinder diameter D . The maximum CFL corresponding to the physical time step size (Δt) in the simulations is 25 based on the local convective speed of sound ($u + c$) and cell size. Four simulations have been performed for the single cylinder flow case, which use the cell-vertex one-to-one interface condition, cell-centred one-to-one interface condition and cell-centred FV interface condition with the FVI and HRI schemes, respectively. The mean flow data are obtained by an average over 1×10^6 time steps, corresponding to approximately 25 oscillation cycles (flow periods). Each simulation used 128 processors for approximately 280 wall clock hours (≈ 12 days).

The instantaneous flow features are illustrated in Figure 4.13, which shows the Q -criteria and density perturbations. In the simulation with cell-vertex one-to-one interface condition (Figure 4.13(a)), discontinuities in the density field occur at the one-to-one interfaces. The downstream five-block connection point is demonstrated to be a source of grid-induced errors by the plot of Q -criteria, and the spurious flow structures originated at this point are then convected downstream. However, the velocity and density profiles are continuous across the block interfaces in the cell-centred simulation with the one-to-one condition (Figure 4.13(b)), which shows the effectiveness of changing the control points from cell vertices to cell centres. The grid related errors are also not observable in the cell-centred FV simulations using either the FVI schemes (Figure 4.13(c)) or the HRI schemes (Figure 4.13(d)), implying that the FV method can correctly communicate information between two connected blocks at interfaces.

The simulation data were collected to compare with experimental studies by Roshko [112] and Anchenbach [113] and the DES (based on the S-A turbulence model) numerical simulations by Travin *et al.* [114]. In the following discussions, an observer angle θ is defined as the angle measured from the upstream stagnation point, which is positive in the clockwise direction. Figure 4.14(a) demonstrates the mean pressure coefficient (C_p) profile along the cylinder surface. The numerical results from both the cell-centred

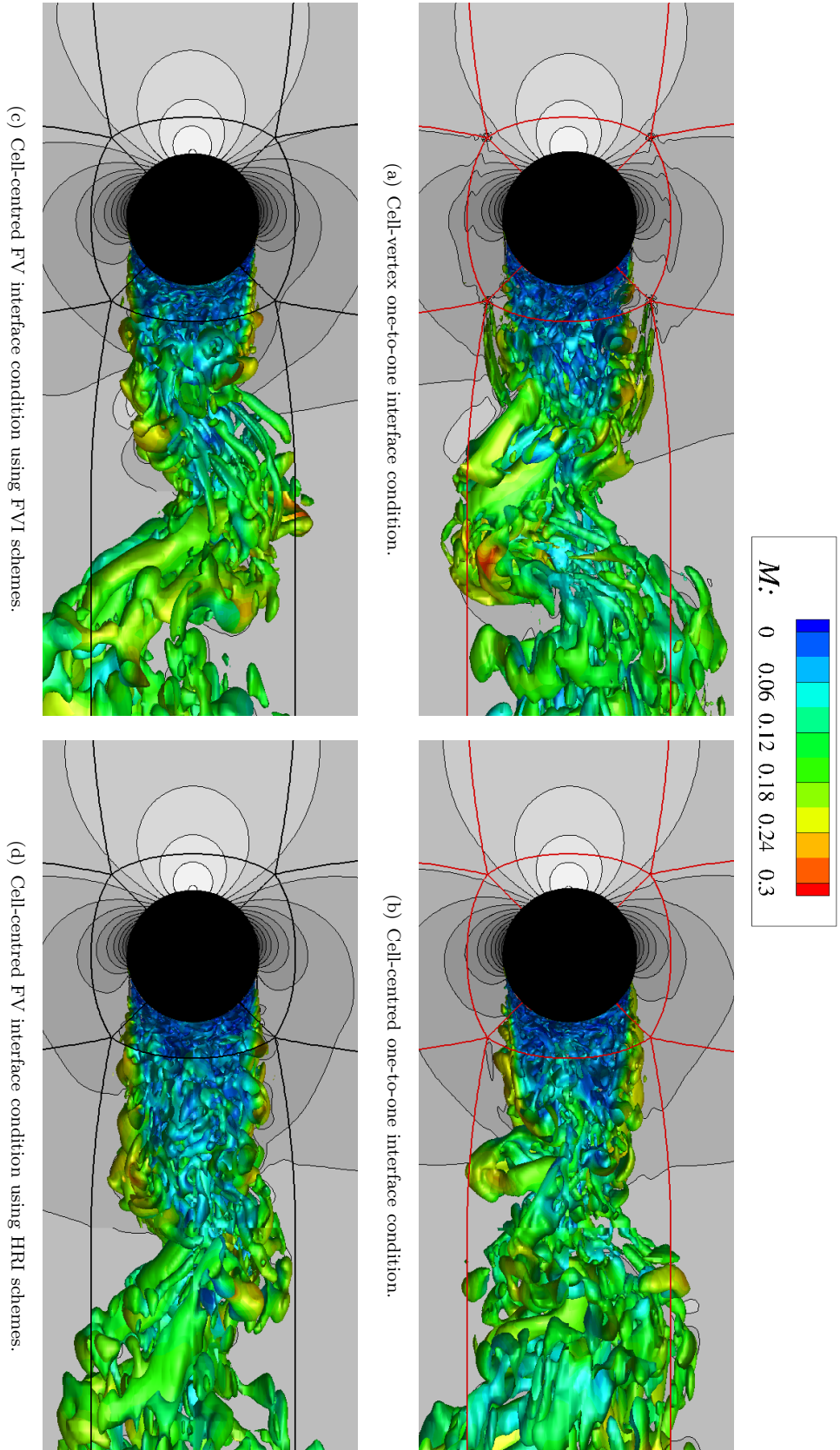


Figure 4.13: Instantaneous iso-contour of $Q = 1.0 \times U_\infty^2 / D^2$ colored by local Mach number, where the grey scale shows instantaneous density in a range of $0.94 < \rho / \rho_\infty < 1.02$. The one-to-one interfaces and FV interfaces are highlighted by — and —, respectively.

one-to-one and the FV interface conditions show a good comparison with experimental and Travin's simulation data. However, the C_p predicted by the cell-vertex one-to-one simulation shows an early recovery after the flow acceleration region compared to the other numerical and experimental results, indicating an early flow separation.

The mean skin friction coefficient (C_f) profile is shown in Figure 4.14(b). Compared to the experimental database, the current simulation results are in better agreement with the DES data from Travin *et al.* [114]. In the current simulations and Travin's DES simulation, the eddy viscosity ratio $\tilde{\nu}/\nu_\infty$ is set to 5 at the inlet. When the fluid reaches the boundary layer, the production term will be activated, and the eddy viscosity will develop rapidly into equilibrium, resulting in a turbulent boundary layer profile [114]. Thus, the boundary layers before separation in the numerical simulations are fully turbulent. However, in the experiments by Achenbach, the boundary layer was not tripped, and it was laminar until close to the separation line [114]. Therefore, the turbulent boundary layer velocity profile in the numerical simulations leads to a higher prediction of C_f compared to the laminar boundary layer velocity profile in the experiment. An earlier flow separation in the cell-vertex one-to-one simulation is also demonstrated in Figure 4.14(b). The C_p profile in Figure 4.14(a) and the C_f profile in Figure 4.14(b) demonstrate that similar predicted values along the cylinder surface including the FV interface region are obtained from the cell-centred one-to-one simulation and the FV interface simulations. This implies that, firstly, the one-to-one interface condition can be applied to collect the surface data for this single cylinder flow case, which is advantageous as mentioned in Section 4.2.2. Secondly, the FV method can provide an accurate prediction at the interfaces.

Table 4.4 is the summary of the Strouhal number St at the shedding frequency, the lift coefficient R.M.S. C_L^{rms} and the mean drag coefficient \bar{C}_D based on the frontal projected area, the separation angle θ_{sep} based on $C_f = 0$ and the length of the recirculation bubble L_r and the location of the $\overline{v'v'}_{\text{max}}$ with respect to the cylinder diameter D , and the resolved $\overline{u'v'}_{\text{max}}$ and $\overline{v'v'}_{\text{max}}$ in the wake normalised by the freestream velocity U_∞ . A good comparison with Travin's DES simulation data is demonstrated by the cell-centred one-to-one and FV interface simulations. The cell-vertex one-to-one simulation shows an early separation angle by 2° (approximately two grid size resolutions in the circumferential direction) compared to the other simulations, which leads to an underprediction of St and an overprediction of \bar{C}_D and L_r .

The computational cost using different interface treatments is summarised in Table 4.5. The computational speed is defined as the total CPU time per grid point per time step. The cell-centred one-to-one simulation is the fastest. The FV interface condition is more computationally expensive, due to the additional calculation of interpolation schemes at the FV interfaces. The FVI schemes require to solve the East and West face interpolations separately, and thus they are relatively less efficient than the HRI schemes. However, the difference in the computational expense between the FVI and

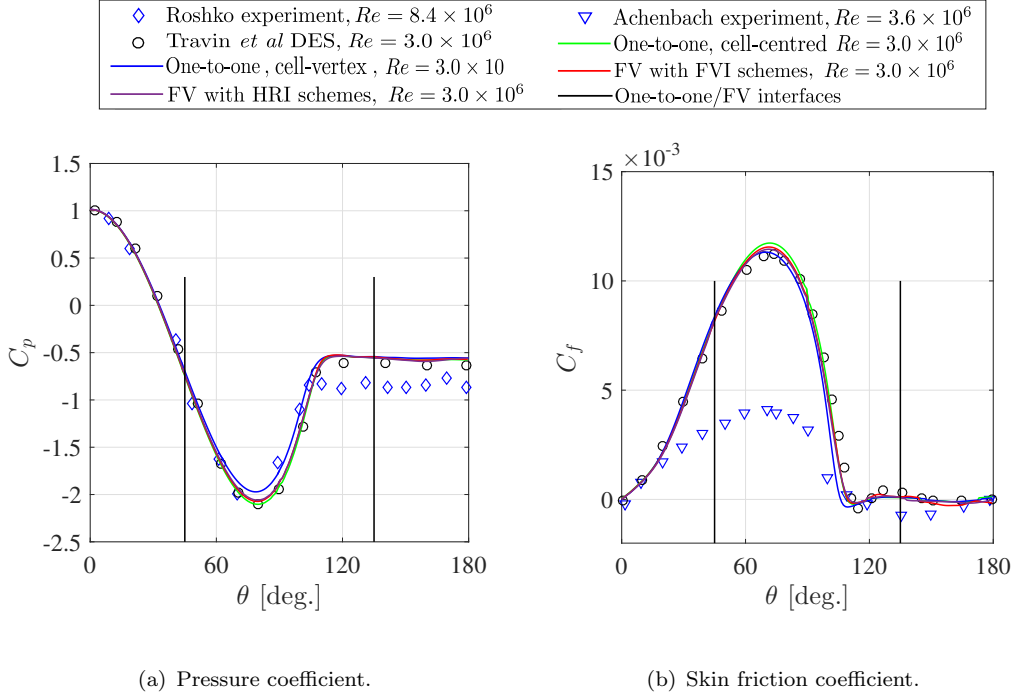


Figure 4.14: Mean pressure and skin friction coefficients for the cylinder flow case.

Case	St	C_L^{rms}	\bar{C}_D	θ_{sep}
Cell-vertex one-to-one	0.29	0.05	0.49	107°
Cell-centred one-to-one	0.32	0.05	0.42	109°
FV with FVI schemes	0.32	0.07	0.43	109°
FV with HRI schemes	0.33	0.06	0.41	110°
Travin <i>et al.</i> DES [114]	0.35	0.06	0.41	111°

Case	L_r	L_{vv}	$\overline{u'v'}_{\text{max}}$	$\overline{v'v'}_{\text{max}}$
Cell-vertex one-to-one	1.2	1.1	0.08	0.26
Cell-centred one-to-one	1.1	1.2	0.08	0.23
FV with FVI schemes	1.1	1.1	0.08	0.25
FV with HRI schemes	1.1	1.2	0.08	0.22
Travin <i>et al.</i> DES [114]	1.0	1.2	0.08	0.27

Table 4.4: Steady and unsteady statistics for the single cylinder case.

HRI schemes is 3%. The majority of the computational cost in the simulations is spent on the implicit time stepping method ($\sim 50\%$), and the FV interface treatment increases the computational expense by less than 20% in this single cylinder case.

4.6.2 Tandem cylinders flow

A benchmark tandem cylinders case [26] was simulated using both cell-vertex and cell-centred formulations. The flow interactions in this case were demonstrated to be sensitive to numerical methods [26, 115], which is helpful to further assess the accuracy of different

Case	Computational speed [$\times 10^{-5}$ s]	Relative expense
Cell-vertex one-to-one	1.48	1.05
Cell-centred one-to-one	1.41	1.00
FV with FVI schemes	1.66	1.18
FV with HRI schemes	1.62	1.15

Table 4.5: The computational cost in the single cylinder simulations. The computational speed is defined as the total CPU time per grid point per time step, and the relative expense is obtained by comparing with the cell-centred one-to-one interface condition. The total number of processors is 128.

interface treatments. The domain extent is the same with the single cylinder case. Two cylinders with a diameter of $D = 5.715 \times 10^{-2}$ m are separated by a distance of $L = 3.7D$. An infinite span was modelled by applying periodic boundary conditions across a spanwise length of $L_z = 3D$. The freestream conditions were, $M = 0.128$ and $Re = 1.66 \times 10^5$, as prescribed in the experiment [26]. A total number of 13×10^6 grid points was used in the simulations. The maximum CFL number was approximately 20 in the simulations. The number of time steps for this simulation was over 1.5×10^6 , corresponding to approximately 1.0 second ($\approx 700D$ for the convective distance), using 144 processors for approximately 650 wall clock hours (≈ 27 days). Four simulations have been tested, which apply the cell-vertex one-to-one interface condition, cell-centred one-to-one interface condition and cell-centred FV interface condition with the FVI and HRI schemes, respectively. However, when employing the FV interface condition using the HRI schemes, numerical instabilities occurred at the FV interfaces inside the boundary layer on the surface of the upstream cylinder ($\theta = 135^\circ$ and $\theta = 225^\circ$). In this region, the flow is expected to be separated and highly unsteady with nonlinear effects. The other three simulations were found to be stable. Comparing to the HRI schemes, the success of FVI schemes for the FV interface condition indicates that the FVI schemes are more stable. In the following discussions, only the stable numerical solutions are provided.

Table 4.6 shows the computational cost in the tandem cylinders simulations. The cell-centred one-to-one interface condition is the most efficient approach. The additional computational expense in the simulation using the FV interface treatment is 12%.

Case	Computational speed [$\times 10^{-5}$ s]	Relative expense
Cell-vertex one-to-one	1.65	1.04
Cell-centred one-to-one	1.58	1.00
FV with FVI schemes	1.77	1.12

Table 4.6: The computational cost in the single cylinder simulations. The computational speed is defined as the total CPU time per grid point per time step, and the relative expense is obtained by comparing with the cell-centred one-to-one interface condition. The total number of processors is 144.

Figure 4.15 shows the interface grid quality evaluated by the grid quality metric method. The grid quality tends to be poorer towards the five-block connection points, as occurs in the single cylinder case. The grid quality is shown to be higher in the cell-centred formulation (Figure 4.15(b)) over the cell-vertex space (Figure 4.15(a)), implying that the grid-related errors can be reduced by changing control points from cell vertices to cell centres. There are fewer interfaces highlighted in Figure 4.15(b), and these interfaces can be treated by the FV interface condition to further reduce grid-induced errors.

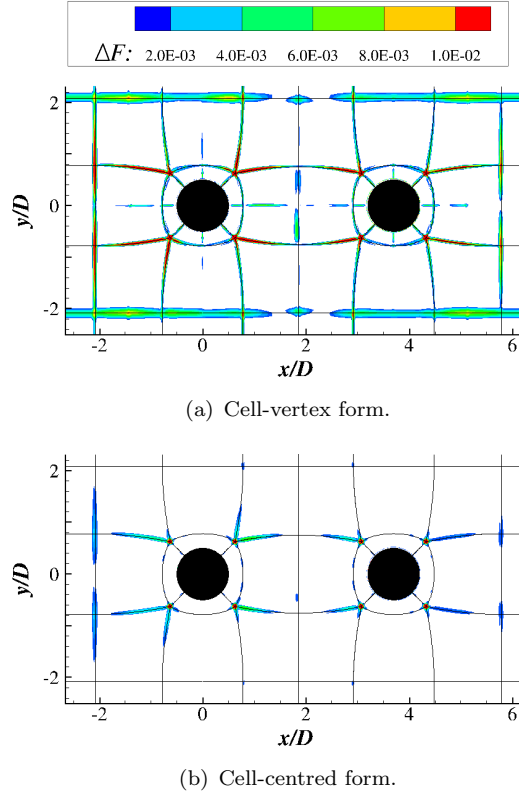
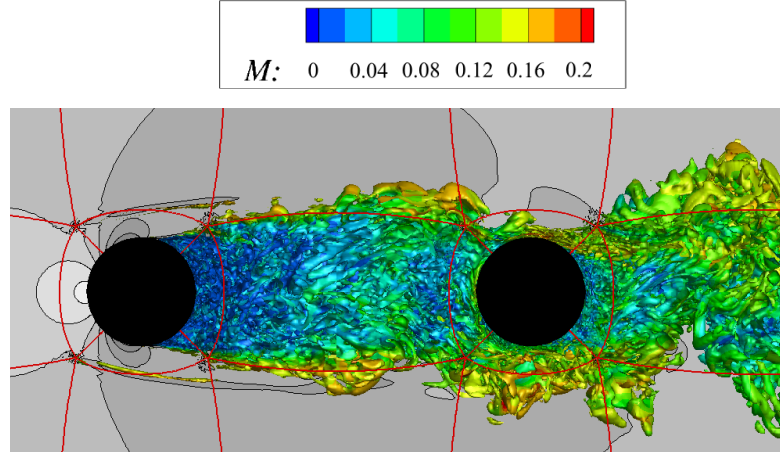


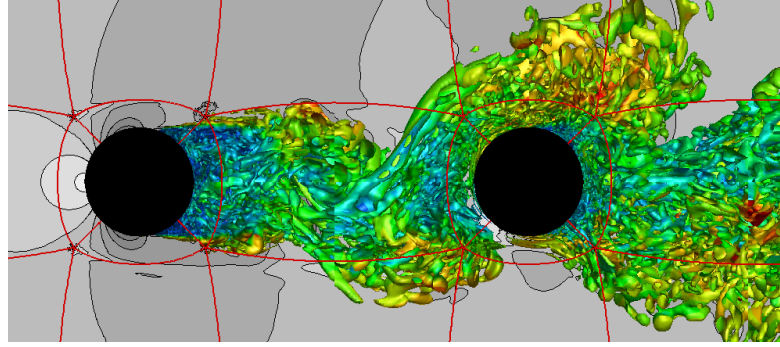
Figure 4.15: Grid quality metric values at block interfaces (—) for the tandem cylinders case.

Instantaneous flow field and steady states

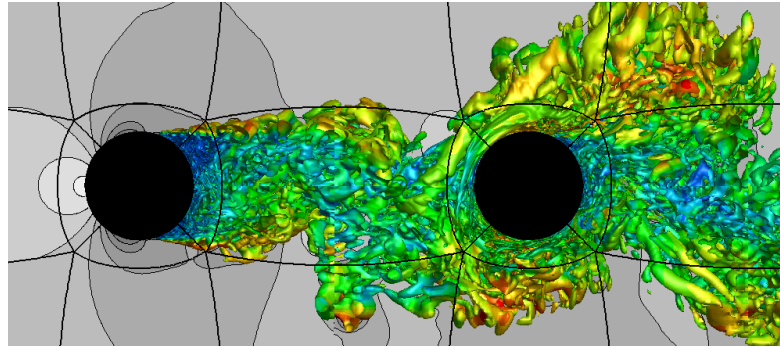
Figure 4.16 illustrates the instantaneous Q -criteria together with density fluctuations around the tandem cylinders. Similar to the single cylinder flow case in Figure 4.13(a), significant numerical errors occur in the cell-vertex one-to-one simulation (Figure 4.16(a)), which was originally generated at the five-block connection point and convected downstream. These errors are largely reduced but still noticeable at the upstream five-block connection point in the cell-centred one-to-one simulation in Figure 4.16(b). These errors were generated by grid metric discontinuities across block interfaces, and they were avoided when applying the FV interface condition in Figure 4.16(c), since the FV method is employed in the physical domain without using the grid metrics. Figure 4.16



(a) Cell-vertex one-to-one interface condition.



(b) Cell-centred one-to-one interface condition.



(c) Cell-centred FV interface condition.

Figure 4.16: Instantaneous iso-contour of $Q = 1.0 \times U_\infty^2 / D^2$ colored by local Mach number, where the grey scale shows instantaneous density in a range of $0.97 < \rho / \rho_\infty < 1.01$. The one-to-one interfaces and FV interfaces are highlighted by — and —, respectively.

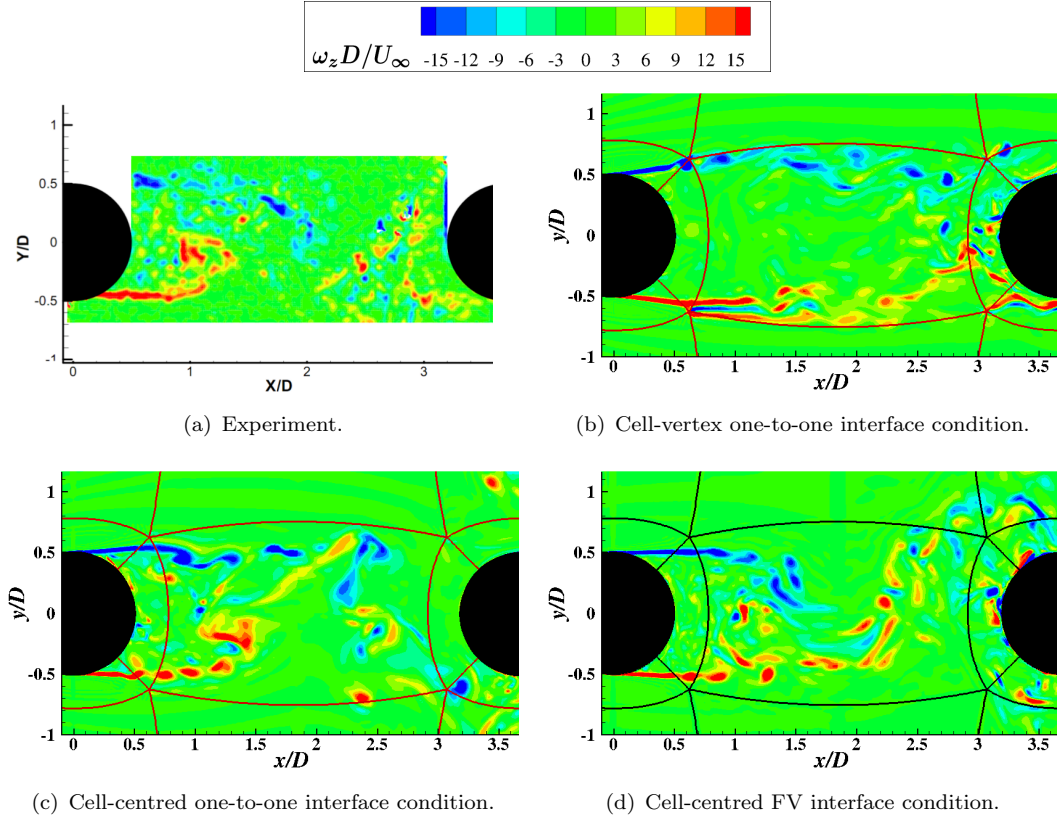


Figure 4.17: Instantaneous spanwise vorticity on $x - y$ plane for the tandem cylinders case with one-to-one interfaces (—) and FV interfaces (—).

demonstrates that at block interfaces containing grid metric discontinuities, the simulation in the cell-centred space is more robust than the cell-vertex space, and the FV interface condition is more accurate than the one-to-one interface condition.

The instantaneous spanwise vorticity is plotted in Figure 4.17, with the growth of Kelvin-Helmholtz instabilities in the shear layer clearly captured. In the cell-centred simulations (Figures 4.17(c) and 4.17(d)), the shear layer from the upstream cylinder is shown to firstly roll up and then impinge on the downstream cylinder (the co-shedding behaviour reviewed in Section 2.2.2), with both cylinders shedding vortices. However, in the cell-vertex one-to-one simulation (Figure 4.17(b)), the flow separates earlier from the upstream cylinder and the shear layer reattaches on the downstream cylinder without vortex shedding from the upstream cylinder, demonstrating a reattached type flow field. The two different states were further demonstrated by the plot of time-averaged streamlines in Figure 4.18. It shows that, in the gap region, the flow reversed distance is much larger in the cell-vertex simulation (Figure 4.18(a)) than the cell-centred simulation (Figure 4.18(b)). These two different steady states are also obtained by other numerical simulations with the same flow conditions and separation distance, which are summarised in Ref. [26], showing that these two states are very sensitive to the grids, turbulence models and numerical methods. However, in the experiment of this benchmark case, only the co-shedding state in Figure 4.18(b) was observed at this gap distance

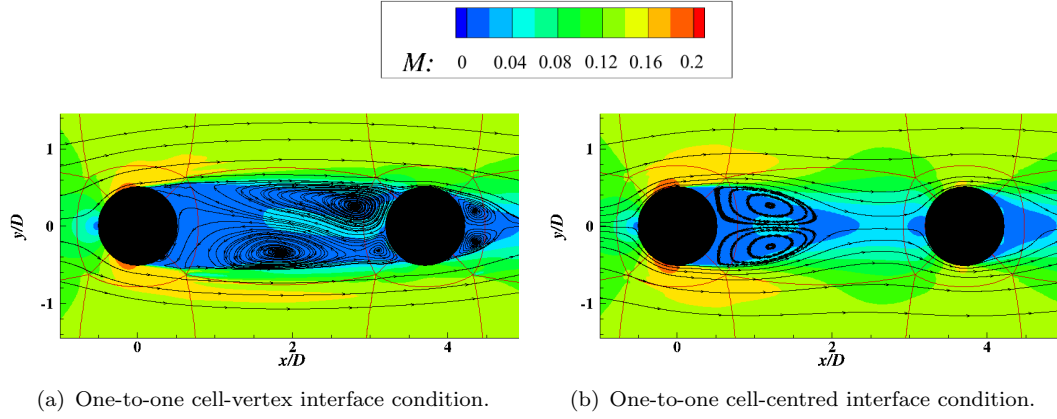


Figure 4.18: Two steady states observed in simulations using the one-to-one interface condition, where interfaces are given by —.

of $L = 3.7D$, whereas the reattached state in Figure 4.18(a) occurred for shorter cylinder separation distances [26]. In the other experiments, a critical value of L/D for these two different states was demonstrated in the range of $3.0 < L/D < 3.8$ [24, 116–118], depending on the Reynolds number, which covers the current value of $L/D = 3.7$, indicating the high flow sensitivity to the current numerical setup. The different states in the tandem cylinders flow case highlight the importance of accurate block interface treatments in the high-order numerical simulations, and the significance of reducing grid-induced errors by using the cell-centred space.

Force coefficients

Table 4.7 summarises the lift and drag force coefficients (C_L and C_D), separation angle θ_{sep} and shedding frequency St , where the subscript ‘up’ and ‘down’ denote the upstream cylinder and downstream cylinder, respectively. The cell-centred one-to-one and cell-centred FV interface conditions show similar predictions of separation angle ($\theta_{\text{sep, up}} = 96.1^\circ$ and 96.3°) for the upstream cylinder. The separation angle predicted by the cell-vertex one-to-one simulation is $\theta_{\text{sep, up}} = 94.7^\circ$, which is 1.4° (approximately 1.5 grid size resolutions in the circumferential direction) earlier in comparison to the cell-centred one-to-one simulation. Thus, the mean drag coefficient for the upstream cylinder is underestimated. For the downstream cylinder, the drag coefficient in the cell-centred one-to-one result ($\bar{C}_{D, \text{down}} = 0.50$) is slightly higher than the prediction by the FV interface condition ($\bar{C}_{D, \text{down}} = 0.45$), and they both fall in the range of databases given by other simulations that are summarised in Ref. [26]. However, for the cell-vertex one-to-one condition, the $\bar{C}_{D, \text{down}}$ is much lower. The cell-vertex one-to-one simulation showed a reattached state, and thus no regular flow shedding was obtained. The predicted Strouhal number at the shedding frequency is $St = 0.21$ and 0.22 in the cell-centred one-to-one and FV interface simulations, and these two predicted values are close to $St = 0.23$ in the experiment. For the R.M.S. of the lift and drag coefficients, the cell-centred one-to-one and FV interface treatments show similar predictions compared to

the other simulation databases. However, significant discrepancies are shown by the cell-vertex one-to-one simulation due to the reattached state shown in Figure 4.18(a).

Case	$\bar{C}_{D, \text{ up }}$	$\bar{C}_{D, \text{ down }}$	$\theta_{\text{sep, up}}$	St
Cell-vertex one-to-one	0.45	0.11	94.7°	N/A
Cell-centred one-to-one	0.54	0.50	96.1°	0.21
FV with FVI schemes	0.53	0.45	96.3°	0.22
Other simulations [26]	0.33- 0.80	0.29- 0.52	N/A	0.20- 0.29
Experiment [26]	N/A	N/A	N/A	0.23

Case	$C_{D, \text{ up }}^{\text{rms}}$	$C_{D, \text{ down }}^{\text{rms}}$	$C_{L, \text{ up }}^{\text{rms}}$	$C_{L, \text{ down }}^{\text{rms}}$
Cell-vertex one-to-one	0.005	0.079	0.012	0.238
Cell-centred one-to-one	0.030	0.095	0.127	0.731
FV with FVI schemes	0.031	0.089	0.091	0.625
Other simulations [26]	0.006- 0.034	0.028- 0.096	0.035- 0.225	0.341- 0.733

Table 4.7: Steady and unsteady statistics for the tandem cylinders case.

The earlier separation angle predicted by the cell-vertex one-to-one simulation can lead to a wider wake, which requires a longer gap distance for the flow behind the upstream cylinder to reverse and the wake to roll up. For the current setup, the gap distance is $L = 3.7D$ which is likely not long enough for the development of vortex shedding before reaching the downstream cylinder, and thus a different flow state (reattached type) was observed. For the single cylinder flow case in Section 4.6.1, the separation angle in the cell-vertex one-to-one condition is also demonstrated to be earlier than the other three interface conditions. The underprediction of the separation angle is likely due to grid-induced errors from the cell-vertex space, and these errors are significantly reduced as shown in Figure 4.16. As a result, more accurate predictions are obtained by the cell-centred simulations using either the one-to-one interface condition or the FV interface condition.

Surface pressure

The comparisons of the mean and R.M.S. pressure coefficients (C_p and C_p^{rms}) along the surface of tandem cylinders with experimental data [26] are shown in Figure 4.19 and 4.20, respectively, where C1 denotes the upstream cylinder and C2 denotes the downstream cylinder. BART and QFF are the basic aerodynamics research tunnel and quiet flow facility, respectively. The C_p predictions by the cell-centred simulations are in good agreements with the experimental databases. As mentioned in the previous single cylinder case, the boundary layer in the simulations is fully turbulent, and thereby the agreement with experiments is better when the upstream and downstream cylinder boundary layers were tripped in the experiments. However, different patterns are demonstrated by the cell-vertex one-to-one simulation due to a different flow state. The agreements of C_p between the cell-centred one-to-one interface condition and cell-centred

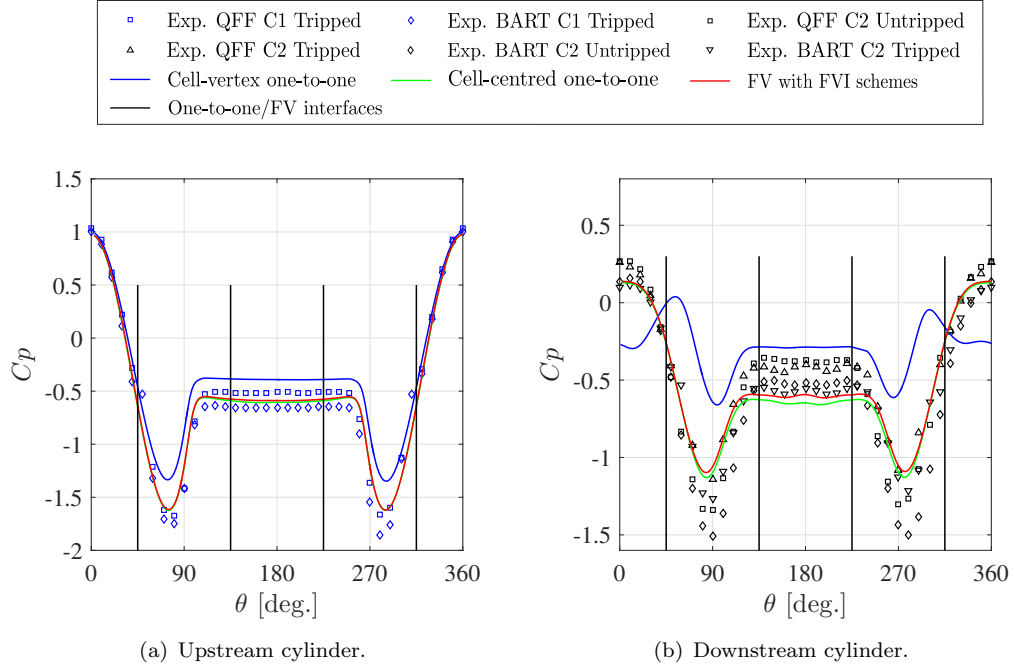


Figure 4.19: Mean surface pressure coefficients for the tandem cylinders case.

FV interface condition suggest that the information between two connected blocks can be correctly communicated by the FV method using the FVI schemes.

For the C_p^{rms} in Figure 4.20, significant underpredictions are shown by the cell-vertex one-to-one simulation for both the upstream and downstream cylinders. In the cell-vertex one-to-one simulation, the shear layer from the upstream cylinder reattaches straightly on the downstream cylinder without vortex shedding. This reduces the flow unsteadiness in the gap region, thereby underpredicting C_p^{rms} . The cell-centred one-to-one simulation shows a slight overprediction of C_p^{rms} in comparison to the cell-centred FV simulation. However, both are in reasonable agreements with experiments.

The surface pressure Power Spectral Density (PSD) at two locations (135° on the surface of the upstream cylinder and 45° on the surface of the downstream cylinder) are compared with the experimental data in Figure 4.21. Both the cell-centred one-to-one and the cell-centred FV interface conditions show good agreements with experiments. However, the spectral levels in the cell-vertex one-to-one case is underpredicted, as demonstrated by the C_p^{rms} profiles, and the shedding spectral peak is not observed. It should be emphasised that these two surface pressure monitors are located at the FV interfaces for the cell-centred FV simulation, and the agreement confirms the accuracy of the FV interface treatment.

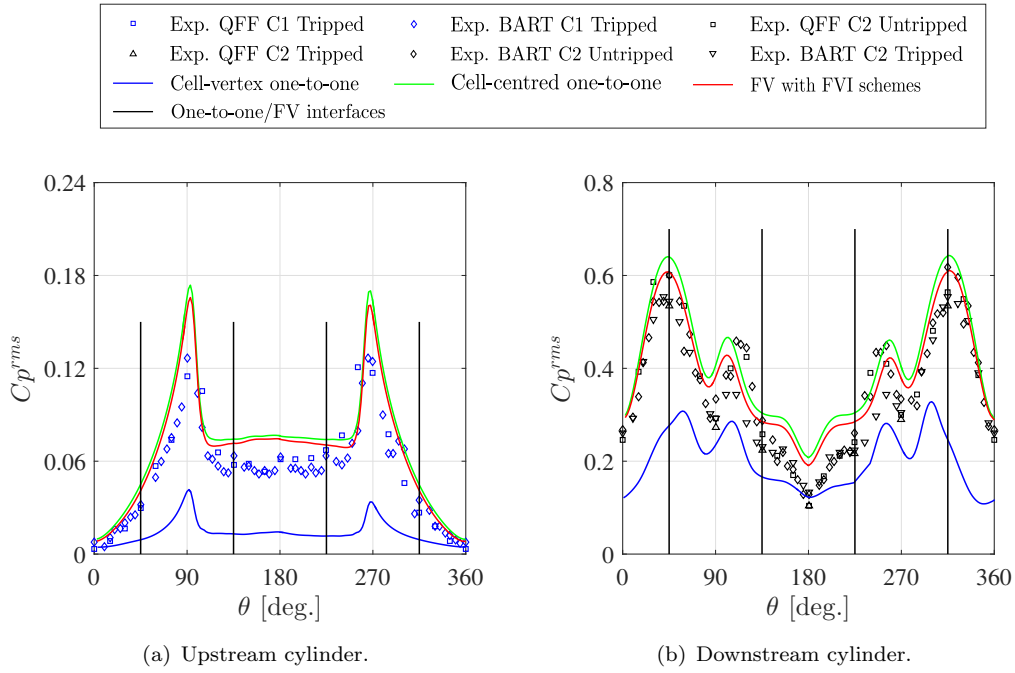


Figure 4.20: Root-mean-square surface pressure coefficients for the tandem cylinders case.

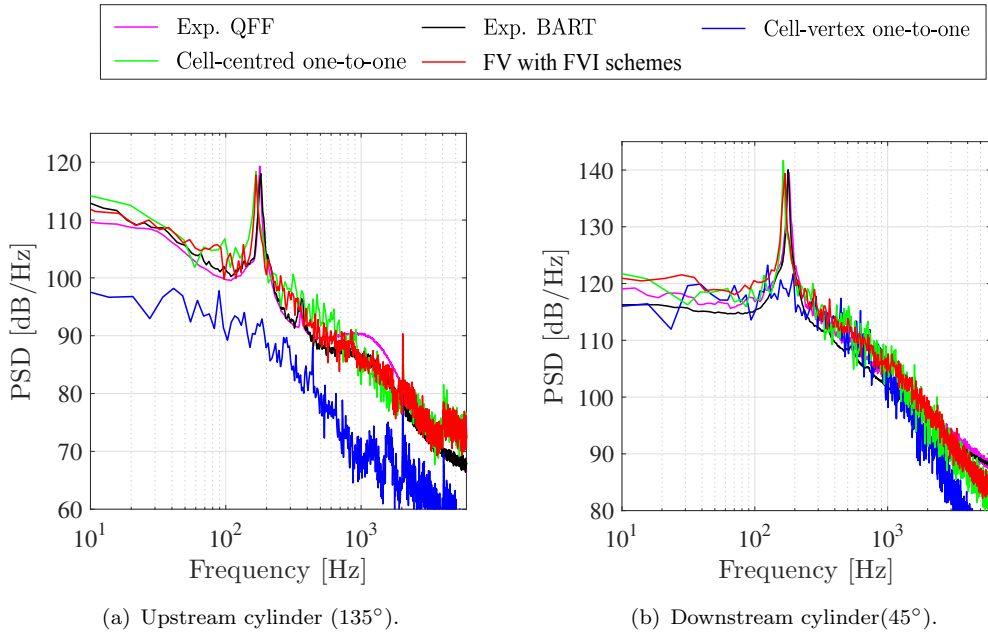


Figure 4.21: Surface pressure spectra at FV interfaces for the tandem cylinders case.

2D turbulence kinetic energy

The resolved two dimensional turbulence kinetic energy (2D TKE), given by Equation 4.33, in the gap and behind the downstream cylinder are plotted in Figures 4.22, 4.23, 4.24, and 4.25 against experimental data.

$$\text{2D TKE} = \frac{1}{2} (\langle u'u' \rangle + \langle v'v' \rangle). \quad (4.33)$$

The 2D TKE in the gap region is well predicted by the cell-centred simulations in Figure 4.22. Compared to the cell-centred one-to-one simulation, the cell-centred FV interface condition shows a slightly better agreement in the gap region with experiments along the line $y = 0$ (Figure 4.24(a)) and $x/D = 2$ (Figure 4.24(b)). In the region behind the downstream cylinder, the 2D TKE is overpredicted by both the cell-vertex and the cell-centred one-to-one simulations, but is well predicted by the cell-centred FV interface condition, in Figure 4.25. In Figures 4.23 and 4.25, the 2D TKE profiles in the cell-centred one-to-one and cell-centred FV cases are more smoothly distributed across the interfaces than the cell-vertex one-to-one simulation. This is due to the fact that the cell-centred space is less sensitive to the grid metric discontinuities. Overall, the cell-centred FV interface condition demonstrates the most accurate prediction of 2D TKE, addressing the significance and accuracy of the FV interface treatment for the prediction of flow unsteadiness for complex cases.

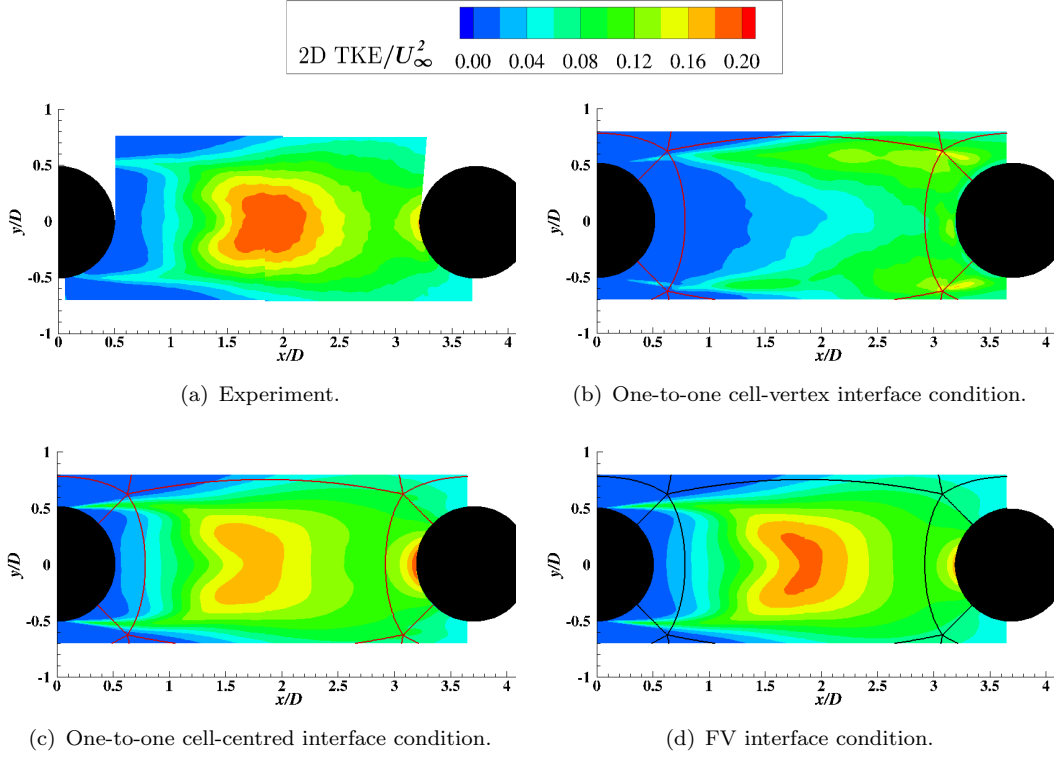


Figure 4.22: Resolved 2D TKE in the gap region for the tandem cylinders case, with one-to-one interfaces and FV interfaces highlighted by — and —, respectively.

Acoustic results

The far-field acoustic pressures are obtained using the FW-H method and the comparisons are plotted at three microphone positions (M1, M2 and M3). These three microphones are located at $(-8.33D, 27.815D)$, $(9.11D, 32.49D)$ and $(26.55D, 27.518D)$, with respect to the centre of the upstream cylinder. The FW-H integral surface was set at the surface of the two cylinders. In the experiment, the spanwise length of the cylinder is $L_z = 16D$. The corrections to the acoustic predictions with a short spanwise length ($L_z = 3D$) in the numerical simulations are based on a method using the spanwise coherence length scale [119], and this method is provided in Appendix E.

Figure 4.26 shows the comparison to experimental measurements. Good agreements are demonstrated by the cell-centred FV interface simulation, whereas the cell-centred one-to-one condition slightly overpredicts the spectral peak.

Figure 4.27 is the plot of instantaneous pressure perturbations in the cell-centred simulation with FV interface condition, where the acoustic pressures are well captured across the FV interfaces and a dipole behaviour is demonstrated.

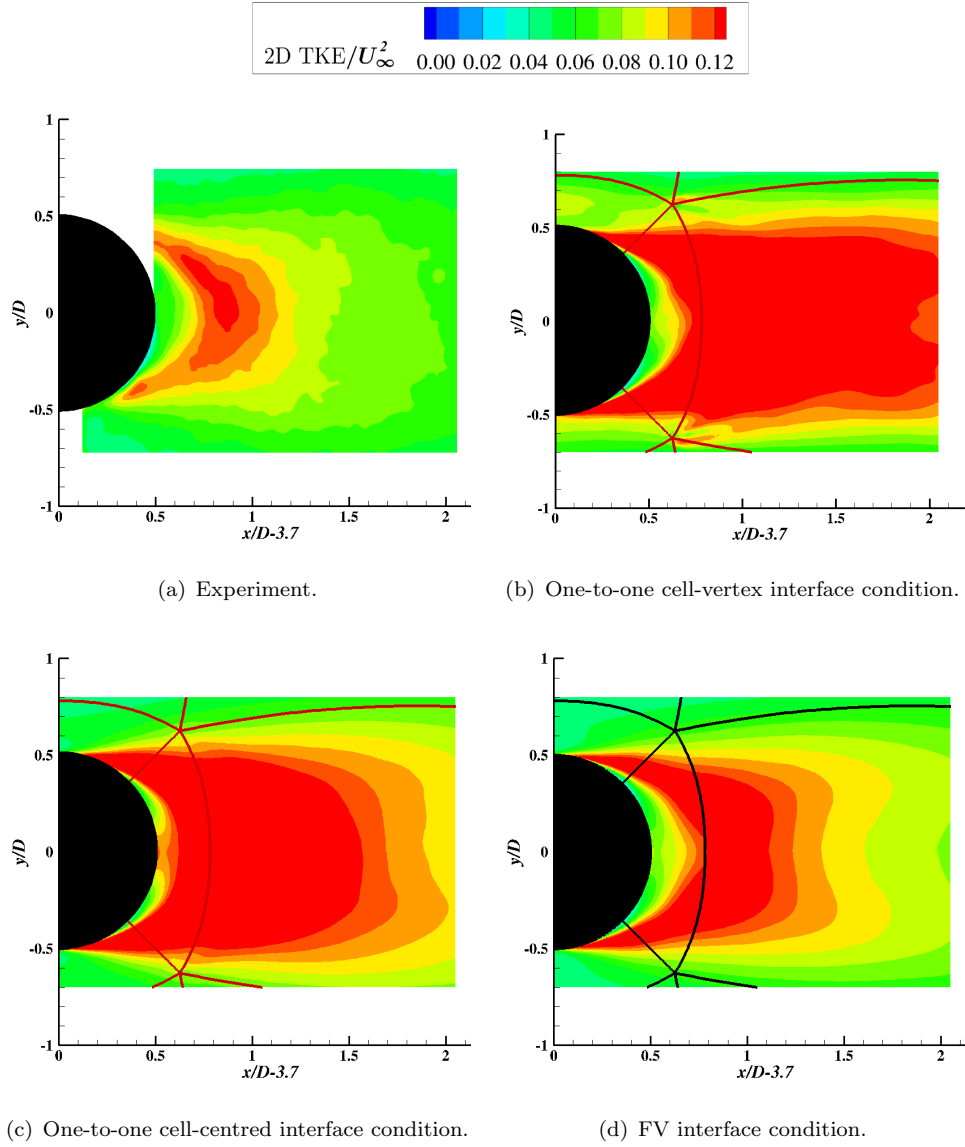


Figure 4.23: Resolved 2D TKE around the downstream cylinder for the tandem cylinders case, with one-to-one interfaces and FV interfaces highlighted by — and —, respectively.

4.6.3 Section summary

In this section, two three-dimensional test cases (flow around a single circular cylinder and tandem circular cylinders) were simulated. For each test case, four different interface conditions were employed; they are the cell-vertex one-to-one condition, the cell-centred one-to-one condition and the cell-centred FV condition using FVI and HRI interpolation schemes, respectively.

In the single cylinder test case, the cell-centred formulations show advantages over the cell-vertex formulation on the reduction of grid-induced errors, especially at the five-block connection point. The separation angle is predicted to be earlier by the cell-vertex

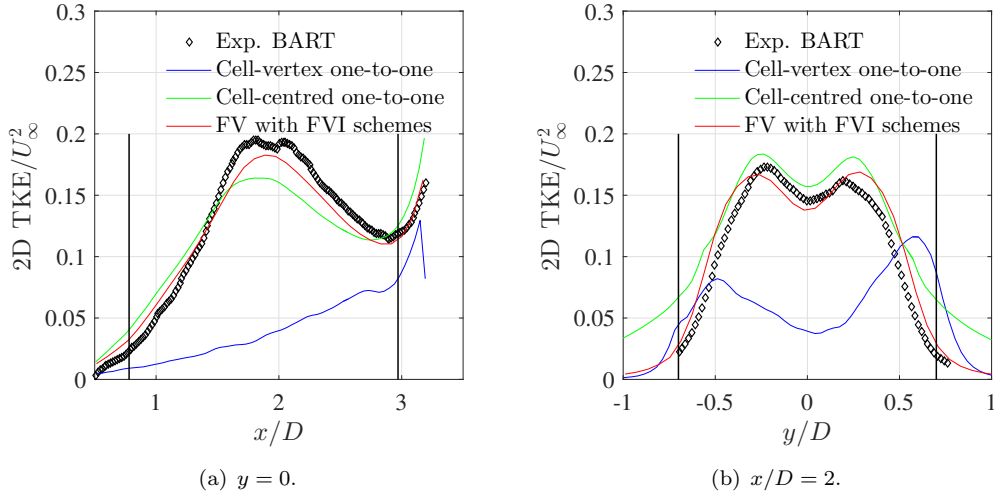


Figure 4.24: Resolved 2D TKE along two lines of $y/D = 0$ and $x/D = 3$ in the gap region, with the location of FV interfaces indicated by —.

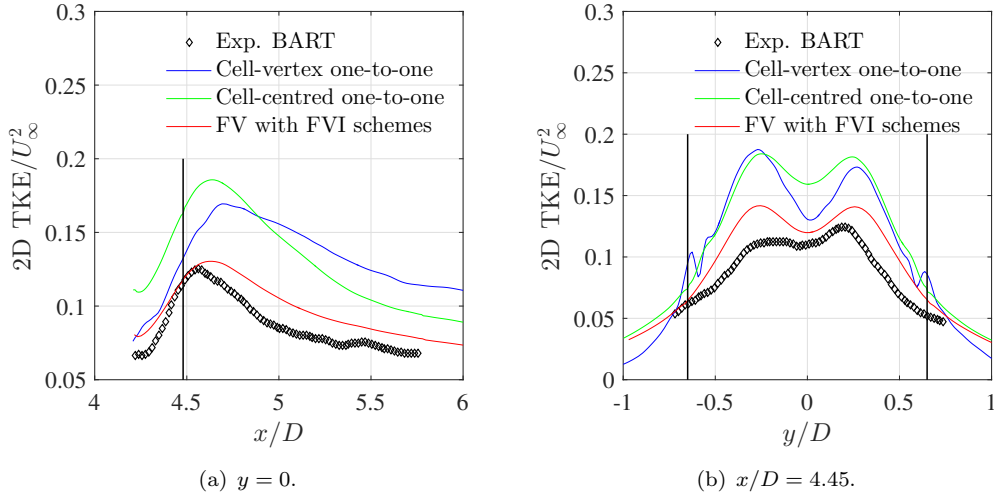


Figure 4.25: Resolved 2D TKE along two lines of $y/D = 0$ and $x/D = 4.45$ around the downstream cylinder, with the location of FV interfaces indicated by —.

one-to-one simulation than the other three cell-centred simulations. The cell-centred results demonstrate better agreements with the experiment and the DES numerical simulations by Travin *et al.* [114]. The FVI and HRI interpolation schemes show comparable performances in the cell-centred simulations with the FV interface treatment.

In the tandem cylinders test case, the HRI schemes failed to provide a stable solution. The numerical instability occurred at $\theta = 135^\circ$ on the upstream surface. This location is firstly at the FV interface where the HRI schemes are applied to communicate flow information between the two connected blocks. Secondly, this region is on the wall surface, inside the boundary layer, with high velocity gradients and strong non-linear

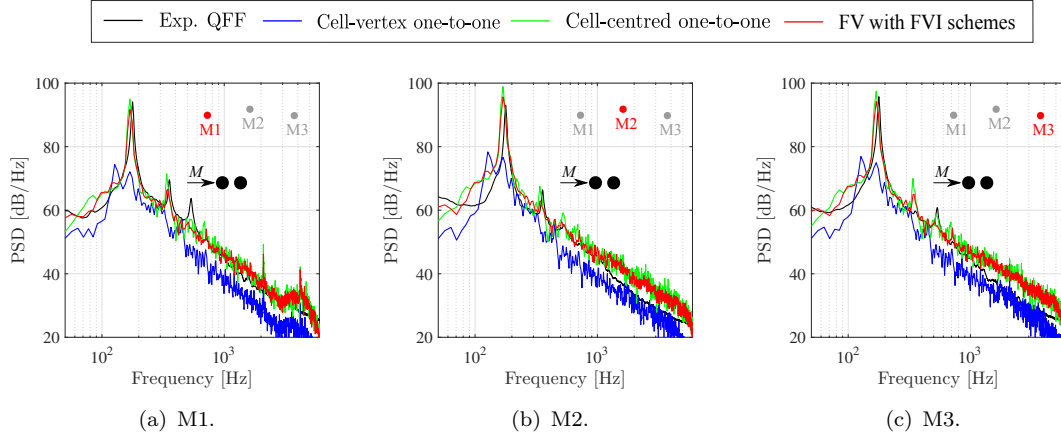


Figure 4.26: Far-field acoustic pressure spectra at three microphone positions for the tandem cylinder case using different interface conditions.

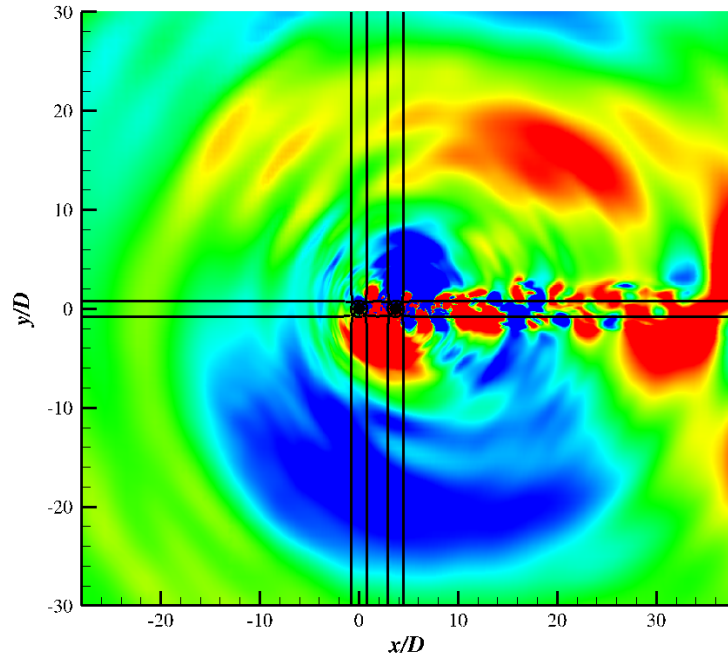


Figure 4.27: Pressure perturbations ($-1.5 \times 10^{-4} < p'/\rho_\infty c_\infty^2 < 1.5 \times 10^{-4}$) for the tandem cylinders case obtained by FV interface (—) condition.

effects. However, the FVI schemes are able to handle large gradients and discontinuities, as shown by Popescu *et al.* [109] in their FV treatment of the DRP scheme, and the simulations with FVI schemes are stable and accurate. The cell-vertex one-to-one simulation underpredicts the separation angle for the front cylinder. As a result, the shear layer from the upstream cylinder reattaches straightly on the downstream cylinder and no vortex shedding was observed. The cell-centred simulations demonstrate a more accurate prediction of the co-shedding flow field. For the cell-centred simulations, more accurate estimations of the flow unsteadiness (2D TKE) and far-field acoustics are shown by the FV interface condition, in comparison to the one-to-one interface treatment.

Overall, the cell-centred formulations are less sensitive to the grid metric discontinuities, and thus are suggested in high-order numerical simulations. The FV interface treatment is robust and can provide more accurate predictions of flow unsteadiness for computational aeroacoustic problems. Therefore, the cell-centred FV interface treatment with FVI schemes is applied for the next single wheel and tandem wheels simulations.

4.7 Chapter summary

In this chapter, a hybrid cell-centred method for computational aeroacoustics has been developed. The FD approach is more accurate with smooth grid metrics and the FV method is more capable of handling discontinuous grids. Therefore, the hybrid method employs high-order FD schemes at interior control points, and applies a FV solution along block interfaces that contain discontinuities in the grid metrics. Two interpolation schemes (FVI and HRI) have been developed and their comparisons can be summarised below:

- The FVI schemes contain two individual interpolations for the East face and West face, respectively, and they are second-order accurate. However, for a linear case, the third-order and fourth-order truncation errors can be cancelled when combining the East face and West face interpolation schemes. For a non-linear case, the grid convergence test of a vortex convection problem shows that the accuracy is close to fourth order. The HRI schemes are four-order accurate, and the transfer functions are optimised to provide improved spectral resolutions.
- During the linear eigenvalue analysis, the FVI schemes (less dissipative) demonstrated a wider resolved wavenumber range compared to the HRI schemes (more dissipative). However, the high-wavenumber modes resolved by the FVI schemes are unstable, and they need to be filtered out to provide stable solutions. All the modes resolved by the HRI schemes are stable without filtering, and the high-wavenumber modes resolved by the FVI schemes are dissipated by in the HRI schemes.

Two test cases of single and tandem cylinders were conducted to validate the proposed hybrid cell-centred method. Firstly, compared to the cell-vertex method, the cell-centred formulation can reduce grid-induced errors along block interfaces containing abrupt changes in the grid line profiles. Secondly, the FV interface treatment has been validated in these two test cases, and the comparisons to experimental data show that the FV interface condition can provide accurate mean and unsteady predictions. Additionally, in the tandem cylinders flow case, the simulation using HRI schemes was not stable and the instability occurred at the FV interface inside the boundary layer with large velocity gradients. The FVI schemes are more robust for non-linear cases and can provide stable and accurate predictions.

The grid-induced errors at discontinuous block interfaces in the cell-vertex simulations are due to grid metric discontinuities. Those numerical errors can be avoided by the application of the FV interface condition in the physical space. Considering that the FVI scheme is more robust in non-linear simulations, the FV interface condition with FVI schemes in the cell-centred space is used for the high-order simulations of single and tandem landing gear wheels in the following two chapters.

Chapter 5

An Isolated Landing Gear Wheel

5.1 Introduction

Landing gears are recognised as one of the most significant contributors to airframe noise for commercial aircraft in the approach configuration [29]. A landing gear is an assembly of a large number of components with different sizes and shapes. Wheels are one of the major large-scale landing gear components, which can be considered as the most significant noise sources for simplified two-wheel nose landing gears [3] and important noise contributors for four-wheel main landing gears [4]. Numerical studies of wheel noise can provide a useful insight into the landing gear noise generation mechanisms and can aid in the design of noise reduction treatments.

In this chapter, high-order numerical simulations are performed to investigate a high-fidelity isolated landing gear wheel and this chapter concentrates on the following questions:

1. What are the aerodynamic and acoustic characteristics of an isolated landing gear wheel?
2. Which part of the wheel is the major noise source at different frequencies and what are the noise generation mechanisms?
3. How much noise reduction can be achieved by covering the hub cavity and rim cavities of an isolated landing gear wheel?

This chapter is structured in the following manner. The grid generation and computational setup are described in Section 5.2. Section 5.3 demonstrates the aerodynamic results. The far-field acoustic results are shown in Section 5.4, with concentration on the hub cavity noise. Finally, the conclusions of the simulations are summarised in Section 5.5.

5.2 Grid detail and computational setup

A 33% scaled isolated landing gear wheel from the Technology Strategy Board CADWIE (Control of Approach Drag Without Impact on the Environment) project [41] is used in this study and the model is illustrated in Figure 5.1. The diameter and the width of the wheel are $D = 0.48$ m and $W = 0.186$ m, respectively. The isolated wheel contains a sidewall and a hub on opposite sides. A large shallow cylindrical cavity with a diameter-to-depth ratio of approximately 0.3 is located around the hub. Surrounding the sidewall and the hub cavity are two rim cavities, which are small-scale features, relative to the wheel size, with a depth of approximately $0.045D$. Three different configurations have been simulated. The unmodified CADWIE wheel is the baseline configuration. A cross section through the baseline configuration is shown in Figure 5.2(a). The second configuration, **No Hub Cavity** (NHC), is shown in Figure 5.2(b), with the hub cavity covered. The geometry in this configuration is symmetrical with respect to $z/D = 0$ plane. The simulation of the NHC configuration aims to determine the contribution of the hub cavity to the far-field acoustics. The third configuration, NHCRC (**No Hub Cavity and Rim Cavities**), is shown in Figure 5.2(c). In this configuration, the hub cavity and the two rim cavities are covered. This configuration is essentially a short aspect ratio circular cylinder and can be compared with the NHC configuration to investigate the noise generated from the rim cavities.

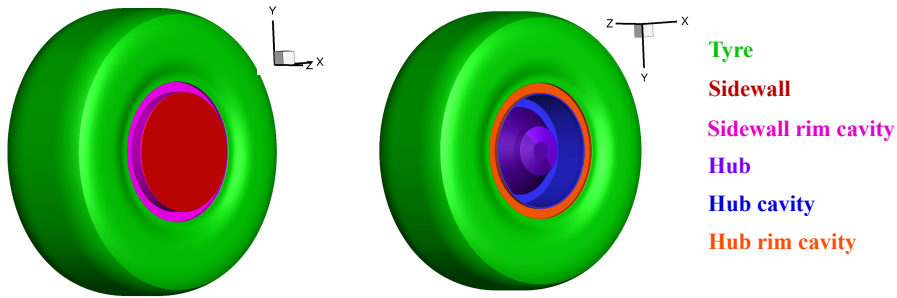


Figure 5.1: The geometry of the CADWIE wheel in the simulations. The origin of the axes is at the wheel centre.

The numerical simulations were performed on multi-block structured grids. The computational domain is shown in Figure 5.3 with the origin of the axes at the centre of the wheel. The computational domain extends $5D$, $4D$ and $16D$ in the upstream, above and below, and downstream directions, respectively. The spanwise length of the domain is $8D$. In the boundary layer region, the value of the wall distance y^+ is smaller than 2.0 and a grid stretching ratio of 1.15 in the wall normal direction is used to relax the grid distribution. For the baseline geometry, two grids with different resolutions around the hub cavity region have been tested. For the coarse grid resolution, the hub cavity walls are meshed by a cylindrical grid with 200, 150 and 45 grid points in the azimuthal, radial and depth directions, respectively. The resolutions in the azimuthal and depth directions are refined by 50% and 78% in the fine resolution mesh, aiming to

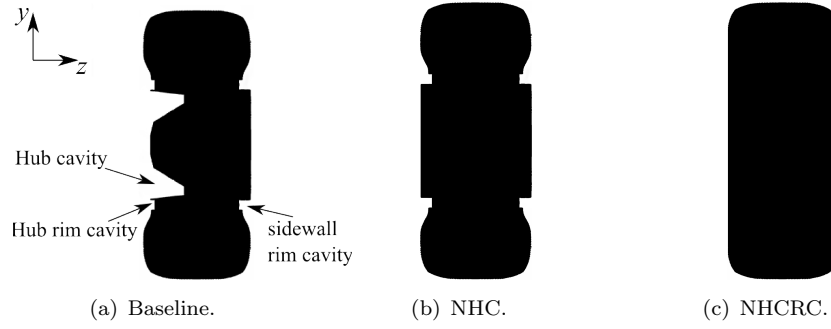


Figure 5.2: The cross section of three geometry configurations on the $x/D = 0$ plane. (a) Baseline geometry; (b) No **H**ub **C**avity (NHC) geometry; (c) No **H**ub **C**avity and **R**im **C**avities (NHCRC) geometry.

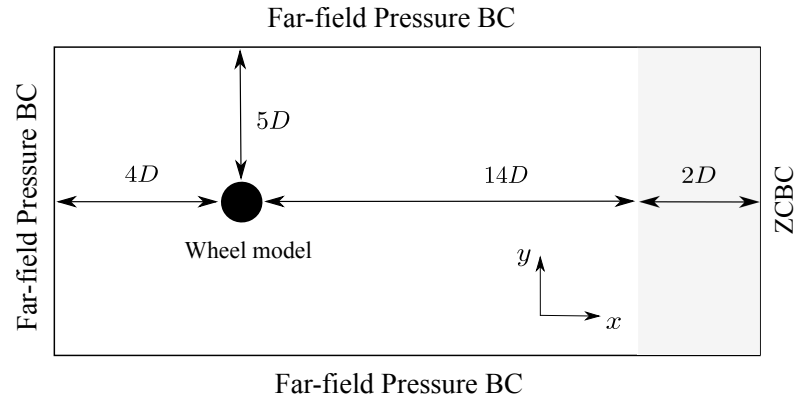


Figure 5.3: The computational domain and boundary conditions in the simulations.

better resolve the flow features in the hub cavity region. The differences between the two meshes are summarised in Table 5.1. For both resolutions, there are 60 grid points distributed along the width of the wheel. For the NHC and NHCRC configurations, the mesh resolutions on the surface of the tyre and sidewall are the same as the baseline case at the fine mesh resolution. Figure 5.4 shows the mesh topology and grid distributions around the CADWIE wheel for the baseline configuration. The wheel is surrounded by an O-type mesh in the near field, which transitions to a H-type mesh away from the wheel. Details of the mesh around the sidewall rim cavity and the hub cavity are shown in Figures 5.4(c) and 5.4(d).

	Coarse	Fine
$N_{\text{azimuthal}}$	200	300
N_{radial}	150	150
N_{depth}	45	85
N_{total}	12×10^6	25×10^6
Maximum resolvable frequency, PPW=10	3.0 kHz	5.7 kHz

Table 5.1: Summary of two grid resolutions for the CADWIE wheel case.

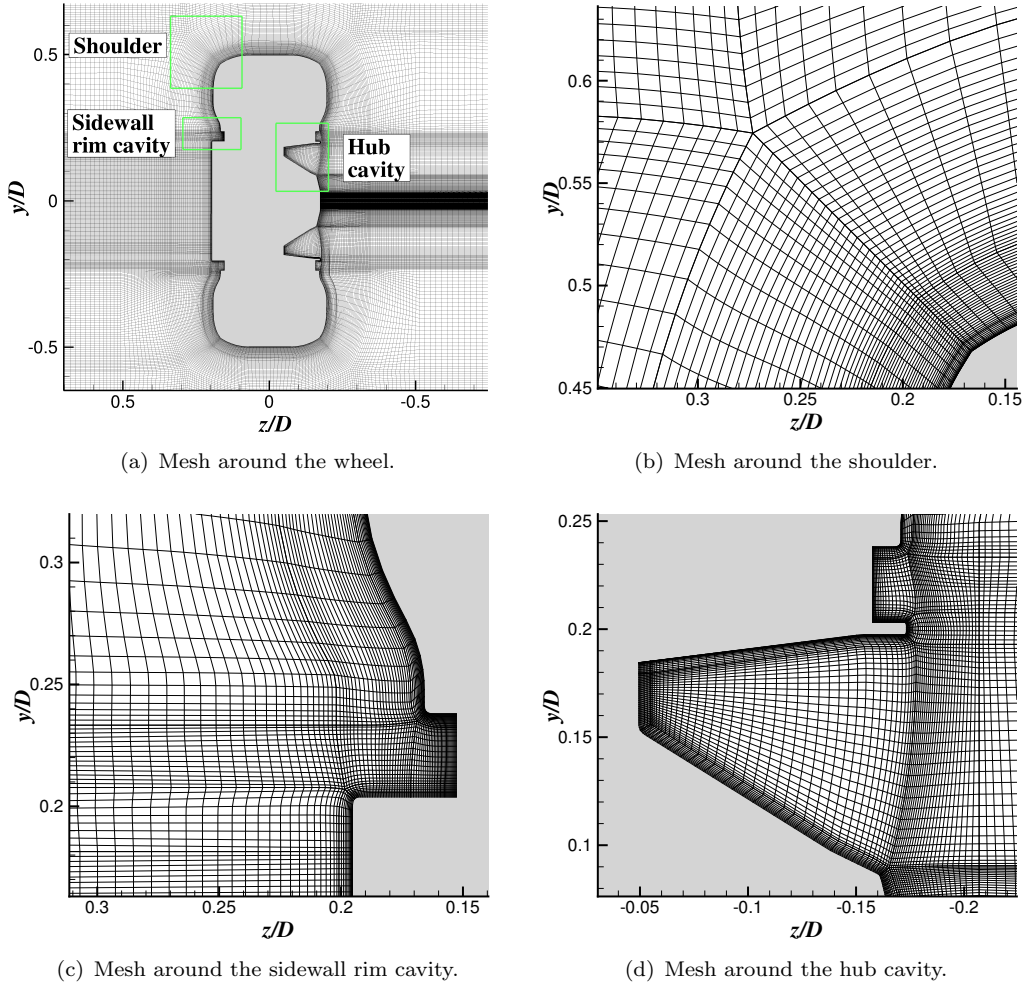


Figure 5.4: Mesh topology and grid distribution around the CADWIE wheel on the $x/D = 0$ plane.

The three-dimensional Navier-Stokes equations are solved with the Delayed Detached Eddy Simulation (DDES) turbulence model [60]. The cut-off wavenumber for the compact filters is $\kappa_c = 0.75\pi$. At block interfaces with grid metric discontinuities, a finite volume method is applied to reduce grid-induced errors. The inflow boundary condition is a far-field pressure condition based on Riemann invariants and a Zonal Characteristic Boundary Condition (ZCBC) is applied at the outflow boundary. The eddy viscosity ratio at the inlet is 5, aiming to model a fully turbulent boundary layer case. The experimental database used to validate the current simulations is obtained from free transition, and it is demonstrated that at this scale, the experimental measurements of force coefficients are relatively insensitive to the transition treatment [41]. No-slip isothermal wall boundary conditions are imposed on the wheel surface. A second-order implicit time-stepping method with Newton-like subiterations is used to march the solution in time. The far-field acoustics are computed using the Ffowcs-Williams and Hawkings (FW-H) method, based on the Farassat 1A formulation [75]. The FW-H integral surface in the simulations is coincident with the solid surface of the wheel. The solid FW-H integral

surface has two advantages. Firstly, it is able to reduce the risk of noise contamination by large vortical wave fluctuations convecting through the permeable surface [65], since the velocities are zeros on the solid surface. Secondly, the mesh is stretched away from the wheel, and thus the solid FW-H integral surface can resolve the acoustic waves to a higher frequency range.

The freestream quantities are $\rho_\infty = 1.22 \text{ kg/m}^3$, $p_\infty = 99456 \text{ Pa}$ and $T_\infty = 288.16 \text{ K}$. The fluid viscosity is calculated using Sutherland's law. Two flow conditions with different Mach numbers have been tested in the simulations. The first one is $M = 0.118$, which is the inflow condition in the aerodynamic wind tunnel tests. The second Mach number is 0.23, aiming to validate the acoustic results against experimental measurements in the *QinetiQ* Noise Test Facility (NTF). It should also be mentioned that the experimental measurements are only available for the baseline configuration (CADWIE wheel geometry). The corresponding Reynolds numbers are 1.3×10^6 and 2.5×10^6 based on the wheel diameter D and the inflow velocity. Five simulations have been conducted with different inflow conditions and grid resolutions, which are summarised in Table 5.2. The physical time step size for the simulations is $\Delta t = 6 \times 10^{-7}$ seconds (CFL=20). The flow was fully developed after a convective time of approximately 10 wheel diameters, after which the FW-H surface data were collected for 0.6 seconds (a convective time of approximately 100 wheel diameters). Each simulation was completed using 240 processors with 600 cpu hours (approximately 25 days).

Case	Grids	Mach number	Geometry
1	Coarse	0.118	Baseline
2	Fine	0.118	Baseline
3	Fine	0.23	Baseline
4	Fine	0.23	NHC
5	Fine	0.23	NHCRC

Table 5.2: Different computational cases in the isolated landing gear wheel simulations.

5.3 Aerodynamic results

The aerodynamic experiments were performed in a closed section wind tunnel at the University of Southampton. The experimental data includes mean and unsteady aerodynamic information on the surface and in the wake of the CADWIE wheel (baseline configuration). Figure 5.5 shows the experimental setup. It should be emphasised that the support strut is excluded in the numerical simulations. Additionally, the wind tunnel walls are replaced by far-field pressure boundary conditions in the simulations (as shown in Figure 5.3), aiming to reduce acoustic reflections at boundaries. The inflow velocity speed in the experiments is 40 m/s ($M = 0.118$).

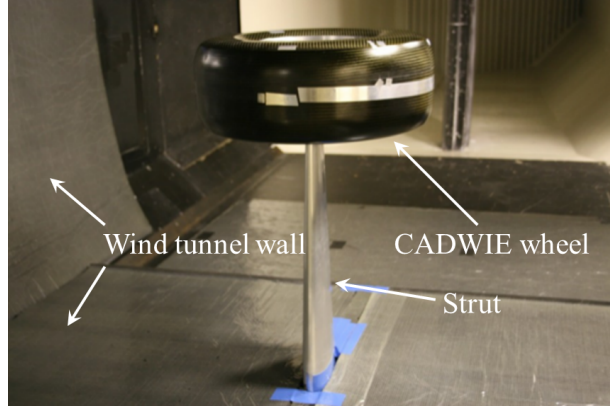


Figure 5.5: Aerodynamic experimental setup of the CADWIE wheel in closed section wind tunnel tests [41].

5.3.1 Forces

The coefficients of lift C_L , drag C_D and side force C_S from different geometries are summarised and compared with the experiment in Table 5.3. The reference area is the wheel frontal projected area give by $W \times D$. The baseline case results provided in Table 5.3 are at $M = 0.23$ with the fine mesh resolution, and similar predictions are also obtained at $M = 0.128$. Good agreements in \bar{C}_D and \bar{C}_S with the experiment are demonstrated by the baseline case.

Case	\bar{C}_L	\bar{C}_D	\bar{C}_S	C_L^{rms}	C_D^{rms}	C_S^{rms}
Baseline	0.022	0.237	0.019	0.030	0.010	0.019
NHC	0.007	0.220	0.002	0.027	0.009	0.018
NHCRC	0.006	0.183	0.007	0.024	0.007	0.016
Experiment [41]	N/A	0.239	0.020	N/A	N/A	N/A

Table 5.3: Force coefficients from different geometries for the isolated landing gear wheel simulations.

The invariants of geometrical configurations induce changes in the three force coefficients. Firstly, the NHC case shows a reduction in the mean drag coefficient \bar{C}_D by 7%, compared with the baseline case. The drag reduction further reaches 20% in the NHCRC case with the rim cavities covered. Compared with the rim cavities, the hub cavity is thus a secondary contributor to the drag, which is consistent with the experimental measurements by Spagnolo *et al.* [42], who performed experiments on a simplified landing gear wheel and observed limited decrease in the drag coefficient by covering the hub cavity. After covering the rim cavities (NHCRC), the side face of the wheel is flat, as shown in Figure 5.2(c). In this case, the pressure variance on the side face cannot contribute to the drag, which accounts for the 20% reduction by the NHCRC case.

Secondly, all the three configurations illustrate that the fluctuating lift force (C_L^{rms}) is larger over the fluctuating side force (C_S^{rms}) and the fluctuating drag force (C_D^{rms}). The PSD of the force coefficients are plotted in Figure 5.6. The lift force spectrum

dominates the side force spectrum and the drag force spectrum at $f < 30$ Hz, and the spectral level of the side force is slightly higher than the lift force and the drag force at $70 \text{ Hz} < f < 100 \text{ Hz}$. It will be shown in Section 5.4.2 that the far-field acoustics in these two frequency ranges display a lift dipole pattern and a side force dipole pattern, respectively. For any of the three force coefficients in Figure 5.6, similar spectral levels are shown by the three configurations in the low frequency range of $f < 100$ Hz, indicating that the large-scale flow structures are less affected by the hub cavity and rim cavities. However, the rim cavities are demonstrated to be the major contributors to the force fluctuations produced by small-scale flow structures at $f > 2000$ Hz.

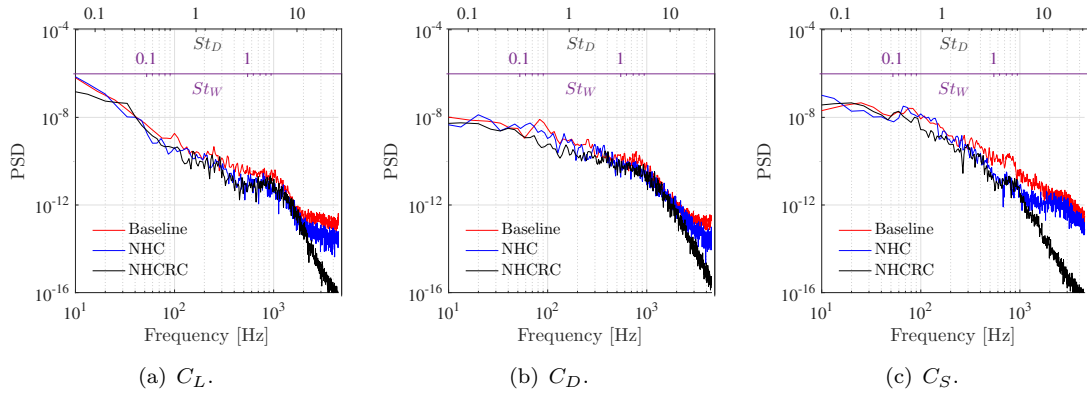


Figure 5.6: PSD of force coefficients for different geometry configurations.

Thirdly, a non-zero mean lift coefficient \bar{C}_L is predicted in the simulations, indicating that the mean flow field is asymmetric with respect to the $y/D = 0$ plane. This flow asymmetry has been investigated by Zdravkovich *et al.* [13] in their experiment that was performed to measure the flow features around short circular cylinders, as reviewed in Section 2.2.1 (Figure 2.3). Zdravkovich *et al.* [13] showed that there are two stable states for flow over short cylinders, and the flow field can be biased to either side, depending on the flow conditions. Additionally, Table 5.3 shows that the mean lift coefficient becomes closer to zero with the hub cavity covered. The depth-to-diameter ratio of the hub cavity is $\varpi = 0.3$, and the mean flow is shown in Appendix G.4 to be asymmetric at $\varpi = 0.3$. Thus, the hub cavity can contribute to the asymmetry of mean flow field around the wheel.

5.3.2 Instantaneous flow field

The instantaneous flow features on the side of the wheel for the three different configurations are shown in Figure 5.7. For the baseline configuration in Figure 5.7(a), the flow first separates from the tyre at point F and forms a vortex in the hub rim cavity. After separation, Kelvin-Helmholtz (K-H) instabilities in the shear layer begin to develop and the shear layer interacts with the flow recirculation region inside the hub cavity. The

highly turbulent flow in the hub cavity region is visualised by the plot of Q -criterion shown in Figure 5.7(a). When the hub cavity is covered in the NHC configuration, the separated flow, which separates at point F, reattaches to the sidewall, as shown in Figure 5.7(b). This reduces the turbulent flow generated by the hub cavity. In the NHCRC configuration, due to the absence of the hub cavity and rim cavities, the flow is fully attached to the sidewall (Figure 5.7(c)). The turbulent flow associated with the hub cavity and rim cavities is eliminated. The effect of these flowfield changes on the far-field acoustics will be quantified in Section 5.4.3.

5.3.3 Time-averaged flow quantities

Mean pressure coefficient

The mean surface pressure coefficient (C_p) profiles on the $z/D = 0$ plane from the numerical simulations are plotted in Figure 5.8 against the experimental measurements of the CADWIE wheel (baseline configuration) at the same Reynolds number ($Re = 1.3 \times 10^6$) and also a simplified landing gear wheel without hub and rim cavities tested by Spagnolo *et al.* [42] at a lower Reynolds number ($Re = 5 \times 10^5$). This simplified wheel has a smaller wheel diameter of $D = 181$ mm but the ratio of W/D is the same as the CADWIE wheel. The boundary layer along the shoulder in the experiments by Spagnolo *et al.* was tripped to reproduce a higher Reynolds number condition, and no boundary layer trip was used in the CADWIE wheel experimental database. Good agreements of the C_p profiles with experimental measurements are shown in Figure 5.8 towards the front and the rear parts of the wheel. A more accurate prediction of C_p at the suction peaks is demonstrated by the fine grid resolution, and the suction peaks are underpredicted by $\Delta C_p \approx 0.25$ by the coarse grid resolution. However, discrepancies with the CADWIE experiments at the suction peaks can also be observed at 90° and 270° for the fine mesh resolution. The experiments were performed in a closed wind tunnel and the blockage caused by the wind tunnel walls and the wheel model can result in increased suction at the suction peak on the wheel. The blockage ratio in the CADWIE wheel experiment and the numerical simulations was approximately 3.2%, higher than 0.5% in the simplified wheel experiment by Spagnolo *et al.* [42]. It was reported that no-slip wind tunnel wall boundary conditions can improve the prediction of surface pressure coefficients at suction peaks in comparison with slip-wall boundary conditions and far-field pressure boundary conditions for the CADWIE wheel simulations with the same computational domain size [120].

Surface shear stress lines topology

Flow separation and attachment can be considered as potential noise sources [33]. The surface shear stress lines are used to characterise the flow separation and attachment. Following the work of Lazos [33], the basic patterns of separation/attachment in the

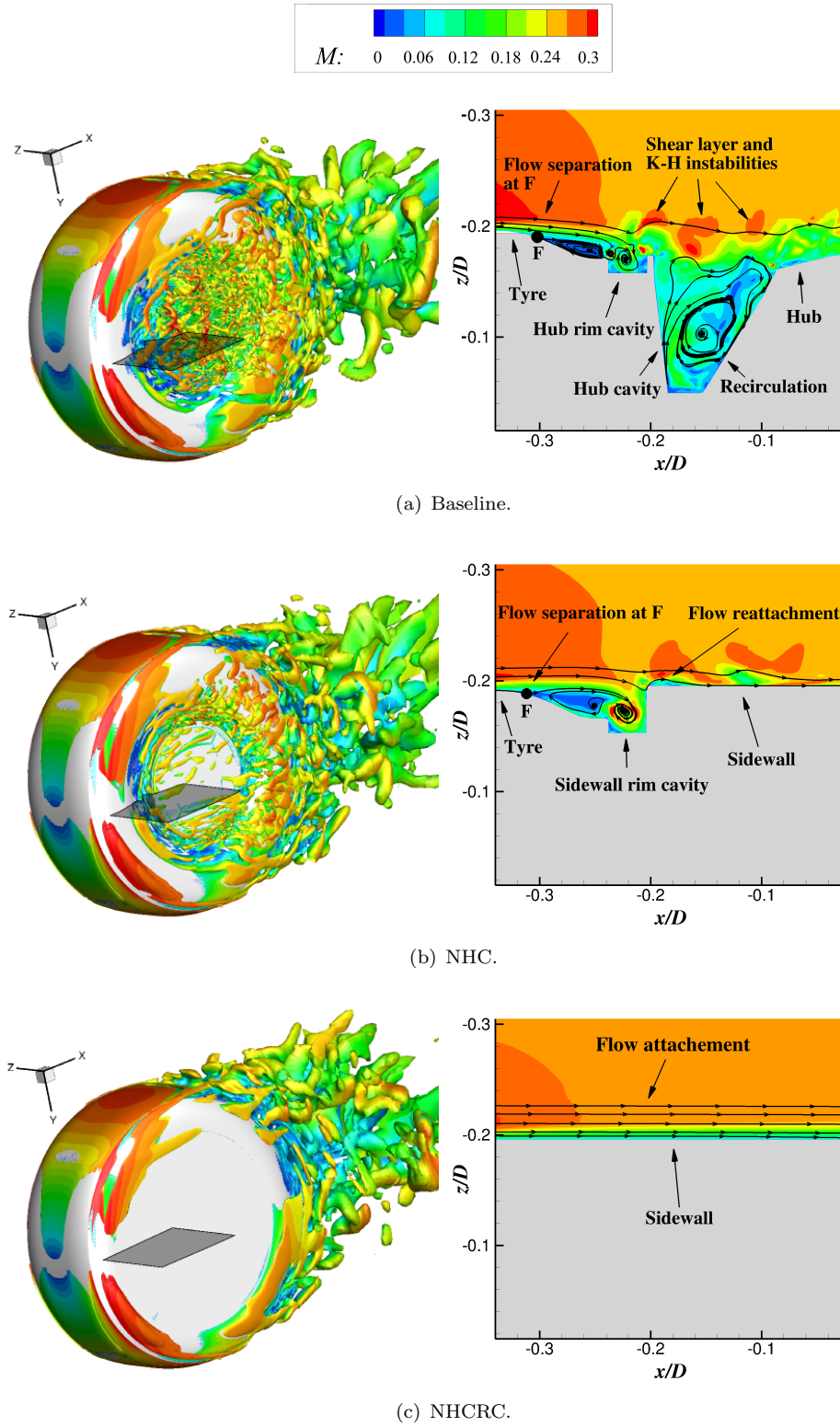


Figure 5.7: Left: instantaneous Q -criterion, where $Q = 10 \times U_\infty^2/D^2$ and is coloured by the local Mach number. Right: instantaneous local Mach number and flow features on the $y/D = 0$ plane highlighted on the left.

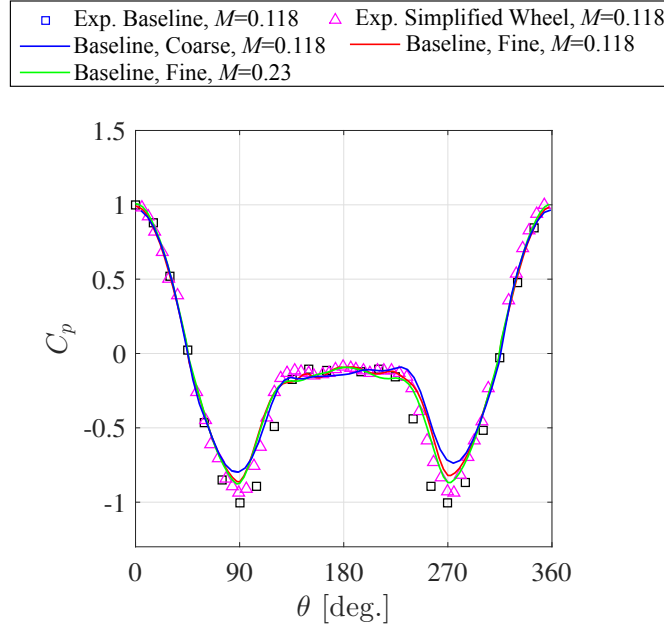


Figure 5.8: Mean surface pressure coefficient on the central plan of the baseline configuration ($z/D = 0$).

shear stress lines of landing gear wheels can be characterised into stable/unstable regular node, negative/positive open bipartition, saddle of separation/attachment, which are summarised in Figure 5.9. The attachment and separation flow patterns are demonstrated on the left and on the right, respectively. A focus is referred to a spiral flow pattern which can be used to indicate vortex. A point where flow diverges from it or converges to it is termed as an unstable or a stable regular node. The unstable/stable spiral and regular nodes are associated with flow attachment/separation. The topological phenomenon of flow attachment or separation along a line is named as a bipartition. The line itself is called a bipartite line which can occur in isolation or together with a saddle point. The attachment/separation is open when the bipartite line is in isolation, while ‘close’ is used to identify the presence of a saddle point at the connection of bipartite lines. The bipartition can be further characterised positive for flow attachment and negative for flow separation. In the following discussions, the bipartite lines will be represented with dashed lines and solid lines for flow attachments and flow separations, respectively. The visualisations of mean shear stress lines, with arrays indicating the flow directions, are demonstrated with the surface pressure coefficients which can be used to reveal flow patterns.

Figure 5.10 shows the surface flow topology on the side of the wheel with the main flow features highlighted. At the leading edge of the baseline configuration in Figure 5.10(b), a favourable pressure gradient exists from the stagnation point A to the leading edge of the shoulder at B. This is evidenced by the surface pressure contours around the shoulder of the wheel. Separation occurs at the saddle of separation B. Just downstream of this point, the flow reattaches at the saddle D. Saddle B and D form negative and positive

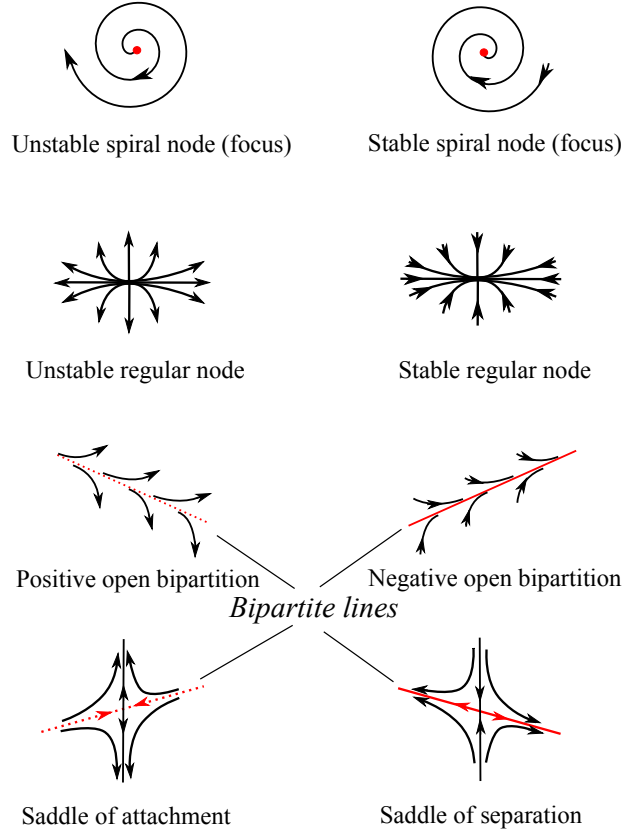


Figure 5.9: Surface topology patterns at locations of flow separation and attachment in the CADWIE wheel case. Left: attachment patterns; right: separation patterns [33].

closed bipartitions, respectively. Between these two points there is a recirculation region where the surface flow direction is predominantly toward the leading edge of the wheel. Further downstream of D, the flow moves towards the hub cavity and separates at F. The separation point F is also highlighted in the plot of instantaneous local Mach number in Figure 5.7(a). The negative open bipartition extends from F along the leading edge of the hub rim cavity to the downstream edge of the wheel G. F-G forms a separation line, which can also be observed in the experimental surface oil flow image in Figure 5.10(a). Downstream of this separation line, the separated flow is highly turbulent as shown in Figure 5.7(a). Further downstream of the saddle of separation F, the flow reattaches at the saddle of attachment H. On the downstream edge of the hub rim cavity, the two positive open bipartite lines converge at the saddle of attachment I. The flow features of the NHC configuration are similar to the baseline case, except that the separated flow from the upstream rim cavity reattaches to the sidewall at J and then remains attached until the downstream rim cavity. For the NHCRC configuration, the flow is fully attached to the sidewall after the saddle of attachment D. The complexity of flow separation and attachment patterns in the baseline and NHC configurations is significantly reduced in the NHCRC configuration.

The ground side view of the experimental oil flow image and numerical shear stress

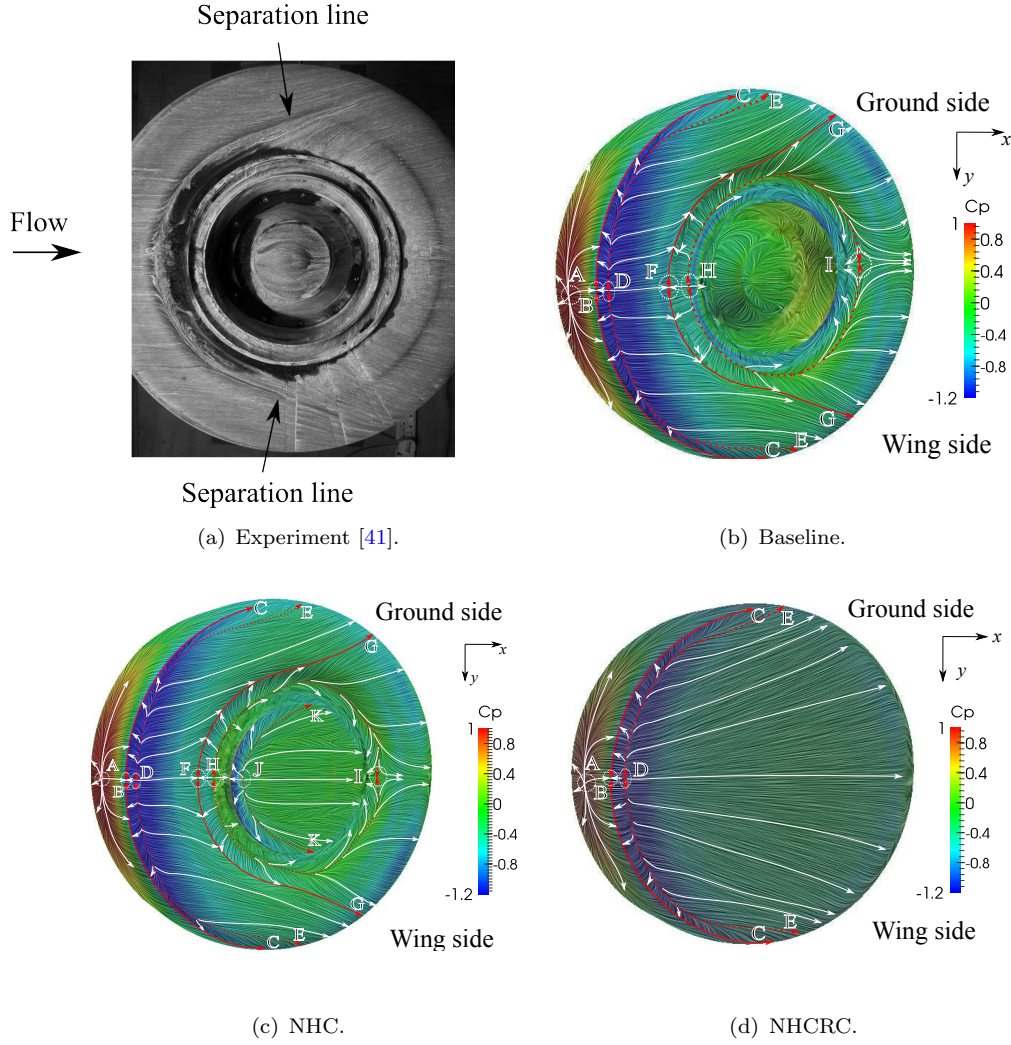


Figure 5.10: Surface shear stress lines on the side face with typical flow features highlighted. A: unstable regular node; B, F: saddle of separation; D, H, I, J: saddle of attachment; —: positive open bipartite line; ---: negative open bipartite line.

lines (baseline configuration only) are illustrated in Figure 5.11. The flow diverges from the stagnation point A before reaching the middle of the tyre B, where an acceleration region exists because of the low pressure gradient. After the acceleration region, the flow separates due to the adverse pressure gradient. The flow patterns becomes complex towards the rear of the tyre as an indication to highly turbulent features in this region. A negative open bipartite line is present at the rear extending from C to F on the sidewall side. F is a focus of separation with low a pressure coefficient, indicating vortex structures. Negative close bipartite lines form at the saddle of separation E.

To further study the flow patterns towards the wake, the experimental oil flow image and numerical shear stress lines (baseline configuration only) on the rear face are provided in Figure 5.12. A and C are stable and unstable regular nodes, indicating flow separation and attachment. Close to A is the saddle of separation B and two negative open bipartite

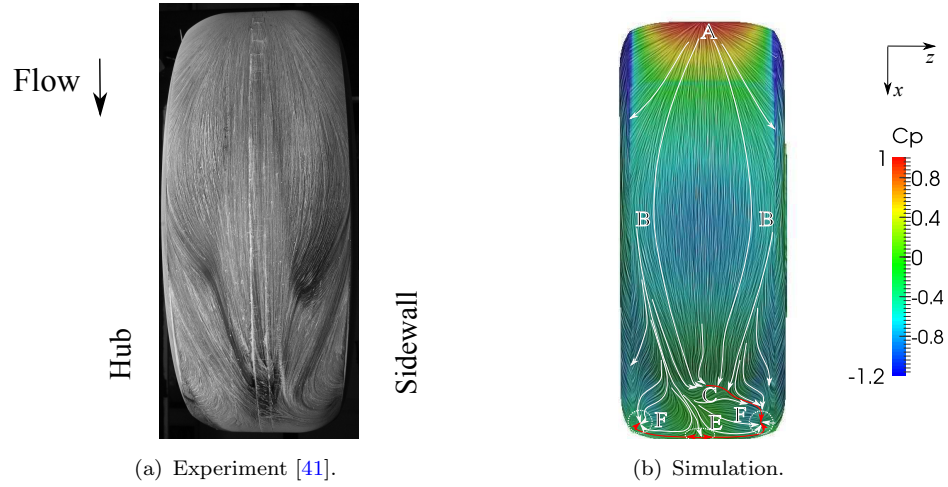


Figure 5.11: Ground side of shear stress lines from the baseline configuration. A: unstable regular node; F: stable spiral node (focus); E: saddle of separation; —: positive open bipartite line.

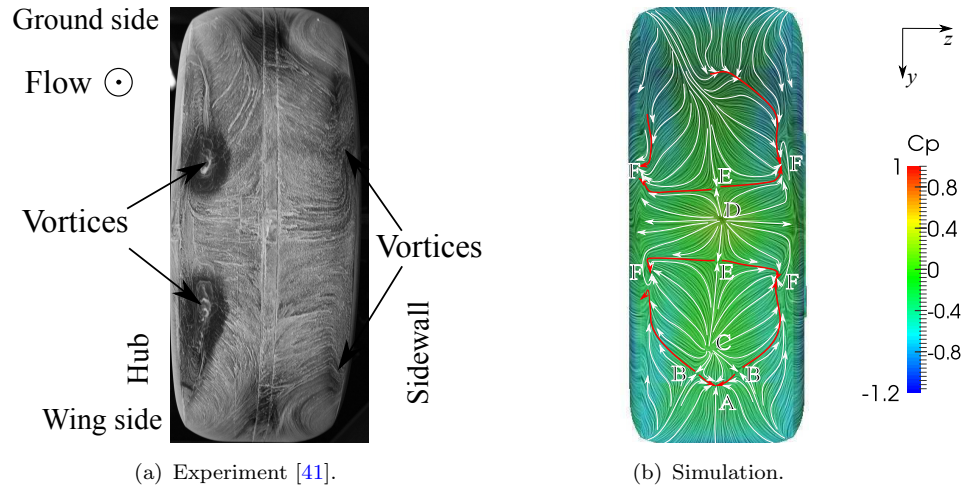


Figure 5.12: Rearward face of shear stress lines from the baseline configuration. A: stable regular node; B, E: saddle of separation; C, D: unstable regular node; F: stable spiral node (focus); —: positive open bipartite line.

lines extends from B to the side edge of the tyre. At the centre of the tyre on the rear view is the flow reattachment node D with a high pressure coefficient. After this reattachment, the flow diverges and forms two saddles of separation at E. F is a stable focus and suggests vortices, which can also be observed from the experimental oil image in Figure 5.12(a). However, in the experiments, the vortices on the sidewall side are less clear compared to the numerical simulations in Figure 5.12(b), which is likely due to the extra strut that was installed on the sidewall to fix the CADWIE wheel model in the experiment. This strut can affect the formation of vortices at the rear of the CADWIE wheel. The surface shear stress lines at the rear of the CADWIE wheel are not symmetric with respect to the central horizontal plan ($y/D = 0$ plane), which is an

indication of asymmetric flow structures in the wake region. This asymmetry will be further demonstrated in Figure 5.13.

Wake features

The flow characteristics in the wake region are investigated and compared to the experimental database. Two Particle Image Velocimetry (PIV) measurements were combined to obtain the streamwise and transverse velocities on the $z/D = 0$ plane in the experiment. Figure 5.13 demonstrates the comparisons of the streamwise and transverse velocities and the streamline profiles in the wake of the baseline configuration, where good agreements were obtained. In Figure 5.13, the mean velocity distributions are not symmetric with respect to the $y/D = 0$ plane and the velocity profiles are shifted downwards slightly, therefore resulting in non-zero mean lift coefficient in Table 5.3. This asymmetry has also been observed in the NHC and NHCRC cases. Zdravkovich *et al.* [13] performed experiments to investigate the flow features past free-end circular cylinders of spanwise length to diameter ratio W/D between 1 and 10, and an asymmetric flow pattern was found when $W/D < 3$. The asymmetry was demonstrated by Zdravkovich *et al.* to be bistable and can be biased to either side of the short span cylinder [13]. The asymmetry found in the current CADWIE wheel simulations is consistent with the experimental measurements by Zdravkovich *et al.* for short spanwise length cylinders. More details on this asymmetry is provided by the literature review in Section 2.2.1 (Figure 2.3).

To further investigate the asymmetric behaviour in the wake, the vorticity magnitude of mean flow on different downstream planes is plotted in Figure 5.14, which shows four large vortices. This is different from long spanwise cylinder flows where two large vortical structures dominate the wake. This difference is generated by the vortices are shedding from both the rear outboard (hub side) and rear inboard (sidewall side) edges. However, for long spanwise cylinder flows, the side edge vortices only exist at the ending of the cylinder and can hardly change the wake behaviour globally.

Figure 5.14 also shows that, firstly, the wing side pair of vortices dominates the ground side pair, which thus shifts the mean flow downwards and leads to the asymmetric wake behaviour in Figure 5.13. Secondly, the magnitude of vorticity on the hub side is higher. This is consistent with the experimental oil flow image at the rearward face of the CADWIE wheel in Figure 5.12(a), where the hub vortices are clearer than the sidewall vortices. The higher vorticity magnitude at the hub side is due to the presence of the hub cavity, the flow around which is less stable compared to the sidewall side, and therefore the vortices at the hub side are shedding more intensively. The hub cavity is also a contributor to the mean flow asymmetry, considering that the mean lift coefficient tends to be lower when the hub cavity is covered, as shown by the NHC case in Table 5.3.

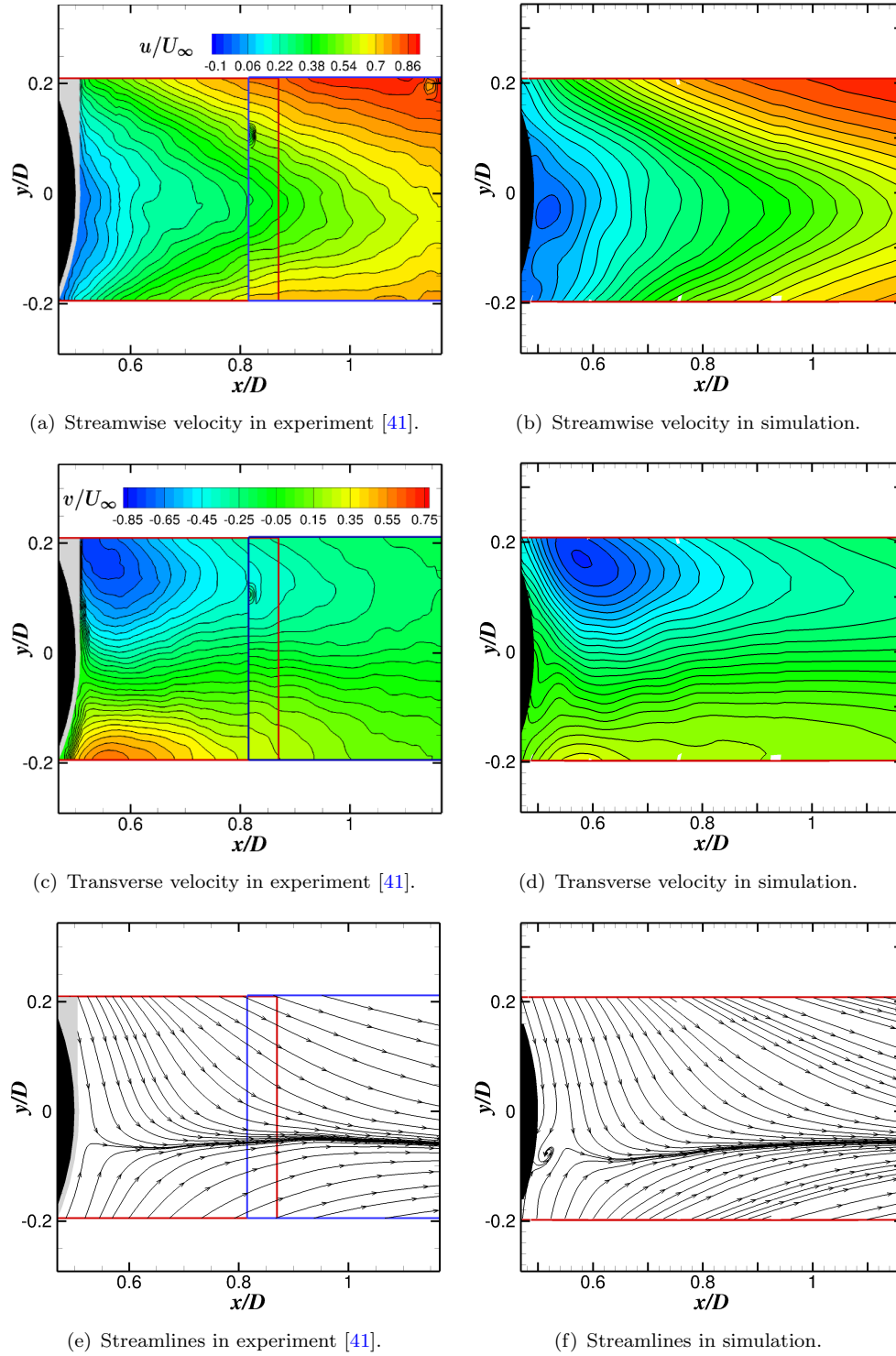


Figure 5.13: Comparisons of streamwise, transverse velocities and streamlines in the wake region on $z/D = 0$ plane (baseline configuration).

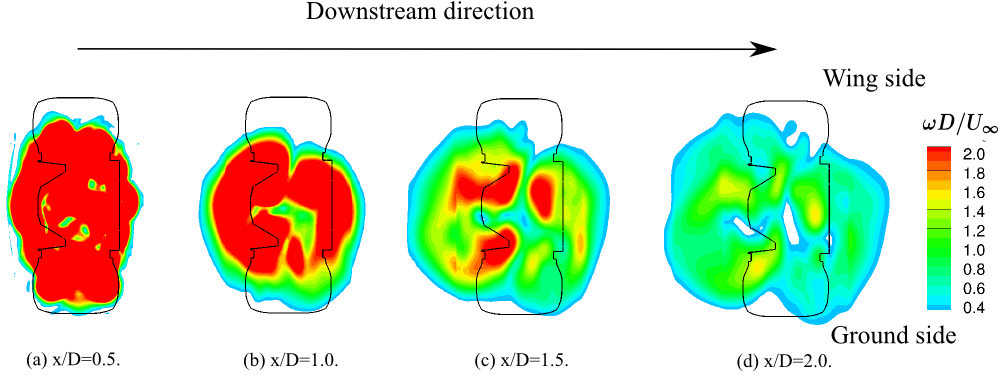


Figure 5.14: Vorticity magnitude on different downstream x planes in the wake region.

5.3.4 Unsteady flow data

The surface pressure signals at four different positions on the hub were measured during the simulations at a sample frequency of 1.7×10^4 Hz. A Fast Fourier Transform (FFT) was performed on the pressure signals evenly divided into 35 segments with a 50% overlap resulting in a frequency bin width of 16.6 Hz. Figure 5.15 plots the comparisons of the wall pressure spectral profiles at the hub monitors against two Strouhal numbers St_D and St_W , based on the wheel diameter D and the width of the shoulder W , respectively. The PSD values in Figure 5.15 have been scaled using a M^4 power law. The simulation with the coarse grid resolution under-predicts the wall pressure spectra in the range of $St_D > 20$ compared to the experiments, due to the insufficient resolution around the hub cavity. A more accurate prediction was achieved with the finer grid. The wall pressure spectra collapse well using a M^4 power law, suggesting that the wall pressures are dominated by hydrodynamic effects. However, slight over-predictions in the range of $St_W < 0.8$ are also present for the fine mesh resolution. This range corresponds to the large scales of flow, and the discrepancies are mostly likely due to the installation of the support strut in the experiments, and this support has been found to dominate the far-field acoustics at $St_W < 0.8$ [41]. It will be demonstrated in Sections 5.4.1 and 5.4.2 that the acoustics of interest are in the range of $1 < St_W < 5$, and the surface pressure fluctuations are well predicted in this range by the fine mesh resolution.

The Dynamic Mode Decomposition (DMD) method, which is introduced in Section 3.11, is performed on the surface pressures. The number of snapshots is $N = 512$ with a fixed interval of $\Delta t = 1.175 \times 10^{-4}$ s (the corresponding sampling frequency is $f = 1.7 \times 10^4$ Hz). The instantaneous dynamic modes of the surface pressures on the CADWIE wheel at different frequencies are plotted in Figure 5.16. Firstly, a lift dipole pattern is formed at $f = 20$ Hz, with the high pressure (HP) region and the low pressure (LP) region highlighted on the upper and lower surfaces of the tyre. The HP and LP distributions at $f = 90$ Hz are more distorted in Figure 5.16(b), and at the rear of the wheel, a side force dipole is weakly illustrated. It will be shown in Section 5.4 that the far-field

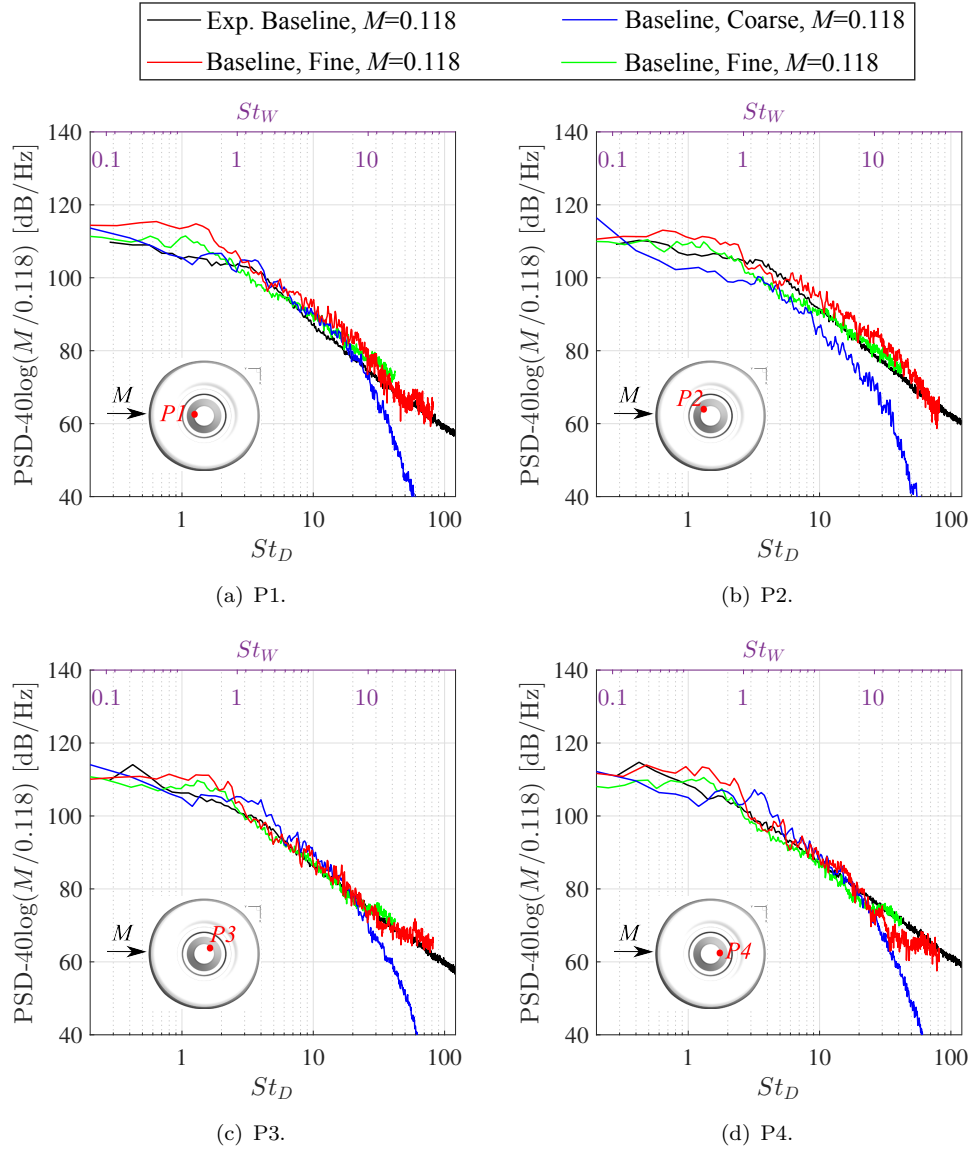


Figure 5.15: Wall pressure spectra at four monitors on the hub.

acoustics at these two frequencies demonstrate a lift dipole directivity pattern and a side force directivity pattern, respectively. At $f = 650$ Hz and $f = 1290$ Hz, the dynamic modes are mainly located around the hub cavity region after the separation line (SL). This separation line is formed at the leading edge of the hub rim cavity as demonstrated in Figure 5.10(b). These two frequencies are corresponding to the first and second depth modes of the hub cavity resonance (please refer to Appendix F.2 for more details). This implies that the dynamic modes in Figure 5.16(c) and 5.16(d) are produced by the flow interactions with the hub cavity, which will be confirmed by the investigations of far-field acoustics at these two frequencies in Section 5.4. The dynamic modes at $f = 4000$ Hz in Figure 5.16(e) correspond to the highly unsteady small-scale structures, and they are distributed around the hub and the downstream rim cavity, which will be shown in Section 5.4 to generate high frequency noise.

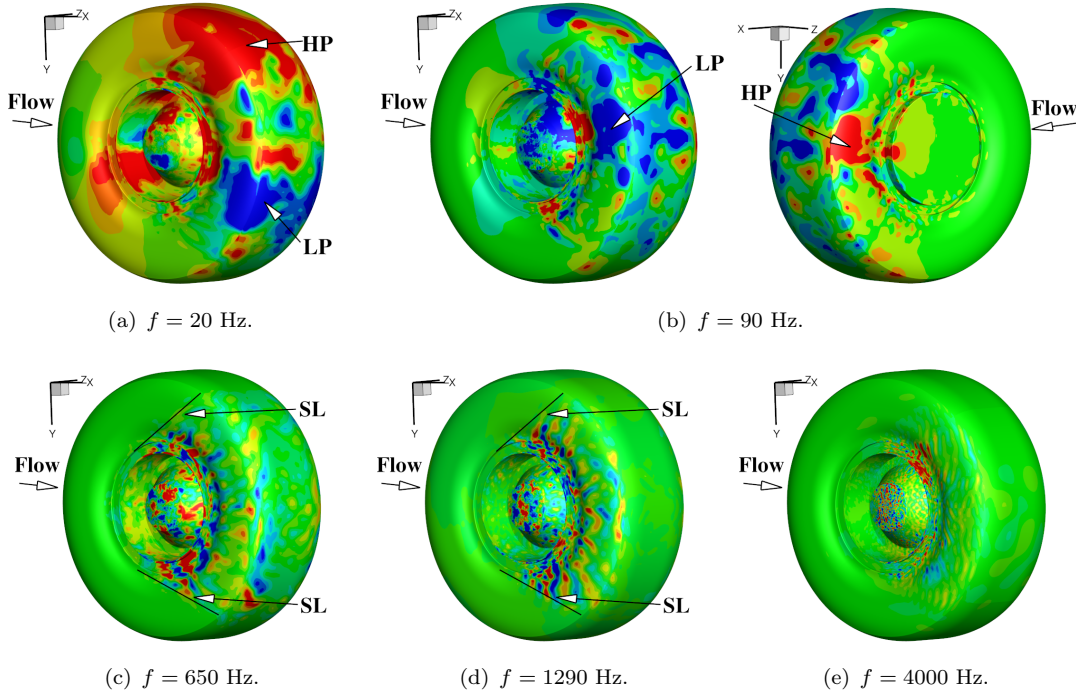


Figure 5.16: Instantaneous dynamic modes of surface pressures on CADWIE wheel at different frequencies, with low pressure (LP) regions, high pressure (HP) regions and separation lines (SL) highlighted. Only the real part of the dynamic modes is plotted.

5.3.5 Section summary

Three geometry configurations have been investigated in the simulations at two Mach numbers ($M = 0.118$ and $M = 0.23$) with two mesh resolutions. The baseline case is a high-fidelity isolated landing gear wheel model containing a tyre, a hub cavity, a sidewall and two rim cavities. The two additional simulations are conducted with the hub cavity covered (NHC), and both the hub cavity and rim cavities covered (NHCRC). The simulations are validated against the steady and unsteady experimental statistics, and the results from the fine mesh resolution demonstrate higher accuracy in the prediction of the mean pressure coefficient C_p along the centreline of the wheel and the unsteady surface pressure spectra on the hub, compared to the coarse grid.

The rim cavities are more important contributors to the total drag than the hub cavity, and their contributions are 20% and 7%, respectively. In the NHCRC case with both hub and rim cavities covered, the side face becomes flat. Therefore, on the side face, only the skin friction can affect the drag from, and the pressure invariants do not have contributions. Among the three force coefficients R.M.S., C_L^{rms} is the largest due to the higher PSD levels in the low frequency range of $f < 30$ Hz. The flow around the rim cavities can produce high-frequency ($f > 2000$ Hz) fluctuations in all the three force coefficients. A non-zero mean lift coefficient \bar{C}_L is observed for the three geometries,

which is primarily due to the asymmetric nature of flow field around short circular cylinders. Additionally, the mean field around a cylindrical cavity, at the same depth-to-diameter ratio of $\varpi = 0.3$ as the hub cavity, is shown to be asymmetric in Appendix G.4. Thus, the hub cavity can also affect the asymmetry of flow around the CADWIE wheel, and a reduction in \bar{C}_L is also demonstrated by the NHC case with the hub cavity covered.

In the illustrations of the instantaneous Q -criterion and mean shear stress lines, the flow separations and attachments are dramatically reduced by covering the hub and rim cavities, and the flow is fully attached on the side face until the rear of the wheel. However, two separation lines originating from the leading edge of the rim cavities are shown in the baseline and NHC configurations. The shear stress lines at the rear face show four vortices, which are also confirmed by the plot of vorticity magnitude on different downstream x planes. One pair of the vortices is formed at the rear edge on the wing side and the other pair on the ground side. The vorticity magnitude on the hub side is higher than the sidewall side, due to the flow interactions with the hub cavity. The mean streamlines in the wake shift slightly downwards, thus leading to a non-zero mean lift coefficient \bar{C}_L .

The surface pressure spectra on the hub are broadband, and they are dominated by hydrodynamic effects, since they follow a M^4 power law. The dynamic modes of the surface pressures are analysed at different frequencies. Firstly, a lift dipole pattern and a side force dipole pattern are shown at low frequencies of $f = 20$ Hz and $f = 90$ Hz, respectively. They correspond to the large scales on the tyre. In the middle frequency range ($f = 650$ Hz and $f = 1290$ Hz), the dominant dynamic modes are distributed around the hub cavity after two separation lines on the side face, which are due to the flow interactions with the depth modes of the hub cavity resonance. The small-scale fluctuations on the hub and on the rim cavities are responsible for the dynamic modes at $f = 4000$ Hz.

5.4 Acoustic results

The acoustic experimental measurements were collected at three different Mach numbers, $M = 0.118, 0.23, 0.29$, in the UK's NTF anechoic wind tunnel [41]. The acoustic experimental database at $M = 0.23$ is the most complete and also the signal to noise ratio is the highest at this Mach number. Therefore, this Mach number was used to validate the current simulation results (at $M = 0.23$ with the fine mesh resolution). The far-field acoustic measurements were acquired using a traversing circular array with a diameter of $25D$ moving in the flow direction with a range of polar angles ($70^\circ < \psi < 140^\circ$) around the wheel. The position of observers are described by a polar angle ψ on the plane $y/D = 0$ and an azimuthal angle ϕ on the plane $x/D = 0$, which are

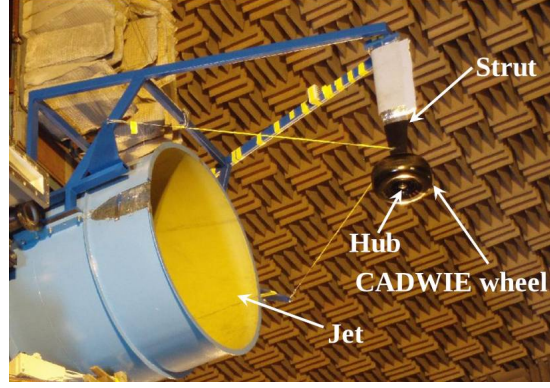


Figure 5.17: Acoustic experimental setup of the CADWIE wheel in the NTF anechoic wind tunnel [41].

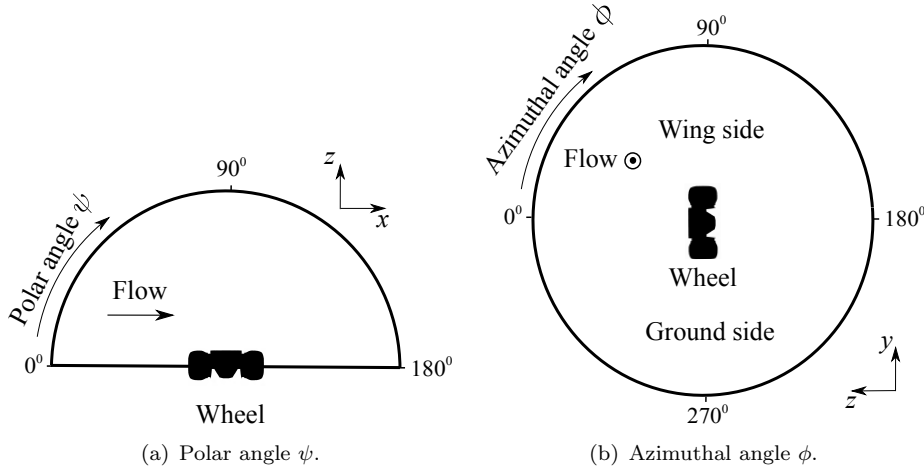


Figure 5.18: Demonstrations of observer angles, where the hub side observer, sidewall side observer and ground side observer refer to the positions of $(\psi = 90^\circ, \phi = 180^\circ)$, $(\psi = 90^\circ, \phi = 0^\circ)$ and $(\psi = 90^\circ, \phi = 270^\circ)$, respectively.

defined in Figures 5.18(a) and 5.18(b), respectively. In the following discussions, the hub side observer, sidewall side observer and ground side observer refer to the positions of $(\psi = 90^\circ, \phi = 180^\circ)$, $(\psi = 90^\circ, \phi = 0^\circ)$ and $(\psi = 90^\circ, \phi = 270^\circ)$. In the experiments, the facility noise and strut noise limit the acoustic measurements of the wheel noise to a reliable frequency range of $f > 300$ Hz. As a result, the numerical simulations are validated in this reliable frequency range, especially in the azimuthal range $120^\circ < \phi < 230^\circ$ where the acoustic measurements are less effected by the strut noise. The experimental data were corrected for shear layer refraction effects using Amiet's method [121]. Only the fine mesh resolution data are collected to compute the far-field acoustics, because they demonstrate a better agreement in the surface pressure spectra compared to the experimental measurements. In the simulations, the data for FW-H calculations are collected for 0.6 seconds. In the FFT processing, the far-field pressure signals were evenly divided into 20 segments with a 50% overlap resulting in a frequency bin width of 16.6 Hz.

The validations of the acoustic simulation of the baseline configuration are firstly provided in Section 5.4.1. Section 5.4.2 details the analysis of the baseline geometry. The acoustic results of the other two configurations are presented in Section 5.4.3.

5.4.1 Validation of far-field acoustics

The PSD of far-field acoustic pressures at different observer positions is compared with experiments in Figure 5.19, where the agreements are within 3 dB/Hz in the resolvable frequency range. The frequency scale is divided into low frequency range ($f < 400$ Hz), middle frequency range ($400 \text{ Hz} < f < 2000$ Hz) and high frequency range ($f > 2000$ Hz). It was found that, for the far-field observers at the hub side in Figures 5.19(a), 5.19(b) and 5.19(c), intensive sound is present in the middle frequency range around the first ($f = 646$ Hz) and second ($f = 1292$ Hz) hub cavity depth modes (refer to the Appendix F.2 for the summary of resonant frequencies). These two frequencies are close to the values of 630 Hz and 1250 Hz observed in the experimental measurements in Figure 5.19(b) that shows two weak spectral peaks, considering that the frequency bin width in the experiments is 10 Hz [41]. However, the middle frequency noise is much weaker in the sidewall direction (Figure 5.19(d)). The difference in the middle frequency noise is better demonstrated by the comparison between the sound at the hub side ($\psi = 90^\circ$, $\phi = 180^\circ$) and at the sidewall side ($\psi = 90^\circ$, $\phi = 0^\circ$) in Figure 5.20. The spectrum of the sidewall side observer is similar to the hub side observer in the low and high frequency ranges, but they are significantly different in the middle frequency range. Compared to the sidewall side, the additional middle frequency noise that radiates towards the hub side observer is due to the presence of the hub cavity.

Further evidence that the noise generated in this frequency range is due to the depth modes of the hub cavity resonance is shown in Figure 5.21. In Figure 5.21, the experimental far-field acoustic pressure spectra at the hub side observer at three different Mach numbers are provided [41]. The noise sources distributed on the wheel surface can be considered as dipoles, which follow the M^6 power law [6]. The magnitude of the power has been scaled by this Mach number exponent. The facility noise dominates the low frequency noise in the experiments ($f < 300$ Hz) and is therefore excluded in Figure 5.21. The spectra are plotted against Strouhal numbers, based on the diameter of the wheel D and the width of the wheel W , in Figure 5.21(a) and against frequency in Figure 5.21(b). Compared to the Strouhal number scale, a better collapse using the frequency scale is demonstrated in Figure 5.21(b), particularly in the middle frequency range, indicating that the middle frequency noise is fixed by the dimensions of the geometry. This middle frequency range also corresponds to the first and second depth modes, which provides further evidence that the middle frequency noise is from the depth modes of the hub cavity resonance.

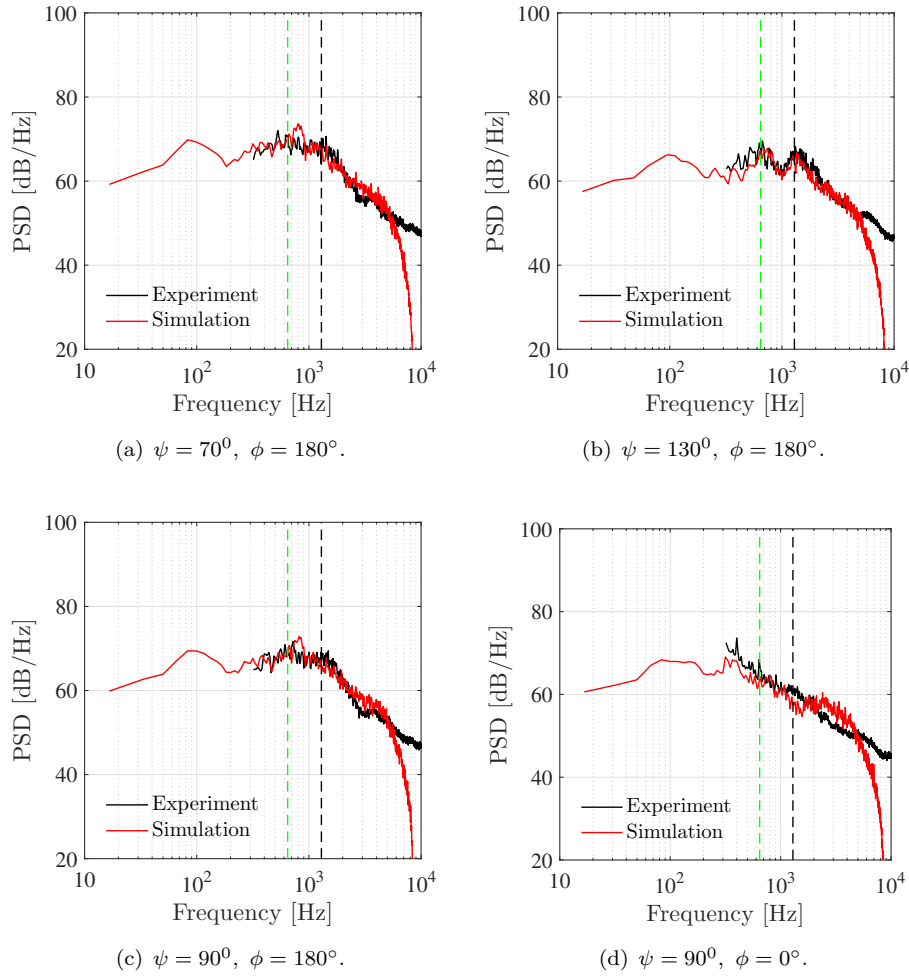


Figure 5.19: Comparisons of acoustic pressure spectra at different far-field observers. The experimental data are plotted in the most reliable frequency range, i.e. $f > 300$ Hz; --- first depth mode (646 Hz), --- second depth mode (1292 Hz). The observer angle is defined in Figure 5.18.

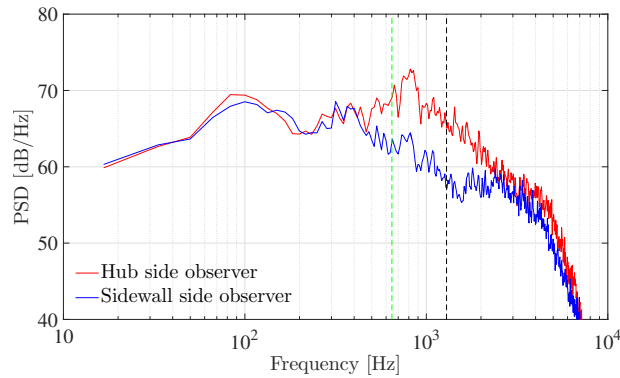


Figure 5.20: Far-field acoustic spectra at the hub side ($\psi = 90^\circ, \phi = 180^\circ$) and sidewall side ($\psi = 90^\circ, \phi = 0^\circ$), in the simulation. --- first depth mode (646 Hz), --- second depth mode (1292 Hz).

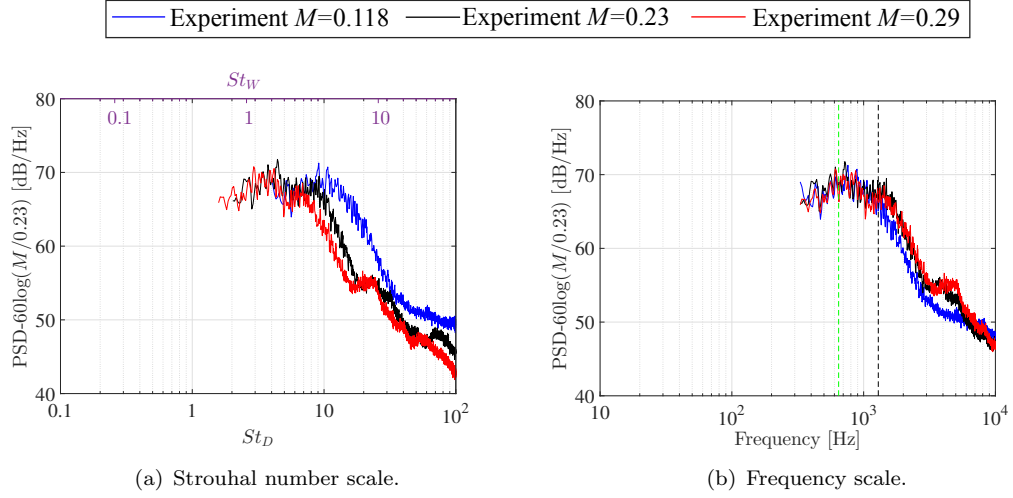


Figure 5.21: Far-field experimental acoustic spectra at the hub side ($\psi = 90^\circ$, $\phi = 180^\circ$) in Strouhal number scale and frequency scale. The spectra are collapsed using the M^6 power law. --- first depth mode (646 Hz), --- second depth mode (1292 Hz).

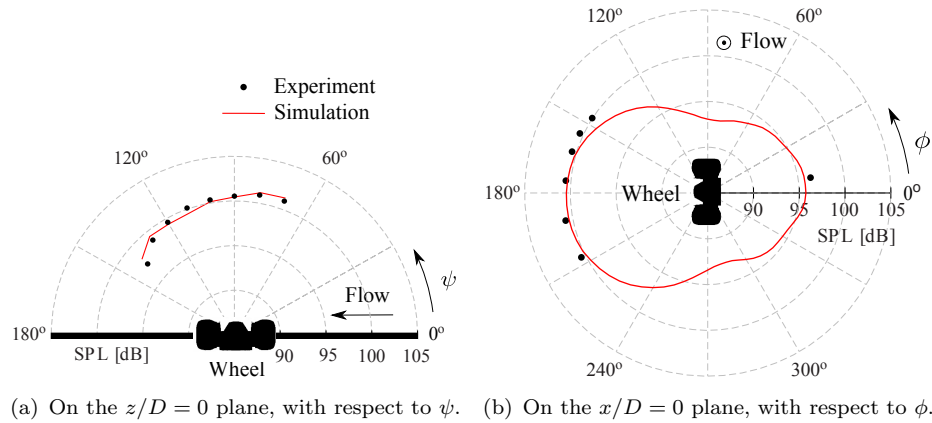


Figure 5.22: Far-field acoustic directivity comparisons. The SPL is integrated between 300 Hz and 6000 Hz.

Comparisons of the SPL directivity, which were obtained by integrating the PSD between 300 Hz and 6000 Hz, are illustrated in Figure 5.22. The deviation of the agreement with experiments is within 2 dB. For the far-field noise at the hub side in Figure 5.22(a), more sound is shown to radiate towards the upstream direction. The SPL of the hub side noise in Figure 5.22(b) is approximately 4 dB higher than the sidewall side noise, which is mainly due to the difference of the acoustic spectra in the middle frequency range as shown in Figure 5.20. This directivity pattern suggests that the hub cavity noise is a significant middle frequency noise source.

In conclusion, the numerical predictions of the far-field acoustics show good agreements with the experimental data. However, in the experiments, the acoustic measurements

were limited to a few microphone positions, and the measured acoustics were contaminated by the strut and background noise, especially in the low frequency range of $f < 300$ Hz. The numerical database is more complete and reliable. The following discussion is therefore based on the numerical simulation results to provide further analysis on the CADWIE wheel noise source locations and acoustic radiating characteristics.

5.4.2 Far-field acoustics of the baseline geometry

Coherence analysis at the hub cavity depth modes

The coherence function between wall pressure fluctuations and far-field acoustic pressures is given by,

$$\gamma^2 = \frac{S_{p_w p_a}^2}{S_{p_a^{\text{hub}}} S_{p_a^{\text{hub}}} S_{p_w p_w}}, \quad (5.1)$$

where γ^2 is the coherence function, p_w and p_a^{hub} are the wall pressure fluctuations and far-field acoustic pressures at a far-field observer at the hub side. The coherence function is used to give an insight into potential noise sources.

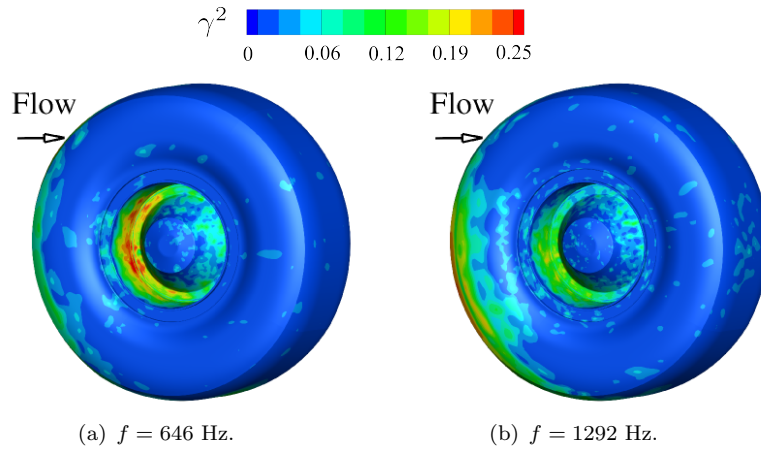


Figure 5.23: The value of coherence function γ^2 between the wall pressure fluctuations and the far-field acoustic pressures at the hub side ($\psi = 90^\circ$, $\phi = 180^\circ$).

Figure 5.23 demonstrates the coherence function at frequencies corresponding to the hub cavity depth modes. The coherence (γ^2) is largest in the hub cavity region, showing that the middle frequency noise is generated from the hub cavity. The largest value of γ^2 is 0.28, suggesting that the shallow hub cavity noise is more broadband than the deep cylindrical cavity noise in the work by Marsden *et al.* [46], where a stronger coherence function is present at the depth mode. This broadband cavity noise is consistent with previous work on shallow cylindrical cavities by Marsden *et al.* [56].

Contributions from different parts of the wheel

For a closed FW-H integral surface containing multiple components, the far-field acoustics can be obtained firstly by using the information on each component individually, which will give an auto power spectral density (PSD), and then by considering the cross correlation between any two components, which will give a cross power spectral density (CPSD). The CPSD is a measure of the coherence and phase shift of the two signals, which can be used to indicate flow and acoustic interactions, as the interactions will give non-zero cross power at the interaction frequency.

In the current study, the solid FW-H integral surface on the CADWIE wheel was divided into three components, i.e. the hub cavity (including the surrounding hub rim cavity), the sidewall (including the surrounding sidewall rim cavity) and the tyre. The far-field acoustic pressures in the time domain are computed by,

$$p(t) = p_{hc}(t) + p_s(t) + p_t(t) \quad , \quad (5.2)$$

where p is the acoustic pressures at far-field observer positions, p_{hc} , p_s and p_t are from the hub cavity including the hub rim cavity (hc), sidewall including the sidewall rim cavity (s) and tyre (t), respectively. Applying a Fourier transform to both sides of Equation 5.2 yields,

$$p(f) = p_{hc}(f) + p_s(f) + p_t(f) \quad . \quad (5.3)$$

The far-field pressure spectral power can be obtained by multiplying the complex conjugate to both sides of Equation 5.3,

$$S_{pp} = S_{p_{hc}p_{hc}} + S_{p_s p_s} + S_{p_t p_t} + S_{p_{hc}p_s} + S_{p_s p_{hc}} + S_{p_{hc}p_t} + S_{p_t p_{hc}} + S_{p_s p_t} + S_{p_t p_s} \quad , \quad (5.4)$$

where $S_{p_i p_i}$ is the auto PSD and $S_{p_i p_j}$ is the CPSD. Since $S_{p_i p_j}$ is the complex conjugate of $S_{p_j p_i}$, Equation 5.4 can be simplified as,

$$S_{pp} = S_{p_{hc}p_{hc}} + S_{p_s p_s} + S_{p_t p_t} + \text{real}(2S_{p_{hc}p_s}) + \text{real}(2S_{p_{hc}p_t}) + \text{real}(2S_{p_s p_t}) \quad . \quad (5.5)$$

The real part of the CPSD can be negative. For visualisation purpose, only the absolute value of the CPSD's real part is plotted in Figure 5.24.

The PSD and CPSD profiles at three observer locations are plotted in Figure 5.24 against frequency and two Strouhal numbers (St_D and St_W). Firstly, the auto powers are discussed. The hub cavity auto power $S_{p_{hc}p_{hc}}$ at the frequencies around the two depth modes is higher at the hub side (approx. 70 dB/Hz in Figure 5.24(a)) than the sidewall side (approx. 60 dB/Hz in Figure 5.24(c)) and ground side (approx. 60 dB/Hz in Figure 5.24(e)), due to the fact that most of the hub cavity noise is radiated towards observers facing the hub. For the sidewall auto power $S_{p_s p_s}$, a spectral hump is present

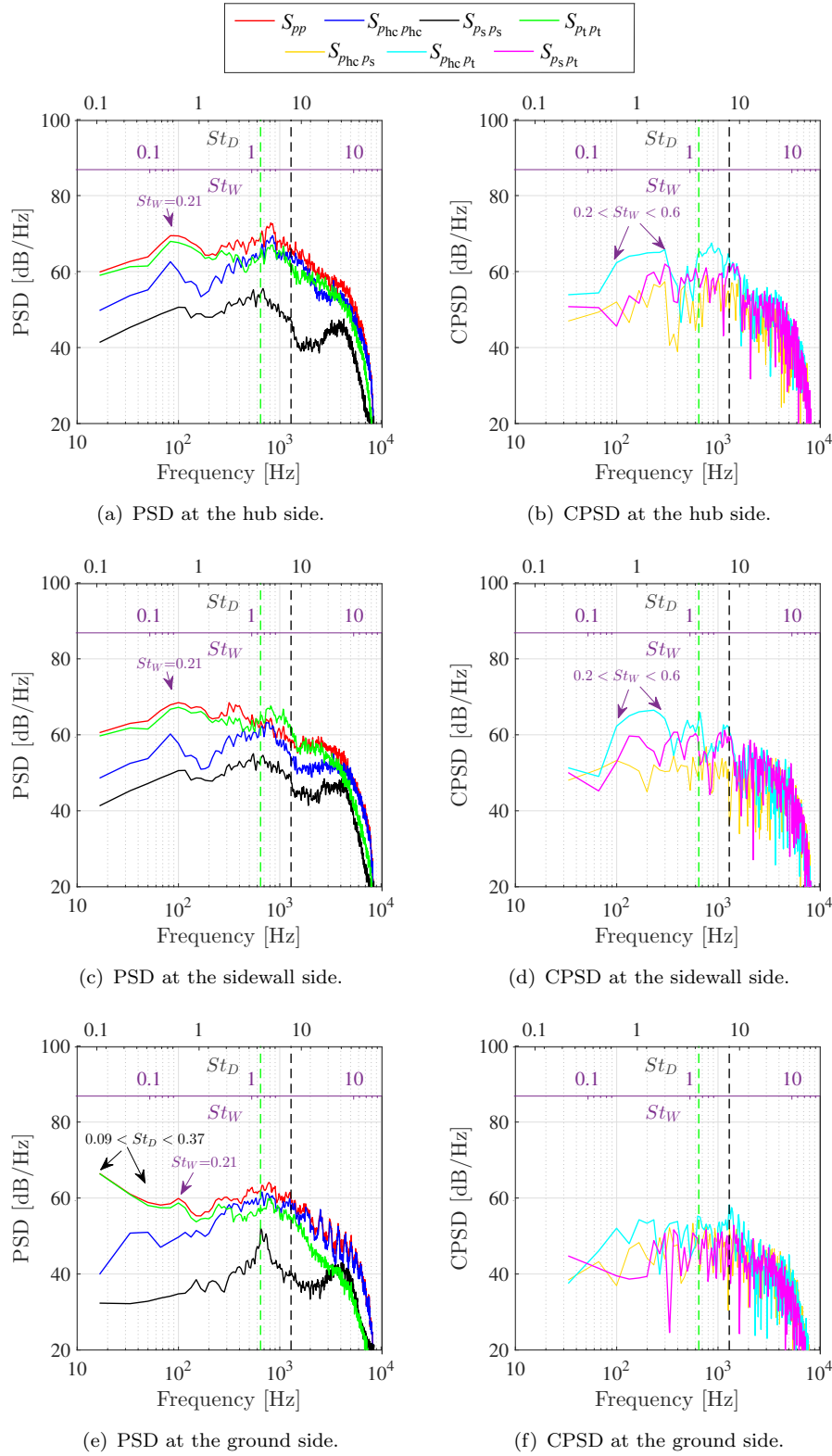


Figure 5.24: PSD and CPSD of far-field acoustic pressures from different parts of the wheel, against both frequency and two Strouhal numbers. ---: first depth mode (646 Hz); ---: second depth mode (1292 Hz). *hc*, *s* and *t* are hub cavity, sidewall and tyre respectively. *p* is the farfield acoustic pressure.

at $f = 4000$ Hz, which is in the high frequency range and indicates that the small-scale flow features at the sidewall rim cavity, and their corresponding pressure fluctuations on the surface, are responsible for the far-field noise radiated at this frequency. The tyre auto power ($S_{p_t p_t}$) shows a spectral hump at a Strouhal number based on the wheel width of $St_W = 0.21$. The tyre auto power at $St_W = 0.21$ is higher at the hub side (approx. 70 dB/Hz) and sidewall side (approx. 70 dB/Hz) than the ground side (approx. 60 dB/Hz), indicating a directivity pattern corresponding to a force dipole aligned with the z axis (side force). In Figure 5.24(e), the tyre auto power $S_{p_t p_t}$ is dominant at very low frequencies ($f < 50$ Hz). This frequency range corresponds to a Strouhal number of $0.09 < St_D < 0.37$. The tyre auto power is higher at the ground side (> 60 dB/Hz) than the hub side (approx. 60 dB/Hz) and sidewall side (approx. 60 dB/Hz). This indicates a directivity pattern corresponding to a force dipole aligned with the y axis (lift force), which shows a lift dipole directivity pattern. The directivity patterns of the overall wheel are further discussed in the next section. From the auto powers at the three observer angles, the tyre auto power $S_{p_t p_t}$ is dominant over the hub cavity auto power $S_{p_{hc} p_{hc}}$ and the sidewall auto power $S_{p_s p_s}$ in the frequency range of $f < 200$ Hz. Therefore, the tyre is the main low frequency noise source.

The cross powers (CPSD) are noisier than the auto powers due to the limited length of the FW-H signals. The real part of the cross power is a measure of the power shared at a given frequency by the farfield pressure signals of two different parts of the wheel. At the hub side observer in Figure 5.24(b) and sidewall side observer in Figure 5.24(d), a spectral hump is shown by the Fourier transform of the cross-correlation between the hub cavity and tyre signals ($S_{p_{hc} p_t}$) at $0.2 < St_W < 0.6$, which is not present at the ground side observer in Figure 5.24(f). This spectral hump is the effect of the hub cavity on the tyre noise that dominates at low frequencies in this frequency range ($0.2 < St_W < 0.6$). A second spectral hump in the Fourier transform on the cross correlation between the hub cavity and tyre signals ($S_{p_{hc} p_t}$) occurs between the first and second depth modes at the hub side observer in Figure 5.24(b). This does not occur at the sidewall observer in Figure 5.24(d) and ground side observer in Figure 5.24(f). This spectral hump around the depth modes is due to the interactions of hub cavity flow with the downstream tyre. For the ground side observer in Figure 5.24(f), the level of Fourier transform of the cross correlation between the hub cavity and sidewall ($S_{p_{hc} p_s}$), hub cavity and tyre ($S_{p_{hc} p_t}$) and sidewall and tyre ($S_{p_s p_t}$) are all lower compared to the hub side observer (Figure 5.24(b)) and the sidewall side observer (Figure 5.24(d)). Since the ground side is the least efficient radiation direction for the hub cavity noise and sidewall noise, the coherent power of the acoustics from the three components is lower.

Directivity

The directivity of OASPL is shown as a function of polar angle (ψ) and azimuthal angle (ϕ) in Figure 5.25. The definition of the angles is given in Figure 5.18. In Figure 5.25, most of the noise is radiating towards the hub side ($\phi = 180^\circ$) in the upstream direction

($\psi < 90^\circ$), which is consistent with the directivity profile from the shallow cylindrical simulations at $\varpi = 0.3$ in Figure G.19(a).

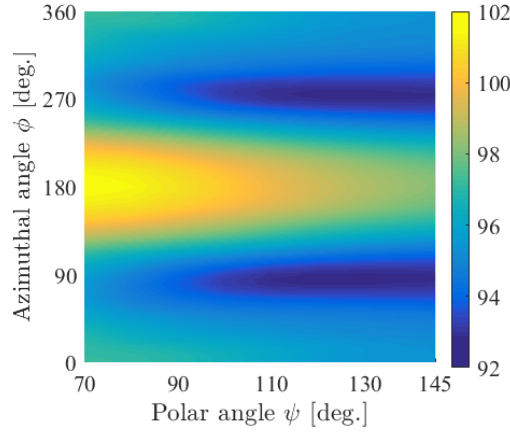


Figure 5.25: Directivity of OASPL [dB] against polar and azimuthal angles.

The directivity of narrowband SPL (with a band width of 8 Hz) at different frequencies is plotted in Figure 5.26 to give an insight into how the radiation patterns vary with frequency. Firstly at 20 Hz ($St_D = 0.13$) in Figure 5.26(a), the peak directivity is towards the wing side ($\phi = 90^\circ$) and the ground side ($\phi = 270^\circ$), showing a lift dipole pattern (aligned with y axis). This directivity at 20 Hz is determined by the tyre noise as shown in Figures 5.24(a), 5.24(c) and 5.24(e). At 90 Hz ($St_W = 0.21$) in Figure 5.26(b), the directivity still shows a dipole pattern but with the favourable directions

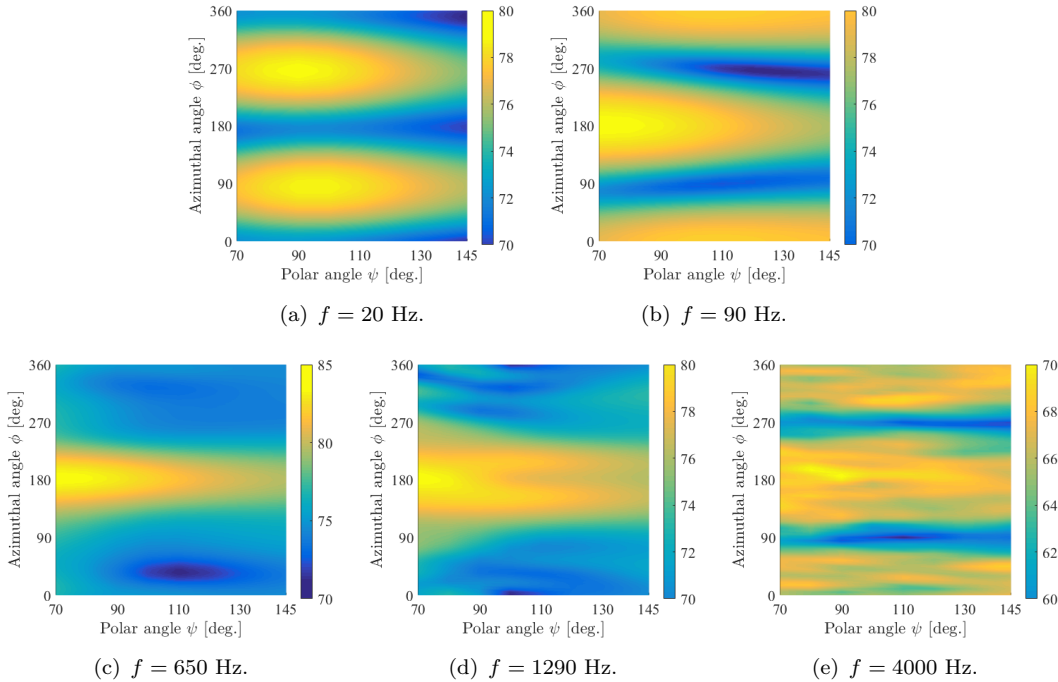


Figure 5.26: Directivity of narrow band SPL [dB] against polar and azimuthal angles at different frequencies.

changing to the sidewall side ($\phi = 0^\circ$) and hub side ($\phi = 180^\circ$), presenting a side force dipole pattern (aligned with the z axis). The lift dipole at 20 Hz and side force dipole at 90 Hz are generated by the large-scale flow separations and oscillations at the rear of the wheel in the y axis direction and z axis direction, respectively. As the frequency increases to 650 Hz (first depth mode) and 1290 Hz (second depth mode), the dipole behaviour disappears and there is only one single radiation direction towards the hub side. The noise generated at the first and second depth modes radiates more in the upstream direction towards the hub side, which determines the OASPL directivity in Figure 5.25. At 4000 Hz, the directivity is again dipole in nature, radiating towards both the sidewall and hub sides. As discussed in the previous section, this noise is due to the small-scale turbulent fluctuations generated by the rim cavities. This will also be shown in Section 5.4.3, when the rim cavities are covered.

Noise sources localisation

When the FW-H integral surface is coincident with the solid wheel surface and neglecting the quadrupole sources, the FW-H equation in the frequency domain can be expressed as,

$$p_a(\mathbf{x}, f) = \int_S \mathcal{P}(\mathbf{y}, f) dS, \quad (5.6)$$

where,

$$\mathcal{P}(\mathbf{y}, f) = \frac{1}{4\pi r} p_w(\mathbf{y}, f) \hat{\mathbf{n}} \cdot \hat{\mathbf{r}}, \quad (5.7)$$

where \mathbf{x} and \mathbf{y} are the observer and source locations and their distance is r , S is the FW-H integral surface, $\hat{\mathbf{n}}$ is the unit outward normal vector to the surface S and $\hat{\mathbf{r}}$ is the unit vector pointing from the source point \mathbf{y} to the observer location \mathbf{x} . $\mathcal{P}(\mathbf{y}, f)$ is the noise source strength at each FW-H panel on the integral surface, and thus can be used to indicate the noise source locations at different frequencies. The noise source strength converted to a log scale is therefore,

$$\mathcal{N}(\mathbf{y}, f) = 10 \log \left(\frac{\mathcal{P}^2(\mathbf{y}, f)}{p_{\text{ref}}^2} \right), \quad (5.8)$$

where p_{ref} is the reference pressure (20 μPa).

The plots of noise source strength $\mathcal{N}(\mathbf{y}, f)$ for far-field observers at the hub side is shown in Figure 5.27, which shows that the dominant noise sources are the wall pressure fluctuations on the hub and downstream of the hub cavity. For low frequencies at 20 Hz and 90 Hz, the rear part of the tyre is the major noise source. At the cavity depth modes at frequencies of 646 Hz and 1292 Hz, there is a triangular region that originates from the leading edge of the hub rim cavity. This triangular region has also been highlighted

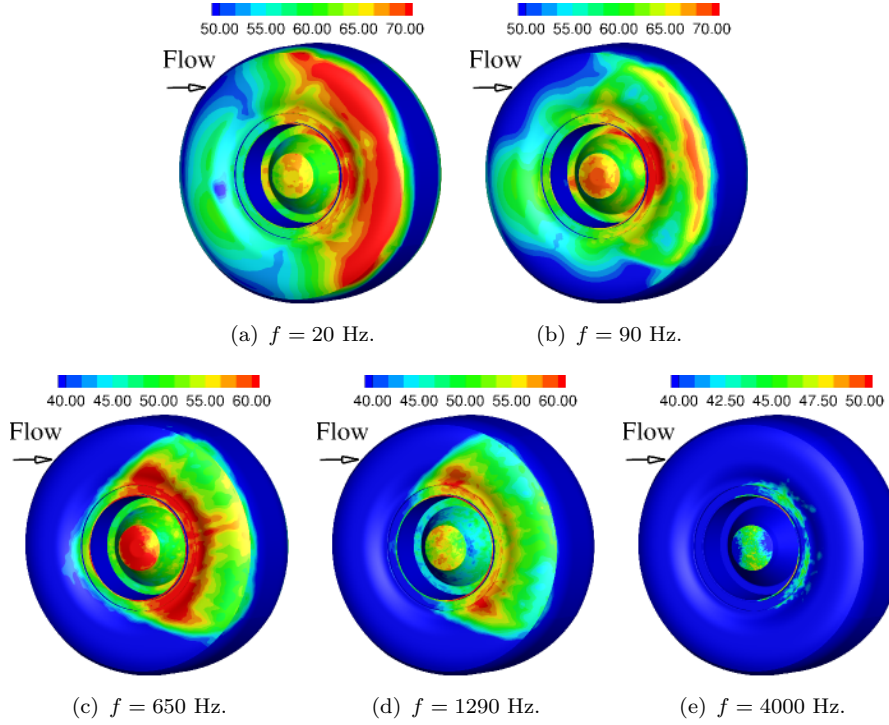


Figure 5.27: The noise source strength $\mathcal{N}(\mathbf{y}, f)$ for the far-field observer at the hub side ($\psi = 90^\circ$, $\phi = 180^\circ$).

in the plot of dynamic modes in Figures 5.16(c) and 5.16(d), which corresponds to the separation line in Figure 5.10 and the flow field in this region is highly turbulent. At a frequency of 4000 Hz in Figure 5.27(e), the dominant far-field noise is due to the pressure fluctuations around the hub and the downstream part of the hub rim cavity. Similar patterns of $\mathcal{N}(\mathbf{y}, f)$ for the sidewall side observer are shown in Figure 5.28. The pressure fluctuations on the surface of the sidewall are not shown to have strong effects on the far-field acoustics. For the ground side observer in Figure 5.29, the major noise sources are the tyre and the hub cavity region in the low and middle frequency ranges, respectively.

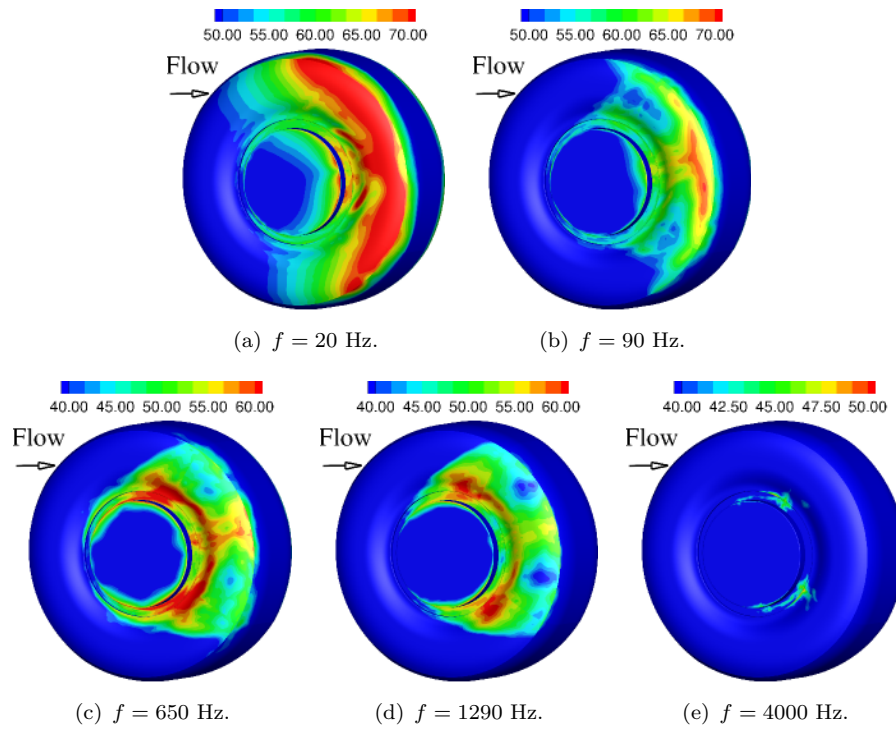


Figure 5.28: The noise source strength $\mathcal{N}(\mathbf{y}, f)$ for the far-field observer at the sidewall side ($\psi = 0^\circ$, $\phi = 180^\circ$).

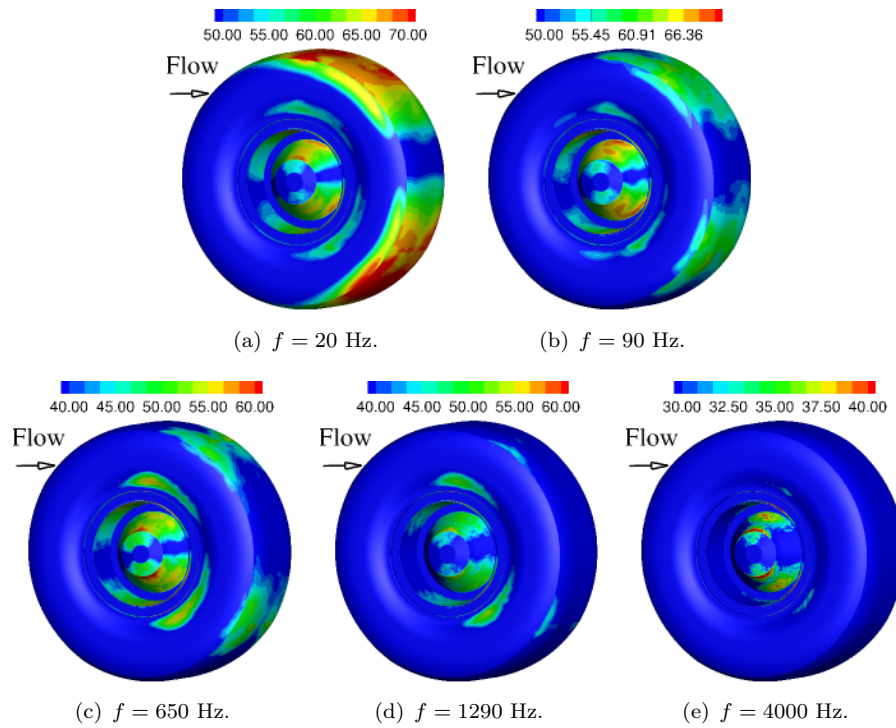


Figure 5.29: The noise source strength $\mathcal{N}(\mathbf{y}, f)$ for the far-field observer at the ground side ($\psi = 270^\circ$, $\phi = 180^\circ$).

5.4.3 Effects of covering hub and rim cavities

The effect of covering the hub cavity and rim cavities on the farfield acoustic spectra is shown in Figure 5.30 for three different observer angles. The different configurations are shown in Figure 5.2. The NHC configuration is with the hub cavity covered. The NHCRC configuration is with the hub and rim cavities covered. At low frequencies, the three different configurations have similar levels at all three observer locations. Therefore the low frequency noise is mainly due to the tyre and the presence of the hub and rim cavities have relatively little effect on this low frequency noise. This is consistent with the discussion on the auto PSD in Figure 5.24. For the hub side observer in Figure 5.30(a), there is a significant reduction of noise in the middle frequency range around the hub cavity depth modes when the hub cavity is covered (NHC). Again this shows that the mid frequency noise around the first and second cavity depth modes is generated by the hub cavity. The high frequency noise is significantly decreased when the rim cavities are additionally covered (NHCRC). The high frequency noise is dominated by the flow generated by the rim cavities.

For the far-field observer at the sidewall side in Figure 5.30(b), there are smaller differences between the baseline configuration and the configuration with the hub cavity covered (NHC) showing that the noise at the sidewall side is relatively less affected by the presence of the hub cavity. Covering both the hub cavity and the rim cavities (NHCRC configuration), results in a significant reduction in the high frequency noise. For the observer at the ground side in Figure 5.30(c), there is a reduction in the middle frequency range compared to the baseline and NHCRC cases. However, this reduction is not as significant as the hub side observer (Figure 5.30(a)), due to most of the hub cavity noise being radiating towards the hub side rather than the ground side. When the rim cavities are covered, a reduction of the high frequency noise at the ground side is also illustrated by the NHCRC configuration.

The OASPL for the three configurations are shown in Figure 5.31. Compared to the baseline configuration, when the hub cavity is covered (NHC configuration), a significant reduction of 6.4 dB is achieved at the hub side, most of which is from the middle frequency noise around the hub cavity depth modes, as shown in Figure 5.30(a). The far-field noise reductions achieved by covering the hub cavity at the sidewall side and ground side observers are less. The effect of the rim cavities on the far-field acoustics can be demonstrated by comparing the NHC case and the NHCRC case. This shows that most of the rim cavity noise is radiated towards the hub side and sidewall side observers. As shown in Figures 5.30(a), 5.30(b) and 5.30(c), most of the reductions by additionally covering the rim cavities (NHCRC configuration) are in the high frequency range. Compared with the baseline configuration, the NHCRC configuration shows reductions of 10.3 dB, 6.1 dB and 5.8 dB at the hub side, sidewall side and ground side observers respectively.

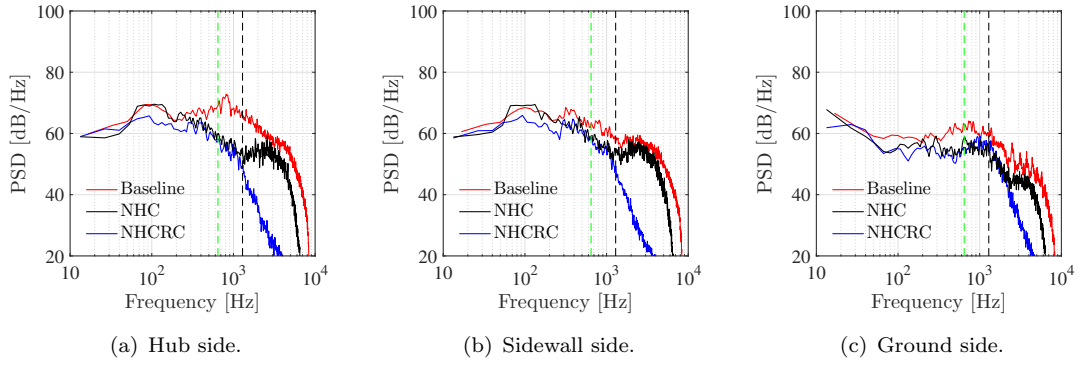


Figure 5.30: Far-field acoustic pressure spectra obtained from simulations of the baseline configuration, No Hub Cavity (NHC) configuration and No Hub Cavity and Rim Cavities (NHCRC) configuration. --- first depth mode (646 Hz), --- second depth mode (1292 Hz).

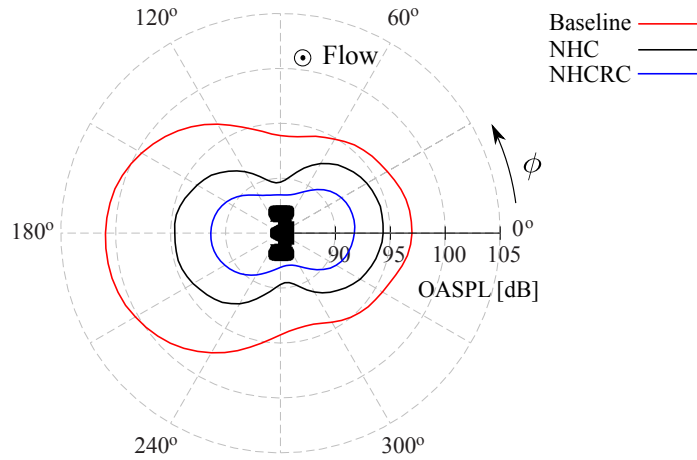


Figure 5.31: Comparisons of the far-field acoustic directivity obtained from different configurations.

5.4.4 Section summary

The numerical results of the far-field acoustics generated by the baseline geometry at $M = 0.23$ are firstly validated against the experimental measurements at different observer positions in the most reliable frequency range ($f > 300$ Hz), and demonstrate good agreements. The deviation of the directivity is within 2 dB.

The analysis of far-field acoustic pressure spectra of the baseline configuration shows that a significant noise source is present in the middle frequency range around 646 Hz and 1292 Hz both in the experiment and in the simulations, related to the first and the second depth modes of the hub cavity geometry. This middle frequency noise is fixed by the cylindrical hub cavity dimensions and does not scale with flow velocities. Higher coherence between the hub side far-field acoustics and the wall pressure fluctuations around the hub cavity region is demonstrated at the two depth mode frequencies. The acoustic predictions using different parts of the wheel surface show that the tyre is the

main low frequency noise source. A lift and a side force dipole are present at $f = 20$ Hz and $f = 90$ Hz, which are also demonstrated by the analysis of far-field acoustic directivity at different frequencies. The flow interaction noise between the tyre and the hub cavity is demonstrated to be at the depth modes and at $0.2 < St_W < 0.6$ by the analysis of CPSD. The directivity of OASPL shows that more noise is radiated towards the hub side observer. Most of the contribution to the OASPL comes from the hub cavity noise in the middle frequency range. The noise source strength function, which is obtained from the FW-H equation in the frequency domain, shows the hub cavity area is the dominant noise source in the middle frequency range.

The configurations with the hub cavity covered (NHC) and with both the hub cavity and rim cavities covered (NHCRC) show that the tyre, hub cavity and rim cavities are the main noise sources in the low, middle and high frequency ranges, respectively. When the hub cavity and rim cavities are covered, reductions of 10.3 dB, 6.1 dB and 5.8 dB in the far-field acoustic OASPL are achieved at the hub side, sidewall side and ground side observers respectively.

5.5 Chapter summary

In this chapter, high-order CAA simulations were performed to investigate the flow features and far-field acoustics of three different landing gear wheel configurations at two Mach numbers ($M = 0.118$ and $M = 0.23$) with two mesh resolutions to isolate the effects of a hub cavity and rim cavities on landing gear wheel noise. The baseline configuration is the same with the geometry used in the experimental work by Zhang *et al.* [41], which is a high-fidelity isolated landing gear wheel model containing a tyre, a hub cavity, a sidewall and two rim cavities. The two additional simulations are conducted with the hub cavity covered (NHC), and both the hub cavity and rim cavities covered (NHCRC).

The aerodynamic and acoustic results are well validated against the experimental measurements at $M = 0.118$ and $M = 0.23$, respectively. The finer mesh demonstrates better agreements of the mean pressure coefficient C_p along the centreline of the wheel and the unsteady surface pressure spectra on the hub, compared to the coarse grid. The deviations of the far-field acoustic pressure PSD and the directivity of SPL are within 3 dB/Hz and 2 dB with the experiments. The key findings of the numerical simulations are summarised as:

1. Reductions of the flow complexity

The surface flow topology is visualised by the shear stress lines, which shows that there are separations and attachments in the baseline and the configuration with the hub cavity covered (NHC), whereas the flow is fully attached to the side face for the

configuration when both the hub cavity and rim cavities are covered (NHCRC). As a result, the R.M.S. of the force coefficients shows a decrease by the NHCRC case, and most comes from the high frequency range ($f > 2000$ Hz). The fully attached flow on the side face for the NHCRC case also provides a 20% reduction in the total drag, which is higher than the 7% by just covering the hub cavity (NHC).

2. Asymmetry of the mean flow

The mean flow around the wheel is asymmetric, which is demonstrated by the non-zero \bar{C}_L , the shear stress lines on the rearward face and the mean streamlines in the wake. This asymmetry is observed in all the three configurations. The NHCRC geometry is essentially a short circular cylinder, and the asymmetry in this configuration indicates that the asymmetric state is more stable for short cylinders than the symmetric state observed in long spanwise length cylinders, which is consistent with the experimental work by Zdravkovich *et al.* [13] who demonstrated a bistable asymmetric flow pattern for circular cylinder flows at $W/D < 3$ and it can be biased to either side.

The hub cavity is also a significant contributor to the mean flow asymmetry, which is confirmed by the reduction in \bar{C}_L when covering the hub cavity (NHC). The depth-to-diameter ratio for the hub cavity is 0.3, and the mean flow demonstrates an asymmetric feature at this ratio in the numerical simulations of a flat plate mounted cylindrical cavity in Appendix G.

There are four large vortices in the wake shown by the shear stress lines and the vorticity magnitude on different downstream planes. This distinguishes the wheel geometry from long spanwise circular cylinders where the wake is dominated by two large vortices. The four vortices are formed at the rear edge of the shoulder, and one pair of the vortices on the wing side dominates the other pair on the ground side. As a result, the mean streamlines in the wake shift downwards, thereby leading to a non-zero mean lift coefficient \bar{C}_L .

3. Hub cavity depth modes

The hub cavity acoustics are characterised by its resonance, and the resonance is evidenced firstly by the fact that the far-field noise in the middle frequency range is fixed by the cavity dimensions, and the noise does not scale with flow velocity. This middle frequency range corresponds to the first ($f = 646$ Hz) and second ($f = 1292$ Hz) hub cavity depth modes. Secondly, two weak spectral peaks in the acoustic pressure spectrum are demonstrated close to these two frequencies in the experiments and numerical simulations. Thirdly, the middle frequency noise around these two frequencies radiates more to the hub side than the sidewall side. Fourthly, the dynamic modes, coherence analysis and noise source map all highlight the hub cavity region at $f = 646$ Hz and $f = 1292$ Hz. Fifthly, reductions in this middle frequency noise are obtained with the hub cavity covered (NHC). Therefore, the depth modes are the driving mechanisms for the hub cavity noise, and the hub cavity is also the

most significant middle frequency noise source for the CADWIE wheel. However, this shallow hub cavity noise is characterised by a broadband spectrum, different from the tonal noise by the deep cylindrical cavities. As shown in Appendix G, the interaction between the depth modes and the shear layer at the cavity opening tends to be weaker at small depth-to-diameter ratios.

4. Noise source locations and far-field acoustic directivities

The noise sources are determined firstly by applying the FW-H equation on the surface pressures in the frequency domain, and secondly by comparing the acoustic predictions from different geometry configurations. The far-field acoustic directivities at different frequencies are analysed by using the surface pressure information on each individual and total FW-H components.

The tyre is the dominant low frequency ($f < 400$ Hz) noise source due to the large-scale flow structures shedding from the wheel, and the tyre demonstrates a lift dipole directivity and a side force directivity at $f = 20$ Hz and $f = 90$ Hz, respectively. These two dipole patterns are also highlighted by the dynamic modes. This low frequency noise is less affected by the hub cavity and two rim cavities.

The hub cavity sound dominates the middle frequency ($400 \text{ Hz} < f < 2000 \text{ Hz}$) noise, which is generated by the flow interactions with the hub cavity depth modes. A source region with a triangular shape, corresponding to the surface flow separation lines, is demonstrated by the dynamic mode decomposition technique and the noise source localisation method. This middle frequency noise is mainly radiating towards the far-field positions at the hub side in the upstream direction.

There are two rim cavities on opposite sides. The small-scale pressure fluctuations on the surface of these two rim cavities are identified to generate high frequency ($f > 2000$ Hz) noise, which shows a dipole pattern in the side directions.

The directivity of OASPL of the whole CADWIE wheel noise shows that more sound is radiated towards the hub cavity side. The ground side is the least efficient sound radiation direction.

5. Reductions of the far-field acoustics

Compared with the baseline configuration, reductions of 10.3 dB, 6.1 dB and 5.8 dB in the far-field acoustic OASPL are achieved at the hub side, sidewall side and ground side, respectively, in the NHCRC case. These reductions are mainly from the middle frequency noise from the hub cavity and the high frequency noise from the rim cavities.

Covering the hub cavity and rim cavities is an effective approach to reduce both the aerodynamic drag and the far-field noise.

Chapter 6

Landing Gear Wheels in Tandem

6.1 Introduction

For wheels in a tandem configuration, flow interactions can occur, and they are significant noise sources for four-wheel and six-wheel landing gear configurations [4]. However, the acoustics of tandem landing gear wheels, especially with realistic wheel geometries, have not been investigated individually in the literature. In this chapter, the interaction noise between two wheels in tandem at a separation distance of $L = 1.5D$ will be studied. These two wheels have a detailed geometry, which is the same as the one used in the previous isolated wheel case. This chapter focuses on the following questions:

1. What are the aerodynamic and acoustic characteristics of flow interactions between two wheels in tandem?
2. What are the effects of the downstream wheel hub and rim cavities on far-field acoustics?
3. How much noise reduction can be achieved by applying a gap fairing to reduce flow interactions?
4. What are the effects of angle of attack on the near-field flow features and the far-field acoustics?

This chapter is structured in the following manner. The computational setup is firstly provided in Section 6.2. Then, the aerodynamic and acoustic results at zero angle of attack are detailed in Sections 6.3 and 6.4, including the effects of covering the downstream hub and rim cavities and the effects of a gap fairing. The aerodynamic and acoustic comparisons at different angles of attack are given in Section 6.5. Section 6.6 finally summarises the key findings in this chapter.

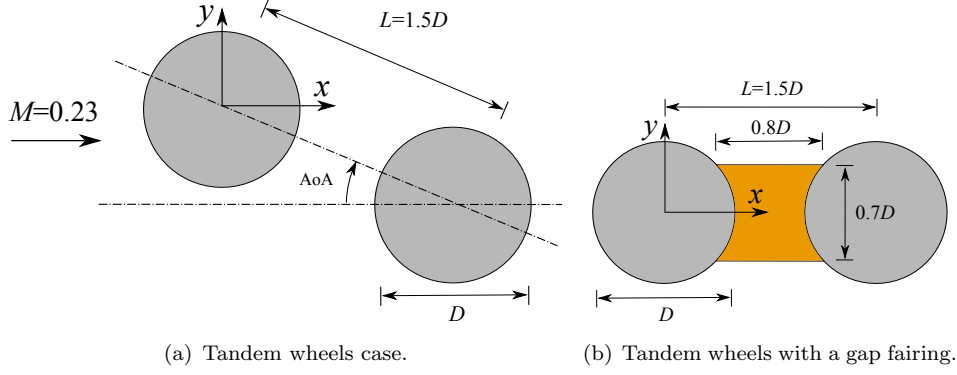


Figure 6.1: The numerical setup of the tandem wheels.

6.2 Computational setup

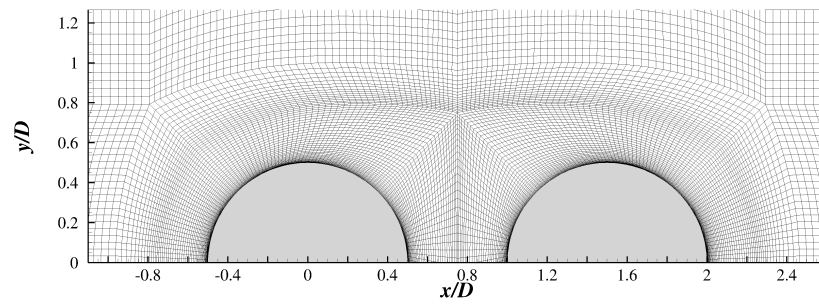
Two landing gear wheels are set in tandem with a separation distance of $L = 1.5D$, and the setup is shown in Figure 6.1(a), where the origin of the axes is at the centre of the upstream wheel. This tandem wheels configuration represents half of a simplified four-wheel landing gear geometry. A gap fairing is simulated to control the wheel interaction noise. Figure 6.1(b) shows the setup of this gap fairing, the height and the width of which are $0.7D$ and $0.8D$, respectively. In practice, the fairing is not connected to the wheel directly, and there should be a gap between the fairing and the wheels. However, the size of this gap is much smaller than the wheel diameter D . Thus, this gap should not have large effects on the main flow features around the two wheels and this fairing, since the large-scale flow structures are less affected by the small geometrical features. The geometrical complexity is reduced in the simulation by assuming that the gap fairing is solidly connected with wheels. The far-field acoustic observer locations are the same with the previous isolated single landing gear wheel case, and they are defined in Figure 5.18, with respect to the upstream wheel centre.

Seven simulations have been performed, and they are summarised in Table 6.1. For all seven cases, the geometry of the Upstream Wheel (UW) is the baseline CADWIE wheel configuration in Figure 5.2(a), which contains a hub cavity and two rim cavities. This baseline CADWIE configuration is also the default geometry for the Downstream Wheel (DW). However, two more geometries (NHC in Figure 5.2(b) and NHCRC in Figure 5.2(c)) are additionally tested to isolate the effects of hub cavity and rim cavities on the downstream wheel noise. The wheel interaction noise is investigated at four different angles of attack (AoA), i.e. 0° , 10° , 20° and 30° , and the angle of attack is defined in Figure 6.1(a). It should be emphasised that the angle of attack in the tandem wheels configuration is caused by the bogie angle of the landing gear and not the aircraft angle of attack. The gap fairing is only applied in the control case (see Table 6.1) at $\text{AoA} = 0^\circ$.

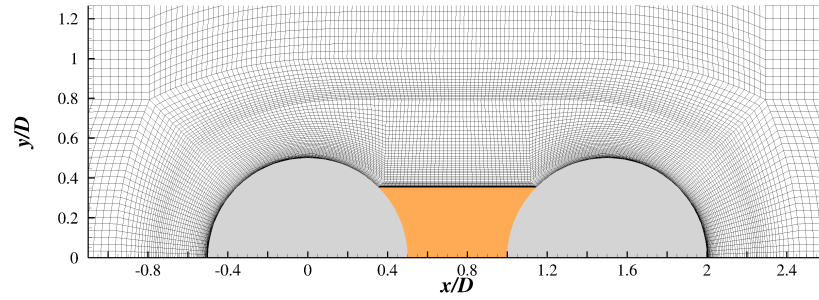
The grids around the upstream and downstream wheels are the same as the fine-resolution mesh employed in the isolated landing gear wheel simulations in Chapter

Case	AoA	UW geometry	DW geometry	Gap fairing
Baseline	0°	Baseline	Baseline	×
	10°	Baseline	Baseline	×
	20°	Baseline	Baseline	×
	30°	Baseline	Baseline	×
NHC	0°	Baseline	NHC	×
NHCRC	0°	Baseline	NHCRC	×
Control	0°	Baseline	Baseline	✓

Table 6.1: Summary of seven cases in the simulations, where UW and DW represent the upstream wheel and downstream wheel, respectively.



(a) Tandem wheels case.



(b) Tandem wheels with a gap fairing.

Figure 6.2: The grid distributions around the tandem wheels.

5. The grid distributions between the tandem wheels are provided in Figure 6.2. All the simulations are conducted at $M = 0.23$. The computational domain size, boundary conditions and numerical parameters are the same as the previous isolated landing gear wheel simulations.

6.3 Aerodynamic results at zero angle of attack

6.3.1 Instantaneous flow field

The instantaneous Q -criterion is shown in Figure 6.3. The turbulent structures around the upstream wheel in Figure 6.3(a) are similar to the previous isolated single wheel simulation in Figure 5.7(a), particularly in the hub cavity region, which indicates that the upstream wheel noise is similar to the isolated single wheel case in the middle and high frequency ranges. The gap region is dominated by large-scale features that are due to flow separations from the upstream wheel. The wake of the upstream wheel then impinges on the downstream wheel. The front face of the downstream wheel is shown in Figure 6.3(a) to be surrounded by large-scale flow fluctuations. Since the flow field around the downstream wheel contains more large-scale turbulent structures, the downstream wheel is expected to be the dominant noise source, which should be characterised by low frequency interaction noise. The effect of a gap fairing on the change of near-field flow fluctuations is shown in Figure 6.3(b), where the large-scale structures in the gap region are eliminated. The low frequency interaction noise will be shown in Section 6.4.3 to be significantly reduced by the addition of this gap fairing.

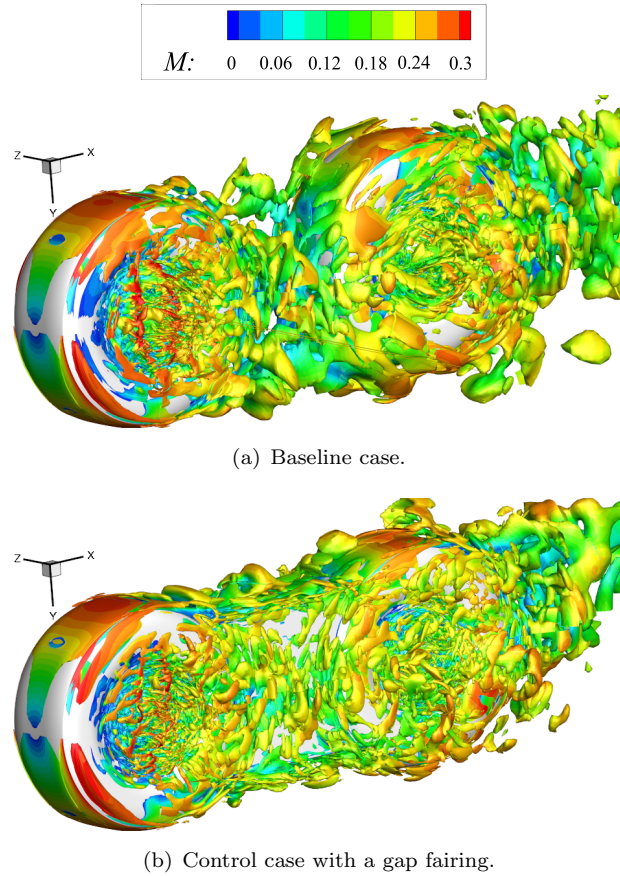


Figure 6.3: Instantaneous iso-contour of $Q = 10 \times U_\infty^2 / D^2$ colored by the Mach number.

6.3.2 Forces

Three force coefficients (C_L , C_D and C_S) of the baseline case and the control case with a gap fairing, together with the isolated single wheel case, are provided in Table 6.2.

Case		$ \bar{C}_L $	\bar{C}_D	\bar{C}_S	C_L^{rms}	C_D^{rms}	C_S^{rms}
Isolated Single Wheel		0.022	0.237	0.019	0.030	0.010	0.019
Baseline	UW	0.219	0.217	0.024	0.017	0.020	0.038
	DW	0.018	0.426	0.013	0.033	0.038	0.075
	Total	0.201	0.643	0.037	0.035	0.036	0.082
Control		0.121	0.315	0.049	0.032	0.016	0.036

Table 6.2: Summary of force coefficients from the isolated Single Wheel (SW) case, the Upstream Wheel (UW) and Downstream Wheel (DW) of the tandem wheels baseline case, and the control case with a gap fairing applied.

Firstly, the mean lift coefficient $|\bar{C}_L|$ is significantly larger for the tandem wheels case (0.201), compared with the isolated single wheel geometry (0.022), suggesting a highly asymmetric mean flow in the tandem wheels configuration. Though the mean lift coefficient becomes smaller after the application of a gap fairing in the control case, it is still significantly non-zero.

Secondly, the mean drag coefficient \bar{C}_D of the upstream wheel (0.217) is slightly smaller than the isolated single wheel (0.237). The downstream wheel has a major contribution of 66% to the total drag (0.643), due to it being in the wake of the upstream wheel. This total drag is reduced by 50% with the application of a gap fairing, since the flow impingement on the front face of the downstream wheel is avoided.

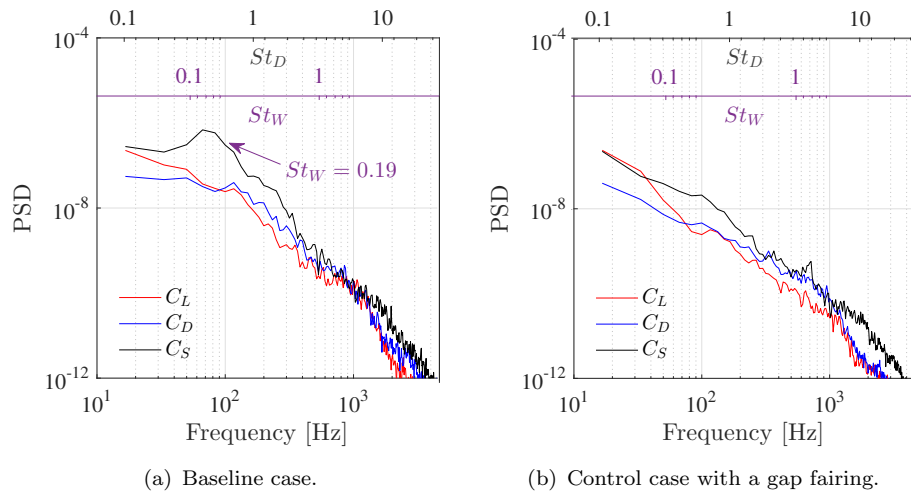


Figure 6.4: PSD of the force coefficients in the baseline and control cases.

Thirdly, the R.M.S. of the three force coefficients of the downstream wheel are higher than the upstream wheel. For both wheels, the fluctuating side force dominates the fluctuating lift and drag forces, which is different from the isolated single wheel case,

where the lift force R.M.S. (C_L^{rms}) is the largest. The fluctuating side force is an indication of the shear layer flapping in the side direction. This will be demonstrated in the next Section. Compared to the isolated single wheel case, the higher fluctuation in the side force coefficient in the tandem wheels case is caused by flow interactions, suggesting that the dominant interactions are in the side direction. Figure 6.4 shows the PSD of the force coefficients. In the baseline case, a peak is illustrated only by the side force at $St_W = 0.19$, and this peak is eliminated with a gap fairing applied. The R.M.S. and PSD of the force coefficients show that the flow interactions are mainly in the side direction at a non-dimensional frequency of $St_W = 0.19$. In the control case using a gap fairing, the fluctuating side force demonstrates the largest reduction among the three force coefficients R.M.S., and the fluctuating lift force (0.032) is comparable with the fluctuating side force (0.036).

6.3.3 Steady and unsteady statistics

Mean and R.M.S. pressure coefficients

The mean and R.M.S. pressure coefficients on the wheel centreline are compared to the experimental measurements by Spagnolo *et al.* [122] in Figures 6.5 and 6.6, respectively. It should be mentioned that no experimental data, with the same wheel geometry and flow conditions as the current simulations, are available. The experiment by Spagnolo *et al.* [122] was performed at $Re = 5 \times 10^5$, and their measurements presented in the comparisons are with the upstream wheel boundary layer tripped with zigzag tape to reproduce a higher Reynolds number condition. The current simulation simulates a fully turbulent boundary layer at $Re = 2.6 \times 10^6$. The wheel geometry used by Spagnolo *et al.* [122] is a simplified wheel without hub and rim cavities. As discussed in the isolated wheel case, the hub cavity and rim cavities have minor effects on the large-scale structures around the wheel, and those large scales dominate the R.M.S. of surface pressure fluctuations. Additionally, the hub and rim cavities are located at the side of the wheel. On the wheel centreline, the flow is less effected by the presence of hub and rim cavities. Thus, the distributions of C_p and C_p^{rms} on the wheel centreline in the current wheel configuration can be expected to be similar to the experimental measurements by Spagnolo *et al.* [122], which are used to validate the simulation results.

In Figure 6.5, the mean pressure coefficient (C_p) distributions, obtained from three different geometry configurations, show good agreements with the experimental data. A significant asymmetry is demonstrated in both the numerical and the experimental results. The stagnation point on the downstream wheel is at $\theta = 335^\circ$. This asymmetry accounts for a highly non-zero mean lift coefficient in Table 6.2. In the numerical predictions, there are two separation bubbles along the upstream wheel surface and two separation bubbles on the downstream wheel surface. These four separation bubbles are better demonstrated in Figure 6.7(a). The downstream wheel separation bubble at

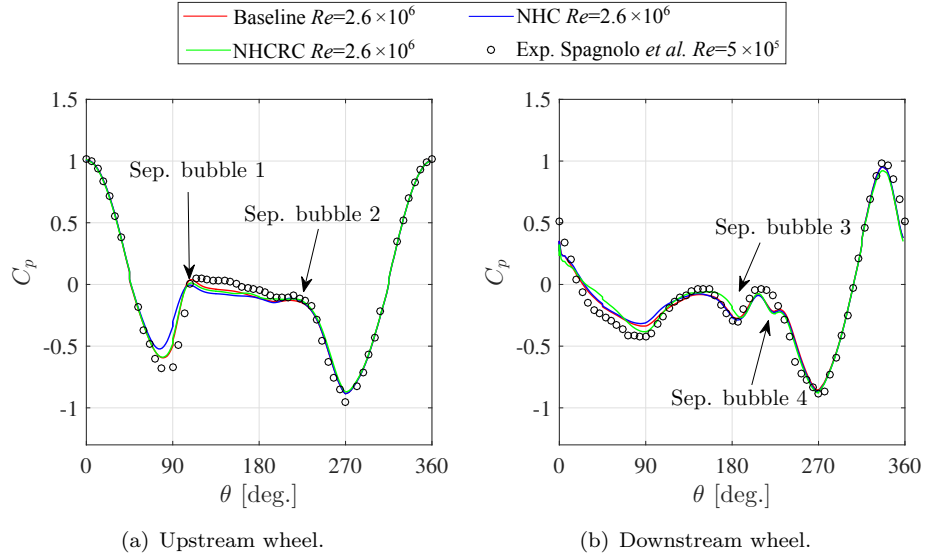


Figure 6.5: Mean pressure coefficient C_p on the central plane ($z/D = 0$) of the upstream and downstream wheels.

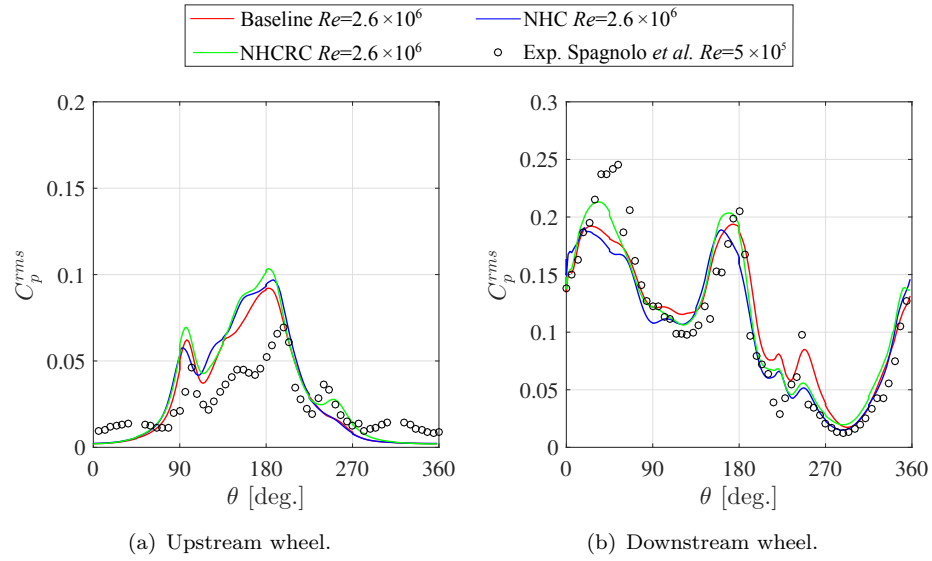


Figure 6.6: Pressure coefficient R.M.S. C_p^{rms} on the central plane ($z/D = 0$) of the upstream and downstream wheels.

$\theta = 225^\circ$ in Figure 6.5(b) was not observed in the experimental measurements. The numerical predictions of C_p^{rms} are provided in Figure 6.6, and they are relatively less comparable than C_p with the experiments. The discrepancies are most likely due to the difference in Reynolds number. However, reasonable agreements in the levels and distribution patterns of C_p^{rms} are achieved in the simulations.

Flow structures and coherence in the gap region

Figure 6.7 plots the mean z -vorticity and x -vorticity, together with the streamlines, on the $z/D = 0$ plane and $x/D = 0.75$ plane (the central plane in the gap region),

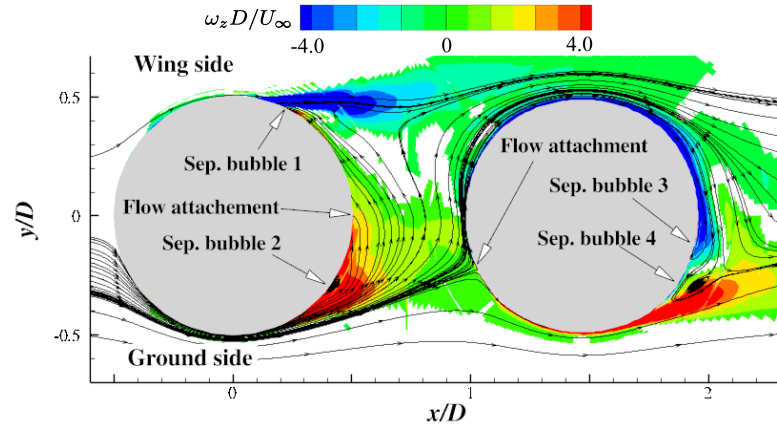
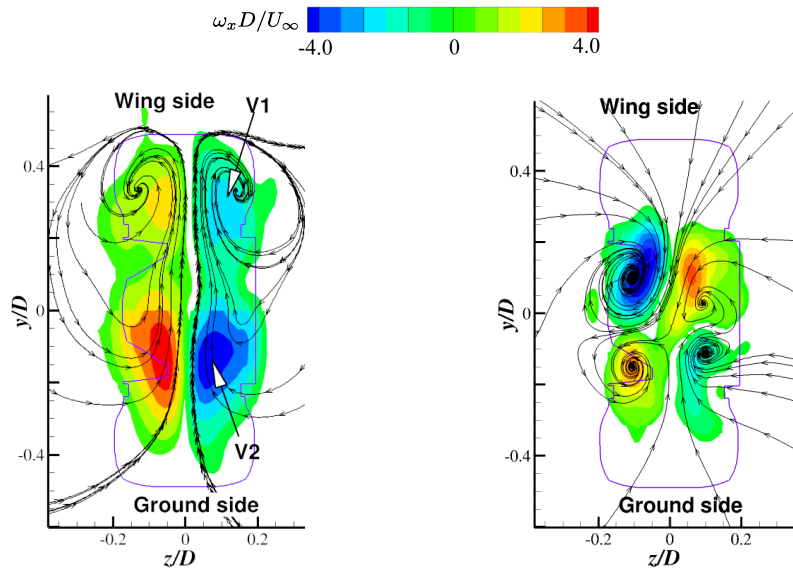
(a) $z/D = 0$, tandem wheels case.(b) $x/D = 0.75$, tandem wheels case.(c) $x/D = 0.75$, isolated single wheel case.

Figure 6.7: The vorticity and streamlines of mean flow in the gap region, in comparison with the isolated single wheel case.

respectively. For the tandem wheels case on the $z/D = 0$ plane (Figure 6.7(a)), four separation bubbles are highlighted, as indicated by the C_p profiles in Figure 6.5. The mean streamlines show that the flow around the upstream wheel first separates at $\theta = 230^\circ$, forming a separation bubble, and then reattaches to the surface until $\theta = 110^\circ$, where the boundary layer separates again and a shear layer is developed at the wing side. The separated flow from the lower surface of the upstream wheel directly impinges on the downstream wheel surface at $\theta = 335^\circ$. Then, the flow bifurcates to the upward and downward directions along the downstream wheel surface. The upward flow is merged with the shear layer from the upper surface of the upstream wheel at the wing side. The mean flow field displayed in Figure 6.7(a) is highly asymmetric.

The comparison of x -vorticity in the tandem wheels case and the isolated single wheel

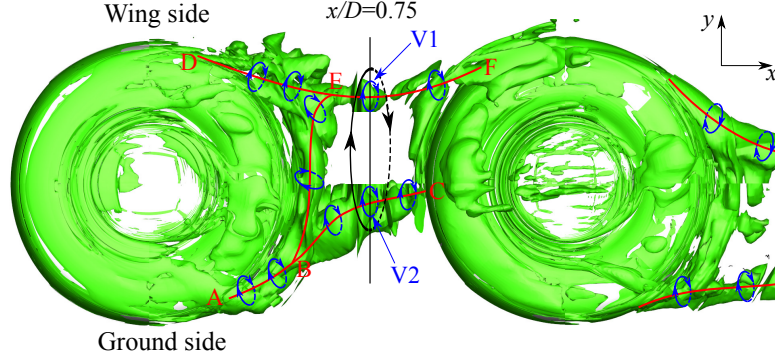


Figure 6.8: The vortex structure visualised by λ_2 criterion.

case is given in Figures 6.7(b) and 6.7(c). For the tandem wheels case, the flow is deflected towards the wing side, and forms two large vortices with vortex core at $y/D = 0.35$. However, the isolated single wheel case shows a four-vortex structure in Figure 6.7(c), one pair on the wing side and one pair on the ground side. The two-vortex structure in Figure 6.7(b) is induced by the asymmetry of the flow stagnation point on the downstream wheel surface. The stagnation point shifts towards the ground side by $\Delta\theta = 25^\circ$, allowing more flow at the ground side to deflect into the gap region. Therefore, the development of vortices on the wing side is enhanced, and a two-vortex structure is finally formed. Similar flow patterns have also been found in the experiment by Lazos [27], as reviewed in Figure 2.5 in Section 2.3.1. In this experiment, the separated flow from the upstream wheel at the ground side and wing side reattached on the downstream wheel surface at two asymmetric positions, and a large vortex was formed at the ground side. In the tandem wheels cases performed at $\text{AoA} = 10^\circ, 20^\circ$ and 30° , the two-vortex mode also occurs in the simulations, suggesting that this state is more persistent for the tandem wheels configuration, compared to a four-vortex mode in the single wheel case.

The vortex structures in the gap are visualised by using the λ_2 criterion, and the detailed flow topology is shown in Figure 6.8. Firstly, the flow around the upstream wheel separates at A and D, and forms two vortex tubes convecting downstream. The ground side vortex tube is divided into bipartite branches at B. One branch ends at C on the downstream wheel surface, close to the stagnation point shown in Figure 6.7(a). The second branch moves upwards and joins the wing side vortex tube at E, and this combined vortex structure finally terminates at F. The vortex at the ground side (V2) has the same rotation direction with the wing side vortex (V1). V1 and V2 are merged together to form one large vortex (highlighted in black) in the gap ($x/D = 0.75$), and this large vortex is also demonstrated in Figure 6.7(b). For the isolated wheel case in Figure 6.7(c), the wing side vortex and ground side vortex are, however, counter-rotating, demonstrating a pair of vorticity of opposite sign. This leads to a four-vortex mode for the isolated single wheel case. The vortex structures at other three angles of attack are provided in Appendix H, and they also show a two-vortex mode in the gap region.

The instantaneous streamwise velocity in the gap region on the $y/D = 0$ plane is shown in Figure 6.9. The separated shear layers from the upstream wheel form two large vortices, dominating the gap. P1 and P2 are two surface pressure monitors at the leading edges of the downstream wheel tyre where the shear layers directly impinge. Figure 6.10 shows the coherence of surface pressures at these two monitors. The coherence is noisier in the middle and high frequency ranges, due to the limited length of signal recorded in the numerical simulation. A stronger coherence occurs at $St_W = 0.19$. The phase difference between the two surface pressures at $St_W = 0.19$, which was computed by applying the Fourier transform to each signal separately, is 173° , close to 180° . This indicates that the shear layers impinge at the two downstream wheel leading edges alternatively at a shear layer flapping frequency of $St_W = 0.19$, which will also be shown by the following dynamic mode decomposition analysis.

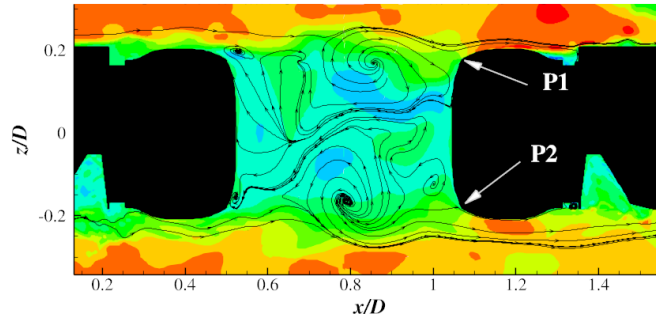


Figure 6.9: The instantaneous streamwise velocity in the range of $-0.15 < u/c < 0.3$, and the streamlines, on the $y/D = 0$ plane. P1 and P2 are two surface pressure monitors at the leading edge of the downstream wheel shoulder.

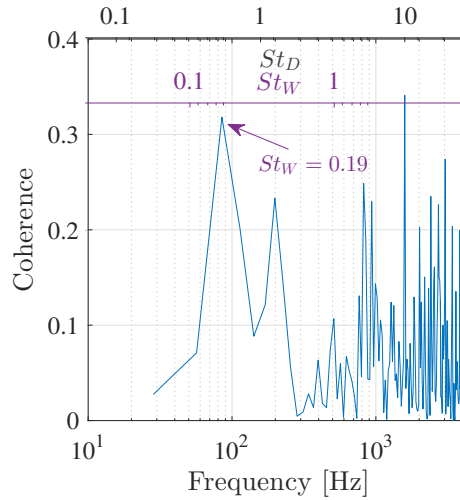


Figure 6.10: The coherence between surface pressures monitored at two points (P1 and P2) at the leading edge of the downstream wheel in Figure 6.9.

Dynamic mode decomposition

The Dynamic Mode Decomposition (DMD) method, which is introduced in Section 3.11, is performed on the surface pressures. The number of snapshots is $N = 512$ with a fixed interval of $\Delta t = 1.175 \times 10^{-4}$ s (the corresponding sampling frequency is $f = 8500$ Hz).

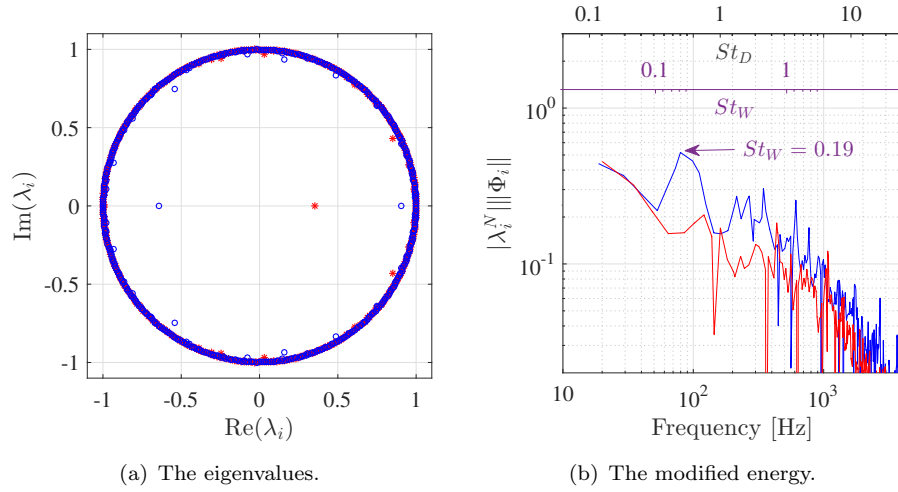


Figure 6.11: The eigenvalues and modified energy of the dynamic modes for the tandem wheels case, where the blue and the red symbols represent the baseline case and control case, respectively. The number of snapshots is $N = 512$.

Figure 6.11 shows the distribution of the dynamic modes' eigenvalues λ_i and the modified energy $||\lambda_i^N|| ||\Phi_i||$ plotted as a function of frequency, for the surface pressures. In Figure 6.11(a), for both the baseline case and the control case with a gap fairing, most of the dynamic modes are located at the unit circle, which is typical for flows at high Reynolds number [123]. The spectral profile in the modified energy peaks at $St_W = 0.19$ for the baseline case in Figure 6.11(b), indicating the presence of a highly energetic dynamic

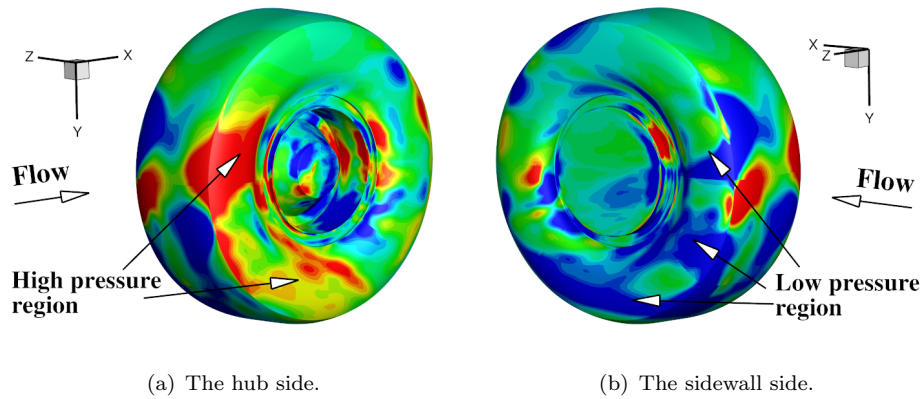


Figure 6.12: The instantaneous dynamic mode of the surface pressure on the downstream wheel at $St_W = 0.19$ for the baseline case, where the scale range is $-0.008 < p/\rho_\infty c_\infty^2 < 0.008$ and only the real part of the dynamic mode is plotted.

mode. However, after the application of the gap fairing, this spectral peak is eliminated. This is also consistent with the spectral plots of the side force coefficient C_S in Figure 6.4. The instantaneous dynamic mode of the surface pressures on the downstream wheel in the baseline configuration at $St_W = 0.19$ is provided in Figure 6.12. It shows that the tyre surface at the hub side (Figure 6.12(a)) is generally dominated by high pressures, whereas low pressures are distributed on the tyre surface at the sidewall side (Figure 6.12(b)), demonstrating a side force dipole pattern. This side force dipole is also illustrated by the dynamic mode at $St_W = 0.19$ at other instantaneous time steps (which are not presented). Figures 6.11 and 6.12 show that the flow interactions cause a side force dipole mode for the downstream wheel surface pressures, and this side force dipole pattern is generated by the alternative impingements of shear layers from the upstream wheel on the two side faces of the downstream wheel.

6.3.4 Section summary

This section has shown the aerodynamic results of two wheels in a tandem configuration at zero angle of attack. Four configurations have been tested in the simulations, and they are the baseline case, no hub cavity (NHC) case, no hub cavity and rim cavities (NHCRC) case and control case with a gap fairing. It should be noted that the geometry changes made to the hub and rim cavities are only applied to the downstream wheel.

For the mean flow features, good agreements are obtained for the pressure coefficients along the wheel centreline. The downstream wheel demonstrates a larger drag coefficient, due to the fact that it is fully located in the wake of the upstream wheel. The mean flow field of the uncontrolled case is highly asymmetric, with the stagnation point of the downstream wheel deflected towards the ground side by $\Delta\theta = 25^\circ$. This asymmetry forces more flow to go into the gap region towards the wing side, enhancing the development of vortices at the wing side. As a result, the gap region is characterised by a two-vortex mode, different from the four-vortex state presented in the isolated single wheel case. The flow asymmetry also leads to a highly non-zero mean lift coefficient. After the application of a gap fairing in the control case, the large-scale flow structures in the wake are eliminated, and the flow interactions are reduced. A 50% reduction in the total drag coefficient is achieved in the control case.

For the unsteady flow results, reasonable agreements with experiments in the surface pressure R.M.S. along the wheel centreline are demonstrated. The lift, drag and side force coefficients R.M.S. from the downstream wheel are larger than the upstream wheel. The side force coefficient R.M.S. dominates the other two directions, with a spectral peak shown at $St_W = 0.19$. This spectral peak does not occur in the other two force coefficients. This indicates a side force dipole pattern induced by the flow separations from the two side faces of the upstream wheel and alternative flow impingements on the two side faces of the downstream wheel, which is also shown by the plot of the

dynamic mode at $St_W = 0.19$. In the control case with a gap fairing, due to the reduced flow interactions by covering the gap region, all the three force coefficients R.M.S. are decreased, and the largest reduction is in the side force coefficient. The spectral peak at $St_W = 0.19$ in the dynamic mode analysis is also eliminated in the gap control case.

From the mean and unsteady flow analysis, it can be concluded that the flow interactions are mainly in the side directions, and in the large-scale range. This will generate low frequency interaction noise radiating towards the two side directions.

6.4 Acoustic results at zero angle of attack

6.4.1 Acoustics of the baseline geometry

Far-field acoustics

The far-field acoustic observer locations are the same with the previous isolated single landing gear wheel case, and they are defined in Figure 5.18, with respect to the upstream wheel centre. The far-field acoustics from the upstream wheel and downstream wheel at three observer positions (hub side, sidewall side and ground side) are compared to the isolated single wheel case in Figure 6.13. Firstly, by comparing the upstream wheel noise with the single wheel noise at the hub side (Figure 6.13(a)), the middle frequency and high frequency spectral levels are shown to be comparable. This is due to the fact that the middle frequency and high frequency upstream wheel noise is mainly generated by the hub and rim cavities, where the flow field is less affected by the presence of the downstream wheel, as shown in Figure 6.3(a). The difference between the upstream wheel noise and the single wheel noise is mostly in the low frequency range. This low frequency difference is caused by the large-scale flow interactions. This difference is larger at the hub side (Figure 6.13(a)) and sidewall side (Figure 6.13(b)) and is relatively smaller at the ground side (Figure 6.13(c)), which indicates that the interaction noise has a favourable side radiation direction. This also implies that the near-field flow interactions are mainly on the $y/D = 0$ plane, due to the alternative shear layer impingements on the downstream wheel two side faces at a shear layer flapping frequency based on the width of the wheel W . A small spectral hump is shown at $St_W = 0.21$ in the isolated single wheel case at the hub side (Figure 6.13(a)) and sidewall side (Figure 6.13(b)), presenting a side force dipole pattern. This hump becomes more prominent and moves to $St_W = 0.19$ for the tandem wheels case. This movement is most likely due to the flow interactions between the two wheels. It has been reviewed in Section 2.2.2 that, in the tandem circular cylinders case, the downstream cylinder can act as a splitter plate, which can reduce the vortex shedding frequency compared to a single circular cylinder flow [20].

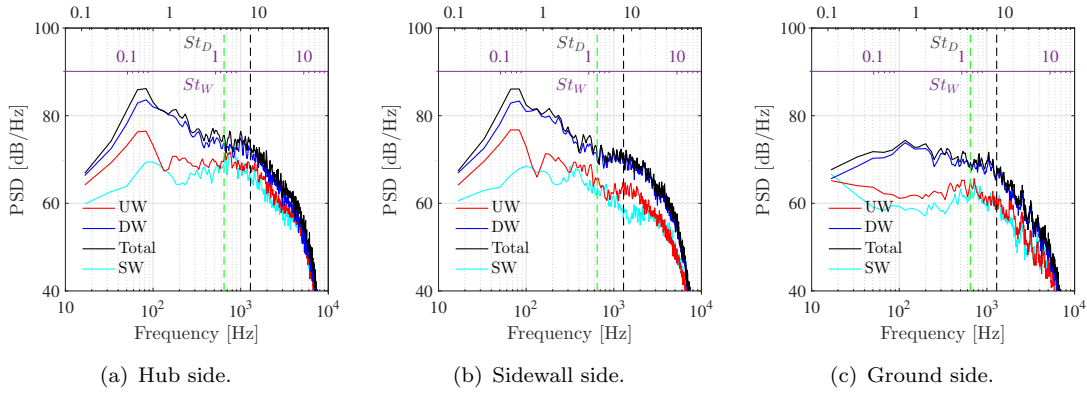


Figure 6.13: Far-field acoustics from the Upstream Wheel (UW), Downstream Wheel (DW) and both wheels (Total), in comparison with the isolated Single Wheel (SW) case. --- first depth mode (646 Hz), --- second depth mode (1292 Hz).

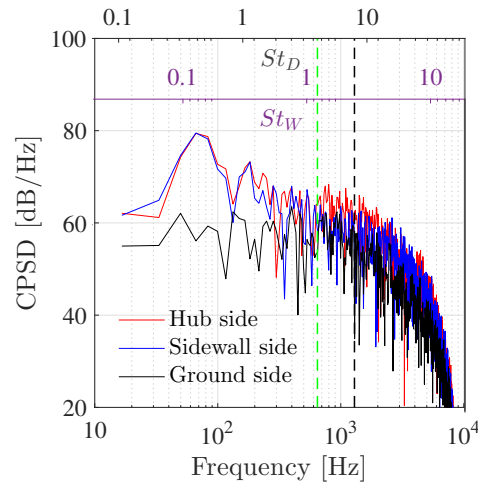


Figure 6.14: CPSD of the far-field acoustics at three different observer positions, using the upstream wheel and downstream wheel acoustic data. --- first depth mode (646 Hz), --- second depth mode (1292 Hz).

Secondly, at all the three observer locations, the downstream wheel noise dominates the upstream wheel noise, especially in the low and middle frequency ranges. The downstream wheel noise in the middle frequency range (centred around the hub cavity depth modes) at the hub side and the sidewall side shares similar spectral profiles and levels, whereas the hub side middle frequency noise is louder than the sidewall side middle frequency noise in the isolated single wheel case. This suggests that, in the tandem wheels configuration, the middle frequency downstream wheel noise is generated by both flow interactions and hub cavity resonances (depth modes). Further analysis of the middle frequency noise source locations is shown in the noise source map in Figures 6.20 and 6.21. By comparing the downstream wheel noise with the single wheel noise, the interaction noise shows a broadband spectrum, radiating more to the two side directions. The interaction noise is analysed by the plots of CPSD between the upstream

wheel acoustics and the downstream wheel acoustics at three observer locations in Figure 6.14, where the spectral peak at $St_W = 0.19$ only occurs in the two side directions. At the ground side in Figure 6.14, the CPSD level in the low frequency range is lower than the levels in the other two side directions, since the interaction noise radiates less to the ground side.

Directivities

The OASPL on two different planes is displayed in Figure 6.15, and is summarised in Table 6.3 at the three observer locations. The OASPL of the upstream wheel is approximately 1.1 dB to 3.3 dB higher than the isolated single wheel case, and they share similar directivity patterns on both the z/D plane (Figure 6.15(a)) and the $x/D = 0$ plane (Figure 6.15(b)). Both the upstream wheel and the downstream wheel acoustics demonstrate a side force dipole directivity in Figure 6.15(b), due to the flow interactions on the side plane. This side force dipole is also shown by the isolated single wheel case, but which is generated by the hub cavity and rim cavities noise. The tandem wheels noise is louder by 8.3 dB, 11.7 dB, and 8.8 dB than the single wheel noise at the hub side, sidewall side and ground side, respectively.

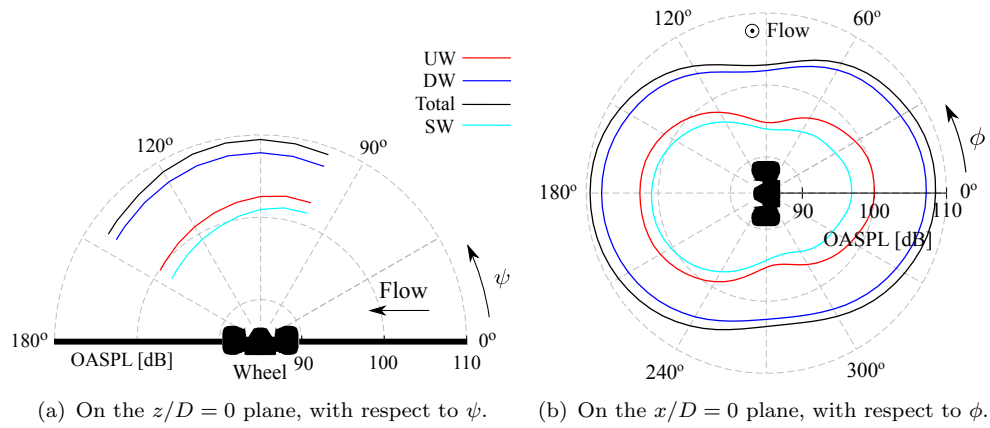


Figure 6.15: Directivity of the OASPL [dB] on different planes.

	SW	UW	DW	Total
hub side	101.0	102.7	107.7	109.3
sidewall side	96.8	100.1	107.2	108.5
ground side	94.0	95.3	101.8	102.8

Table 6.3: Summary of the OASPL [dB] at different far-field observers obtained from Single Wheel (SW) case, and Upstream Wheel (UW), Downstream Wheel (DW) and both wheels (Total) in the tandem wheels case.

The plot of OASPL against the polar angle ψ and azimuthal angle ϕ is provided in Figure 6.16, and a side force dipole is clearly depicted.

The directivity of narrowband SPL (with a band width of 8 Hz) at different frequencies is plotted in Figure 6.17 to give an insight into how the radiation patterns vary with

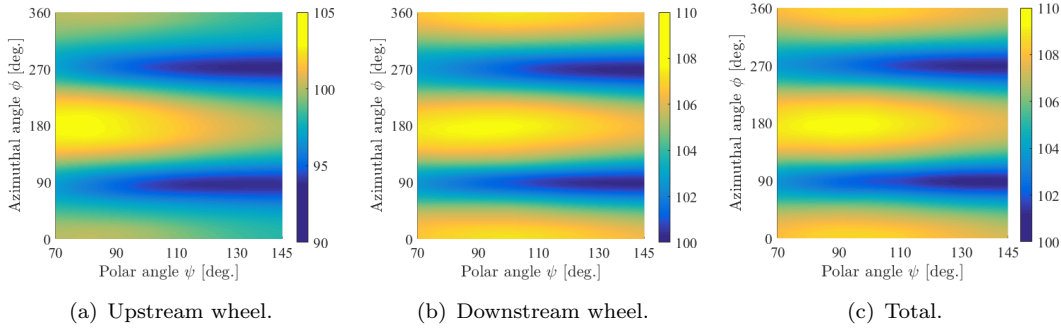


Figure 6.16: Directivity of OASPL [dB] against polar angle ψ and azimuthal angle ϕ .

frequency. Firstly at 20 Hz ($St_D = 0.13$) in Figures 6.17(a), 6.17(b) and 6.17(c), the peak directivity is towards the wing side ($\phi = 90^\circ$) and the ground side ($\phi = 270^\circ$), which shows a lift dipole pattern (aligned with y axis). However, this lift dipole is asymmetric with respect to the horizontal plane $\phi = 180^\circ$, due to the asymmetric mean flow field around the tandem wheels. At the flow interaction frequency of $f = 80$ Hz ($St_W = 0.19$) in Figures 6.17(d), 6.17(e) and 6.17(f), the directivity still shows a dipole pattern but the favourable direction changes to the sidewall side ($\phi = 0^\circ$) and hub side ($\phi = 180^\circ$), presenting a side force dipole pattern (aligned with the z axis), since the flow interactions are mainly on the side plane. The directivity at $St_W = 0.19$ also determines the OASPL directivity in Figure 6.16. At $f = 650$ Hz (first depth mode) and $f = 1290$ Hz (second depth mode), the hub cavity noise of the upstream wheel demonstrates similar directivity patterns to the isolated single wheel case (Figure 5.26). However, the downstream wheel noise at these two hub cavity depth modes is more affected by the flow interactions than the upstream wheel noise, and the directivity pattern is more distorted. At 4000 Hz, the directivity is again dipole in nature, radiating towards both the sidewall and hub sides, mostly due to the small-scale fluctuations on the rim cavities.

Coherence analysis

Figure 6.18 shows the coherence between the far-field acoustics from the upstream wheel and from the downstream wheel, on the $x/D = 0$ plane ($\psi = 90^\circ$). The coherence indicates flow interactions, and it peaks at $St_W = 0.19$ at the hub side and sidewall side. The strong coherence extends over a large range of azimuthal angle ϕ by $\Delta\phi = 120^\circ$, indicating that the interaction noise is radiated towards the two side directions in a wide azimuthal range. At the ground side and wing side, the upstream wheel noise and downstream wheel noise are much less coherent, since the ground side and wing side are the least efficient radiation directions for the interaction noise sources on the wheel side faces. A secondary peak at $St_W = 0.38$ is illustrated with the same pattern as that at $St_W = 0.19$. The acoustic coherence tends to be lower in the middle and high frequency ranges, since the hub cavity and rim cavities are also important noise sources in these

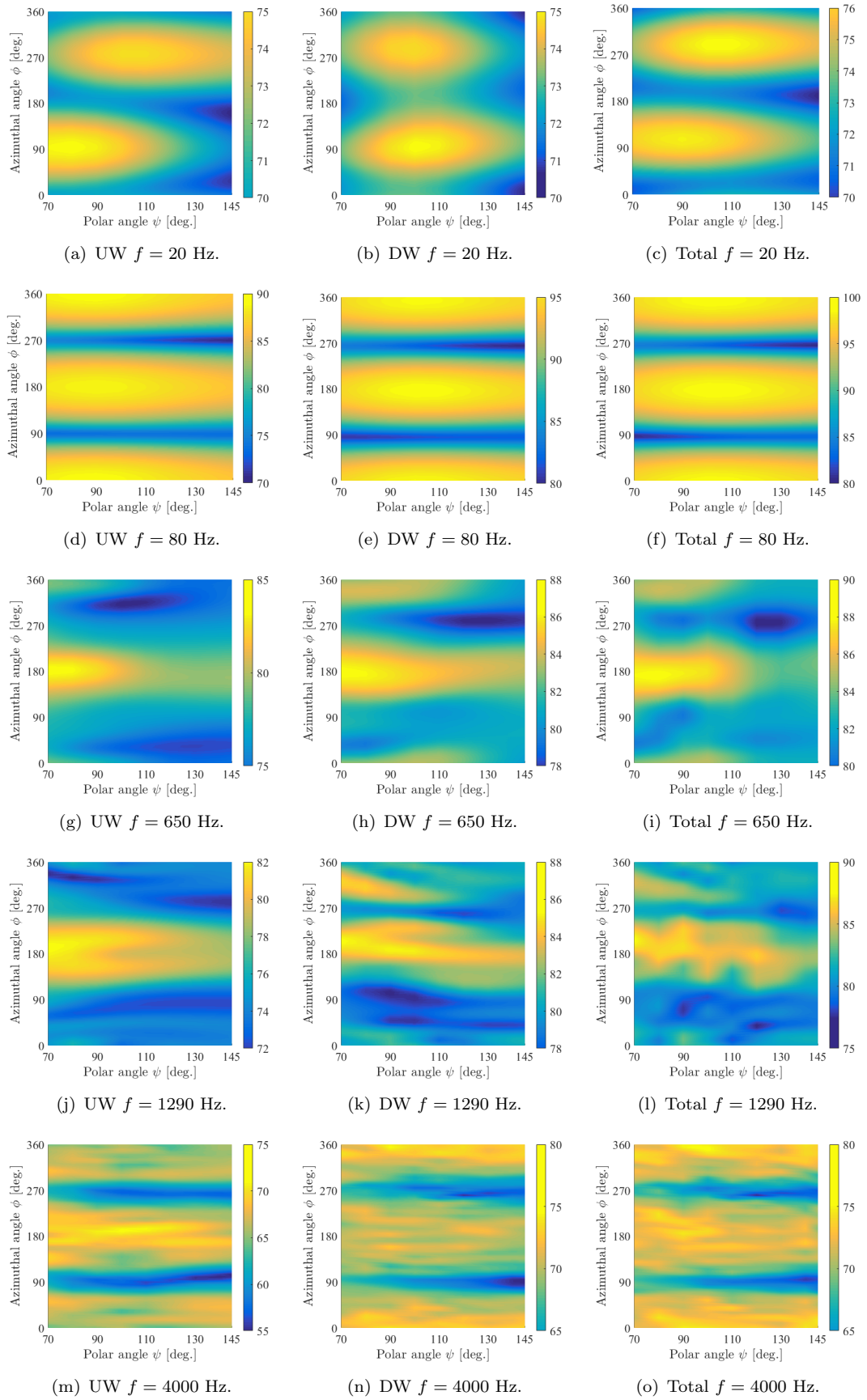


Figure 6.17: Directivity of narrow band SPL [dB] against polar and azimuthal angles at different typical frequencies.

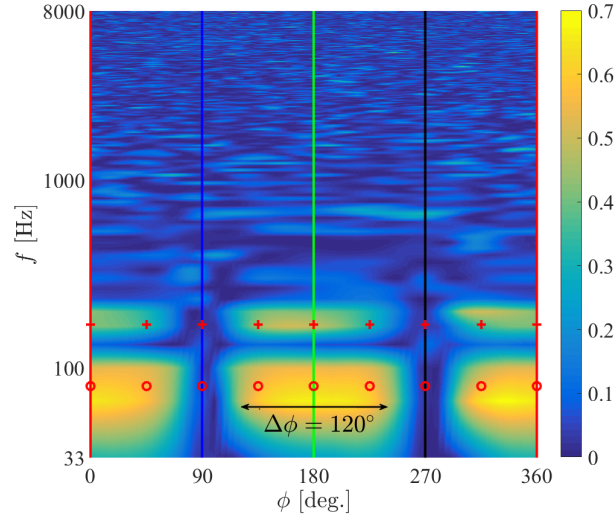


Figure 6.18: Coherence γ^2 between far-field acoustics from the upstream wheel and the downstream wheel on the $x/D = 0$ plane varying with ϕ . \circ $St_W = 0.19$, $+$ $St_W = 0.38$, — sidewall side ($\phi = 0^\circ, 360^\circ$), — wing side ($\phi = 90^\circ$), — hub side ($\phi = 180^\circ$), — ground side ($\phi = 270^\circ$).

frequency ranges. Figure 6.18 confirms that the tandem wheels flow interactions are mainly in the side directions.

Figure 6.19 plots the coherence between the surface pressures and the hub side far-field acoustic pressures, at the interaction frequency of $St_W = 0.19$. The rear part of the upstream wheel shoulder and the front part of the downstream wheel shoulder are highlighted, which further shows that the interactions are due to the flow separations from the side face of the upstream wheel and the flow impingements on the side face of the downstream wheel.

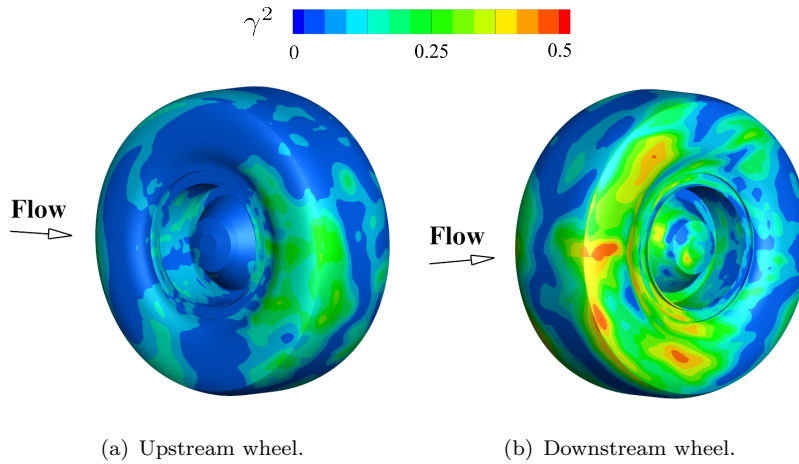


Figure 6.19: Coherence γ^2 at $f = 80$ Hz ($St_W = 0.19$) between wall pressure fluctuations and far-field acoustic pressures at the hub side.

Noise sources localisation

The noise source strength $\mathcal{N}(\mathbf{y}, f)$, which is derived from the FW-H equation in the frequency domain, is used to localise the noise sources at different frequencies. The plots of noise source strength for a far-field observer at the hub side is provided in Figure 6.20, which shows that the dominant noise sources are the wall pressure fluctuations on the side face of the downstream wheel. At the flow interaction frequency of $f = 80$ Hz ($St_W = 0.19$), the rear part of the upstream wheel shoulder and the front part of the downstream wheel shoulder are indicated to be the major noise sources. At the cavity depth modes at frequencies of 650 Hz and 1290 Hz, a triangular region that originates from the leading edge of the hub rim cavity is shown on the surface of the upstream wheel. This pattern is the same as the isolated single wheel case in Figure 5.27. Thus, the depth modes are still the dominant driving mechanisms for the upstream wheel noise in the middle frequency range. For the downstream wheel at these two depth modes, apart from the front part of the shoulder, noise sources are also distributed on the downstream of the hub cavity. The highlighted region (in red color) on the hub cavity downstream region is the cavity wake, and this wake is narrower compared to the hub cavity wake on the upstream wheel. The hub cavity wake of the upstream wheel is determined by the two surface separation lines originating at the leading edge of the hub rim cavity. However, the surface flow separations and attachments on the downstream wheel surface are significantly effected by the flow interactions in the gap region. Thus, the hub cavity source region shows different patterns by the two wheels. The downstream wheel hub cavity flow is more distorted, and the depth modes of the downstream wheel hub cavity are not as significant as the upstream wheel hub cavity. At a frequency of 4000 Hz, the hub and the rim cavities are identified as the dominant noise sources, and this is consistent with the previous isolated single wheel case. The front part of the downstream wheel shoulder is highlighted in the low and middle frequency ranges, suggesting that the flow interactions can generate broadband low and middle frequency noise.

For the sidewall side observer in Figure 6.21, the front part of the downstream wheel shoulder is again demonstrated to generate low and middle frequency noise. In the middle frequency range, different areas are highlighted on the two wheels. Firstly, the upstream wheel shows a triangular shape region, but the most dominant noise source for the downstream wheel is at the leading edge of the sidewall, which is also the case at a high frequency of 4000 Hz. For the ground side observer in Figure 6.22, the major noise sources in the low and middle frequency ranges are the front tyre of the downstream wheel and the hub cavity region, respectively.

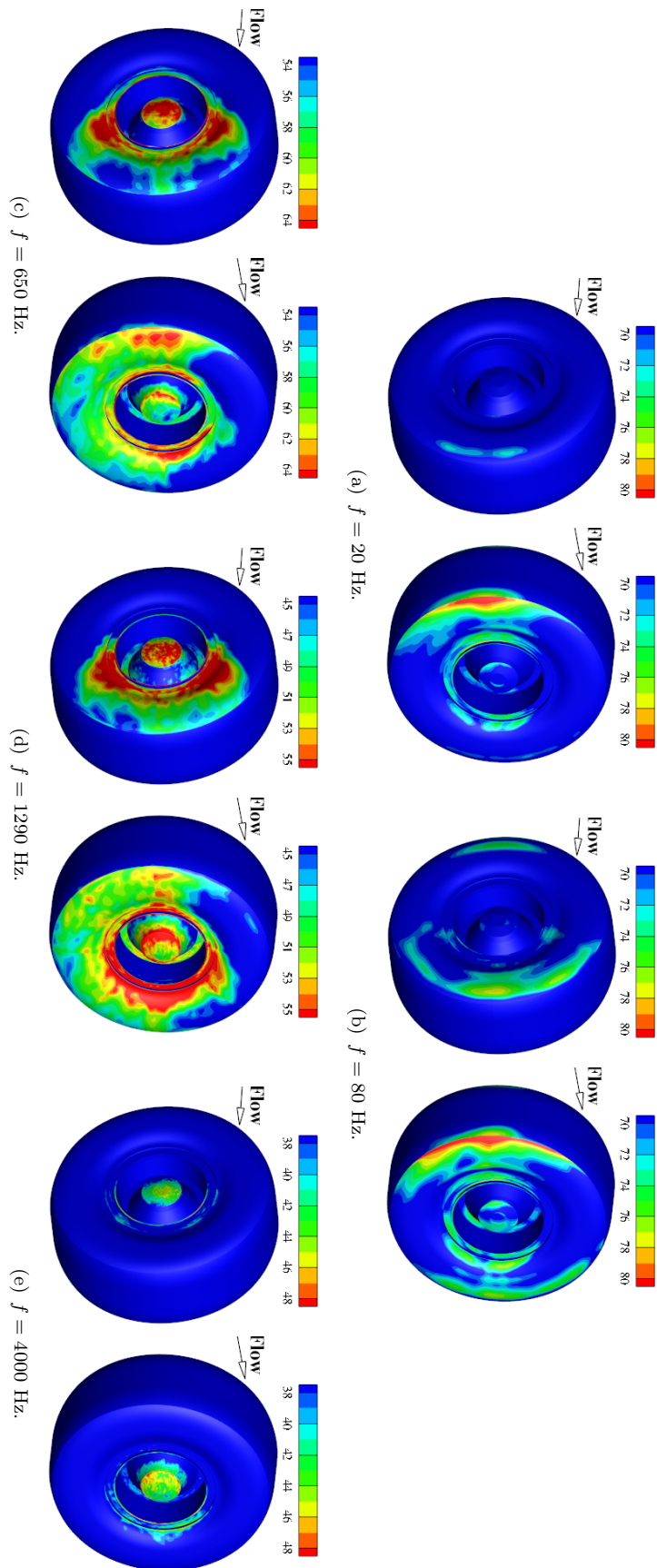


Figure 6.20: The noise source strength $\mathcal{N}(\mathbf{y}, f)$ on the upstream (left) and downstream (right) wheels for the far-field observer at $\phi = 180^\circ$ (hub side).

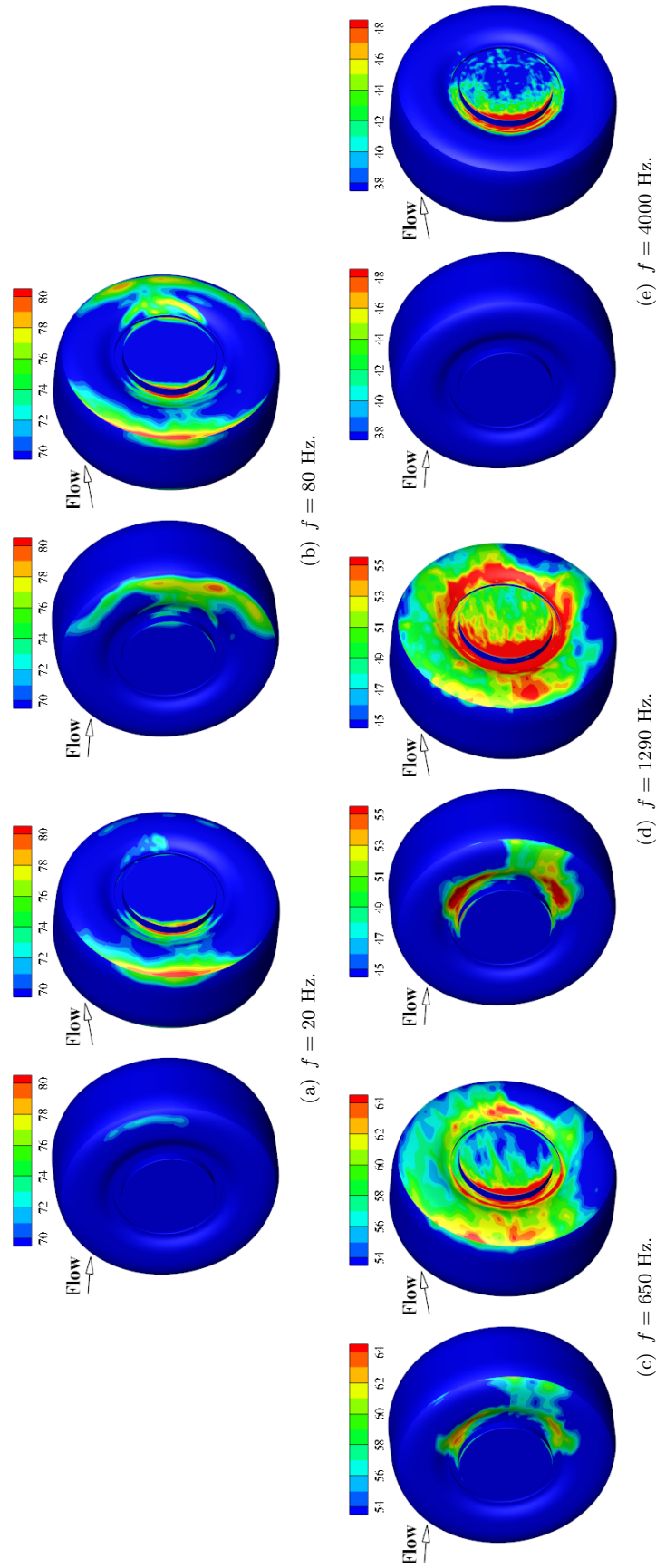


Figure 6.21: The noise source strength $\mathcal{N}(\mathbf{y}, f)$ on the upstream (left) and downstream (right) wheels for the far-field observer at $\phi = 0^\circ$ (sidewall side).

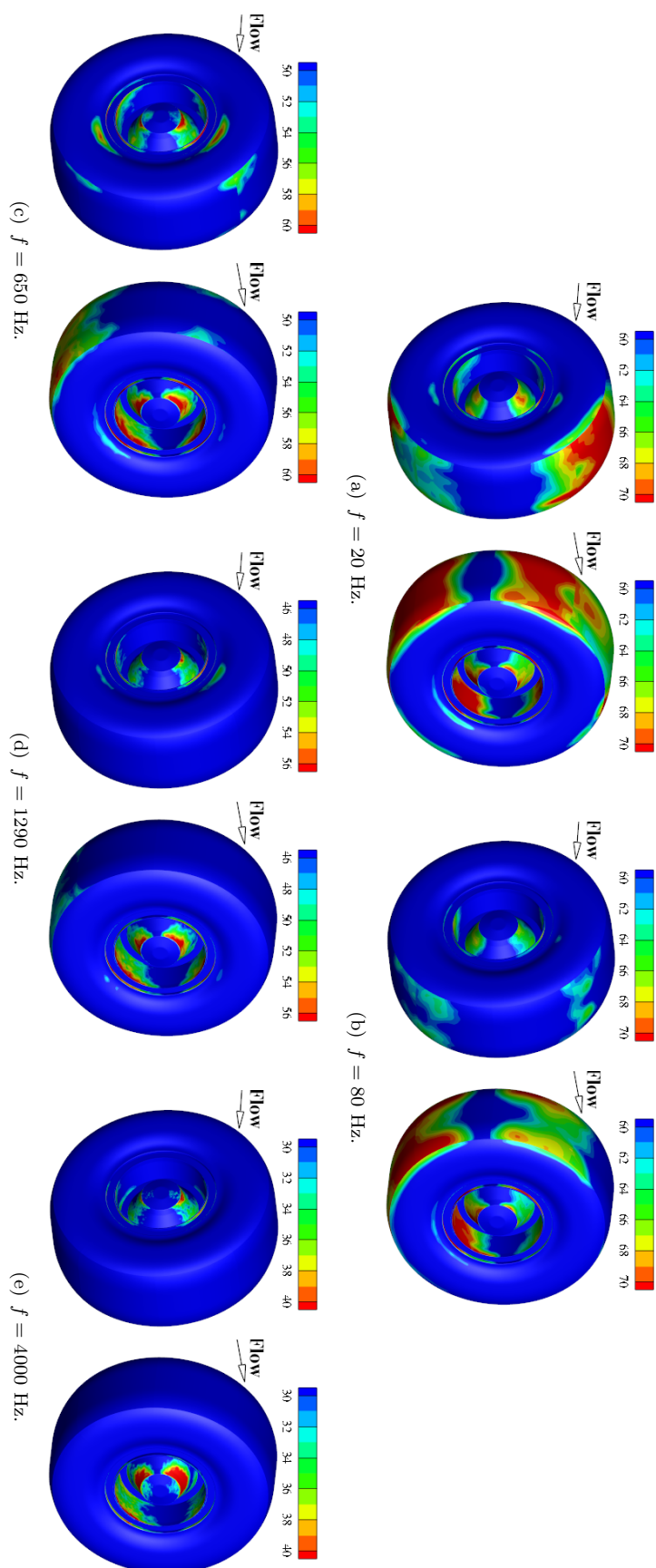


Figure 6.22: The noise source strength $\mathcal{N}(\mathbf{y}, f)$ on the upstream (left) and downstream (right) wheels for the far-field observer at $\phi = 270^\circ$ (ground side).

6.4.2 Effects of covering hub and rim cavities on the downstream wheel

The effect of covering the downstream wheel hub cavity and rim cavities on the downstream wheel noise is shown in Figure 6.23 at three different observer positions. The different configurations are shown in Figure 5.2. The NHC configuration is with the hub cavity covered. The NHCRC configuration is with the hub and rim cavities covered. Only the geometry of the downstream wheel is modified and the hub cavity and rim cavities on the upstream wheel are kept for all the cases. At low frequencies, the three different configurations have comparable levels at all three observer locations, since the low frequency noise is mainly from flow interactions. There is a slight reduction in the middle frequency noise at the hub side (Figure 6.23(a)) in the NHC configuration. However, this reduction is not as much as that for the isolated single wheel case (Figure 5.30(a)), due to the fact that the wheel interactions are also significant contributors to this middle frequency noise. After covering the rim cavities (NHCRC), the spectrum at the ground side in Figure 6.23(c) demonstrates a reduction in the high frequency range, whereas the reduction is less distinguishable at the hub side and sidewall side. This is due to the fact that the sideline acoustics are also produced by the broadband flow interactions. Overall, the downstream wheel hub cavity and rim cavities do not have significant effects on the downstream wheel noise, and the flow interactions are the dominant sources for the downstream wheel noise.

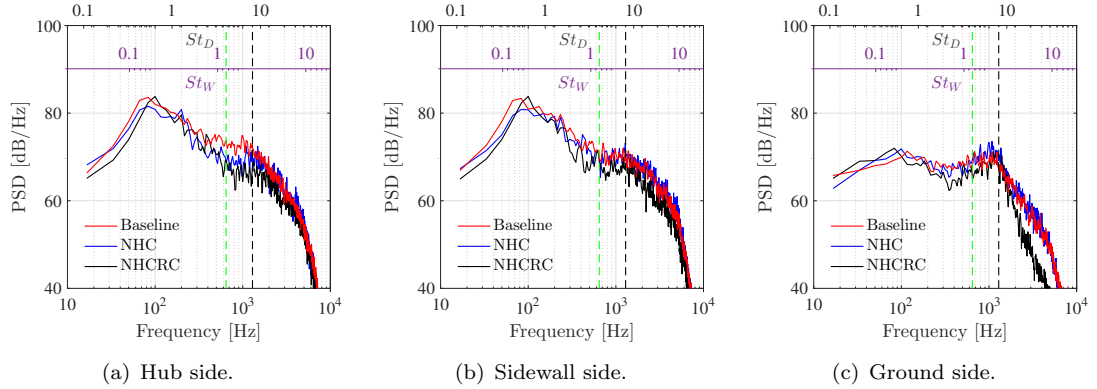


Figure 6.23: Effects of covering the hub cavity and rim cavities on the sound generated by the downstream wheel. --- first depth mode (646 Hz), --- second depth mode (1292 Hz).

6.4.3 Effects of a gap fairing

The comparisons between the control case and baseline case are shown in Figure 6.24. It shows that both the low frequency and middle frequency acoustics are reduced, but mostly in the low frequency range. The low frequency noise in the baseline case is generated by the large scale flow interactions in the gap, which are eliminated by the application of a gap fairing. The comparisons of the far-field acoustic OASPL are shown

in Figure 6.25. All the cases demonstrate a side force dipole pattern. The control case with a gap fairing applied shows reductions in the OASPL of 5.1 dB, 7.1 dB and 4.5 dB at the hub side, sidewall side and ground side, respectively. These reductions are mainly from the low frequency noise generated by large-scale flow interactions.

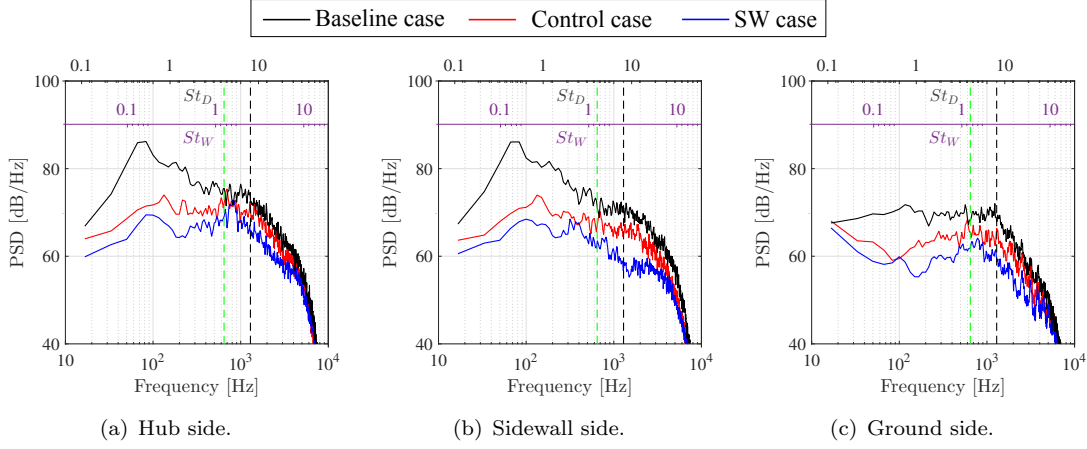


Figure 6.24: Effects of the gap fairing on the far-field acoustics at three observer positions. --- first depth mode (646 Hz), --- second depth mode (1292 Hz).

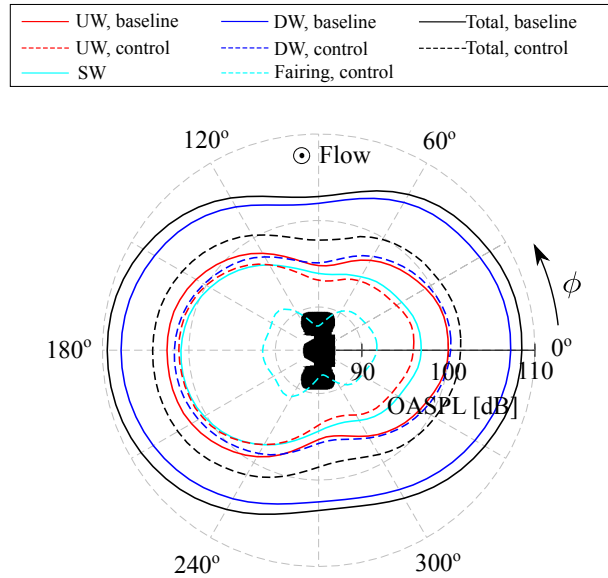


Figure 6.25: Directivity of OASPL [dB] for the baseline case and control case, on the $x/D = 0$ plane.

6.4.4 Section summary

This section has shown the acoustic results at zero angle of attack. Four configurations are demonstrated, and they are the baseline case, no hub cavity (NHC) case, no hub cavity and rim cavities (NHCRC) case and control case with a gap fairing.

For the baseline case, the flow interaction noise is broadband, and mainly radiating towards the side directions in the low and middle frequency ranges. Both the upstream wheel noise and downstream wheel noise show a spectral peak at $St_W = 0.19$ at the hub side and the sidewall side. The maximum coherence between the upstream wheel noise and downstream wheel noise is obtained also at $St_W = 0.19$ in the two side directions. In the noise source strength plots, the rear part of the upstream wheel shoulder and the front part of the downstream wheel shoulder are demonstrated to be the dominant noise sources at $St_W = 0.19$. A lift dipole pattern and a side force dipole pattern are shown in the low frequency range, depending on the frequency. In the middle frequency range, the upstream wheel noise is still characterised by the hub cavity depth modes, but the downstream wheel acoustics are more effected by the flow interactions in the gap region, resulting in a distorted directivity pattern. The small-scale flow fluctuations around the rim cavities and the hub are shown to generate high frequency noise, which mainly radiates towards the side directions.

The downstream wheel hub cavity and rim cavities do not have a significant contribution to the total far-field acoustics. This is due to the fact that the downstream wheel noise dominates the upstream wheel noise, and the flow interactions on the side plane ($y/D = 0$ plane) are the most significant source for the downstream wheel noise. However, slight reductions in the middle and high frequency noise are also demonstrated at some observer positions. The hub cavity and rim cavities are still the major sources for the upstream wheel noise in the middle and high frequency ranges, respectively, since the flow fields in these two regions of the upstream wheel are less effected by the presence of the downstream wheel.

The flow interactions are characterised by large-scale turbulent structures. After the application of a gap fairing, these structures in the gap region are eliminated. Thus, a broadband noise reduction, particularly in the low frequency range, is obtained.

6.5 Effects of angle of attack

6.5.1 Aerodynamic results

Force coefficients

The total force coefficients (C_L , C_D and C_S) obtained at different angles of attack are provided in Table 6.4. A significant decrease in the mean lift coefficient $|\bar{C}_L|$ is demonstrated at positive angles of attack, indicating reduced asymmetry of near-field flows surrounding the tandem wheels with respect to the x axis. The mean drag coefficient tends to be larger at higher angles of attack due to increased projected frontal areas. The drag coefficient firstly increases with a gradient of 0.01 per degree as the angle of attack is increased from 0° to 10° . A lower gradient of 0.0012 per degree is measured

between 10° and 20° . This implies that the mean flow is more sensitive to angle of attack at $\text{AoA} < 10^\circ$.

AoA	$ \bar{C}_L $	\bar{C}_D	\bar{C}_S	C_L^{rms}	C_D^{rms}	C_S^{rms}
0°	0.201	0.643	0.037	0.035	0.036	0.082
10°	0.080	0.743	0.063	0.047	0.041	0.066
20°	0.010	0.752	0.034	0.042	0.048	0.054
30°	0.018	0.767	0.059	0.040	0.050	0.045

Table 6.4: The force coefficients obtained at different angles of attack in the tandem wheels simulations.

As the angle of attack is increased from 0° to 30° , the fluctuating side force (C_S^{rms}) is decreased by 45%. As mentioned previously, the fluctuating side force is a measurement of flow interactions in the side directions. Thus, the decrease in C_S^{rms} suggests that the aerodynamic interactions are reduced with increased angle of attack, and thereby the interaction noise in the side directions can be expected to be lower. The fluctuating lift coefficient (C_L^{rms}) firstly increases at $\text{AoA} = 10^\circ$ then decreases between 10° and 30° . The largest fluctuating lift coefficient at $\text{AoA} = 10^\circ$ implies a stronger flow interaction in the vertical (transverse) direction and more noise is thus expected to radiate towards the ground and wing sides.

Pressure coefficients

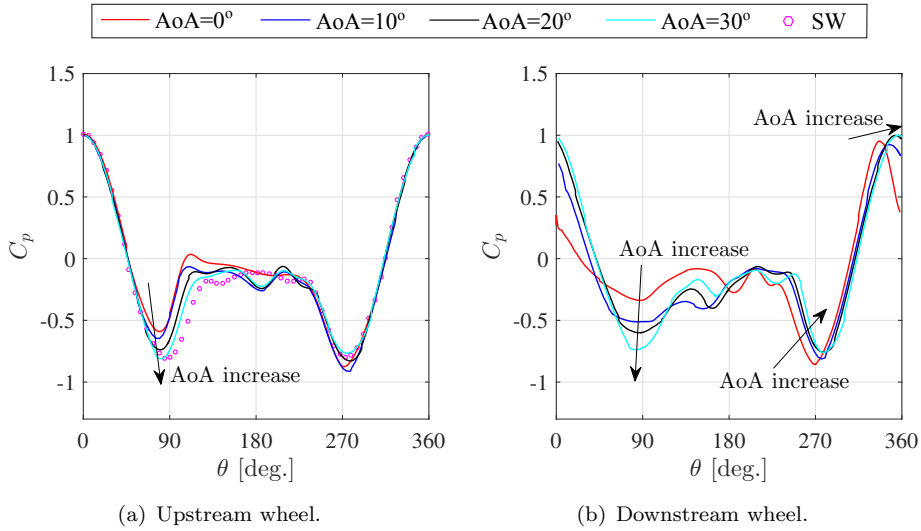


Figure 6.26: Mean pressure coefficient C_p on the central plane ($z/D = 0$) of the upstream and downstream wheels obtained at different angles of attack.

The differences in the mean pressure distributions along the centreline of the upstream wheel surface and downstream wheel surface at four angles of attack are shown in Figure 6.26. For the upstream wheel in Figure 6.26(a), the aerodynamic interactions at $\text{AoA} = 0^\circ$ induce a highly asymmetric pressure distribution. This asymmetry is reduced with increased angle of attack, and the suction peak location at the wing side moves from

$\theta = 76^\circ$ to $\theta = 80^\circ$ between $\text{AoA} = 0^\circ$ and $\text{AoA} = 30^\circ$. The difference in the two suction peak levels at the wing side and ground side becomes smaller at higher angles of attack. Similar pressure distribution patterns in the wake ($120^\circ < \theta < 240^\circ$) are demonstrated at positive angle of attack. Figure 6.26(b) shows that the stagnation point on the downstream wheel surface moves from $\theta = 335^\circ$ at $\text{AoA} = 0^\circ$ to $\theta = 356^\circ$ at $\text{AoA} = 30^\circ$. The suction peak at the wing side tends to be more negative and more comparable with the other suction peak at the ground side. The reduced asymmetric pressure profiles produced by higher angles of attack account for the decrease in the mean lift coefficient $|\bar{C}_L|$ in Table 6.4.

Flow structures in the gap region

Figure 6.27 shows the mean flow streamlines and z -vorticity. The pressure perturbation R.M.S. is shown in Figure 6.28.

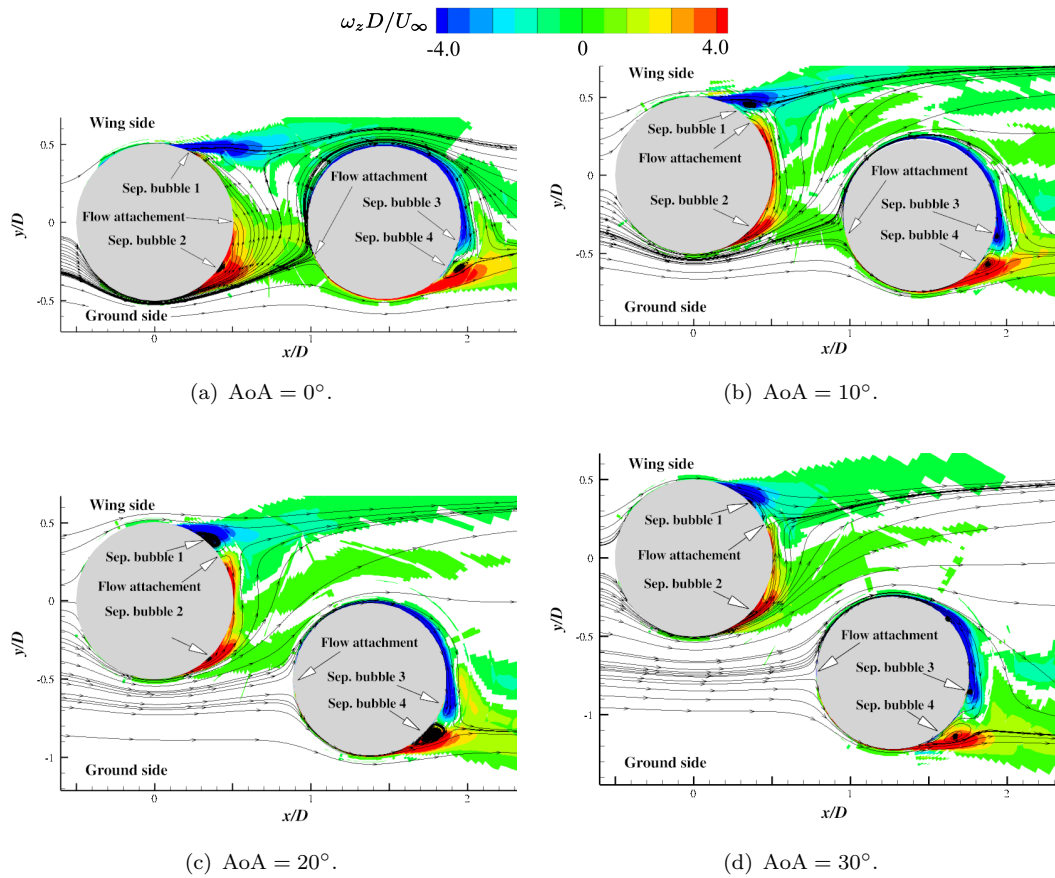


Figure 6.27: The z -vorticity and streamlines of mean flow in the gap region ($z/D = 0$) at different angles of attack.

The mass flow rate measured by the mass flux through the gap region is given by,

$$\dot{m} = \oint_S \rho v \, dS, \quad (6.1)$$

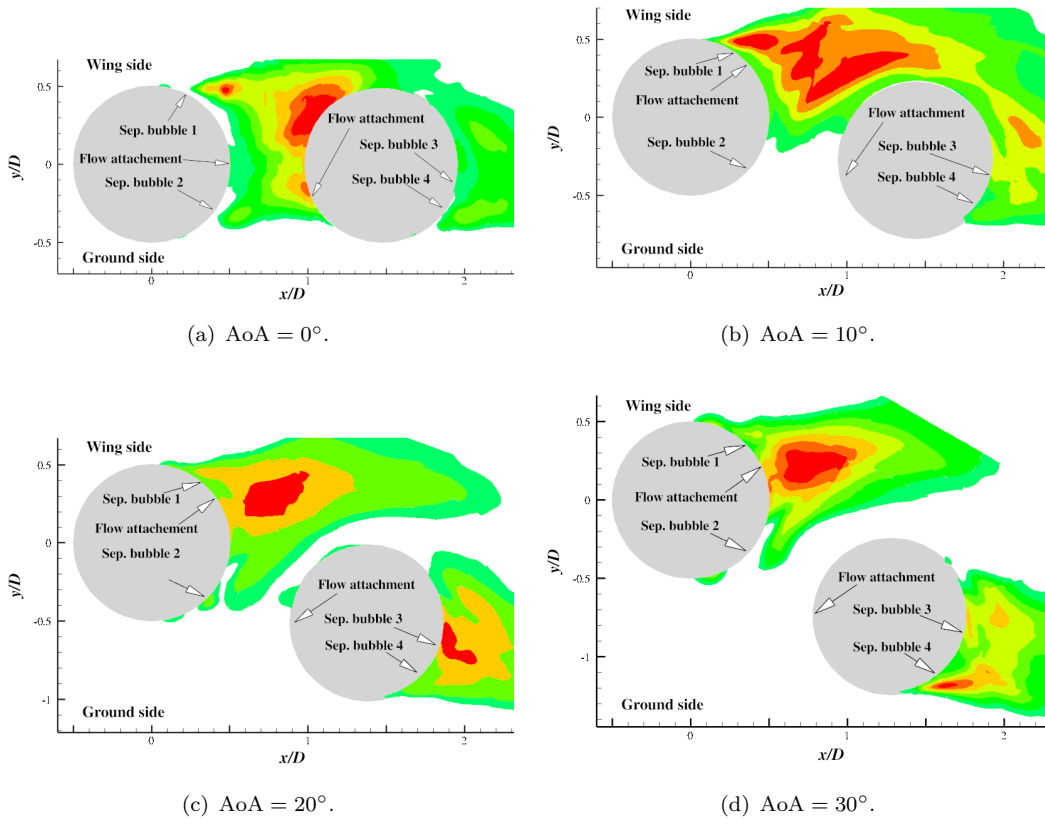


Figure 6.28: The pressure perturbation R.M.S. $-0.07 < p^{rms}/\rho_\infty c_\infty^2 < 0.07$ in the gap region ($z/D = 0$) at different angles of attack.

where \mathbf{v} is the velocity vector and \mathbf{S} represents a line in the gap region connecting centres of the upstream and downstream wheels. The mass flow rate in the vertical (transverse) direction can affect the displacement of the upstream wheel shear layer at the free end (wing side). Thus, an effective mass flow rate is defined as $\dot{m}^e = \dot{m} \times \cos(\text{AoA})$, and is plotted in Figure 6.29 against different angles of attack.

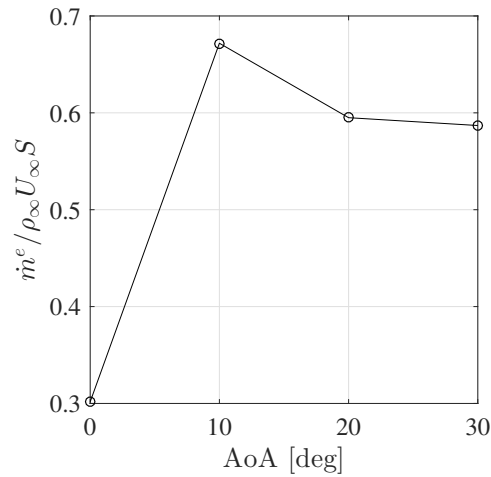


Figure 6.29: The effective mass flow rate through the gap region.

Based on Figures 6.27, 6.28 and 6.29, the flow field at different angles of attack can be categorised into three regimes:

1. Wake impingement regime

This regime describes at flow at $\text{AoA} = 0^\circ$. The downstream wheel is fully immersed in the wake of the upstream wheel, and the flow interactions are thus the most significant. The stagnation point on the downstream wheel and the surface pressure distributions are the most asymmetric, thereby leading to a highest mean lift coefficient $|\bar{C}_L|$ for the four angles of attack investigated. The smallest amount of mass flow moving into the gap occurs in this regime as shown in Figure 6.29. The far-field interaction noise at $\text{AoA} = 0^\circ$ is also expected to be the largest.

2. Wake deflection regime

This regime describes at flow at $\text{AoA} = 10^\circ$. More than half of the downstream wheel is located in the wake of the upstream wheel, and the downstream wheel stagnation point is still in the upstream wheel wake. This flow regime is characterised by the largest displacement of the upstream wheel shear layer at the free end (wing side). This is due to the fact that more mass flow is going through the gap region (as shown in Figure 6.29), which deflects the shear layer more towards the wing side as shown in Figure 6.27(b). The upstream wheel shear layer at the ground side still impinges on the downstream wheel surface. In this flow regime, the gap region is dominated by higher pressure fluctuations in Figure 6.28(b), and the lift coefficient R.M.S. C_L^{rms} is the largest in Table 6.4, indicating more sound radiating towards the wing side and ground side.

3. Independent wake regime

This regime describes at flow at $\text{AoA} = 20^\circ$ and 30° . A small part of the downstream wheel is located in the upstream wheel wake with the downstream wheel stagnation point facing freestream. In this flow regime, flow interactions are weaker, and flow fields around two wheels are more independent, as shown by the pressure perturbations in Figures 6.28(c) and 6.28(d). The mass flow rate through the gap decreases. The upstream wheel shear layer shows less deflection at the wing side, and the shear layer at the ground side is deflected into the gap region. The surface pressure distributions on the two wheels tend to be more symmetric, and the mean lift coefficient $|\bar{C}_L|$ becomes smaller.

At all the four angles of attack, the gap region is characterised by a two-vortex mode (shown in Appendix H).

6.5.2 Acoustic results

The far-field acoustic observer locations are the same with the previous isolated single landing gear wheel case and tandem wheels case at $\text{AoA} = 0^\circ$, and the observer angles are defined in Figure 5.18, with respect to the upstream wheel centre. The acoustic spectra at four different angles of attack are shown in Figure 6.30, together with the isolated single wheel (SW) case. At the hub side and sidewall side, a general reduction in the low frequency interaction noise occurs at positive angles of attack. The acoustics in the middle and high frequency ranges are less effected. The low frequency noise reduction at the hub side and sidewall side is not demonstrated at the ground side, since most of the low frequency interaction noise is radiating towards the side directions.

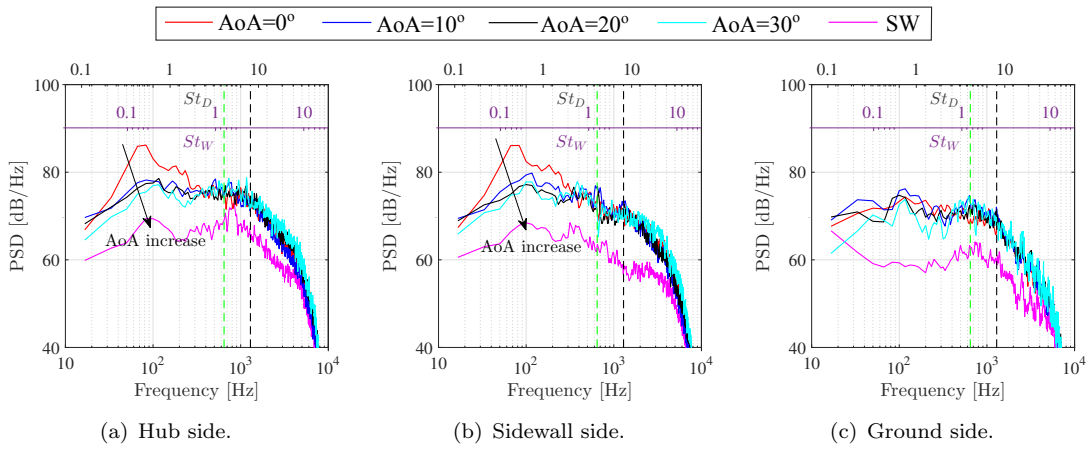


Figure 6.30: Far-field acoustics at different angles of attack. --- first depth mode (646 Hz), --- second depth mode (1292 Hz).

The directivity of OASPL is shown in Figure 6.31. The noise reduction in the two side directions is clearly demonstrated at positive angles of attack, due to the reduced flow interactions that are induced by the flow separations from the upstream wheel side face and flow impingements on the downstream wheel side face. At the wing side and ground side, the loudest configuration is at $\text{AoA} = 10^\circ$. This is due to larger pressure perturbations in the gap region as shown in Figure 6.28(b).

6.5.3 Section summary

This section has detailed the aerodynamic and acoustic results at four angles of attack, i.e. 0° , 10° , 20° and 30° . An increase in the mean drag coefficient is demonstrated with angle of attack increasing, since the projected frontal area increases. The surface pressure distributions tend to be more symmetric and the mean lift coefficient becomes smaller with increased angle of attack. Three flow regimes are found based on the flow characteristics in the gap region. A general reduction in the sideline noise is obtained at positive angles of attack. The OASPL of the wing side acoustics and ground side

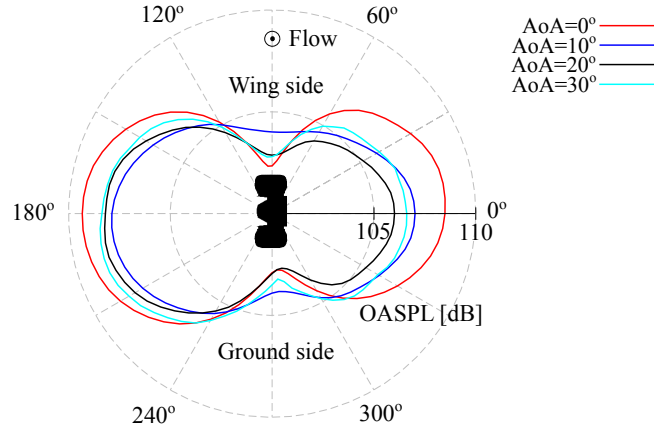


Figure 6.31: Directivity of OASPL [dB] at different angles of attack.

acoustics is the highest at $AoA = 10^\circ$ due to the largest pressure fluctuations in the gap region.

6.6 Chapter summary

In this chapter, high-order CAA simulations were performed to investigate the flow and acoustic interactions between two wheels in tandem, with a separation distance of $L = 1.5D$, at $M = 0.23$. The numerical methodology and computational setup were the same as the previous isolated single landing gear wheel simulations. Seven cases are tested with different wheel geometries, noise control treatments and angles of attack. The mean and R.M.S. surface pressure distributions are compared to the experimental measurements by Spagnolo *et al.* [122] that were obtained by using two simplified wheels without hub and rim cavities. However, the hub and rim cavities have minor effects on the large flow scales that mainly influence the distributions of C_p and C_p^{rms} . Thus, the experimental databases by Spagnolo *et al.* [122] can be used to validate the numerical simulations, and good agreements have been obtained. The key findings of the tandem wheels simulations are summarised as:

1. Asymmetry of the mean flow

A significant asymmetric mean flow field occurs at $AoA = 0^\circ$ for the baseline configuration. The separated flow from the upstream wheel forms two large vortices in the gap, and the vortex centres are deflected towards the wing side. This is different to the four-vortex mode observed in the single wheel case. The downstream wheel stagnation point is at $\theta = 335^\circ$ due to the impingement of the shear layer from the upstream wheel at the ground side. This asymmetry allows more flow to deflect into the gap region, forcing the development of vortices on the wing side. This flow asymmetry also leads to a highly non-zero mean lift coefficient, which is much larger than the single landing gear wheel case.

The flow fields at positive angles of attack have a reduced flow asymmetry with respect to the x axis, compared to the flow field at zero angle of attack. The stagnation point on the downstream wheel moves towards to $\theta = 0^\circ$ (or 360°), and the pressure distributions along the upstream and downstream wheels tend to be more symmetric, with angle of attack increasing. As a result, the mean lift coefficient decreases gradually towards zero.

The control case with a gap fairing also shows non-zero lift coefficient at $\text{AoA} = 0^\circ$.

2. Flow interactions at $\text{AoA} = 0^\circ$

Flow interactions are most significant at $\text{AoA} = 0^\circ$ due to the fact that the downstream wheel is fully immersed in the wake of the upstream wheel. The force fluctuation R.M.S. is the largest in the side directions for both of the tandem wheels, which is caused by the alternative flow impingements on the two side faces of the downstream wheel. A spectral peak is demonstrated at $St_W = 0.19$ for the side force coefficient and the modified dynamic mode energy. The instantaneous dynamic mode of surface pressures at $St_W = 0.19$ also shows a side force dipole pattern.

The interaction noise demonstrates a broadband spectral range, and the most significant interactions are in the low frequency range, due to the large-scale vortical structures in the gap region. The far-field acoustics show a peak at $St_W = 0.19$ in the two side directions, and this peak does not occur at the ground side observer position. Strong coherence between the upstream wheel noise and the downstream wheel noise is shown only in the side directions, at $St_W = 0.19$ and $St_W = 0.38$. The side face surrounding the hub cavity of the downstream wheel is shown to be the most coherent region for the far-field acoustics at the hub side.

These findings prove that the flow interactions and radiated sound are mainly in the side directions, and in the low frequency range peaking at $St_W = 0.19$.

3. Noise source locations and far-field acoustic directivities

The noise sources are determined firstly by applying the FW-H equation on the surface pressures in the frequency domain, and secondly by the analysis of coherence. The far-field acoustic directivities at different frequencies are analysed by using the wall pressures on the upstream wheel surface and downstream wheel surface, respectively.

The rear part of the upstream wheel shoulder and the front part of the downstream wheel shoulder are the dominant noise sources in the low frequency ranges ($f < 400$ Hz), because of the large-scale flow interactions in the gap region. A lift dipole pattern is shown at $f = 20$ Hz, and this dipole is asymmetric due to the flow asymmetry around the tandem wheels. A side force dipole dominates at $f = 80$ Hz ($St_W = 0.19$), which is also highlighted by the dynamic mode decomposition analysis. There is a spectral peak at $f = 80$ Hz in the hub side and sidewall side acoustics, and this spectral peak does not occur in the ground side and wing side acoustics. The side force dipole directivity at $f = 80$ Hz determines the directivity of OASPL.

The hub cavity acoustics dominate the upstream wheel middle frequency ($400 \text{ Hz} < f < 2000 \text{ Hz}$) noise. This middle frequency noise is generated by the hub cavity first and second depth modes, which is consistent with the isolated single wheel case. The upstream wheel hub cavity noise is less effected by the presence of the downstream wheel. The source region on the upstream wheel surface is a triangular shape, corresponding to the flow separation lines. This upstream wheel middle frequency noise is mainly radiating towards the far-field positions at the hub side in the upstream direction. However, the directivity of the downstream wheel middle frequency noise is distorted, since the flow interactions between tandem wheels are also significant contributors to the downstream wheel acoustics. In the noise source location map of the downstream wheel acoustics, both the hub cavity region and the front area of the shoulder are highlighted.

There are two rim cavities on opposite sides, one surrounding the hub cavity and the other surrounding the sidewall. The small-scale pressure fluctuations on the surface of these two rim cavities and the hub are shown to generate high frequency ($f > 2000 \text{ Hz}$) noise, which shows a dipole pattern in the side directions.

4. Effects of covering the downstream wheel hub and rim cavities

Different from the isolated single wheel case, the downstream wheel hub cavity and rim cavities do not have significant contributions to the total far-field acoustics in a tandem configuration. This is due to the fact that the separated flow from the upstream wheel impinges on the downstream wheel surface, generating significant interaction noise that dominates the hub and rim cavities noise. Despite limited effects, slight reductions in the middle and high frequency noise are demonstrated at the hub side and ground side, respectively. For the upstream wheel noise in the middle and high frequency ranges, the upstream wheel hub cavity and rim cavities are still the major sources, since the flow fields in these two regions are less effected by the presence of the downstream wheel.

5. Effects of covering the gap region

In the control case, the gap region is covered by a gap fairing. As a result, the large-scale turbulent structures in the gap region are eliminated, and significant reductions in the low frequency noise are achieved at different observer positions. For the directivity of OASPL, the noise reductions are 5.1 dB, 7.1 dB and 4.5 dB at the hub side, sidewall side and ground side, respectively. The control case also shows reductions in the fluctuating lift, drag and side force coefficients.

6. Effects of angle of attack

The angle of attack affects both the aerodynamic and acoustic results. Firstly, an increase in the mean drag coefficient is demonstrated with angle of attack increasing, due to the increased projected frontal area. Secondly, the mean lift coefficient decreases with increased angle of attack, because the surface pressure distributions are more symmetric.

The flow fields are grouped into three regimes based on the flow characteristics in the gap region. The first regime refers to $\text{AoA} = 0^\circ$, and is characterised by the strongest flow interaction, since the downstream wheel is fully immersed in the wake of the upstream wheel. The second flow regime at $\text{AoA} = 10^\circ$ shows a largest displacement of the shear layer from the upstream wheel at the wing side, due to the fact that more flow is going through the gap to the wing side. In this second flow regime, the pressure fluctuations in the gap region are stronger, and an increase in the acoustic OASPL at the ground side and wing side is thus shown. $\text{AoA} = 20^\circ$ and 30° belong to the third regime, where the flow interactions are weaker and the flow fields around the two wheels are more independent.

A general reduction in the sideline noise is demonstrated at non-zero angles of attack, since only a part of the downstream wheel is immersed in the wake of the upstream wheel.

Chapter 7

Conclusions and Recommendations

7.1 Conclusions

Landing gear are recognised as one of the most significant contributors to airframe noise for commercial aircraft in the approach configuration [29]. Wheels are considered as significant low and middle frequency landing gear noise sources [3, 4, 28–32]. Previous work on landing gear noise focused on the complete landing gear geometry, which is an assembly of a large number of components with different sizes and shapes. The mechanisms of wheel noise generation cannot be revealed due to complex flow interactions. Thus, there is a need to investigate the aerodynamic and acoustic characteristics of isolated wheels. This project applied high-order numerical simulation method to systematically study the isolated and tandem wheels with high-fidelity geometries, which has provided insights into landing gear noise generation mechanisms and aided in noise reduction treatment.

This project contained three main parts. They were numerical development of a cell-centred method, simulations of an isolated landing gear wheel, and tandem landing gear wheels simulations. The detailed summary and conclusion of each part were provided in Sections 4.7, 5.5 and 6.6, respectively. This section will highlight the most significant findings of these three parts.

7.1.1 Cell-centred numerical method development

A high-order hybrid cell-centred method was developed for computational aeroacoustic simulations. The control points were located at cell centres instead of cell vertices (grid points). This hybrid method applied a FD approach at block interior control points and

at block interfaces containing smooth grid metrics. Along discontinuous block interfaces, a FV method was employed serving as an interface condition.

The cell-centred formulation was chosen as it can reduce grid metric discontinuities by shifting control points away from the origin of discontinuities at interface grid points (cell vertices), and thereby enable more interfaces to be treated by the conventional one-to-one interface condition. This advantage of cell-centred space was confirmed by simulations of a 2D vortex convection case and a 2D circular cylinder flow case. For a test case of a 3D cylinder flow, the cell-centred method showed a better agreement of the steady and unsteady statistics with experiments and other simulation databases. Despite the improved numerical accuracy demonstrated by the cell-centred approach, numerical errors were still inevitable at interfaces with large grid metric discontinuities. At such interfaces, a FV method was applied to further reduce grid-induced errors in high-order simulations.

In order to implement the FV method at interfaces, two interpolation schemes have been developed. The first one was Finite Volume Interpolation (FVI) schemes, which were derived from the optimised FD schemes and had two interpolations for the East face and West face, respectively. The second interpolation scheme was obtained by optimising the transfer function profile, and called High Resolution Interpolation (HRI) schemes. The FVI schemes were second-order accurate. However, for a linear case, the third-order and fourth-order truncation errors were cancelled when combining the East face and West face interpolation schemes. For a non-linear case, the grid convergence test of a vortex convection problem showed that the accuracy was close to fourth order. The HRI schemes were four-order accurate. In the eigenvalue analysis, the FVI schemes showed a wider spectral resolution, and instabilities in the high wavenumber range were avoided by applying numerical filtering. The HRI schemes were more dissipative, and stable in nature in the linear wave eigenvalue analysis. However, for tandem cylinders simulations, the FVI schemes were shown to be more stable for non-linear problems.

The FV interface condition using the FVI schemes in the cell-centred space was well validated against the 3D simulations of a single cylinder and tandem cylinders flow, demonstrating the most accurate numerical predictions compared with experiments. Therefore, this interface treatment was recommended at block interfaces containing grid metric discontinuities for the high-order simulations in this thesis.

7.1.2 Isolated landing gear wheel simulations

Numerical simulations of a high-fidelity single landing gear wheel (baseline case) configuration were performed. This geometry contained a large shallow hub cavity, a sidewall and two rim cavities. In the baseline case, good agreements with experimental measurements were obtained. Two additional configurations were tested with the hub cavity and

both hub and rim cavities covered (NHC case and NHCRC case), to isolate the effects of hub and rim cavities on the near-field flow features and far-field acoustics.

The mean flow around the wheel was asymmetric, as shown by the non-zero mean lift coefficient \bar{C}_L , the shear stress lines on the rearward face and the mean streamlines in the wake. This asymmetry was observed for all three configurations, which was firstly due to the asymmetric flow characteristics of short aspect ratio circular cylinders. The hub cavity was also a significant contributor to the mean flow asymmetry, which was confirmed by the reduction in \bar{C}_L when covering the hub cavity (NHC). The depth-to-diameter ratio for the hub cavity was 0.3, and the mean flow demonstrated an asymmetric feature at this ratio by numerical simulations of flat plate mounted cylindrical cavity.

The tyre was the dominant low frequency ($f < 400$ Hz) noise source due to the large-scale flow structures shedding from the wheel, and the tyre demonstrated a lift dipole directivity and a side force directivity at $f = 20$ Hz and $f = 90$ Hz, respectively. These two dipole patterns were also highlighted by the dynamic modes. This low frequency noise was less effected by the hub cavity and two rim cavities. The hub cavity sound dominated the middle frequency ($400 \text{ Hz} < f < 2000 \text{ Hz}$) noise, which was generated by the flow interactions with the hub cavity depth modes. A source region with a triangular shape, which was in vicinity of the hub cavity after the surface flow separation lines, was demonstrated by the dynamic mode decomposition technique and the noise source localisation method. This middle frequency noise was mainly radiating towards the far-field positions at the hub side in the upstream direction. There were two rim cavities on opposite sides. The small-scale pressure fluctuations on the surface of these two rim cavities were identified to generate high frequency ($f > 2000$ Hz) noise, which showed a dipole directivity pattern in the side directions.

The baseline configuration and the configuration with the hub cavity covered (NHC) demonstrated complex separation and attachment patterns in the rim cavity region on the two side faces, whereas the flow was fully attached to the side face for the configuration when both the hub cavity and rim cavities are covered (NHCRC). As a result, the R.M.S. of the force coefficients showed a decrease for the NHCRC case, mostly in the high frequency range ($f > 2000$ Hz). The fully attached flow on the side face for the NHCRC case also provided a 20% reduction in the total drag, which was higher than the 7% by just covering the hub cavity (NHC). Compared to the baseline configuration, reductions of 10.3 dB, 6.1 dB and 5.8 dB in the far-field acoustic OASPL were achieved at the hub side, sidewall side and ground side, respectively, by the NHCRC case. These reductions were mainly from the middle frequency noise from the hub cavity and the high frequency noise from the rim cavities. Therefore, covering the hub cavity and rim cavities was an effective approach to reduce both landing gear wheel drag and acoustics.

7.1.3 Tandem landing gear wheels simulations

Numerical simulations were performed to investigate the flow and acoustic interactions between two wheels in tandem. Seven cases were tested with different wheel geometries, noise control treatments and angles of attack (AoA). The mean and R.M.S. surface pressure distributions were validated against experimental measurements with good agreements.

Firstly, a significant asymmetric mean flow field was demonstrated at $\text{AoA} = 0^\circ$ in the baseline configuration. The separated flow from the upstream wheel formed two large vortices in the gap, and the vortex centres were deflected towards the wing side. The downstream wheel stagnation point was at $\theta = 335^\circ$ due to the impingement of shear layer from the upstream wheel at the ground side. This asymmetry allowed more flow deflecting into the gap region, forcing the development of vortices on the wing side. This flow asymmetry also led to a highly non-zero mean lift coefficient, which was much larger than the single landing gear wheel case. The flow fields at positive angles of attack demonstrated less asymmetry. The stagnation point on the downstream wheel moved towards to $\theta = 0^\circ$ (or 360°), and the pressure distributions along the upstream and downstream wheels tended to be more symmetric, with increasing angle of attack. As a result, the mean lift coefficient decreased gradually towards zero.

At $\text{AoA} = 0^\circ$, the rear part of the upstream wheel shoulder and the rear part of the downstream wheel shoulder were the dominant noise sources in the low frequency ranges ($f < 400$ Hz), because of the large-scale flow interactions in the gap region. A lift force dipole pattern and a side force dipole pattern were shown at $f = 20$ Hz and $f = 80$ Hz, respectively. The flow interactions caused a spectral peak in the far-field acoustics at the hub side and sidewall side. For the upstream wheel, the hub cavity acoustics were generated by depth modes, dominating the upstream wheel middle frequency ($400 \text{ Hz} < f < 2000 \text{ Hz}$) noise. However, the flow interactions were more significant contributors to the downstream wheel middle frequency noise. In the high frequency range ($f > 2000$ Hz), the rim cavities were shown to be the major noise sources with a side force dipole pattern.

Flow interactions were most significant at $\text{AoA} = 0^\circ$ due to the fact that the downstream wheel was fully immersed in the wake of the upstream wheel. The force coefficient R.M.S. was the largest in the side directions for both of the tandem wheels, which was caused by the flow separations from the upstream wheel and the alternative flow impingements on the two side faces of the downstream wheel. The interaction noise demonstrated a broadband spectral range, and the most significant interactions were in the low frequency scale, due to the large-scale vortical structures in the gap region. The far-field acoustics peaked at $St_W = 0.19$ in the two side directions, and this peak did not occur at the ground side observer position. Strong coherence between the upstream wheel noise and the downstream wheel noise was shown only in the side directions, at $St_W = 0.19$ and

$St_W = 0.38$. The hub side face of the downstream wheel was shown to be the most coherent region for the far-field acoustics at the hub side.

Three more configurations were tested at $AoA = 0^\circ$. The first two were the no hub cavity (NHC) and no hub cavity and rim cavities (NHCRC) geometries and the third was with a gap fairing applied (control case). The downstream wheel hub cavity and rim cavities do not have significant contributions to the total far-field acoustics in a tandem configuration. This is due to the fact that the downstream wheel was immersed in the wake of the upstream wheel and the flow interactions were more significant noise sources. Despite limited effects, slight reductions in the middle and high frequency noise were also demonstrated at the hub side and ground side, respectively. In the control case with a gap fairing applied, the large-scale turbulence in the gap region was eliminated, and significant reductions in the low frequency noise were achieved at different observer positions. For the directivity of OASPL, the noise reductions were 5.1 dB, 7.1 dB and 4.5 dB at the hub side, sidewall side and ground side, respectively. The control case with a gap fairing applied also showed reductions in the three force coefficients R.M.S.

A general reduction in the sideline noise was demonstrated at $AoA \neq 0^\circ$. Additionally, at $AoA = 10^\circ$, the shear layer of the upstream wheel at the wing side was deflected by the greatest amount, and higher pressure fluctuations in the gap region were demonstrated. An increase in the acoustic OASPL at the ground side and wing side was also shown. At $AoA = 20^\circ$ and 30° , the flow interactions were weaker and the flow fields around the two wheels were more independent, since only a small part of the downstream wheel was immersed in the wake of the upstream wheel.

7.2 Recommendations for future work

7.2.1 Development of numerical techniques

In the simulations of tandem circular cylinders, the HRI schemes were not stable at the FV interface inside boundary layers where significant non-linear effects were present. The FVI schemes, while stable and accurate, contain two interpolations, and therefore they are more computationally expensive compared to the HRI schemes. Thus, it is desirable to derive a new set of stable and accurate interpolation schemes that contain only one interpolation at cell faces to reduce computational demand.

The FV interface condition has been demonstrated to be accurate and robust for simulations around complex geometries. However, it has only been implemented on multi-block structured grids with perfectly patched block interfaces. For complex configurations, it is time-consuming to generate such grids. It is hence advantageous to implement an overset grid technique with interpolations between the overset region shared by two

grids. The overset technique [124] can enable grids in different regions generated separately without considering their interfaces, and thereby can reduce the efforts in grid generation for complex geometries. Another advantage of the overset grid technique is that it can reduce the total number of grid points by using different mesh resolutions in different regions. This is helpful to reduce the total computational cost in the high-order numerical simulations. On the other hand, the immersed boundary condition [125] is also able to reduce computational efforts in the mesh generation process, since it does not use body fitted mesh and the wall boundary condition is set implicitly by adding a body force to resist the flow at grid points located inside the geometry.

The current simulations are computationally expensive, mostly due to the fine grid resolution in the wall-normal direction. In simulations where CFL is a constant, reducing the grid size will decrease the time step size Δt , thus requiring more time steps to complete simulations. The fine mesh resolution in the wall-normal direction is due to the fact that the S-A turbulence model needs to resolve the boundary layer down to the viscous layer. On the other hand, wall functions [126] can directly model the wall behaviour in the log layer using a large grid size in the wall-normal direction. Therefore, wall functions can reduce the computational cost and they are recommended to be implemented in SotonCAA as a future work.

7.2.2 Physics of landing gear wheel flows and acoustics

A landing gear wheel can be simplified as a circular cylinder with a small spanwise length-to-diameter ratio W/D , and the mean flow field around such a cylinder is asymmetric as demonstrated by Zdravkovich *et al.* [13]. There might be a critical ratio, under which flow asymmetry can occur. This critical ratio might also be dependent on the Reynolds number. It is recommended in the future work to investigate the mechanisms of this asymmetry, focusing on the end effects, by performing numerical simulations at different W/D .

The tandem wheels in this thesis are set with a separation distance of $L/D = 1.5$. Spagnolo *et al.* [42, 43] experimentally and numerically studied the aerodynamic forces (lift and drag) of tandem wheels at three different separation distances ($L/D = 1.1, 1.3$ and 1.5). They demonstrated that smaller separation distance can result in larger flow interactions and higher surface pressure fluctuations. It will be beneficial to study tandem CADWIE wheels with different separation distances, which can help to determine how the separation distance affects the flow interactions and if the current findings at $L/D = 1.5$ are applicable to smaller separation distances.

Appendix A

Temporal Scheme Error Analysis

In this appendix, the implementation of the Implicit Time Stepping (ITS) method in Section 3.5 is validated by simulating an inviscid vortex convection case and a 2D circular flow case. The efficiency of the implicit time marching approach is demonstrated by comparing with the explicit Low-Dispersion and low-Dissipation Runge-Kutta (LDDRK) method of Hu *et al.* [96].

In the current simulations, the CFL number is defined by,

$$\text{CFL} = \max \{ \text{CFL}_x, \text{CFL}_y, \text{CFL}_z \}, \quad (\text{A.1})$$

with

$$\text{CFL}_x = \frac{(u + c) \Delta t}{\Delta x}, \quad \text{CFL}_y = \frac{(v + c) \Delta t}{\Delta y}, \quad \text{CFL}_z = \frac{(w + c) \Delta t}{\Delta z}, \quad (\text{A.2})$$

where u, v, w are the flow convective speeds in the x, y, z directions, respectively, c is the speed of sound, and Δt is the time step size.

A.1 Inviscid vortex convection

The prescribe of the vortex and its analytical solution are given in Section 4.2.1. The simulation is performed on a 2D Cartesian grid, with a domain size of $L \times L = 50 \text{ m} \times 50 \text{ m}$, at $\text{CFL}=0.5$ using both the ITS and LDDRK methods. The vortex core starts at $(x, y) = (-\frac{L}{2}, 0)$, with the origin of the axes at the centre of the domain, and the errors in pressure are measured when the vortex core reaches $(x, y) = (\frac{L}{2}, 0)$ by

$$\text{Error} = \max \{ |p - p_a| / p_\infty \}, \quad (\text{A.3})$$

where p_a is the analytical pressure given by Equation 4.1d. The pressure errors are computed at different grid resolutions and are plotted in Figure A.1. The ITS and LDDRK methods demonstrate the same convergence rate with comparable performance.

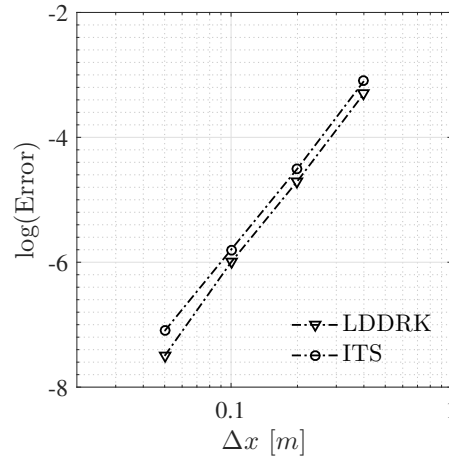


Figure A.1: Pressure errors against different grid resolutions using the Implicit Time Stepping (ITS) method and the explicit Low-Dispersion and low-Dissipation Runge-Kutta (LDDRK) method.

A.2 Circular cylinder flow

The second test case is a 2D URANS simulation of flow around a circular cylinder. Details of the numerical setup and flow conditions are provided in Section 4.2.2. The flow data was collected for approximately 100 oscillation cycles. The CFL number for the LDDRK scheme was set to be 0.7 to maintain the numerical stability. The implicit temporal method can reach a larger CFL number without instability, and it was set to be $0.7 \leq \text{CFL} \leq 25$ in the simulations.

The surface pressure coefficient C_p obtained by the ITS and LDDRK schemes at different CFL numbers is plotted in Figure A.2, where the predictions are very close, indicating that the application of the ITS scheme at a larger CFL number can still provide comparable results with the explicit scheme at a small CFL number. However, the simulations of 100 oscillation cycles show that the choice of ITS scheme at CFL=25 is about $20\times$ faster than the LDDRK scheme at CFL=0.7, which confirms the efficiency of the implicit time stepping method for wall-bounded viscous flow at high Reynolds number. The PSD of the lift coefficient C_L is given in Figure A.3. It shows that the shedding frequency and amplitude are well predicted by the implicit scheme at a higher CFL number. The predicted mean drag coefficient is summarised in Table A.1, where the variance of \bar{C}_D is within 2%.

The local CFL number at each grid point is provided in Figure A.4, where the globally maximum CFL number is 25. It demonstrates that only a small part of the boundary layer region has a CFL number larger than 1, whereas the majority of the domain shows $\text{CFL} < 0.1$, suggesting that the aerodynamic and acoustic features in the majority of the computational domain can be well captured.

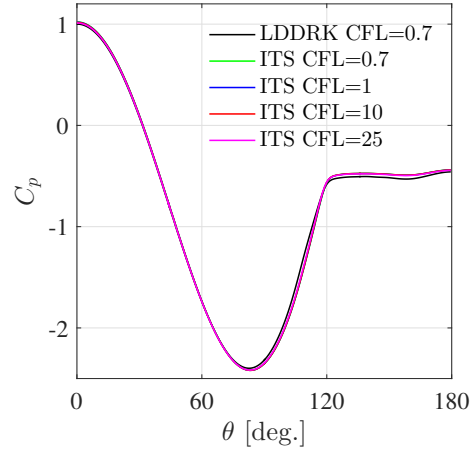


Figure A.2: Mean pressure coefficient using two time-stepping methods with different CFL numbers.

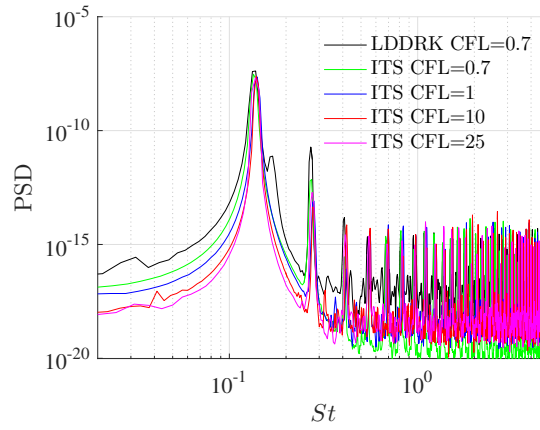


Figure A.3: PSD of the lift coefficient C_L using the two time-stepping methods with different CFL numbers.

Scheme	CFL	\bar{C}_D
LDDRK	0.7	0.378
ITS	0.7	0.378
	1	0.377
	10	0.375
	25	0.373

Table A.1: Mean drag coefficient \bar{C}_D using two time-stepping schemes with different CFL numbers.

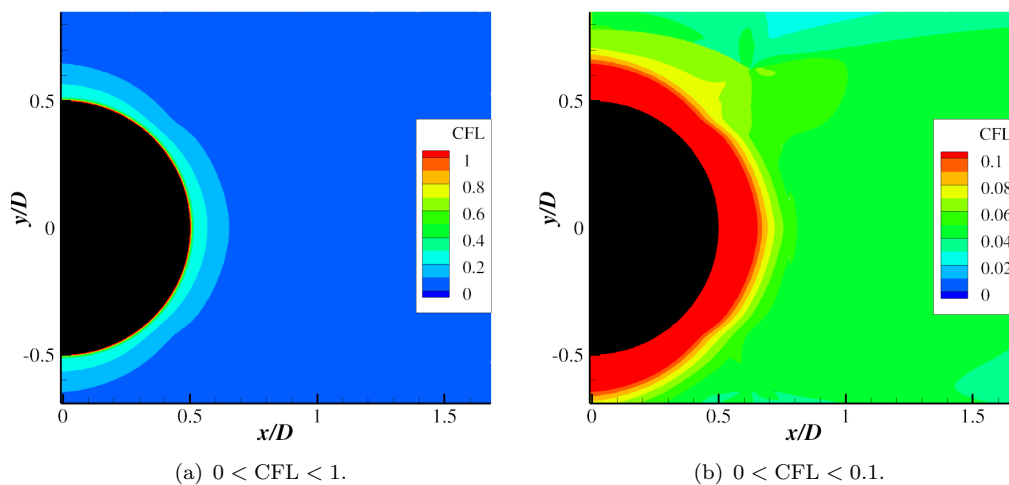


Figure A.4: Instantaneous local CFL number with the global $\text{CFL}_{\max} = 25$.

In conclusion, the implicit temporal scheme can provide comparable results with the explicit temporal scheme, and can reduce the computational cost by using a larger CFL number. For wall-bounded viscous flows, the maximum CFL number is in the boundary layer region, where the aerodynamic effects dominate the acoustic effects. For the rest of the computational domain, the CFL number is normally smaller than 0.1, and both the aerodynamic and acoustic properties can be well captured at such a small CFL number in the simulations.

Appendix B

Validation of S-A Turbulence Model

The S-A turbulence model in Section 3.7.1 is validated by a flat plate simulation, against CFL3D data from NASA [127]. The computational setup is demonstrated in Figure B.1. The mesh consists of 545 and 385 grid points in the x and y directions, respectively. The convergent solution was obtained with an average of 5×10^5 time steps at CFL= 15. The comparisons of nondimensional velocity profiles and turbulent eddy viscosity profiles at $x = 0.97$ are plotted in Figure B.2, where good agreements with CFL3D results and empirical solutions have been obtained. At $y = 0.018$ in Figure B.2(b), the eddy viscosity predicted by SotonCAA is slightly higher than CFL3D data. However, the discrepancy is of one grid size resolution and is most likely due to the different numerical methods between SotonCAA and CFL3D.

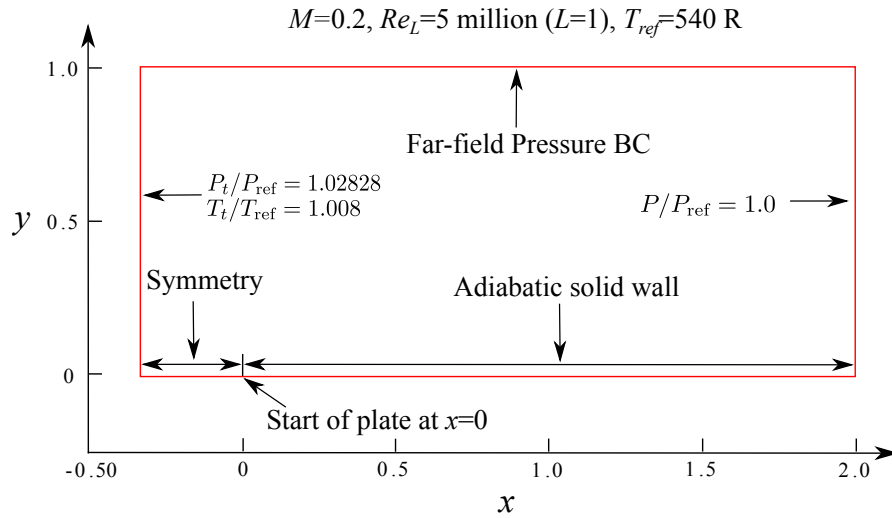


Figure B.1: The computational setup for the 2D flat plate case [127].

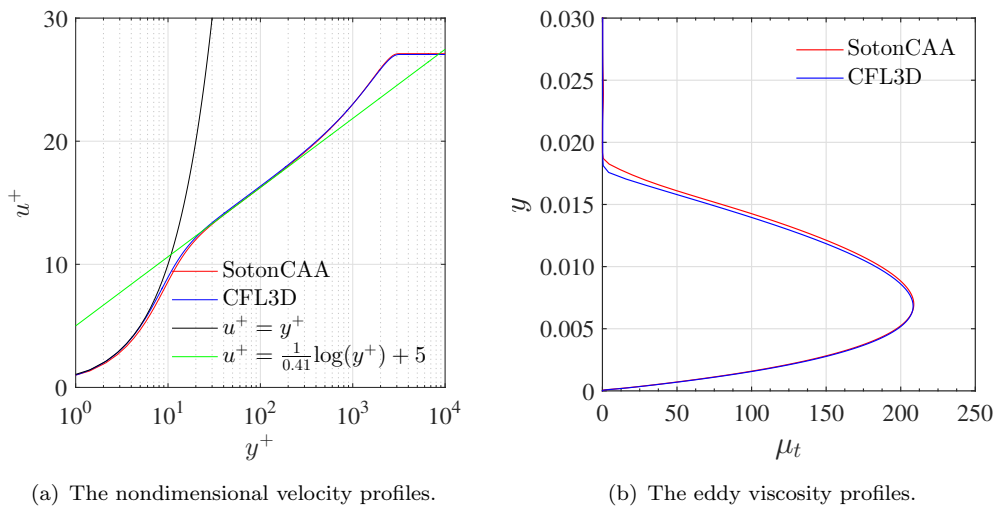


Figure B.2: Comparisons of non-dimensional velocity profiles and eddy viscosity profiles at $x = 0.97$ for the 2D flat plate case.

Appendix C

Cell-Centred Interpolation Schemes

C.1 FVI boundary closure schemes

Following the same procedure in the derivation of interior FVI schemes in Section 4.3.1, the boundary closure schemes without halo points can be expressed as,

$$i = 0 : \quad \left\{ \begin{array}{l} f_0^e + \gamma_{01}f_1^e + \gamma_{02}f_2^e = \sum_{m=0}^6 b_{0m}^e f_m, \\ f_0^w + \gamma_{01}f_1^w + \gamma_{02}f_2^w = \sum_{m=0}^6 b_{0m}^w f_m. \end{array} \right. \quad (\text{C.1a})$$

$$i = 1 : \quad \left\{ \begin{array}{l} \gamma_{10}f_0^e + f_1^e + \gamma_{12}f_2^e + \gamma_{13}f_3^e = \sum_{m=0}^6 b_{1m}^e f_m, \\ \gamma_{10}f_0^w + f_1^w + \gamma_{12}f_2^w + \gamma_{13}f_3^w = \sum_{m=0}^6 b_{1m}^w f_m. \end{array} \right. \quad (\text{C.1b})$$

$$i = 2 : \quad \left\{ \begin{array}{l} \gamma_{20}f_0^e + \gamma_{21}f_1^e + f_2^e + \gamma_{23}f_3^e + \gamma_{24}f_4^e = \sum_{m=0}^6 b_{2m}^e f_m, \\ \gamma_{20}f_0^w + \gamma_{21}f_1^w + f_2^w + \gamma_{23}f_3^w + \gamma_{24}f_4^w = \sum_{m=0}^6 b_{2m}^w f_m. \end{array} \right. \quad (\text{C.1c})$$

with the new coefficients written as,

$$i = 0 : \quad \left\{ \begin{array}{l} b_{00}^e = b_{06}^w = 0, \\ b_{01}^e = b_{00}^w = b_{01} + b_{02} + b_{03} + b_{04} + b_{05} + b_{06}, \\ b_{02}^e = b_{01}^w = b_{02} + b_{03} + b_{04} + b_{05} + b_{06}, \\ b_{03}^e = b_{02}^w = b_{03} + b_{04} + b_{05} + b_{06}, \\ b_{04}^e = b_{03}^w = b_{04} + b_{05} + b_{06}, \\ b_{05}^e = b_{04}^w = b_{05} + b_{06}, \\ b_{06}^e = b_{05}^w = b_{06}. \end{array} \right. \quad (\text{C.2a})$$

$$i = 1 : \quad \left\{ \begin{array}{l} b_{10}^e = b_{16}^w = 0, \\ b_{11}^e = b_{10}^w = -b_{10}, \\ b_{12}^e = b_{11}^w = b_{12} + b_{13} + b_{14} + b_{15} + b_{16}, \\ b_{13}^e = b_{12}^w = b_{13} + b_{14} + b_{15} + b_{16}, \\ b_{14}^e = b_{13}^w = b_{14} + b_{15} + b_{16}, \\ b_{15}^e = b_{14}^w = b_{15} + b_{16}, \\ b_{16}^e = b_{15}^w = b_{16}. \end{array} \right. \quad (\text{C.2b})$$

$$i = 2 : \quad \left\{ \begin{array}{l} b_{20}^e = b_{26}^w = 0, \\ b_{21}^e = b_{20}^w = -b_{20}, \\ b_{22}^e = b_{21}^w = -(b_{20} + b_{21}), \\ b_{23}^e = b_{22}^w = b_{23} + b_{24} + b_{25} + b_{26}, \\ b_{24}^e = b_{23}^w = b_{24} + b_{25} + b_{26}, \\ b_{25}^e = b_{24}^w = b_{25} + b_{26}, \\ b_{26}^e = b_{25}^w = b_{26}. \end{array} \right. \quad (\text{C.2c})$$

And the boundary closure schemes with halo points can be expressed as,

$$i = 0 : \quad \left\{ \begin{array}{l} f_0^e + \gamma_{01}^h f_1^e + \gamma_{02}^h f_2^e = \sum_{m=-3}^4 b_{0m}^{he} f_m, \\ f_0^w + \gamma_{01}^h f_1^w + \gamma_{02}^h f_2^w = \sum_{m=-3}^4 b_{0m}^{hw} f_m. \end{array} \right. \quad (\text{C.3a})$$

$$i = 1 : \quad \left\{ \begin{array}{l} \gamma_{10}^h f_0^e + f_1^e + \gamma_{12}^h f_2^e + \gamma_{13}^h f_3^e = \sum_{m=-3}^4 b_{1m}^{he} f_m, \\ \gamma_{10}^h f_0^w + f_1^w + \gamma_{12}^h f_2^w + \gamma_{13}^h f_3^w = \sum_{m=-3}^4 b_{1m}^{hw} f_m. \end{array} \right. \quad (\text{C.3b})$$

with the new coefficients written as,

$$i = 0 : \left\{ \begin{array}{l} b_{0(-3)}^{he} = b_{04}^{hw} = 0, \\ b_{0(-2)}^{he} = b_{0(-3)}^{hw} = -b_{0(-3)}^h, \\ b_{0(-1)}^{he} = b_{0(-2)}^{hw} = -\left(b_{0(-3)}^h + b_{0(-2)}^h\right), \\ b_{00}^{he} = b_{0(-1)}^{hw} = -\left(b_{0(-3)}^h + b_{0(-2)}^h + b_{0(-1)}^h\right), \\ b_{01}^{he} = b_{00}^{hw} = b_{01}^h + b_{02}^h + b_{03}^h + b_{04}^h, \\ b_{02}^{he} = b_{01}^{hw} = b_{02}^h + b_{03}^h + b_{04}^h, \\ b_{03}^{he} = b_{02}^{hw} = b_{03}^h + b_{04}^h, \\ b_{04}^{he} = b_{03}^{hw} = b_{04}^h. \end{array} \right. \quad (C.4a)$$

$$i = 1 : \left\{ \begin{array}{l} b_{1(-3)}^{he} = b_{14}^{hw} = 0, \\ b_{1(-2)}^{he} = b_{1(-3)}^{hw} = -b_{1(-3)}^h, \\ b_{1(-1)}^{he} = b_{1(-2)}^{hw} = -\left(b_{1(-3)}^h + b_{1(-2)}^h\right), \\ b_{10}^{he} = b_{1(-1)}^{hw} = -\left(b_{1(-3)}^h + b_{1(-2)}^h + b_{1(-1)}^h\right), \\ b_{11}^{he} = b_{10}^{hw} = -\left(b_{1(-3)}^h + b_{1(-2)}^h + b_{1(-1)}^h + b_{10}^h\right), \\ b_{12}^{he} = b_{11}^{hw} = b_{12}^h + b_{13}^h + b_{14}^h, \\ b_{13}^{he} = b_{12}^{hw} = b_{13}^h + b_{14}^h, \\ b_{14}^{he} = b_{13}^{hw} = b_{14}^h. \end{array} \right. \quad (C.4b)$$

C.2 HRI boundary closure schemes using halo point

At boundary $i = 0$ and $i = 1$, where the central schemes in Equation 4.18 cannot be applied, a new set of schemes has been developed to use halo point information. These schemes are fourth-order accurate by satisfying the condition in Equation 4.19. Following the derivation of fully biased boundary treatment for the HRI scheme in Section 4.3.1, a fourth-order polynomial extrapolation is used to predict the cell face variables beyond the boundary. The parameters k_1 and k_2 used in Equations 4.24 and 4.25 to optimise the transfer function profile are listed in Table C.1. The final boundary schemes are expressed in Equation C.5 with coefficients provided in Table C.2. Figure C.1 is an illustration of the transfer function profiles for the boundary schemes using halo points.

	$i = 0$	$i = 1$
k_1	0.48π	0.5π
k_2	0.78π	0.758π

Table C.1: Parameters that are used to optimise the characteristic resolution of HRI boundary schemes using halo point information.

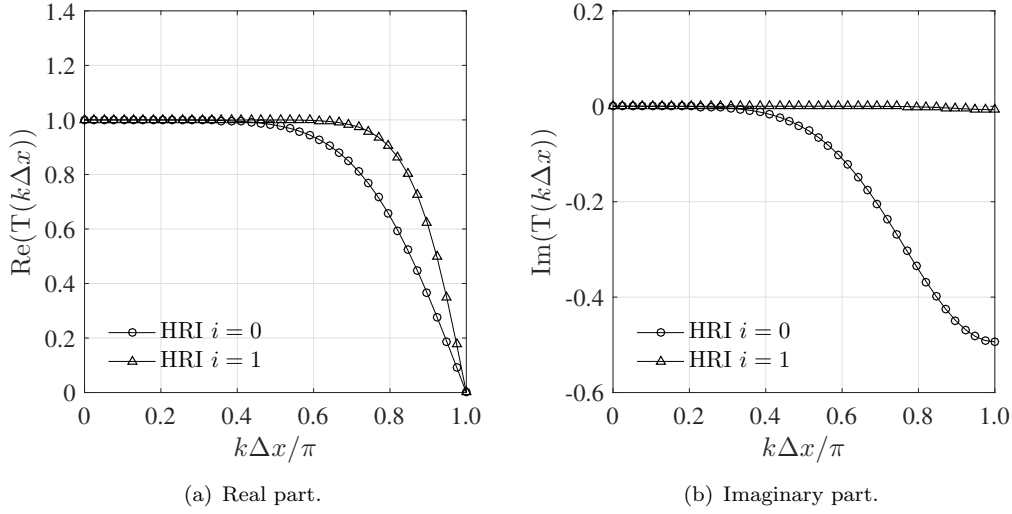


Figure C.1: Transfer function profiles for HRI boundary schemes using halo points.

$$\begin{aligned}
 i = 0 : \quad & f_{-\frac{1}{2}} + \gamma_{01}^{H^2} f_{\frac{1}{2}} + \gamma_{02}^{H^2} f_{\frac{3}{2}} = \sum_{m=0}^5 b_{0m}^{H^2} f_{m-3}, \\
 i = 1 : \quad & \gamma_{10}^{H^2} f_{-\frac{1}{2}} + f_{\frac{1}{2}} + \gamma_{12}^{H^2} f_{\frac{3}{2}} + \gamma_{13}^{H^2} f_{\frac{5}{2}} = \sum_{m=0}^5 b_{1m}^{H^2} f_{m-2}.
 \end{aligned} \tag{C.5}$$

Coefficients	$i = 0$	$i = 1$
$\gamma_{i0}^{H^2}$	N/A	0.389345187935037
$\gamma_{i1}^{H^2}$	0.362913853030715	N/A
$\gamma_{i2}^{H^2}$	0.051255820548616	0.389396524843092
$\gamma_{i3}^{H^2}$	N/A	-0.001019284598410
$\gamma_{i4}^{H^2}$	N/A	N/A
$b_{i0}^{H^2}$	0.002681096680680	-0.003869642868503
$b_{i1}^{H^2}$	-0.046094421322411	0.095147881015648d0
$b_{i2}^{H^2}$	0.450588091452707	-0.133915825896421
$b_{i3}^{H^2}$	0.902677004087481	0.797896515140237
$b_{i4}^{H^2}$	0.083852609173540	0.798655901777178
$b_{i5}^{H^2}$	0.020465293507334	-0.004156870927759

Table C.2: Coefficients in HRI schemes using halo point information in Equation C.5.

Appendix D

Roe's Riemann Solver

The Roe's solution to a Riemann problem can be obtained by firstly considering a one-dimensional hyperbolic system in a conservation form,

$$\frac{\partial \mathbf{Q}}{\partial t} + \frac{\partial \mathbf{F}(\mathbf{Q})}{\partial x} = 0, \quad (\text{D.1})$$

with an initial condition,

$$\mathbf{Q}(x, 0) = \mathbf{Q}_L \quad (x < 0), \quad \mathbf{Q}(x, 0) = \mathbf{Q}_R \quad (x > 0), \quad (\text{D.2})$$

where \mathbf{Q} and \mathbf{F} represent the state variables and fluxes, respectively. The subscripts L and R mean the left part and the right part at the discontinuity. The approximation of $\mathbf{Q}(x, t)$ at the discontinuity can be achieved by modifying the fluxes $\mathbf{F}(\mathbf{Q})$. For the N-S equations, the state variables and inviscid fluxes can be expressed as,

$$\begin{aligned} \mathbf{Q} &= [\rho, \rho u, \rho v, \rho w, \rho E]^T, \\ \mathbf{F} &= [\rho u, \rho u u + p, \rho u v, \rho u w, (\rho E + p) u]^T. \end{aligned} \quad (\text{D.3})$$

The fluxes at the discontinuity can be corrected by discriminating between information with different propagation speed. This is accomplished as follows. Let \mathbf{F}_e be the state obtained from the Roe's solution for $x = 0, t > 0$. Then, it can be expressed as [128],

$$\mathbf{F}_e = \frac{1}{2} (\mathbf{F}(\mathbf{Q}_L) + \mathbf{F}(\mathbf{Q}_R)) = \frac{1}{2} \sum_{i=1}^5 \tilde{a}_i \left| \tilde{\lambda}_i \right| \tilde{K}_i, \quad (\text{D.4})$$

where $\tilde{\cdot}$ is the Roe's average. The averaged dynamic variables at the discontinuity are given by,

$$\begin{aligned}\tilde{\rho} &= [(\sqrt{\rho_L} + \sqrt{\rho_R})/2]^2, \\ \tilde{u} &= (\sqrt{\rho_L}u_L + \sqrt{\rho_R}u_R) / (\sqrt{\rho_L} + \sqrt{\rho_R}), \\ \tilde{v} &= (\sqrt{\rho_L}v_L + \sqrt{\rho_R}v_R) / (\sqrt{\rho_L} + \sqrt{\rho_R}), \\ \tilde{w} &= (\sqrt{\rho_L}w_L + \sqrt{\rho_R}w_R) / (\sqrt{\rho_L} + \sqrt{\rho_R}), \\ \tilde{H} &= (\sqrt{\rho_L}H_L + \sqrt{\rho_R}H_R) / (\sqrt{\rho_L} + \sqrt{\rho_R}), \\ \tilde{c} &= \sqrt{(\gamma - 1) \left(\tilde{H} - \frac{1}{2}(\tilde{u}^2 + \tilde{v}^2 + \tilde{w}^2) \right)},\end{aligned}\tag{D.5}$$

where the total enthalpy H is $E + \frac{p}{\rho}$. $\tilde{\lambda}$ is the eigenvalues of the hyperbolic system,

$$\tilde{\lambda}_1 = \tilde{u} - \tilde{c}, \quad \tilde{\lambda}_2 = \tilde{\lambda}_3 = \tilde{\lambda}_4 = \tilde{u}, \quad \tilde{\lambda}_5 = \tilde{u} + \tilde{c},\tag{D.6}$$

and \tilde{K}_i are the eigenvectors,

$$\begin{aligned}\tilde{K}_1 &= [1, \tilde{u} - \tilde{c}, \tilde{v}, \tilde{w}, \tilde{H} - \tilde{u}\tilde{c}]^T, \\ \tilde{K}_2 &= [1, \tilde{u}, \tilde{v}, \tilde{w}, \frac{1}{2}\tilde{V}^2]^T, \\ \tilde{K}_3 &= [0, 0, 1, 0, \tilde{v}]^T, \\ \tilde{K}_4 &= [0, 0, 1, 0, \tilde{w}]^T, \\ \tilde{K}_5 &= [1, \tilde{u} - \tilde{c}, \tilde{v}, \tilde{w}, \tilde{H} + \tilde{u}\tilde{c}]^T,\end{aligned}\tag{D.7}$$

where $\tilde{V} = \sqrt{\tilde{u}^2 + \tilde{v}^2 + \tilde{w}^2}$. The coefficients \tilde{a} are given by,

$$\begin{aligned}\tilde{a}_3 &= \Delta Q_3 - \tilde{v}\Delta Q_1, \\ \tilde{a}_4 &= \Delta Q_4 - \tilde{w}\Delta Q_1, \\ \tilde{a}_2 &= \frac{\gamma-1}{\tilde{c}^2} \left(\Delta Q_1 (\tilde{H} - \tilde{u}^2) + \tilde{u}\Delta Q_2 - \Delta Q_5 + \tilde{a}_3\tilde{v} + \tilde{a}_4\tilde{w} \right), \\ \tilde{a}_1 &= \frac{1}{2\tilde{c}} (\Delta Q_1 (\tilde{u} + \tilde{c}) - \Delta Q_2 - \tilde{c}\tilde{a}_2), \\ \tilde{a}_5 &= \Delta Q_1 - \tilde{a}_1 - \tilde{a}_2.\end{aligned}\tag{D.8}$$

The corrected fluxes \mathbf{F}_e are then applied to Equation D.1 to get the state variables \mathbf{Q} at the next time step.

Appendix E

Acoustic Corrections for Long-Span Bodies

In the tandem cylinders flow case, in order to reduce computational cost, a periodic boundary condition was applied in the spanwise direction to model a long-span body flow. The spanwise length in the simulation is $3D$, where D is the cylinder diameter. However, the spanwise length in the acoustic experiment is $16D$, and thus an acoustic correction is required to compare the simulation data with the experimental measurements.

Figure E.1 shows a schematic of a long-span body (L), which is divided into N subsections by L_s ($L = N \times L_s$), and L_s is the short span in the simulation. \hat{p}'_s is the acoustic pressure radiated by a subsection in the simulation, and \hat{p}'_L is the total acoustic pressure taking account of all the subsections. The far-field acoustic correction at different frequencies is based on the spanwise coherence length, which was proposed by Seo and

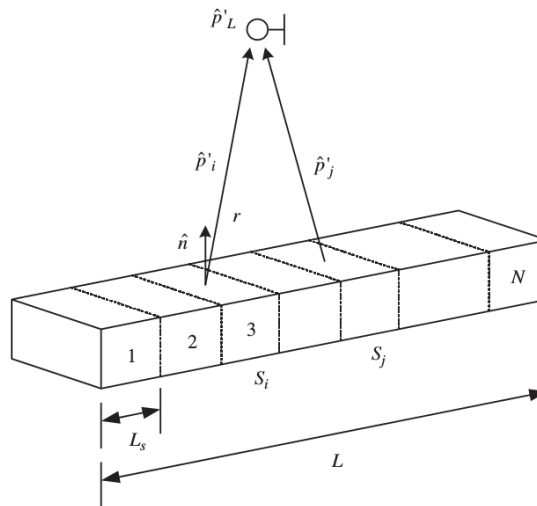


Figure E.1: Schematic of a long-span body divided by N subsections [119].

Moon [119]. The acoustic SPL is given by $\text{SPL}_L = \text{SPL}_s + \text{SPL}_c$, where SPL_c is the correction to the SPL obtained in the simulation (SPL_s),

$$\text{SPL}_c = \begin{cases} 10 \log(N) & L'_c/L_s \leq 1/\sqrt{\pi}, \\ 10 \log(L'_c/L_s) + 10 \log(\sqrt{\pi}N) & 1/\sqrt{\pi} < L'_c/L_s < N/\sqrt{\pi}, \\ 20 \log(N) & L'_c/L_s \geq N/\sqrt{\pi}, \end{cases} \quad (\text{E.1})$$

where L'_c is the spanwise coherence length, which is also a function of the frequency. L'_c can be determined by the following relationship,

$$\gamma'_{ij} = \exp\left(-\frac{(i-j)^2 L_s^2}{L_c'^2}\right), \quad (\text{E.2})$$

where γ'_{ij} is the spanwise coherence function of the acoustic pressure radiated from each subsection surface, and it can be estimated by the spanwise coherence function of the surface pressure [119] at points of interest. In the tandem cylinders simulation, the surface pressure coherence was computed at $\theta = 135^\circ$ on the upstream cylinder surface.

Appendix F

Resonant Frequencies of Acoustic Cavities

F.1 Cylindrical cavities

Figure F.1 is an illustration of the cylindrical cavity geometry used in the current simulations. The depth-to-diameter ratio ϖ is given by $\varpi = H/D$, where H and D represent the height and diameter of the cylindrical cavity. The Resonant frequency for this geometry can be expressed as [47],

$$f_{ijk} = \frac{c_\infty}{2\pi} \sqrt{\left(\frac{4\lambda_{jk}^2}{D^2} + \frac{i^2\pi^2}{4h'^2} \right)}, \quad (\text{F.1})$$

where $i = 0, 1, 3, 5, \dots$, $j/k = 0, 1, 2, \dots$, c_∞ is the speed of sound and λ_{ij} is given by,

$$J'_j(\lambda_{jk}) = 0, \quad (\text{F.2})$$

in which J is the Bessel function of first kind. The effective height taking account of the opening is provided by [129],

$$h' = H + 0.8216 \frac{D}{2}. \quad (\text{F.3})$$

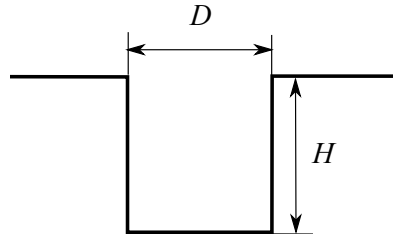


Figure F.1: Schematic of a cylindrical cavity geometry.

In the current work, the diameter of the cavity was chosen as $D = 100$ mm, and four depth-to-diameter ratios have been tested, which are $\varpi = 0.3, 0.6, 1.0$ and 1.5 . The speed of sound is 347.2 m/s. The resonant frequencies in Equation F.1 with different depth-to-diameter ratios are summarised in Table F.1.

(a) $\varpi = 0.3$.				
i, k	$j = 0$	$j = 1$	$j = 2$	$j = 3$
0, 0	0	2.03	3.37	4.64
0, 1	4.23	5.89	7.40	8.85
1, 0	1.22	2.37	3.59	4.80
1, 1	4.40	6.01	7.51	8.94

(b) $\varpi = 0.6$.				
i, k	$j = 0$	$j = 1$	$j = 2$	$j = 3$
0, 0	0	2.03	3.37	4.64
0, 1	4.23	5.89	7.40	8.85
1, 0	0.858	2.21	3.48	4.72
1, 1	4.32	5.95	7.46	8.89

(c) $\varpi = 1.0$.				
i, k	$j = 0$	$j = 1$	$j = 2$	$j = 3$
0, 0	0	2.03	3.37	4.64
0, 1	4.23	5.89	7.40	8.85
1, 0	0.615	2.12	3.43	4.68
1, 1	4.28	5.92	7.43	8.87

(d) $\varpi = 1.5$.				
i, k	$j = 0$	$j = 1$	$j = 2$	$j = 3$
0, 0	0	2.03	3.37	4.64
0, 1	4.23	5.89	7.40	8.85
1, 0	0.45	2.08	3.40	4.66
1, 1	4.26	5.91	7.42	8.86

Table F.1: Cylindrical cavity resonant frequencies [kHz] with different depth-to-diameter ratios.

F.2 Cylindrical cavities with annular volume

Figure F.2 is an illustration of the cylindrical cavity geometry with annular volume at the centre, which is a representation of the hub cavity for the CADWIE wheel case. The Resonant frequency for this geometry can be expressed as [47],

$$f_{ijk} = \frac{c_\infty}{2\pi} \sqrt{\left(\frac{4\lambda_{jk}^2}{D_1^2} + \frac{i^2\pi^2}{4h'^2} \right)}, \quad (\text{F.4})$$

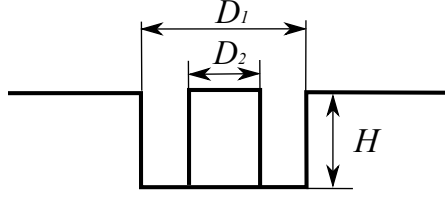


Figure F.2: Schematic of a cylindrical cavity geometry with annular volume at the centre.

where $i = 0, 1, 3, 5, \dots$, $j/k = 0, 1, 2, \dots$, c_∞ is the speed of sound and λ_{ij} is given by,

$$J'_j(\lambda_{jk}) Y'_j\left(\frac{D_2}{D_1} \lambda_{jk}\right) - J'_j\left(\frac{D_2}{D_1} \lambda_{jk}\right) Y'_j(\lambda_{jk}) = 0, \quad (\text{F.5})$$

in which J and Y are the Bessel function of first kind and second kind. λ_{jk} in Equation F.5 can be approximated by [47],

$$\lambda_{jk}^2 \approx \left(\frac{k\pi D_1}{D_1 - D_2}\right)^2 + \left(\frac{2jD_1}{D_1 + D_2}\right)^2, \quad \text{if } \frac{D_2}{D_1} > 0.5. \quad (\text{F.6})$$

It should also be mentioned that the depth mode is associated with the quarter-wave length, i.e. $i = 0, 1, 3, 5, \dots$, and no even integers, which is due to the approximated boundary condition set at the opening of the cavity given by,

$$p_a = 0, \quad (\text{F.7})$$

where p_a is the acoustic pressure. This boundary condition is true if the cavity opens on a very large uniform body of fluid without any pressure perturbations. However, for real cavities, the shear layer will significantly influence the pressure at the opening. Alternatively, Rona [130] proposed another boundary condition of zero velocity perturbations, which can be satisfied by setting the spatial derivatives of pressure in the direction normal to the opening to be zero, i.e.

$$\frac{\partial p_a}{\partial h} = 0, \quad \text{at the cavity opening.} \quad (\text{F.8})$$

Rona [130] also gave a physical interpretation for this boundary condition in Equation F.8. The shear layer motion at the cavity mouth will induce flow separations, forming a jet that dissipates the kinetic energy of the acoustic velocity by viscous stresses. Therefore, the flow oscillation is a damped process. But the resonant frequencies are undamped modes, so setting the acoustic velocity to be zero can help to avoid this dissipative mechanism. By using the boundary condition in Equation F.8, the same resonant frequencies in Equation F.4 can be obtained but with integer i equal to zero or even numbers, i.e. $i = 0, 2, 4, 6, \dots$. Thus, Rona's boundary condition will help to select more frequencies that are not included by the boundary condition in Equation F.7. The range of i in Equation F.4 therefore can be any positive integer or zero.

The effective height taking account of the opening is provided by [129],

$$h' = H + 0.8216 \frac{D_1}{2}. \quad (\text{F.9})$$

In the current work, the geometry parameters are $D_1 = 177$ mm, $D_2 = 114$ mm and $H = 59$ mm. The speed of sound is 340.3 m/s. The resonant frequencies in Equation F.4 are summarised in Table F.2.

i, k	$j = 0$	$j = 1$	$j = 2$	$j = 3$
0, 0	0	0.745	1.489	2.233
0, 1	5.402	5.453	5.603	5.324
1, 0	0.646	0.986	1.623	2.325
1, 1	5.440	5.491	5.640	5.881
2, 0	1.292	1.491	1.971	2.580
2, 1	5.554	5.604	5.750	5.986

Table F.2: Resonant frequencies [kHz] for a cylindrical cavity with annular volume at the centre.

Appendix G

Cylindrical Cavity Simulations

G.1 Introduction

Intensive studies have been performed previously on aeroacoustic and hydrodynamic characteristics of cylindrical cavity flows. The depth-to-diameter ratio (ϖ) has important effects on the mean flow characteristics [56]. However, the acoustic performance of cylindrical cavities with different ϖ is relatively less studied. For deep cylindrical cavities ($\varpi \geq 1.0$), significant tones are found [45, 46, 49], which are due to interactions between acoustic resonances and shear layers. The sound from shallow cylindrical cavities can be more broadband. In this appendix, the effect of depth-to-diameter ratios on both the aerodynamic and acoustic features of cylindrical cavities are investigated by performing simulations at $\varpi = 0.3, 0.6, 1.0$ and 1.5 , and $\varpi = 0.3$ corresponds to a hub cavity on a landing gear wheel.

G.2 Computational setup

The cylindrical cavities in the simulations have a diameter of $D = 100$ mm, with four different heights H , and the corresponding depth-to-diameter ratios ($\varpi = H/D$) are $\varpi = 0.3, 0.6, 1.0$ and 1.5 .

The computational domain is shown in Figure G.1 with the origin of the physical coordinates at the centre of the cavity opening. The cavity is mounted on a flat plate (no-slip wall boundary condition), extending $3.7D$, $5.2D$ and $5D$ in the upstream, downstream and spanwise directions, respectively, similar to the experimental geometry by Marsden *et al.* [46]. The computational domain is $5D$ wide in the transverse direction. Upstream of the flat plate, a symmetry boundary condition is applied in the range of $-5.7 < x/D < -3.7$. A far-field pressure boundary condition is imposed at the inlet

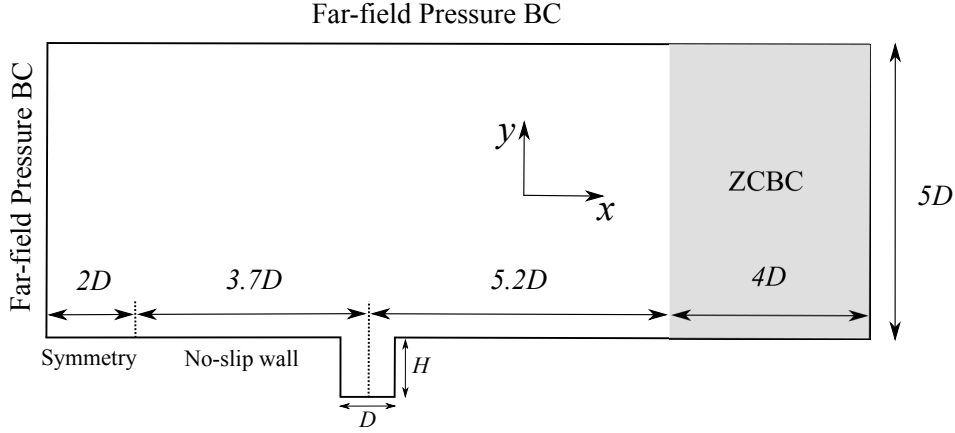


Figure G.1: Computational domain and boundary conditions for cylindrical cavity simulations.

and upper edges, while the outflow boundary condition is supplied by the ZCBC with a width of $4D$. A periodic boundary condition is applied at the spanwise boundary.

The first grid point is at a distance of 1.0×10^{-5} m away from the wall to ensure that the value of the wall distance y^+ is approximately 1.0. A grid stretching ratio of 1.1 in the wall normal direction is used to relax the grid distributions in the boundary layer. The cavity walls are meshed by 160 and 90 grid points in the azimuthal and radial directions. These were further refined to 200 and 125 grid points but no significant improvement in the wall pressure spectra was achieved. Thus, 160 grid points in the azimuthal direction and 90 grid points in the radial direction are used in this work. The resolutions in the depth direction are kept the same for $\varpi = 0.3, 0.6, 1.0$ and 1.5 by 128, 145, 165 and 211 grid points, which give a total number of grid points of 6.1×10^6 , 6.3×10^6 , 6.5×10^6 and 7.1×10^6 , respectively. Figure G.2 is an illustration of the grid distributions on the $y/D = 0$ plane at the cavity opening.

The freestream quantities are $\rho_\infty = 1.16 \text{ kg/m}^3$, $p_\infty = 98151 \text{ Pa}$ and $T_\infty = 300 \text{ K}$. The inflow Mach number is $M_\infty = 0.2$, which is the same value used in the experiment by Marsden *et al.* [46]. The Reynolds numbers based on the cavity diameter D is 4.41×10^5 . The time step size for the simulations is $\Delta t = 2.88 \times 10^{-7}$ seconds, corresponding to a CFL number of 12. The flow was fully developed after a convective time of approximately $10D$, after which the aerodynamic and acoustic data are collected for 0.4 seconds in physical times (approximately $280D$ for the convective time). The far-field observer angles are defined in Figure G.3.

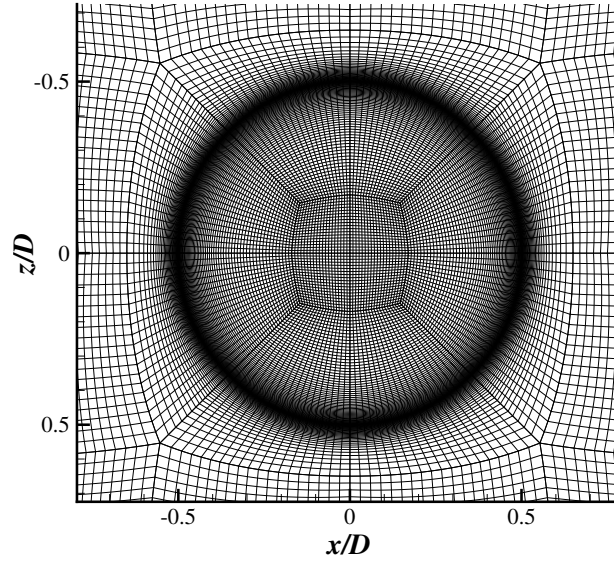


Figure G.2: Mesh topology and grid distributions at cylindrical cavity opening on the $y/D = 0$ plane.

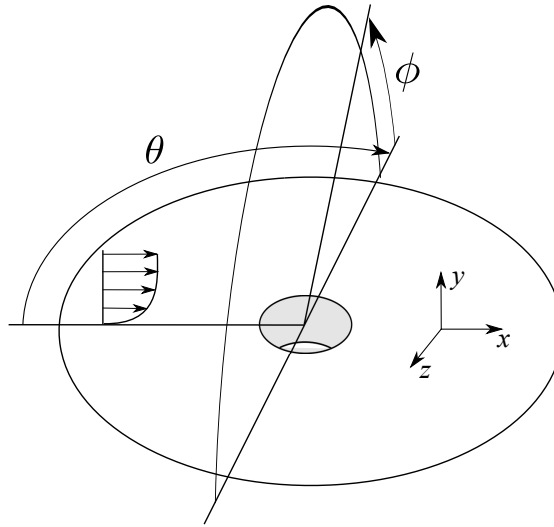
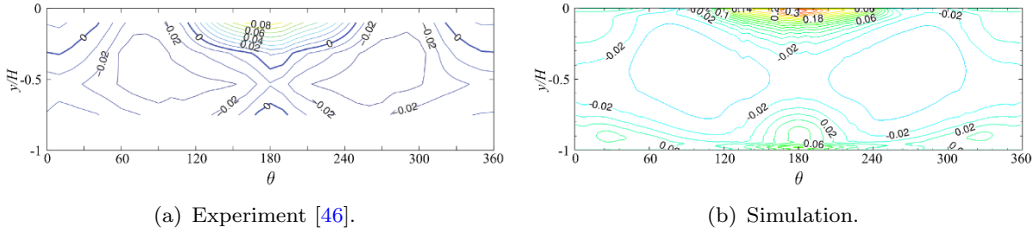


Figure G.3: Definitions of observer angles θ and ϕ .

G.3 Validations and verifications

In this section, the numerical results at $\varpi = 1.0$ are firstly validated and verified against experimental and other numerical measurements, after which the comparisons of aerodynamic and acoustic characteristics at different depth-to-diameter ratios will be presented in Sections G.4 and G.5.

Figures G.4 and G.5 are the comparisons of the pressure coefficient C_p distributions on the cavity walls, where the profiles with respect to the inflow direction are almost symmetric. The shear layer at the cavity opening firstly impinges on the downstream



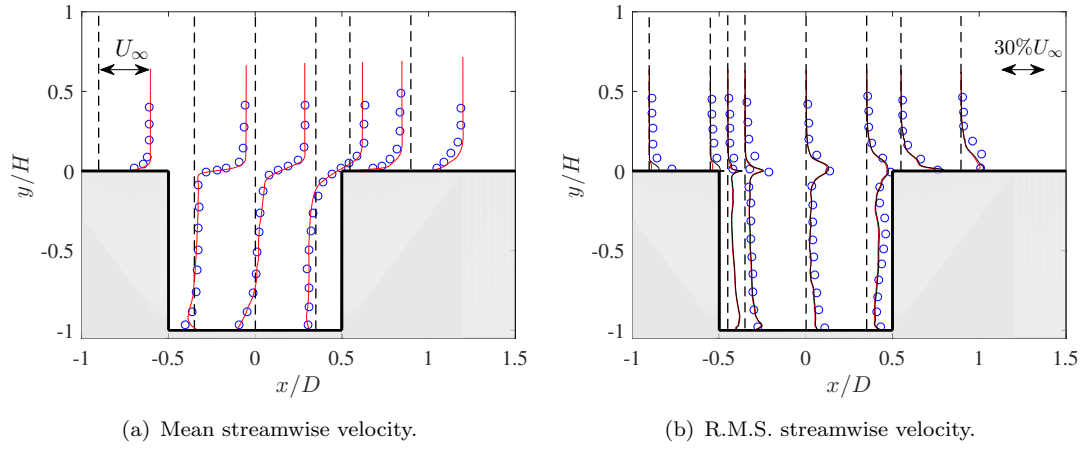


Figure G.6: Comparisons of mean and R.M.S. streamwise velocity profiles. \circ Experiments [54], — simulation (resolved), — simulation (resolved+modelled), --- monitor positions.

Thus,

$$-\overline{u'v'} = 0.3k. \quad (\text{G.2})$$

The Reynolds shear stress can be computed by using the Bossinesq's hypothesis,

$$-\overline{u'v'} = \nu_t \left(\frac{\partial \bar{U}}{\partial y} + \frac{\partial \bar{V}}{\partial x} \right). \quad (\text{G.3})$$

The modelled streamwise velocity fluctuations (\bar{u}') can therefore be obtained from Equations G.1, G.2 and G.3. Figure G.6(b) plots the comparisons of \bar{u}' , which is under-predicted in the upstream of the flat plate boundary layer and at the beginning of the shear layer. The under-prediction is due to the application of the RANS mode in the boundary layer region and thus the modelled fluctuation is much larger than the resolved part. A reasonable agreement of \bar{u}' is achieved towards the downstream of the shear layer and inside the cavity, which are the major noise source regions.

The unsteady pressures in the simulation are measured over a period of 0.4 seconds and then divided into 50 segments with 50% overlaying in the FFT processing. Figure G.7 demonstrates comparisons of the wall pressure spectra at $r/D = 0.35$ on the bottom wall against the experiment [133], LES simulation [133] and LBM simulation [134]. These simulations and experiment have the same flow conditions and geometry. It is clearly illustrated that a significant peak at 660 Hz and a small peak at approximately 2.1 kHz are present in all the spectra, and a third peak at approximately 3.4 kHz is shown at $\theta = 0^\circ, 90^\circ$ in the current DDES simulation and experiment. Both LBM and DDES simulations show a good prediction of the fundamental peak, which is under-predicted by more than 10 dB/Hz by the LES simulation, and the current DDES simulation performs more accurately than LBM and LES at the prediction of the second and third tones. However, DDES and LBM demonstrates an under-prediction of the broadband spectra

at high frequencies compared to the experiment and LES results, which is due to the lack of turbulent fluctuations in the upstream boundary layer. Chicheportiche and Gloerfelt [133] showed that the inclusion of velocity fluctuations in the flat plate boundary layer can help to increase the prediction of the broadband wall pressure spectra. Additionally, the LES simulation has a higher grid resolution (281×122 grid points in the azimuthal, axial directions inside the cavity) than the DDES simulation (160×90 grid points), and LES is less dissipative compared to the DDES model in the cavity wall region, which enables LES to more accurately simulate the broadband spectra. However, the level of the broadband spectra is more than 40 dB/Hz lower in comparison with the fundamental tone, implying that the dominant flow feature of the cavity flow is well captured. The wall pressure spectra on the sidewall are plotted in Figure G.8, where a significant tone again is shown at 660 Hz.

The Resonant frequencies for the cylindrical geometry can be expressed as [47],

$$f_{ijk} = \frac{c_\infty}{2\pi} \sqrt{\left(\frac{4\lambda_{jk}^2}{D^2} + \frac{i^2\pi^2}{4h'^2} \right)}, \quad (\text{G.4})$$

where $i = 0, 1, 3, 5, \dots$, denote the depth modes, and $j, k = 0, 1, 2, \dots$, represent the azimuthal (spinning) and radial modes, and λ_{ij} is given by,

$$J'_j(\lambda_{jk}) = 0, \quad (\text{G.5})$$

in which J is the Bessel function of first kind. The effective height taking account of the cavity opening is provided by [129],

$$h' = H + 0.8216 \frac{D}{2}. \quad (\text{G.6})$$

The resonant frequencies (f_{ijk}) are summarised in Appendix F.1.

Figure G.9 shows the wall pressure spectra on the cavity sidewall at $y/D = -0.1$ and cavity bottom wall at $r/D = 0.375$ as a function of θ , together with the resonant frequencies $f_{100}, f_{110}, f_{120}, f_{130}$. It can be seen that the fundamental spectral peak varies little with θ and has a similar value (approximately 130 dB/Hz) for both sidewall and bottom wall monitors. This fundamental frequency ($f = 660$ Hz) is close to the first depth mode at $f_{100} = 615$ Hz, implying that the cylindrical cavity flow is mainly driven by the acoustic resonance in the depth direction, which is reviewed in detail in Section 2.4.1. The azimuthal modes $f_{110}, f_{120}, f_{130}$ are also observable in both experimental and numerical simulation results. However, they are much weaker than the fundamental peak. A higher PSD level is demonstrated in the impingement zone centred at $\theta = 180^\circ$.

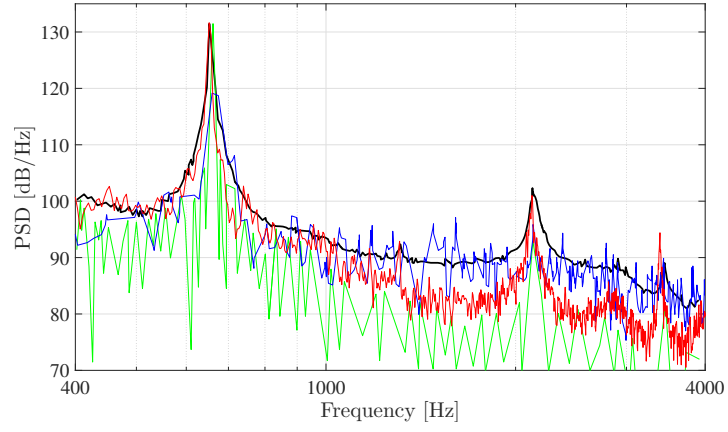
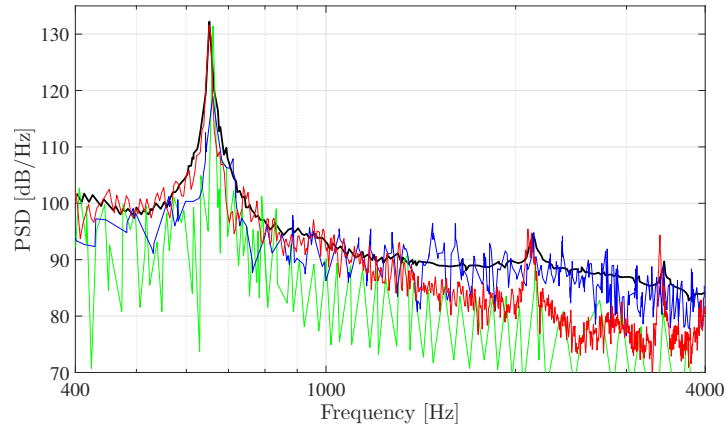
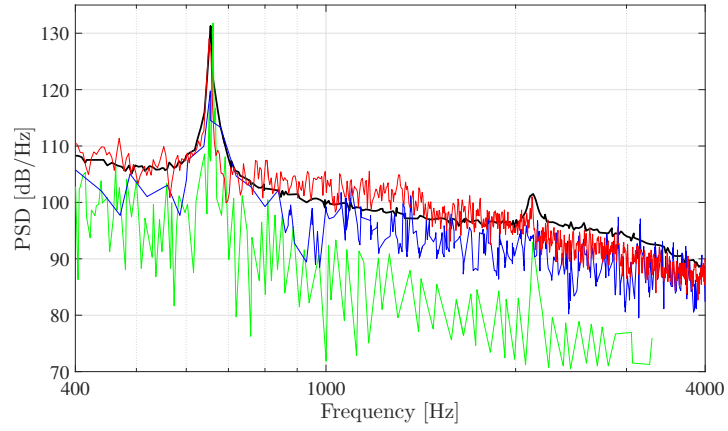
(a) $\theta = 0^\circ$, $x/D = -0.175$.(b) $\theta = 90^\circ$, $z/D = -0.175$.(c) $\theta = 180^\circ$, $x/D = 0.175$.

Figure G.7: Comparisons of wall pressure spectra at $r/D = 0.35$ on the bottom wall. — Experiments [133], — LES simulation [133], — LBM simulation [134], — DDES simulation.

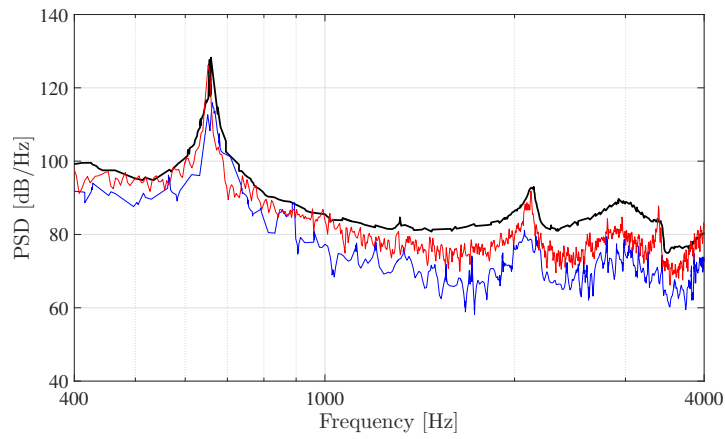
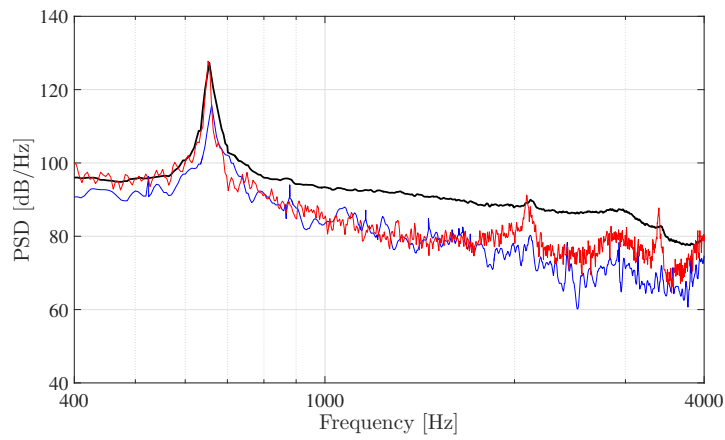
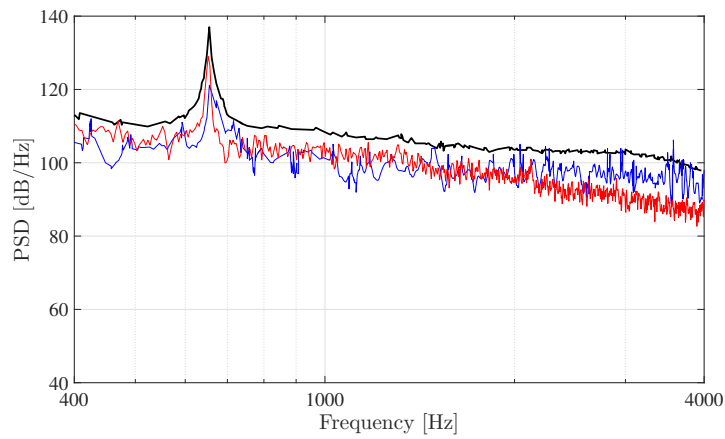
(a) $\theta = 0^\circ$, $y/D = -0.186$.(b) $\theta = 90^\circ$, $y/D = -0.186$.(c) $\theta = 180^\circ$, $y/D = -0.186$.

Figure G.8: Comparisons of wall pressure spectra at $y/D = -0.186$ on the side-wall. — Experiments [133], — LES simulation [133], — DDES simulation.

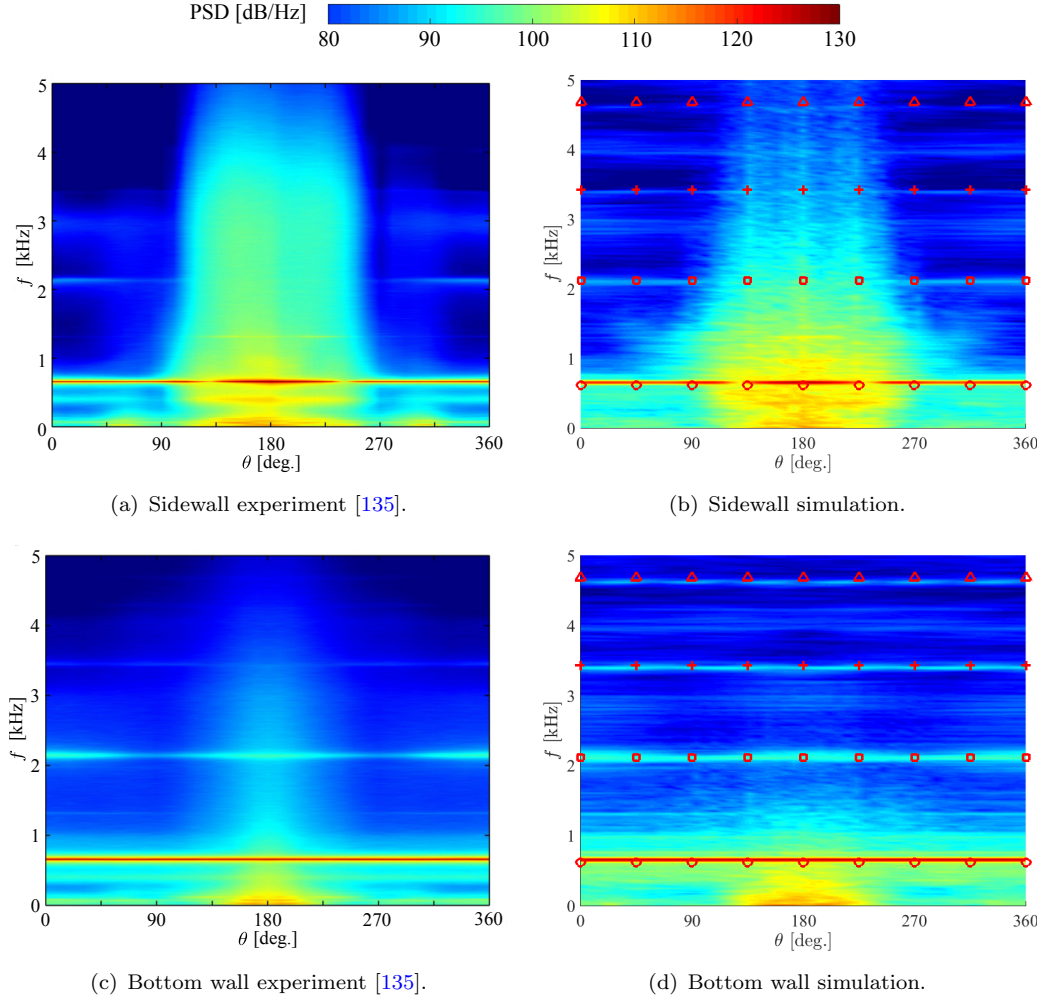


Figure G.9: Wall pressure spectra on the sidewall at $y/D = -0.1$ and bottom wall at $r/D = 0.375$. \circ f_{100} , \square f_{110} , $+$ f_{120} , \triangle f_{130} .

The far-field acoustics on a hemisphere above the cavity with a radius of $10D$ are calculated by solving the FW-H equation. Figure G.10 demonstrates comparisons of the far-field pressure spectra on the $\theta = 90^\circ$ plane (perpendicular to the inflow direction) against the experiment [133], LES simulation [133] and LBM simulation [134]. The LBM acoustic pressures were obtained by solving the FW-H equation, while the LES simulation firstly recorded the pressure signals at $y/D = 6$ directly in the simulation, which were then projected to $y/D = 10$ by an inverse distance law. This process is named as Direct Noise Computation (DNC). The acoustic result from the LES simulation is only available at $\phi = 90^\circ$ ($10D$ overhead the cavity). The current DDES simulation predictions demonstrate a good agreement with the experimental measurements, while the LBM simulation under-predicts the broadband spectra at $f > 1000$ Hz.

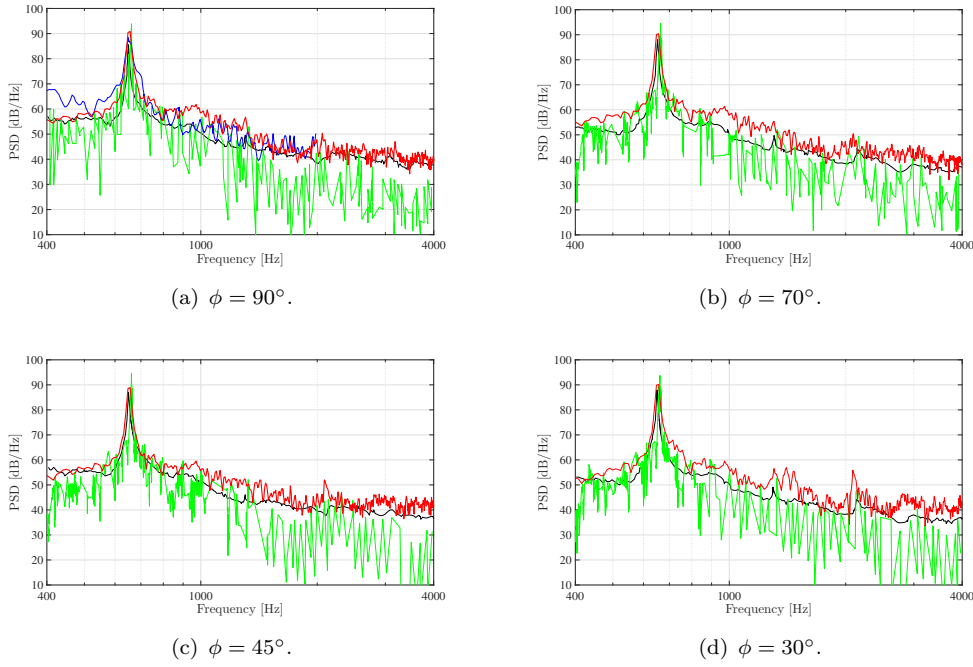


Figure G.10: Comparisons of far-field acoustic spectra at $\theta = 90^\circ$. — Experiments [133], — LES simulation with direct noise computation [133], — LBM simulation with FW-H solution [134], — DDES simulation with FW-H solution.

G.4 Effects of depth-to-diameter ratios on aerodynamic results

G.4.1 Mean pressure coefficients

The mean pressure coefficients on the cavity walls are shown in Figure G.11, where an asymmetric mean flow behaviour is demonstrated at $\varpi = 0.3$ and $\varpi = 0.6$. The asymmetry of mean flow typically happens for relatively shallow cylindrical cavities, which is reviewed in Section 2.4.2. The shear layer impingement zones on the side walls are centred at $\theta = 180^\circ$ for $\varpi = 1.0$ and $\varpi = 1.5$, whereas the impingement moves to $\theta = 175^\circ$ for $\varpi = 0.3$ and $\theta = 190^\circ$ for $\varpi = 0.6$. A visualisation of the large vortex structure inside the cavity is illustrated in Figure G.12 by plotting the iso-contour of pressure coefficient. At $\varpi = 0.3$ and $\varpi = 0.6$, one end of the large vortex is rooted at the cavity wall while the other end extends outside the cavity, indicating an interaction of the flow field inside and outside the cavity. The large vortex is fully located inside the cavity for $\varpi = 1.0$ and $\varpi = 1.5$ and both ends are rooted at the cavity side walls. The vortex axis at $\varpi = 1.0$ and $\varpi = 1.5$ is aligned in the z direction and a relatively more symmetric mean flow field is thus presented in Figures G.11(c) and G.11(d), compared to $\varpi = 0.3$ and $\varpi = 0.6$.

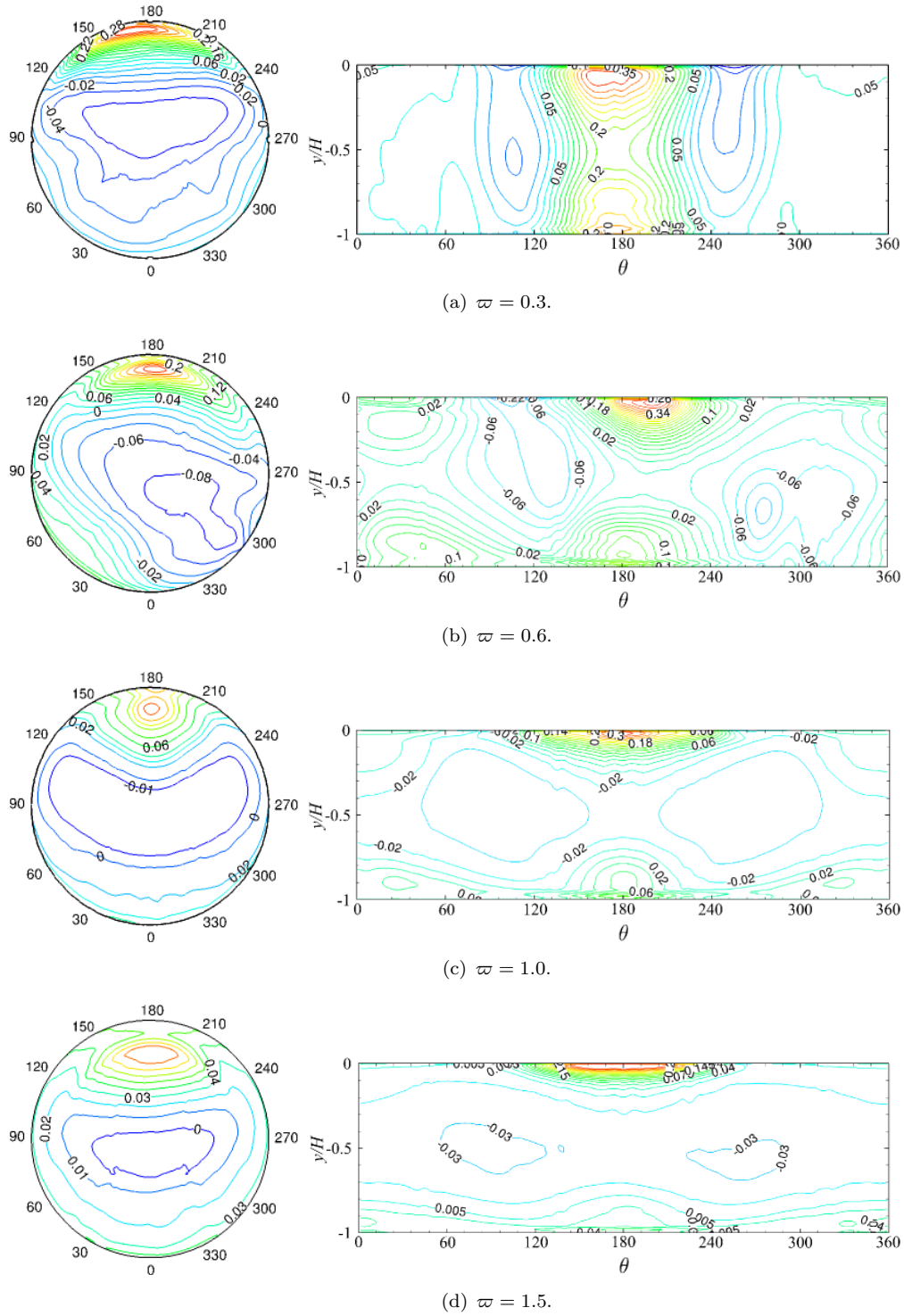


Figure G.11: Pressure coefficients on cavity walls at different depth-to-diameter ratios.

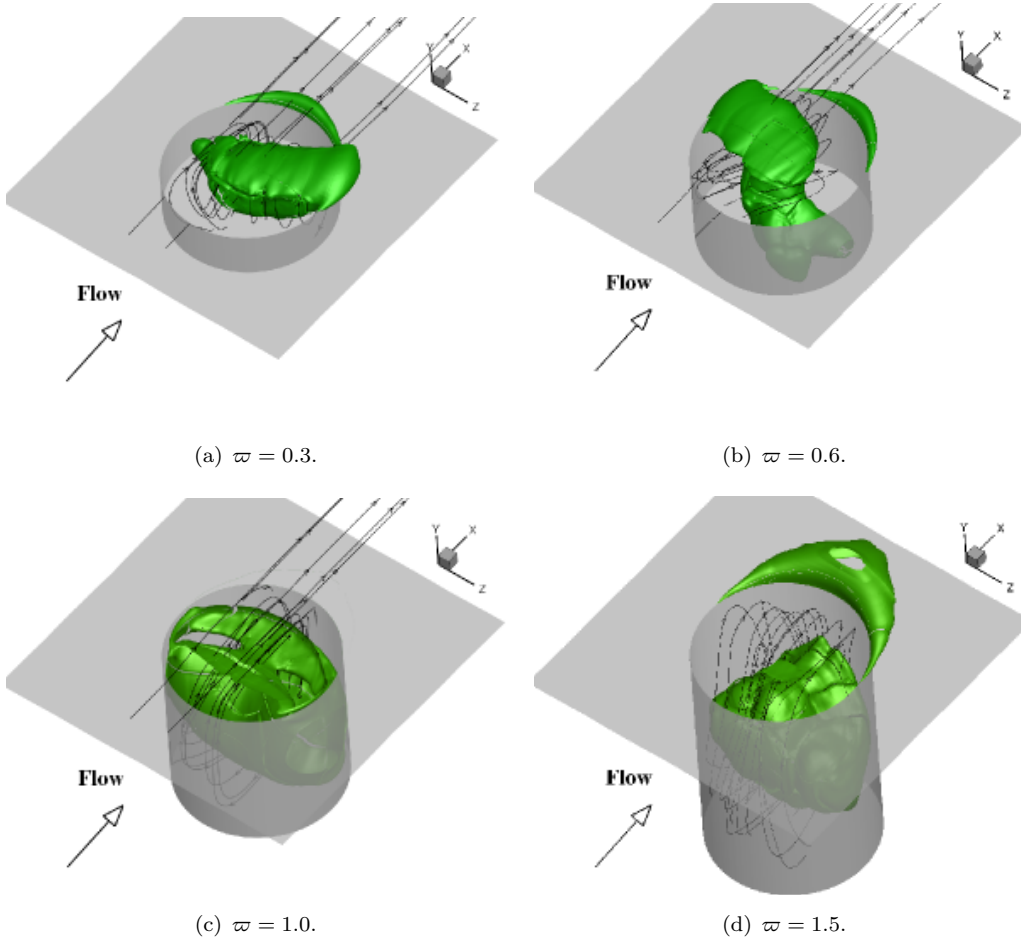


Figure G.12: Visualisation of the vortex structure inside the cavity by plotting iso-contour of pressure coefficient ($C_p = -0.1$).

G.4.2 Wall pressure spectra

The bottom wall pressure spectra at $\theta = 0^\circ$, $r/D = 0.35$ from different depth-to-diameter ratios are plotted in Figure G.13, where significant peaks occur at $f = 660$ Hz and $f = 400$ Hz for $\varpi = 1.0$ and $\varpi = 1.5$, respectively. The spectra tend to be more broadband and the background PSD levels (omitting tones) are approximately 10 dB/Hz higher at $f < 1000$ Hz for $\varpi = 0.3$ and $\varpi = 0.6$ than $\varpi = 1.0$ and $\varpi = 1.5$.

The contour of wall pressure spectral profiles at $r/D = 0.375$, together with the resonant frequencies, are demonstrated in Figure G.14. The azimuthal modes are present in the wall pressure spectra for all the depth-to-diameter ratios, whereas the depth mode is more observable at $\varpi = 1.0$, 1.5, less noticeable at $\varpi = 0.6$ and not shown at $\varpi = 0.3$.

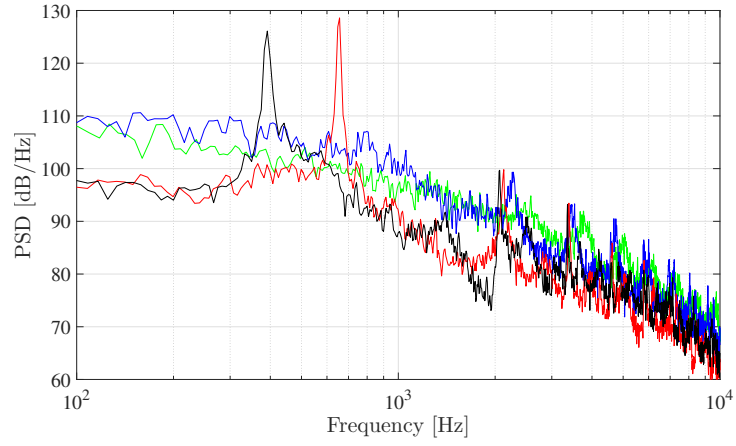


Figure G.13: Wall pressure spectra at $\theta = 0^\circ, r/D = 0.35$ on the bottom wall.
— $\varpi = 0.3$, — $\varpi = 0.6$, — $\varpi = 1.0$, — $\varpi = 1.5$.

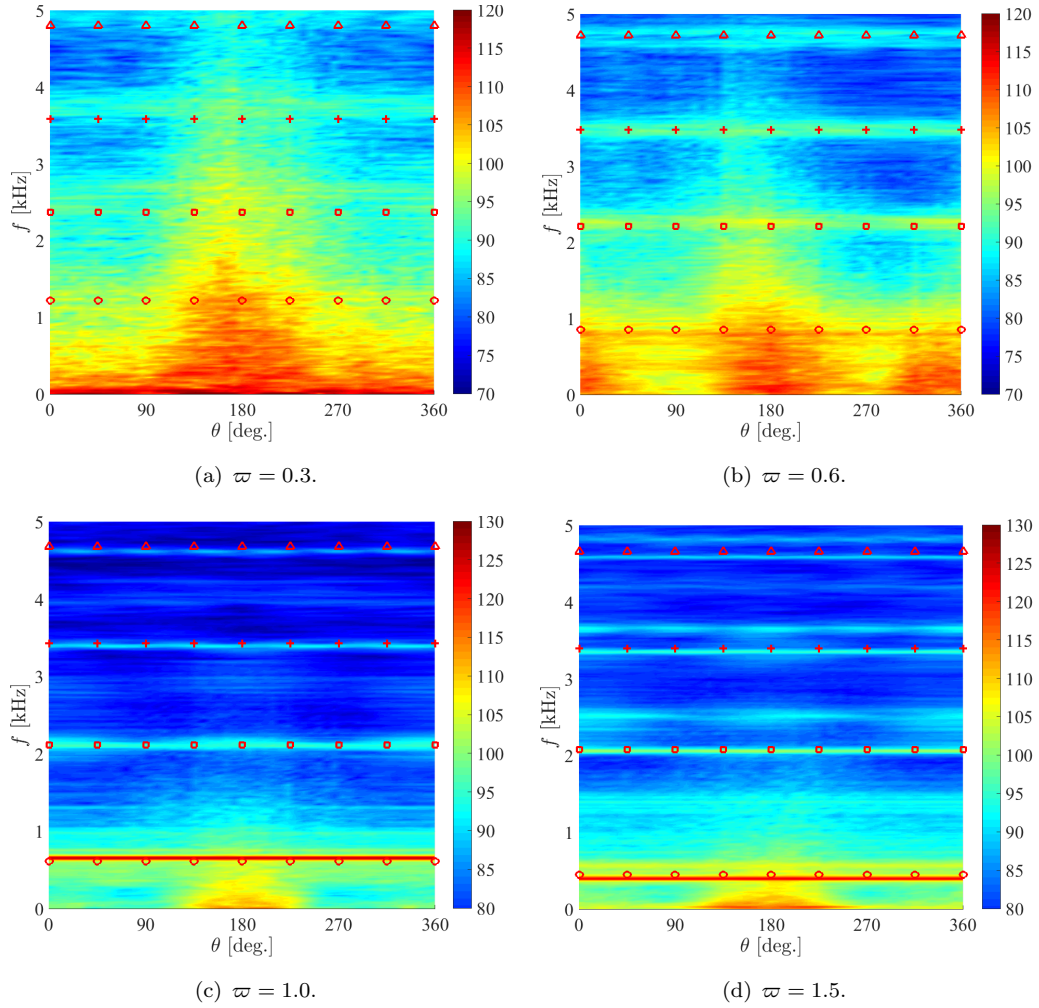


Figure G.14: Wall pressure spectra on the cavity bottom wall at $r/D = 0.375$.
 $\circ f_{100}$, $\square f_{110}$, $+$ f_{120} , $\triangle f_{130}$.

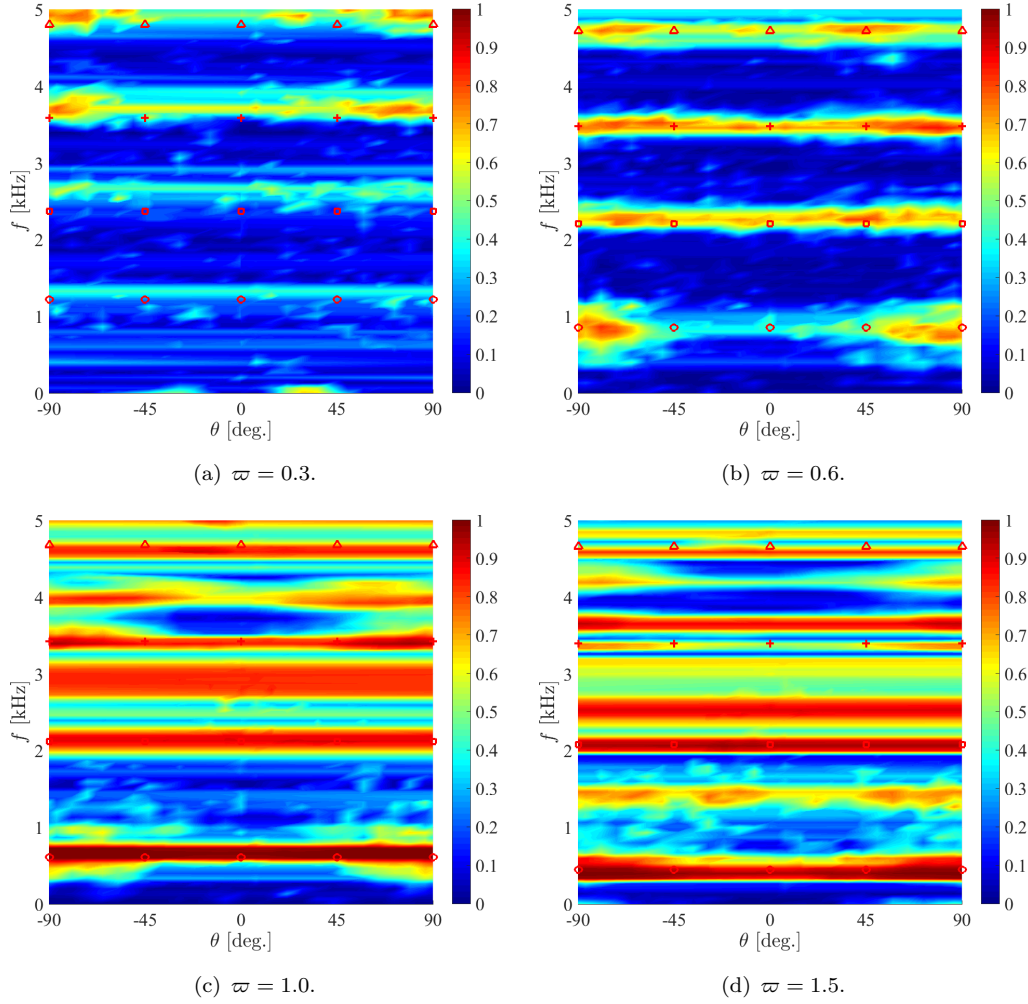


Figure G.15: Coherence γ^2 between $p'(\theta)$ and $p'(\theta + 180^\circ)$ on the bottom wall at $r/D = 0.375$. \circ f_{100} , \square f_{110} , $+$ f_{120} , \triangle f_{130} .

G.4.3 Coherence function

In order to understand the flow structures at different frequencies, the coherence function γ^2 between wall pressure fluctuations $p'(\theta)$ and $p'(\theta + 180^\circ)$ on the cavity bottom wall at $r/D = 0.375$ is plotted in Figure G.15, where a strong coherence is demonstrated close to the resonant frequencies. At $\varpi = 0.3$ in Figure G.15(a), a weak peak is present around the depth mode, indicating weak presence of the acoustic resonance in the depth direction, although the depth mode is not clearly shown in the wall pressure spectral profiles in Figure G.14(a).

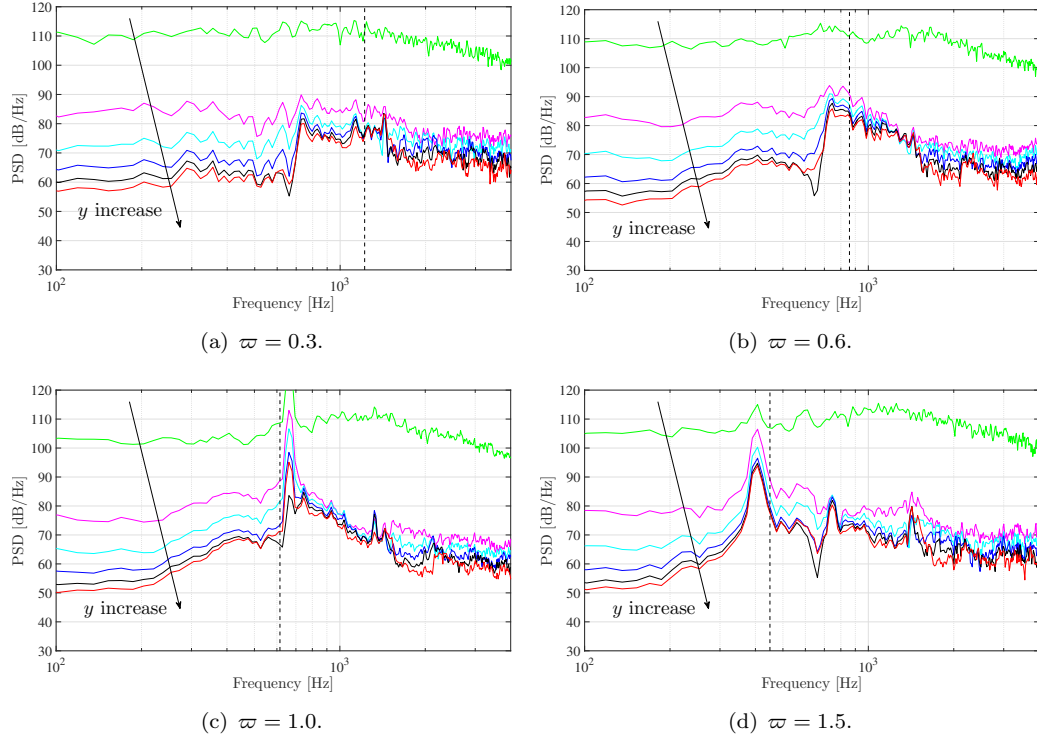


Figure G.16: Pressure spectra measured at overhead positions with varying distances to the cavity. — $y/D = 0$, — $y/D = 0.5$, — $y/D = 1.0$, — $y/D = 1.5$, — $y/D = 2.0$, — $y/D = 2.5$, --- f_{100} .

G.5 Effects of depth-to-diameter ratios on acoustic results

G.5.1 Direct computational results

Figure G.16 plots the pressure spectra directly recorded at different overhead positions in the simulations. At the cavity opening ($y/D = 0$), the spectral peak is not distinguishable at $\varpi = 0.3$ and $\varpi = 0.6$. However, as the distance to the cavity increases, the depth mode tends to be more observable, which can be evidenced from the spectral hump close at f_{100} . Figures G.16(a) and G.16(b) show that the depth mode is still the dominant acoustic mode for the shallow cylinder cavity at $\varpi = 0.3$ and $\varpi = 0.6$, although the depth mode is not clearly shown by the surface pressures at the wall and at the cavity opening, where the spectra are more broadband. For relatively deep cavities in Figure G.16(c) and G.16(d) the depth mode is clearly illustrated in the pressure spectral profiles. The instantaneous pressure perturbations are illustrated in Figure G.17, where the acoustic waves at $\varpi = 0.3$ tend to be more broadband, compared to the other depth-to-diameter ratios.

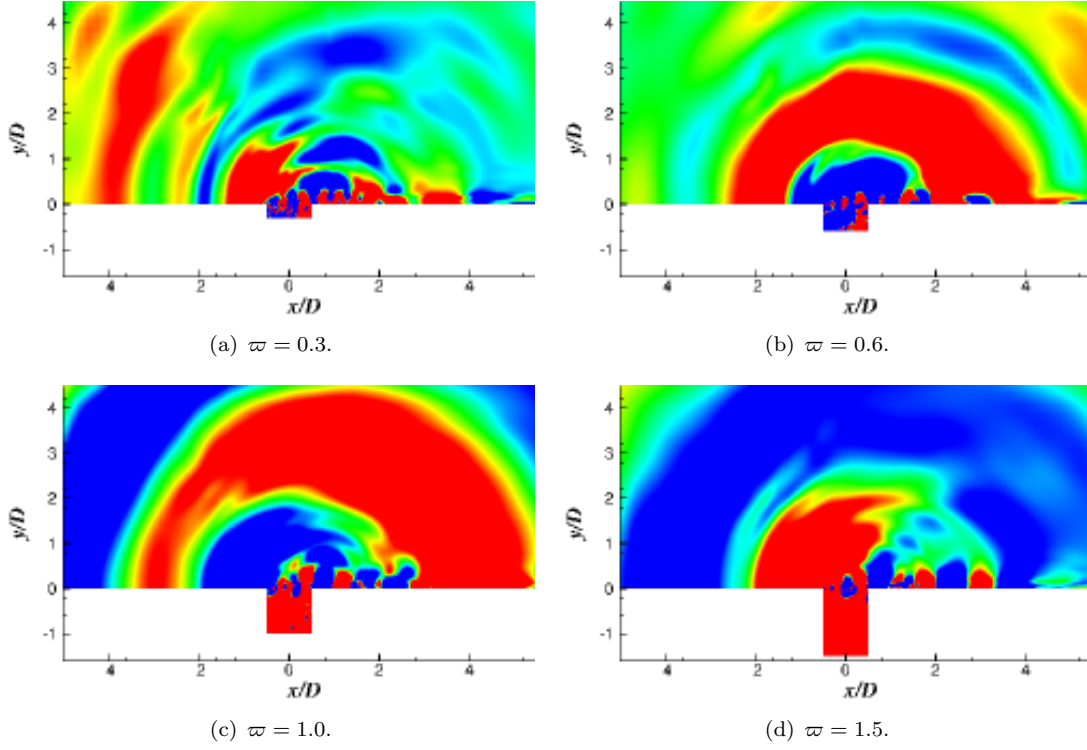


Figure G.17: Instantaneous pressure fluctuations $p'/\rho_\infty c_\infty^2$ in a range of $[-5, 5] \times 10^{-5}$ at different depth-to-diameter ratios.

G.5.2 FW-H results

Figure G.18 plots the far-field acoustic results at $10D$ above the cavity obtained by solving the FW-H equation. For shallow cavities at $\varpi = 0.3$ and $\varpi = 0.6$, there are spectral peaks centred at the depth mode f_{100} in Figures G.18(a) and G.18(b). The depth mode becomes more significant for $\varpi = 1.0$ and $\varpi = 1.5$.

The far-field directivity of OASPL at different depth-to-diameter ratios is shown in Figure G.19. The favourable acoustic radiation direction at $\varpi = 0.6$, $\varpi = 1.0$ and $\varpi = 1.5$ is close to the overhead position, whereas more sound is radiating to the upstream direction at $\varpi = 0.3$.

G.6 Summary

High-order numerical simulations are performed to investigate the flow over cylindrical cavities at different depth-to-diameter ratios. The major conclusions are:

- The simulations are validated against the experimental measurements at $\varpi = 1.0$, and good agreements of both mean and unsteady statistics are obtained.

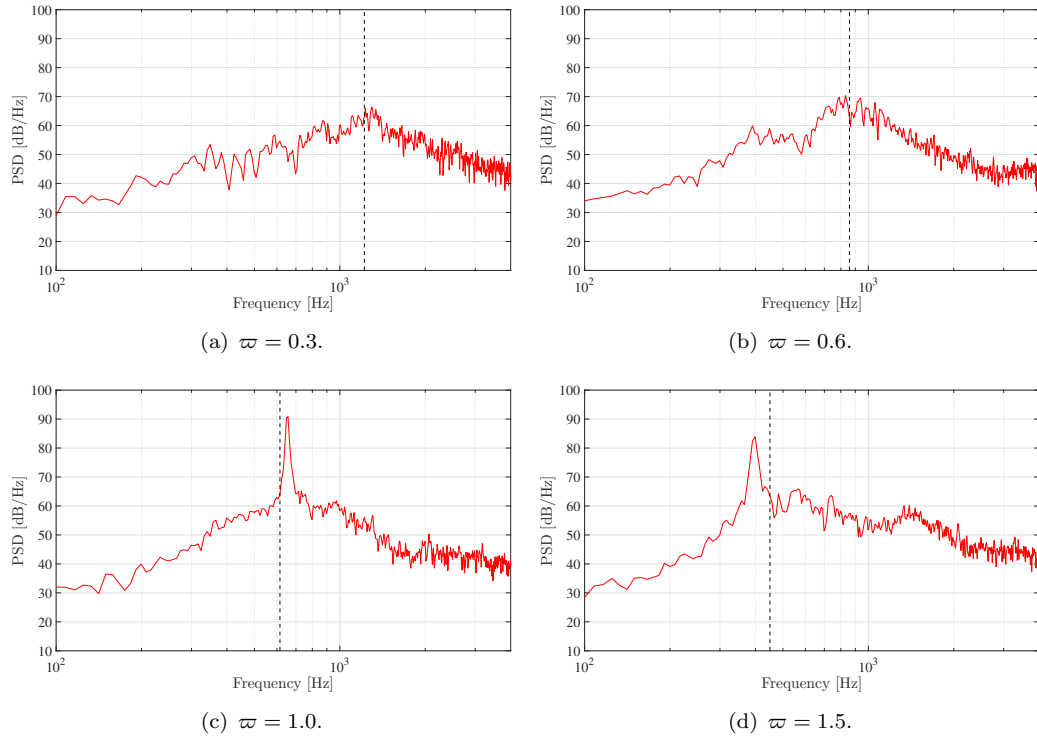


Figure G.18: Far-field acoustic pressure spectra at $\phi = 90^\circ$ (overhead position) from different depth-to-diameter ratios. — FW-H results, --- f_{100} .

- An asymmetric mean flow behaviour with respect to the flow direction is present at $\varpi = 0.3$ and $\varpi = 0.6$.
- The depth mode f_{100} is significantly present in the wall pressure spectra for the relative deep cavities at $\varpi = 1.0$ and $\varpi = 1.5$, whereas it is not clearly shown for $\varpi = 0.3$ and $\varpi = 0.6$. However, there are still coherent structures for $\varpi = 0.3$ and $\varpi = 0.6$ at the depth mode, as demonstrated by the coherent analysis of wall pressures.
- The depth mode is the dominant mode in the far-field acoustics, which can be evidenced from the spectral humps at $\varpi = 0.3$ and $\varpi = 0.6$ and spectral peaks at $\varpi = 1.0$ and $\varpi = 1.5$. The depth mode f_{100} is more significant for relatively deep cavities ($\varpi = 1.0$ and $\varpi = 1.5$), and the pressure spectra from the shallow cavities ($\varpi = 0.3$ and $\varpi = 0.6$) tend to be more broadband.
- The favourable acoustic radiating directivity is the upstream direction for $\varpi = 0.3$, and close to the overhead position for $\varpi = 0.6, 1.0$ and 1.5 .

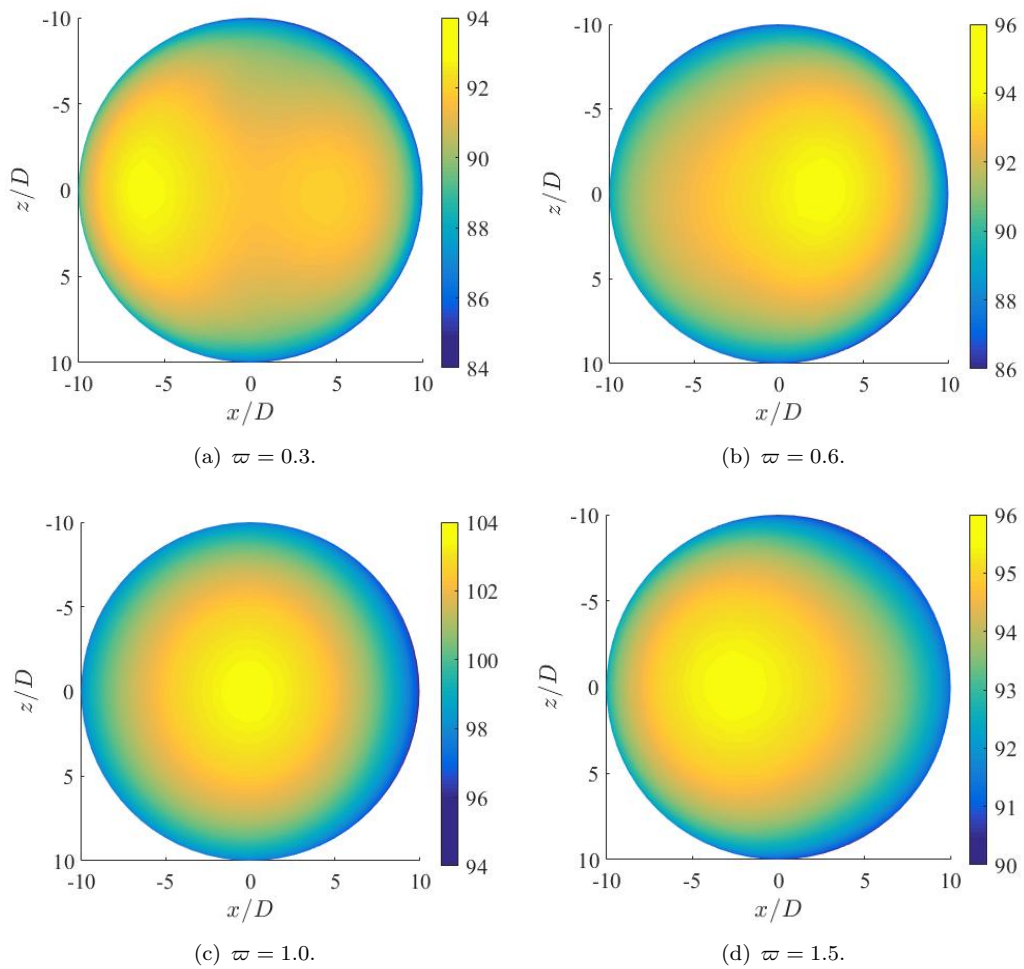


Figure G.19: Far-field acoustic directivity of OASPL [dB] at different depth-to-diameter ratios.

Appendix H

Vortex Structures for Tandem Wheels

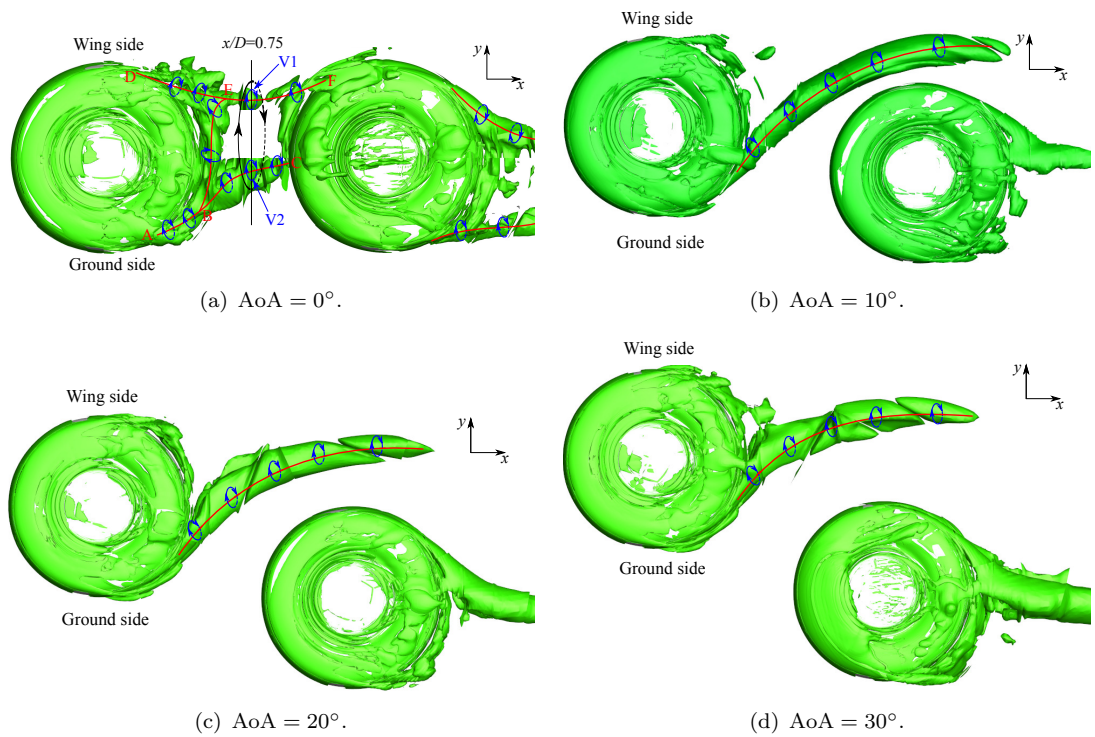


Figure H.1: Vortex structure in the gap region visualised by λ_2 criterion at different angles of attack.

References

- [1] ACARE, “European Aeronautics: A Vision for 2020,” tech. rep., 2001.
- [2] European Commission, “Flightpath 2050 Europe’s Vision for Aviation,” tech. rep., 2011.
- [3] W. Liu, J. W. Kim, X. Zhang, D. Angland, and B. Caruelle, “Landing-Gear Noise Prediction Using High-Order Finite Difference Schemes,” *Journal of Sound and Vibration*, vol. 332, no. 14, pp. 3517–3534, 2013.
- [4] D. P. Lockard, M. Khorrami, and F. Li, “Aeroacoustic Analysis of a Simplified Landing Gear,” in *10th AIAA/CEAS Aeroacoustics Conference*, AIAA 2004-2887, 2004.
- [5] M. J. Lighthill, “On Sound Generation Aerodynamically. I. General Theory,” *Proceedings of the Royal Society of London. Series A, Mathematical and Physical Sciences*, vol. 211, no. 1107, pp. 564–587, 1952.
- [6] N. Curle, “The Influence of Solid Boundaries upon Aerodynamic Sound,” *Proceedings of the Royal Society of London. Series A, Mathematical and Physical Sciences*, vol. 231, no. 1187, pp. 505–514, 1955.
- [7] J. E. Ffowcs Williams and D. L. Hawkings, “Sound Generation by Turbulence and Surfaces in Arbitrary Motion,” *Philosophical Transactions of the Royal Society of London. Series A, Mathematical and Physical Sciences*, vol. 264, no. 1151, pp. 321–342, 1969.
- [8] M. S. Howe, *Theory of Vortex Sound*. Cambridge University Press, 2003.
- [9] V. Strouhal, “Über eine besondere art von tonerzeugung,” *Annalen für Physik und Chemie*, vol. 5, pp. 216–251, 1878.
- [10] T. Karman, “Über den Mechanismus des Widerstandes,” *den ein bewegter Körper in einer Flüssigkeit erfährt*, vol. 3, pp. 547–556, 1912.
- [11] M. M. Zdravkovich, *Flow Around Circular Cylinders: Volume I: Fundamentals*. Oxford Science Publications, 1997.

- [12] B. Etkin, G. Korbacher, and R. Keefe, "Acoustic Radiation from a Stationary Cylinder in a Fluid Stream (Aeolian Tones)," *The Journal of the Acoustical Society of America*, vol. 29, no. 1, pp. 30–36, 1957.
- [13] M. M. Zdravkovich, V. P. Brand, G. Mathew, and A. Weston, "Flow Past Short Circular Cylinders with Two Free Ends," *Journal of Fluid Mechanics*, vol. 203, pp. 557–575, 1989.
- [14] M. M. Zdravkovich, A. J. Flaherty, M. G. Pahle, and I. A. Skelhorne, "Some Aerodynamic Aspects of Coin-Like Cylinders," *Journal of Fluid Mechanics*, vol. 360, pp. 73–84, 1998.
- [15] S. Majumdar and W. Rodi, "Three-Dimensional Computation of Flow Past Cylindrical Structures and Model Cooling Towers," *Building and Environment*, vol. 24, no. 1, pp. 3–22, 1989.
- [16] T. Lee, C. Lin, and C. A. Friehe, "Large-eddy simulation of air flow around a wall-mounted circular cylinder and a tripod tower," *Journal of Turbulence*, vol. 8, no. 29, 2007.
- [17] O. Frederich, E. Wassen, and F. Thiele, "Prediction of the flow around a short wall-mounted finite cylinder Using LES and DES," *Journal of Numerical Analysis, Industrial and Applied Mathematics*, vol. 3, no. 3-4, pp. 231–247, 2008.
- [18] G. Palau-Salvador, T. Stoesser, J. Fröhlich, M. Kappler, and W. Rodi, "Large Eddy Simulations and Experiments of Flow around Finite-Height Cylinders," *Flow Turbulence and Combustion*, vol. 84, no. 2, pp. 239–275, 2010.
- [19] M. M. Zdravkovich, "The Effect of Interference between Circular Cylinders in Cross Flow," *Journal of Fluids and Structures*, vol. 1, no. 2, pp. 239–261, 1987.
- [20] D. Summer, "Two Circular Cylinders in Cross-Flow: A Review," *Journal of Fluids and Structures*, vol. 26, no. 6, pp. 849–899, 2010.
- [21] Y. Zhou and M. W. Yiu, "Flow structure, Momentum and Heat Transport in a Two-Tandem-Cylinder Wake," *Journal of Fluid Mechanics*, vol. 548, pp. 17–48, 2006.
- [22] M. M. Zdravkovich and D. J. Pridden, "Interference between Two Circular Cylinders: Series of Unexpected Discontinuities," *Journal of Wind Engineering and Industrial Aerodynamics*, vol. 2, no. 3, pp. 255–270, 1977.
- [23] J. C. Lin, Y. Yang, and D. Rockwell, "Flow Past Two Cylinders in Tandem: Instantaneous and Averaged Flow Structure," *Journal of Fluids and Structures*, vol. 16, no. 8, pp. 1059–1071, 2002.
- [24] T. Igarashi, "Characteristics of the Flow around Two Circular Cylinders Arranged in Tandem : 1st Report," *Bulletin of JSME*, vol. 24, no. 188, pp. 323–331, 1981.

- [25] Y. O. Ohya, A. Okajima, and M. Hayashi, "Wake Interference and Vortex Shedding," in *Encyclopedia of Fluid Mechanics*, pp. 322–389, Gulf Publishing Company, 1989.
- [26] D. P. Lockard, "Summary of the Tandem Cylinder Solutions from the Benchmark problems for Airframe Noise Computations-I Workshop," in *49th AIAA Aerospace Sciences Meeting including the New Horizons Forum and Aerospace Exposition*, AIAA 2011-353, 2011.
- [27] B. S. Lazos, "Mean Flow Features Around the Inline Wheels of Four-Wheel Landing Gear," *AIAA Journal*, vol. 40, no. 2, pp. 193–198, 2002.
- [28] H. H. Heller and W. M. Dobrzynski, "Sound Radiation from Aircraft Wheel-Well/Landing-Gear Configurations," *Journal of Aircraft*, vol. 14, no. 8, pp. 768–774, 1976.
- [29] Y. Guo, K. J. Yamamoto, and R. W. Stoker, "An Empirical Model for Landing Gear Noise Prediction," in *10th AIAA/CEAS Aeroacoustics Conference*, AIAA 2004-2888, 2004.
- [30] M. Wang, D. Angland, X. Zhang, and R. Fattah, "High-Order Numerical Simulations of An Isolated Landing Gear Wheel with A Hub Cavity," in *22nd AIAA/CEAS Aeroacoustics Conference*, AIAA 2016-2902, 2016.
- [31] Y. Yokokawa, T. Imamura, H. Ura, H. Uchida, H. Kobayashi, and K. Yamamoto, "Experimental Study on Noise Generation of a Two-Wheel Main Landing Gear," in *16th AIAA/CAES Aeroacoustics Conference*, AIAA 2010-3973, 2010.
- [32] W. Dobrzynski and H. Buchholz, "Full-Scale Noise Testing on Airbus Landing Gears in the German Dutch Wind Tunnel," in *3rd AIAA/CEAS Aeroacoustics Conference*, AIAA 1997-1597, 1997.
- [33] B. S. Lazos, "Surface Topology on the Wheels of a Generic Four-Wheel Landing Gear," *AIAA Journal*, vol. 40, no. 12, pp. 2402–2411, 2002.
- [34] D. H. Neuhart, M. R. Khorrami, and M. M. Choudhari, "Aerodynamics of a Gulfstream G550 Nose Landing Gear Model," in *15th AIAA/CEAS Aeroacoustics Conference*, AIAA 2009-3152, 2009.
- [35] P. R. Spalart and K. Mejia, "Analysis of Experimental and Numerical Studies of the Rudimentary Landing Gear," in *49th AIAA Aerospace Sciences Meeting including the New Horizons Forum and Aerospace Exposition*, AIAA 2011-0355, 2011.
- [36] P. R. Spalart and D. A. Wetzel, "Rudimentary Landing Gear Results at the 2012 BANC-II Airframe Noise Workshop," vol. 14, no. 1, pp. 193–216, 2015.

- [37] A. R. Quayle, A. P. Dowling, H. Babinsky, W. R. Graham, and Y. Liu, "Phased Array Measurements from Landing Gear Models," in *28th AIAA/CEAS Aeroacoustics Conference*, AIAA 2007-3463, 2007.
- [38] M. R. Khorrami and D. P. Lockard, "A Landing Gear Noise Reduction Study Based on Computational Simulations," in *35th International Congress and Exposition on Noise Control Engineering*, 2006.
- [39] D. Casalino, A. F. Ribeiro, and E. Fares, "Facing Rim Cavities Fluctuation Modes," *Journal of Sound and Vibration*, vol. 333, no. 13, pp. 2812–2830, 2014.
- [40] S. M. Jaeger, N. J. Burnside, P. T. Soderman, W. C. Horne, and K. D. James, "Microphone Array Assessment of An Isolated 26%-Scale, High-Fidelity Landing Gear," in *8th AIAA/CEAS Aeroacoustics Conference*, AIAA 2002-2410, 2002.
- [41] X. Zhang, Z. K. Ma, M. Smith, and M. Sanderson, "Aerodynamic and Acoustic Measurements of a Single Landing Gear Wheel," in *19th AIAA/CEAS Aeroacoustics Conference*, AIAA 2013-2160, 2013.
- [42] S. Spagnolo, X. Zhang, Z. Hu, O. Stalnov, and D. Angland, "Unsteady Force and Flow Features of Single and Tandem Wheels," in *53rd AIAA Aerospace Sciences Meeting*, AIAA 2015-0261, 2015.
- [43] S. Spagnolo, X. Zhang, Z. Hu, and D. Angland, "Numerical Simulations of Single and Tandem Wheels for Aerodynamic Loads Prediction," in *22nd AIAA/CEAS Aeroacoustics Conference*, AIAA 2015-3066, 2015.
- [44] J. Rossiter, "Wind-tunnel Experiments on the Flow Over Rectangular Cavities at Subsonic and Transonic Speeds," Technical Report 3438, Aeronautical Research Council Reports and Memoranda, 1964.
- [45] S. Parthasarathy, Y. I. Cho, and L. Back, "Sound Generation by Flow over Relatively Deep Cylindrical Cavities," *Journal of Acoustical Society of America*, vol. 78, no. 5, pp. 1785–1795, 1985.
- [46] O. Marsden, C. Bailly, C. Bogey, and E. Jondeau, "Investigation of Flow Features and Acoustic Radiation of a Round Cavity," *Journal of Sound and Vibration*, vol. 331, no. 15, pp. 3521–3543, 2012.
- [47] R. D. Belvins, *Formulas for Natural Frequency and Mode Shape*. Krieger Publishing Company, reprint ed., 1984.
- [48] M. Pollack, "Flow-Induced Tones in Side-Branch Pipe Resonator," *Journal of Acoustical Society of America*, vol. 67, no. 4, pp. 1153–1156, 1980.
- [49] S. Elder, "Self-Excited Depth-Mode Resonance for a Wall-Mounted Cavity in Turbulent Flow," *Journal of the Acoustical Society of America*, vol. 34, no. 3, 1978.

- [50] H. Heller, D. Holmes, and E. Covert, “Flow-Induced Pressure Oscillations in Shallow Cavities,” *Journal of Sound and Vibration*, vol. 18, no. 4, pp. 545–553, 1971.
- [51] L. Gaudet and K. Winger, “Measurements of the Drag of Some Characteristic Aircraft Excrescences Immersed in Turbulent Boundary Layers,” tech. rep., No. TM AERO 1538 (Royal Aircraft Establishment), 1973.
- [52] J. Dybenko and E. Savory, “An Experimental Investigation of Turbulent Boundary Layer Flow over Surface-Mounted Circular Cavities,” *Proceedings of the Institution of Mechanical Engineers, Part G: Journal of Aerospace Engineering*, vol. 222, no. 1, pp. 109–125, 2008.
- [53] M. Hiwada, T. Kawamura, M. I., and K. M., “Some characteristics of flow pattern and heat transfer past a circular cylindrical cavity,” *Bulletin of the JSME*, vol. 26, no. 220, pp. 1744–1752, 1983.
- [54] O. Marsden, C. Bogey, and C. Bailly, “Investigation of Flow Features around Shallow Round Cavities subject to Subsonic Grazing Flow,” *Physics of Fluids*, vol. 24, no. 12, pp. 125–107, 2012.
- [55] D. C. Mincu, I. Mary, S. Redonnet, and E. Manoha, “Numerical Simulations of the Sound Generation by Flow over Surface Mounted Cylindrical Cavities including Wind Tunnel Installation Effects,” in *15th AIAA/CEAS Aeroacoustics Conference*, AIAA 2009-3314, 2009.
- [56] O. Marsden, C. Bogey, and C. Bailly, “Depth Effects on the Flow Features and Noise Signature of Shallow Cylindrical Cavities at a Mach Number of 0.25,” in *18th AIAA/CEAS Aeroacoustics Conference*, AIAA 2012-2232, 2012.
- [57] X. Zhang, “Aircraft Noise and Its Nearfield Propagation Computations,” *Acta Mechanica Sinica*, vol. 28, no. 4, pp. 960–977, 2012.
- [58] S. B. Pope, *Turbulent Flows*. Cambridge University Press, 6 ed., 2000.
- [59] P. R. Spalart, W. H. Jou, M. Strelets, and S. R. Allmaras, “Comments on the Feasibility of LES for Wings and on a Hybrid RANS/LES Approach,” in *Proceedings of the First AFOSR International Conference on DNS/LES*, pp. 137–147, 1997.
- [60] P. R. Spalart, S. Deck, M. L. Shur, K. D. Squires, M. K. Strelets, and A. Travin, “A New Version of Detached-eddy Simulation, Resistant to Ambiguous Grid Densities,” *Theoretical and Computational Fluid Dynamics*, vol. 20, no. 3, pp. 181–195, 2006.
- [61] M. L. Shur, P. R. Spalart, M. Kh, and A. K. Travin, “A hybrid RANS-LES approach with delayed-DES and wall-modelled LES capabilities,” *International Journal of Heat and Fluid Flow*, vol. 29, no. 6, pp. 406–417, 2008.

- [62] S. Deck, “Recent Improvements in the Zonal Detached Eddy Simulation (ZDES) Formulation,” *Theoretical and Computational Fluid Dynamics*, vol. 26, no. 6, pp. 523–550, 2011.
- [63] L. S. Hedges, A. K. Travin, and P. R. Spalart, “Detached-Eddy Simulations Over a Simplified Landing Gear,” *Journal of Fluids Engineering*, vol. 124, no. 2, pp. 413–423, 2002.
- [64] T. Imamura, T. Hirai, K. Amemiya, Y. Yokokawa, S. Enomoto, and K. Yamamoto, “Aerodynamic and aeroacoustic simulations of a two-wheel landing gear,” *Procedia Engineering*, vol. 6, no. 2009, pp. 293–302, 2010.
- [65] D. P. Lockard, M. R. Khorrami, and F. Li, “High Resolution Calculation of a Simplified Landing Gear,” in *10th AIAA/CEAS Aeroacoustics Conference*, AIAA 2004-2287, 2004.
- [66] P. R. Spalart, M. Shur, M. Kh, and A. K. Travin, “Initial noise predictions for rudimentary landing gear,” *Journal of Sound and Vibration*, vol. 330, no. 17, pp. 4180–4195, 2011.
- [67] L. Sanders, E. Manoha, S. Khelil, and C. Francois, “LAGOON : CFD / CAA Coupling for Landing Gear Noise and Comparison with Experimental Database,” in *17th AIAA/CEAS Aeroacoustics Conference*, AIAA 2011-2822, 2011.
- [68] L. Sanders, E. Manoha, S. B. Khelil, and C. Francois, “LAGOON : New Mach Landing Gear Noise Computation and further analysis of the CAA process,” in *18th AIAA/CEAS Aeroacoustics Conference*, AIAA 2012-2281, 2012.
- [69] C. K. Tam and J. C. Webb, “Dispersion-Relation-Preserving Finite Difference Schemes for Computational Acoustics,” *Journal of Computational Physics*, vol. 107, no. 2, pp. 262–281, 1993.
- [70] R. Ewert and W. Schröder, “Acoustic Perturbation Equations based on Flow Decomposition via Source Filtering,” *Journal of Computational Physics*, vol. 188, no. 2, pp. 365–398, 2003.
- [71] X. Zhang and X. Chen, “Linearised Divergence Equations for Sound Propagation,” in *17th AIAA/CEAS Aeroacoustics Conference*, AIAA 2011-2930, 2011.
- [72] A. Lario and R. Arina, “Linearized Navier-Stokes Equations and their Numerical Solution,” in *22nd AIAA/CEAS Aeroacoustics Conference*, AIAA 2016-2973, 2016.
- [73] G. Kirchhoff, “Zur Theorie der Lichtstrahlen,” *Annalen der Physik*, vol. 254, pp. 663–695, 1882.
- [74] K. S. Brentner and F. Farassat, “An Analytical Comparison of the Acoustic Analogy and Kirchhoff Formulation for Moving Surfaces,” *AIAA Journal*, vol. 36, no. 8, pp. 1379–1386, 1998.

- [75] F. Farassat and G. P. Succi, “A Review of Propeller Discrete Frequency Noise Prediction Technology with Emphasis on Two Current Methods for Time Domain Calculations,” *Journal of Sound and Vibration*, vol. 71, no. 3, pp. 399–419, 1980.
- [76] D. Casalino, “An Advanced Time Approach for Acoustic Analogy Predictions,” *Journal of Sound and Vibration*, vol. 261, no. 4, pp. 583–612, 2003.
- [77] P. R. Spalart, M. L. Shur, M. K. Strelets, and A. K. Travin, “Towards Noise Prediction for Rudimentary Landing Gear,” *Procedia Engineering*, vol. 6, pp. 283–292, 2010.
- [78] L. Wang, C. Mockett, T. Knacke, and F. Thiele, “Detached-Eddy Simulation of Landing-Gear Noise,” in *19th AIAA/CEAS Aeroacoustic Conference*, AIAA 2013-2069, 2013.
- [79] E. Manoha and B. Caruelle, “Summary of the LAGOON Solutions from the Benchmark Problems for Airframe Noise Computations-III Workshop,” in *21st AIAA/CEAS Aeroacoustics Conference*, AIAA 2015-2846, 2015.
- [80] R. J. Fattah, *The Noise Generation by a Main Landing Gear Door*. PhD thesis, University of Southampton, 2016.
- [81] M. C. M. Wright and C. L. Morfey, “On the Extrapolation of Acoustic Waves from Flow Simulations with Vortical Outflow,” *International Journal of Aeroacoustics*, vol. 14, no. 1-2, pp. 217–227, 2015.
- [82] S. K. Lele, “Compact Finite Difference Schemes with Spectral-Like Resolution,” *Journal of Computational Physics*, vol. 103, no. 1, pp. 16–42, 1992.
- [83] C. Bogey and C. Bailly, “A Family of Low Dispersive and Low Dissipative Explicit Schemes for Flow and Noise Computations,” *Journal of Computational Physics*, vol. 194, no. 1, pp. 194–214, 2004.
- [84] G. Ashcroft and X. Zhang, “Optimized Prefactored Compact Schemes,” *Journal of Computational Physics*, vol. 190, no. 2, pp. 459–477, 2003.
- [85] J. W. Kim, “Optimised boundary compact finite difference schemes for computational aeroacoustics,” *Journal of Computational Physics*, vol. 225, no. 1, pp. 995–1019, 2007.
- [86] R. Fattah, D. Angland, and X. Zhang, “A Priori Grid Quality Estimation for High-Order Finite Differencing,” *Journal of Computational Physics*, vol. 315, pp. 629–643, 2016.
- [87] J. W. Kim and D. J. Lee, “Characteristic Interface Conditions for Multiblock High-Order Computation on Singular Structured Grids,” *AIAA Journal*, vol. 41, no. 12, pp. 2341–2348, 2003.

- [88] J. Gao, “A Block Interface Flux Reconstruction Method for Numerical Simulation with High Order Finite Difference Scheme,” *Journal of Computational Physics*, vol. 241, pp. 1–17, 2013.
- [89] Y. Du and P. J. Morris, “Improved Block Interface Conditions for Aeroacoustic Problems with Grid Discontinuities,” *AIAA Journal*, vol. 53, no. 6, pp. 1531–1543, 2015.
- [90] M. Wang, R. Fattah, D. Angland, and X. Zhang, “High-Order Hybrid Cell-Centered Method for Computational Aeroacoustics,” in *21st AIAA/CEAS Aeroacoustics Conference*, AIAA 2015-3279, 2015.
- [91] X. Deng, M. Mao, G. Tu, H. Liu, and H. Zhang, “Geometric conservation law and applications to high-order finite difference schemes with stationary grids,” *Journal of Computational Physics*, vol. 230, no. 4, pp. 1100–1115, 2011.
- [92] B. Sjögren and H. C. Yee, *On Skew-Symmetric Splitting and Entropy Conservation Schemes for the Euler Equations*, pp. 817–827. Springer Berlin Heidelberg, 2010.
- [93] J. W. Kim and R. D. Sandberg, “Efficient Parallel Computing with a Compact Finite Difference Scheme,” *Journal of Computers and Fluids*, vol. 58, pp. 70–87, 2012.
- [94] X. L. Zhao and T. Z. Huang, “On the Inverse of a General Pentadiagonal Matrix,” *Applied Mathematics and Computation*, vol. 202, no. 2, pp. 639–646, 2008.
- [95] J. W. Kim, “High-order compact filters with variable cut-off wavenumber and stable boundary treatment,” *Journal of Computers and Fluids*, vol. 39, no. 7, pp. 1168–1182, 2010.
- [96] F. Q. Hu, H. M. Y., and J. L. Manthey, “Low-Dissipation and Low-Dispersion RungeKutta Schemes for Computational Acoustics,” *Journal of Computational Physics*, vol. 124, no. 1, pp. 177–191, 1996.
- [97] J. Blazek, *Computational Fluid Dynamics: Principles and Applications*. Elsevier, 2001.
- [98] R. D. Sandberg and N. D. Sandham, “Nonreflecting Zonal Characteristic Boundary Condition for Direct Numerical Simulation of Aerodynamic Sound,” *AIAA Journal*, vol. 44, no. 2, pp. 402–405, 2006.
- [99] J. W. Kim and D. J. Lee, “Generalized Characteristic Boundary Conditions for Computational Aeroacoustics,” *AIAA Journal*, vol. 38, no. 11, pp. 2040–2049, 2000.

- [100] J. W. Kim and D. J. Lee, “Generalized Characteristic Boundary Conditions for Computational Aeroacoustics, Part 2,” *AIAA Journal*, vol. 42, no. 1, pp. 47–55, 2004.
- [101] P. R. Spalart and S. R. Allmaras, “A One-Equation Turbulence Model for Aerodynamic Flows,” in *30th Aerospace Sciences Meeting and Exhibit*, AIAA 1992-0439, 1992.
- [102] S. R. Allmaras, F. T. Johnson, and P. R. Spalart, “Modifications and Clarifications for the Implementation of the Spalart-Allmaras Turbulence Model,” in *7th International Conference on Computational Fluid Dynamics*, ICCFD7-1902, 2012.
- [103] F. Mechanics, “Dynamic Mode Decomposition of Numerical and Experimental data,” *Journal of Fluid Mechanics*, vol. 656, pp. 5–28, 2010.
- [104] K. K. Chen, J. H. Tu, and C. W. Rowley, “Variants of Dynamic Mode Decomposition : Boundary Condition , Koopman , and Fourier Analyses,” *Journal of Nonlinear Science*, vol. 22, no. 6, pp. 887–915, 2012.
- [105] C. K. Tam, “Computational Aeroacoustics: An Overview of Computational Challenges and Applications,” *International Journal of Computational Fluid Dynamics*, vol. 18, no. 6, pp. 547–567, 2004.
- [106] Y. Du and P. J. Morris, “A New Block Interface Condition for Aeroacoustic Applications,” in *19th AIAA/CEAS Aeroacoustics Conference*, AIAA 2013-2216, 2013.
- [107] M. Bondarenko, Z. Hu, and X. Zhang, “Large-Eddy Simulation of the Interaction of a Jet with a Wing,” in *18th AIAA/CEAS Aeroacoustics Conference*, AIAA 2012-2254, 2012.
- [108] T. Colonius, A. J. Basu, and C. W. Rowley, “Numerical Investigation of the Flow Past a Cavity,” in *5th AIAA/CEAS Aeracoustics Conference*, AIAA 99-1912, 1999.
- [109] M. Popescu, W. Shyy, and M. Garbey, “Finite Volume Treatment of Dispersion-Relation-Preserving and Optimized Prefactored Compact Schemes for Wave Propagation,” *Journal of Computational Physics*, vol. 210, no. 2, pp. 705–729, 2005.
- [110] P. L. Roe, “Approximate Riemann Solvers , Parameter Vectors, and Difference Schemes,” *Journal of Computational Physics*, vol. 43, pp. 357–372, 1981.
- [111] M. H. Carpenter, D. Gottlieb, and S. Abarbanel, “The Stability of Numerical Boundary Treatments for Compact High-Order Finite-Difference Schemes,” *Journal of Computational Physics*, vol. 108, no. 2, pp. 272–295, 1993.
- [112] A. Roshko, “Experiments on Flow Past a Circular Cylinder at Very High Reynolds Number,” *Journal of Fluid Mechanics*, vol. 10, no. 3, pp. 345–356, 1961.

- [113] E. Achenbach, "Distribution of Local Pressure and Skin Friction around a Circular Cylinder in Cross-Flow up to $Re=5$ million," *Journal of Fluid Mechanics*, vol. 34, no. 4, pp. 625–639, 1968.
- [114] A. Travin, M. Shur, M. Strelets, and P. Spalart, "Detached-Eddy Simulations Past a Circular Cylinder," *Flow Turbulence and Combustion*, vol. 63, no. 1, pp. 293–313, 2001.
- [115] M. Weinmann, R. D. Sandberg, and C. Doolan, "Tandem Cylinder Flow and Noise Predictions Using a Hybrid RANS/LES Approach," *International Journal of Heat and Fluid Flow*, vol. 50, pp. 263–278, 2014.
- [116] S. Oka, Z. G. Kostic, and S. Sikmanovic, "Investigation of the Heat Transfer Process in Tube Banks in Cross Flow," in *International Seminar on Recent Development in Heat Exchangers*, 1972.
- [117] Y. Tanida, A. Okajima, and Y. Watanabes, "Stability of a Circular Cylinder Oscillating in Uniform Flow or in a Wake," *Journal of Fluid Mechanics*, vol. 61, no. 4, pp. 769–784, 1973.
- [118] L. Ljungkrona, C. Norberg, and B. Sundén, "Free-Stream Turbulence and Tube Spacing Effects on Surface Pressure Fluctuations for Two Tubes in an In-Line Arrangement," *Journal of Fluids and Structures*, vol. 5, no. 6, pp. 701–727, 1991.
- [119] J. H. Seo and Y. J. Moon, "Aerodynamic noise prediction for long-span bodies," *Journal of Sound and Vibration*, vol. 306, no. 3-5, pp. 564–579, 2007.
- [120] G. Cyril, "Isolated CADWIE wheel ELSA unsteady computation," Technical Report, RP0833855, Airbus France S.A.S, 2008.
- [121] R. K. Amiet, "Refraction of Sound by a Shear Layer," *Journal of Sound and Vibration*, vol. 58, no. 4, pp. 467–482, 1978.
- [122] S. Spagnolo, *Unsteady Aerodynamic Loads on Aircraft Landing Gears*. PhD thesis, University of Southampton, 2016.
- [123] M. Aubert, "Active Control of Landing Gear Loads and Noise Using Momentum Injection," tech. rep., ANTC, University of Southampton, 2015.
- [124] C. K. W. Tam and F. Q. Hu, "An Optimized Multi-Dimensional Interpolation Scheme for Computational Aeroacoustics Applications Using Overset Grids," in *10th AIAA/CEAS Aeroacoustics Conference*, AIAA 2004-2812, 2004.
- [125] Y. Du, *Supersonic Jet Noise Prediction and Noise Source Investigation for Realistic Baseline and Chevron Nozzles Based on Hybrid RANS/LES Simulations*. PhD thesis, The Pennsylvania State University, 2011.

- [126] Y. Hou and D. Angland, “A Comparison of Wall Functions for Bluff Body Aeroacoustic Simulations,” in *22nd AIAA/CEAS Aeroacoustics Conference*, AIAA 2016-2771, 2016.
- [127] NASA, “2D Zero Pressure Gradient Flat Plate Verification Case.” <http://turbmodels.larc.nasa.gov/flatplate.html>.
- [128] Toto E. F, *Riemann Solvers and Numerical Methods for Fluid Dynamics*. New York: Springer, 3rd ed., 2009.
- [129] Y. Nomura, I. Yamamura, and S. Inawashiro, “On the Acoustic Radiation from a Flanged Circular Pipe,” *Journal of the Physical Society of Japan*, vol. 15, no. 3, pp. 510–517, 1960.
- [130] A. Rona, “The Acoustic Resonance of Rectangular and Cylindrical Cavities,” in *13th AIAA/CEAS Aeroacoustics Conference*, AIAA 2007-3420, 2007.
- [131] P. Bradshaw, D. Ferriss, and N. Atwell, “Calculation of Boundary Layer Development Using the Turbulent Energy Equation,” *Journal of Fluid Mechanics*, vol. 28, pp. 593–616, 1967.
- [132] A. Townsend, *The Structure of Turbulent Shear Flow*. Cambridge: Cambridge University Press, 1976.
- [133] J. Chicheportiche and X. Gloerfelt, “Effect of a Turbulent Incoming Boundary Layer on Noise Radiation by the Flow over Cylindrical Cavities,” in *17th AIAA/CEAS Aeroacoustics Conference*, AIAA 2011-2862, 2011.
- [134] A. Hazir, D. Casalino, and R. Denis, “Lattice-Boltzmann Simulation of the Aeroacoustic Properties of Round Cavities,” in *20th AIAA/CEAS Aeroacoustics Conference*, AIAA 2014-2894, 2014.
- [135] S. Desvigne, *Noise Radiated by a Cylindrical Cavity Placed in a Subsonic Flow: Experimental Study and Direct Acoustic Computation Via a High-Order Multidomain Approach*. PhD thesis, Ecole Centrale de Lyon, 2010.